Study - GOME-2 Error Assessment

Final Report

Version 1 December 2002

EUMETSAT Contract No EUM/CO/01/901/DK

serco

GOME-2 Error Assessment Study

Eumetsat Contract: EUM/CO/01/901/DK

Abstract

18th December 2002

R. Siddans, B. G. Latter, B. J. Kerridge *Rutherford Appleton Laboratory*
M. Weber, R. de Beek, J. P. Burrows *University of Bremen*
I. Aben, C. Tanzi, W. Hartmann *Space Research Organisation of Netherlands*
M.G. Wickett *Serco Europe Ltd*

The GOME-2 Error Assessment Study was commissioned to identify the factors which will limit the accuracies of *trace gas column* and *ozone profile* retrievals from GOME-2 and on the basis of quantitative simulation, recommend operational settings for GOME-2 or other necessary action.

The study was based on the application of retrieval schemes for trace-gas column retrieval (IUP) and ozone profile retrieval (RAL) developed over nearly a decade for application to GOME-1 flight data, in conjunction with state-of-the-art radiative transfer code (IUP). In the Task 1 of the study, the schemes were modified to simulate the performance of GOME-2 and applied to construct an error budget, spanning geographical / seasonal observing conditions and including limiting error sources (identified by SRON) as well as measurement noise.

In Task 2 of the study, specific errors and operational settings were investigated and their consequences for constituent retrieval assessed, namely:

- Sampling Options for Band 1 (i.e. Integration times and B1A/1B boundary)
- Spatial Aliasing (i.e. mapping of spatial structure into measured spectra due to sequential read-out during across track scan coupled to finite read-out time).
- Spectral Resolution & Slit-Function Shape
- Errors due to radiative transfer model assumptions including the pseudo-spherical and Lambertian surface approximations.
- The degradation of retrievals at the edge of the swath due to increased cloud obscuration & horizontal refractive index gradients.
- Errors due to incorrect pointing & geolocation.

In Task 3 of the study, the results of these simulations are compared to the base-line error budget and recommendations made with respect to operation of the instrument and for specific further action to mitigate errors which will otherwise significantly degrade the quality of geophysical products from GOME-2.

GOME-2 Error Assessment

Final Report

Version 1-1

Study Team

Dr Brian Kerridge (Science Coordinator)
Dr Richard Siddans
Mr Barry Latter

Space Science Department
Rutherford Appleton Laboratory
Chilton, Didcot
Oxfordshire
OX11 0QX
UK

Prof. Dr Ilse Aben
Dr C. Tanzi
Dr W. Hartmann

SRON
Earth Oriented Science Division
Sorbonnelaan 2
NL-3584 CA Utrecht
The Netherlands

Prof. Dr. J. P. Burrows
Dr Mark Weber
Dr Ruediger de Beek
Dr Vladimir Rozanov
Dr Andreas Richter

FB1 Institute for Environmental Physics (IUP)
University of Bremen
Postfach 33 04 40
D-28334 Bremen
Germany

Eumetsat Technical Officer:

Dr R Munro

EUMETSAT ·
Am Kavalleriesand 31
Postfach 10 05 55 ·
D-64295 Darmstadt
Germany

Study Manager

Mr M.G. Wickett

Serco Europe Ltd
Kempton Point
68 Staines Road West
Sunbury-on-Thames
Middlesex TW16 7AX
UK

Date: January 2003

serco

List of Contents

TASK 2: ANALYSIS OF ERROR SOURCES

Appendix A: Additional figures relating to Task 1 Tool Aadaptation and Definition of Data (RAL)

Contents List of CD-ROM File: GOME-2_FR_App_A.pdf

WP130: Acquisition of Input Data-sets

WP150: Basic GOME-2 retrievals and Instrumental Errors

NOTE:

At the end of this hardcopy version of the Final Report there is a full index of the above figures.

The complete set of additional figures relating to Task 1 is held on the accompanying CD-ROM, in file "GOME-2_FR_App_A.pdf". The CDROM contains an electronic version (in pdf format) of the complete GOME-2 Error Assessment Study Final Report.

Appendix B: Additional figures relating to Task 2 Tool Aadaptation and Definition of Data (RAL)

Contents List of CD-ROM File: GOME-2_FR_App_B.pdf

WP210: Spatial Aliasing

WP220: Processing Options for Band 1A

WP230: Reduction of Spectral Resolution

WP240: Atmospheric Profile Related Effects

WP250: Radiative Transfer Model Assumptions and Earth Curvature

WP260: Non-Lambertian Surface Reflectance

NOTE:

At the end of this hardcopy version of the Final Report there is a full index of the above figures.

The complete set of additional figures relating to Task 2 is held on the accompanying CD-ROM, in file "GOME-2_FR_App_B.pdf". The CDROM contains an electronic version (in pdf format) of the complete GOME-2 Error Assessment Study Final Report.

Appendix C: Optimal Operational Settings and Error Mitigation (RAL)

Contents List of CD-ROM File: GOME-2_FR_App_C.pdf

WP310: Summary plots of Task 1 and Task 2 errors

NOTE:

At the end of this hardcopy version of the Final Report there is a full index of the above figures.

The complete set of additional figures relating to Task 1 is held on the accompanying CD-ROM, in file "GOME-2_FR_App_A.pdf". The CDROM contains an electronic version (in pdf format) of the complete GOME-2 Error Assessment Study Final Report.

Appendix D: Diffuser Plate Spectral Structures

Contents List

Appendix E: Experiences on SCIAMACHY "Dichroic Features" (IUP)

Contents List

List of Tables

List of Figures

1 Introduction to GOME-2 Error Assessment Study

1.1 Scope

The GOME-2 Error Assessment Study was commissioned by Eumetsat with the following scope:

- To identify through quantitative simulations the factors which will limit the accuracies of trace gas column and ozone profile retrievals from GOME-2.
- On the basis of this quantitative assessment, to recommend operational settings for GOME-2 and, if necessary, other action to mitigate errors

1.2 Consortium

The study was conducted by the following consortium:

- Serco Europe Ltd (Prime Contractor, Study Administrator)
- RAL (Technical Coordinator; Ozone Profile Analysis)
- IUP (Trace Gas Column Analysis; Radiative Transfer Model Calculations)
- SRON (Assessment of Instrumental Errors)

1.3 Study Structure

The study was divided into three Tasks:

- Task 1: Tool adaptation and definition of input data
- Task 2: Analysis of error sources
- Task 3: Optimal operational settings and error mitigation

In Task 1, radiative transfer and retrieval models were developed for the simulation of GOME-2. These models were then applied to define a baseline retrieval error budget against which the significance of error sources simulated in Task 2 could be judged. In Task 3, this comparative assessment was made, and recommendations were put forward for operational settings, for other actions to mitigate errors, and for further studies.

An initial review of instrumental error sources and magnitudes was conducted in Task 1 by SRON. This activity benefited from SRON's extensive knowledge of instrumental issues for GOME-1 and GOME-2. An issue of key importance for GOME-2 is the extent to which its improved design for measuring and correcting for polarisation will benefit data quality. The review drew directly on findings from SRON's recent study for ESA, which covered this topic in depth (H.W. Hartmann and I. Aben, Final Report, GOME-2 Phase-B Polarisation Study, RP-GOME2-002SR/00, January 2001).

In Task 2, several key issues, which impact on operational settings and potentially significant error sources, were assessed in the following sub-tasks:

- WP210: Spatial Aliasing
  - mapping of spatial structure into measured spectra due to sequential read-out during across track scan coupled to finite read-out time
- WP220: Processing Options for Band 1A
  - Integration times and B1A/1B boundary
- WP230: Reduction of Spectral Resolution
  - In particular, the extent to which resolution can be degraded (to reduced sensitivity to under-sampling error), but also a consideration of the impact of errors in slit function shape knowledge
- WP240: Atmospheric Profile Related Effects
  - In particular, the degradation of retrievals at the edge of the swath due to increased cloud obscuration & horizontal refractive index gradients.
- WP250: Radiative Transfer Model Assumptions and Earth Curvature
  - Errors due to the use of the pseudo-spherical approximation in retrievals.
- WP260: Non-Lambertian Surface Reflectance BRDF
  - Errors due to the use of the Lambertian surface approximation in retrievals
- WP270: Pointing and Geolocation.
  - Errors due to incorrect pointing and geolocation

In Task 3, the results of these simulations were compared to the base-line error budget and recommendations made with respect to operation of the instrument and for specific further action to mitigate errors which will otherwise significantly degrade the quality of geophysical products from GOME-2.

1.4 General Approach

The schemes employed in retrieval simulations for ozone profiles and trace gas columns are based very closely on those applied to real GOME-1 measurements by RAL and IUP, respectively. Both these schemes are the result of nearly a decade of development work, so are now mature and have been demonstrated to be among the most reliable of their kind. Although the magnitudes of simulated errors are specific to the detailed formulations of these two particular algorithms, the conclusions and recommendations arising from this study are expected to prove quite robust and to be applicable also to other schemes, which might be adopted for operational processing of GOME-2 data.

For ozone profiles, the sensitivity of the *optimal estimation* retrieval scheme to wavelength ranges and *a priori* constraints was explored before embarking on the investigation of instrumental parameters and errors.

State-of-the-art radiative transfer models developed at University of Bremen permitted:

a) Calculations to be performed for a fully-spherical atmosphere using the CDI radiative transfer model[1]

b) Calculations with a pseudo-spherical version of CDI which, apart from numerical differences, is equivalent to the GOMETRAN model that is commonly used in GOME-1 retrievals.

[1] Another spherical radiative transfer code exists, which is named CDIPI. This model is specifically designed for limb viewing LOS. CDI is equivalent to CDIPI without Picard iterations (PI).

Pseudo-spherical and spherical versions of CDI were used to assess errors arising from (a) the pseudo-spherical approximation[2] and (b) the assumption of Lambertian surface BRDFs.

Most simulations in the study were performed for a set of realistic and representative geo-temporal scenarios (12 in total) which spanned a diverse range of observing conditions, including several surface albedos (typically 0.05 and 0.8) and a variety of view-angles spanning two of the GOME-2 swath-width options: 960 km and 1920 km. The conclusions and recommendations from this study are therefore expected to be applicable to GOME-2 observing conditions generally (though not universally).

Except for errors, which were sufficiently large to necessitate iterative, non-linear simulations, *linear mapping* was employed throughout this study. In this approach, the impact of a given error on sun-normalised radiances was calculated by perturbing the forward model, and the spectral signature of this perturbation was then mapped onto the retrieved ozone profile or trace gas column using the matrix algebra of optimal estimation.

1.5 Error Definitions and Baseline Error Budgets

1.5.1 General

In order to gauge the importance of error sources specifically identified for attention in this study, errors known to have affected GOME-1 retrievals were reviewed and a *baseline error* budget compiled. The components of the *baseline error* budgets for ozone profiles and trace gas columns are described below.[3]

1.5.2 Ozone profiles

The baseline *precision* of GOME-2 was defined as the *estimated standard deviation (ESD)* at each retrieval level, evaluated from the diagonal elements of the solution error covariance matrix (S_x) for the retrieval. The ESDs were based solely on linear propagation of *measurement noise* through the optimal estimation retrieval equations, adopting an *a priori* uncertainty of 100% on ozone at each level (with vertical Gaussian correlation lengths as described in the final report). Measurement noise is estimated from a GOME-2 noise model, which combines *photon noise* with *read-out* noise. Based on GOME-1 experience, measurement precision from this model is better than can realistically be achieved in fitting simulated to measured spectra (due to forward model errors and/or unaccounted for instrumental errors). "*Noise-floors*" corresponding to 1% and 0.05% of sun-normalised radiance were therefore imposed in Bands 1 and 2, respectively. Other errors were handled by *linear mapping*.

For retrieval levels at 20 km and above, the ESD is markedly lower than the *a priori* uncertainty. For retrieval levels below 20 km (i.e. at 0, 6, 12 and 16 km), however, the ESDs are often >50% of the *a priori* uncertainties, so the a priori constraint is quite significant. It should be borne in mind that the error estimates obtained by linear mapping will also have been influenced by this *a priori* constraint[4].

The sources and magnitudes of errors included in the *baseline error* budget by linear mapping are as specified in Table 0-1.

[2] The term pseudo-spherical approximation is applied to models in which attenuation of the incoming solar beam is calculated for a spherical atmosphere but the intensity of scattered radiation is calculated for a plane-parallel atmosphere.
[3] It should be noted that the baseline error budgets did not include clouds, spectroscopic or instrumental errors other than those described.
[4] In the limit in which there is no reduction in the *a priori* uncertainty at a given altitude, due to absence of information in the measurements, the retrieved ozone mixing ratio at that altitude will not deviate from the *a priori* value, and linearly mapped errors will be identically zero.

Error Source	Magnitude
Radiometry	2% of sun-normalised radiance
Wavelength-dependent degradation of scan-mirror UV reflectance.	Equivalent to uncorrected GOME-1 degradation after 3-years (excl. from RSS)
Residual error from polarisation correction	SRON prescription for GOME-2
Surface pressure uncertainty	10hPa
Temperature profile uncertainty	Error covariance matrix from IASI retrieval
Aerosol profile uncertainty	LOWTRAN "high" - "background" cases

Table 0-1: Components of baseline error budget for O_3 profiles

Linearly mapped *baseline errors* were combined in a root-sum-squared (RSS) way for comparison with the ESDs and with the specific errors addressed in this study.

It should be noted that, although a realistic *wavelength-independent* error in sun-normalised radiance was included in the RSS (in accordance with the error budget for pre-flight radiometric calibration), *wavelength-dependent* error in sun-normalised UV radiance arising from degradation in the UV reflectivity of the scan mirror was quantified (for a case equivalent to GOME-1 after three-years operation) but was not incorporated into the RSS. The reason for this is two-fold: firstly, it is very difficult to predict the character (e.g. wavelength and time dependencies) that such degradation will exhibit for GOME-2 and, secondly, if similar to GOME-1 Band 1, this would dominate over all other errors after several years of operation, unless corrected for.

Aerosol is highly variable in the troposphere, especially in the boundary layer, and also in the lower stratosphere following volcanic eruption. In this study, the aerosol profile was fixed in the GOME-2 FM to be the LOWTRAN "*background*" profile (as it is in the RAL GOME-1 ozone profile retrieval scheme) and enhancements to aerosol loading were treated as a potential source of error. As discussed in the final report, this error has been estimated by linear mapping of the spectral difference between LOWTRAN "*background*" and "*high*" cases. Aerosol loading in the LOWTRAN "*high*" case makes this a conservative estimate in many circumstances. However, it was beyond the scope of this study to investigate and account for errors in the FM due to neglect of cloud, and the nature of such errors is somewhat similar to that of a large tropospheric aerosol excursion. RSS *baseline errors* were therefore calculated both with and without inclusion of the mapped aerosol error. The latter can be considered to be a lower limit, applicable to a cloud-free, background aerosol situation[5]. The former can be considered to be representative of an extreme aerosol event and also indicative of pervasive, thin cloud.

In considering the specified errors and their importance in relation to the baseline GOME-2 error budget, it is useful to distinguish between those, which vary in a quasi-random way with time and location, and those which vary in a non-random way. The former affect precision but can be reduced by averaging, whereas the latter give rise to systematic biases, which cannot be reduced by averaging but can in certain conditions be amenable to *a posteriori* correction. The more relevant comparisons for the quasi-random and non-random errors are therefore with the ESD and RSS, respectively. In the following sections, quasi-random errors are deemed to be significant if comparable to the ESD and non-random errors are deemed significant if comparable to the RSS. The RSS is typically <5% at 20 km and above and ~10-20% at 16 km and below.

[5] This lower limit would also apply if accurate independent information on aerosol/cloud scattering properties within the GOME-2 pixel could be derived either from other GOME-2 measurements (e.g. O_2 A-band and/or PMDs) or from co-located AVHRR3 images.

1.5.3 Trace gas columns

The standard DOAS approach, as investigated in this study and used in operational GOME-1 retrieval, consists of a two-step procedure. Firstly, a slant column density is retrieved from spectral fitting. Secondly, airmass factors are calculated using a multiple scattering radiative transfer model (RTM), assuming *a-priori* knowledge of the profile shape. Division of the slant column density by the airmass factor results in the vertical column density (total column). Both steps involve errors, which can be combined into an overall error budget. In the application to real data, the error sources from both steps can be distinguished. In this study, however, perfect *a-priori* knowledge has been assumed, so a distinction between AMF and slant column errors for a given error source is not always clear-cut.[6].

Attribution of the error sources to AMF and/or slant column has important implications for strategies of error mitigation. Slant column errors tend to be instrument related and improvable only by operational settings or hardware changes. On the other hand, errors assigned to AMF can be reduced by algorithm improvements.

For trace gas columns, photon noise and read-out noise were combined using the GOME-2 measurement noise model and ESDs were calculated by fitting the Ring cross-section in addition to trace gas columns. Residual errors following the application of the polarisation correction were linearly mapped but found to be negligible. Errors potentially arising from spectral structures in the diffuser plate BRDF were imported directly from a study on GOME-1 (see annex to Final Report), where they had been shown to be dominant for trace gases other than ozone.

In the following sections, the specified error sources analysed as part of this study are referenced to the basic ESDs for an integration time of 0.1875 sec. This corresponds to a 40x 80 km^2 ground pixel area at nominal swath width of 1920 km across-track. In general, error sources are considered significant if they are of same order of magnitude or higher than the baseline ESD.

[6] An extensive study of possible AMF errors due to assumptions made in RTM and imperfect *a-priori* knowledge was beyond the scope of this study.

TASK 1: TOOL ADAPTATION AND DEFINITION OF DATA

2 Introduction to Task 1

2.1 Overview

In Task 1 radiative transfer and retrieval models are developed for the simulation of GOME-2. These models are then applied to define a baseline retrieval error budget against which the significance of error sources and operational settings, simulated in Task 2, can be judged. The work comprises the following sub-tasks:

WP110: Ozone Profile Algorithm (RAL) - adaptation of the RAL GOME-1 ozone profile retrieval scheme for application to GOME-2.

WP120: Tracegas Column Algorithm (IUP) - adaptation of trace-gas column retrieval schemes at IUP

WP130: Acquisition of Input Datasets (RAL, IUP) - definition of geophysical scenarios to simulate for GOME-2 based upon the METOP orbit geometry. Collection of required datasets for Task 2, including Landsat-TM images and ECMWF temperature fields. Under this work package, forward model development was carried out at IUP to allow simulations with the CDI code to provide required inputs for Task 2

WP140: Definition of GOME-2 Instrumental Errors (SRON) - a review of key errors likely to limit retrieval precision for GOME-2 and quantification of error spectra where possible

WP150: GOME-2 Retrievals - models developed in WP110 and WP120 are applied for the scenarios defined in WP130 to define a base-line error budget for ozone profile and trace-gas column retrievals. The impact on retrieval of the key error sources identified in WP140 is quantified

3 WP110: Ozone Profile Algorithm (RAL)

3.1 Introduction

Code, which was developed at RAL to carry out ozone profile retrieval from GOME-1 flight data [3-6], has been adapted and extended to simulate the performance of GOME-2. The code comprises the components described below.

3.2 Radiative transfer model (RTM)

Back-scattered radiances are simulated using the GOMETRAN++ radiative transfer model [3-8] in conjunction with the 0.01 nm resolution solar spectrum of [3-4]. The atmospheric models, surface albedo, solar and viewing geometry used for the simulations to be conducted in this study are described under WP131, below. The Ring effect is calculated using a single-scattering approximation, by convolving the back-scattered radiance (phot/s/cm2/nm/sr) with the Raman cross-sections for N_2 and O_2 from [3-4]. The RTM calculates weighting functions (derivatives with respect to state parameters) analytically.

3.3 Instrument model (IM)

The sampling of the incident back-scattered radiance and direct solar-irradiance in the spectral and field of view (FOV) domains are simulated by appropriate convolutions of intensities calculated by the RTM. For the baseline simulations, reported here, the following parameters are assumed for GOME-2:

Band 1A/B Boundary:	283 nm.
Integration time:	12s (B1A), 0.1875s (B1B, 2, 3, 4)
Swath width:	1920 km (ground pixel size 1920 x 80 km (B1A), 80 x 40 km (B1B, 2, 3, 4)).
Spectral Resolution:	2 pixels (specified by EUMETSAT). Dispersion across the detector array is taken from [3-1], implying resolutions of 0.23, 0.27, 0.43 and 0.42 nm/pixel in Bands 1 to 4.
Slit function:	Gaussian with full-width-half-maximum (FWHM) as above is assumed for the Task 1 simulations. Further investigation of slit function shape and width has been carried in Task 2 (WP230).

To simulate the effect of the FOV, pencil-beam (infinitesimal FOV) spectra are calculated every 5 degrees of scanner angle and averaged over the FOV. The variation in solar geometry across the swath is accounted for by interpolating orbit propagator data supplied by ESTEC for each scenario to the required scanner angle (see WP131).

In Band 2, where a very accurate fit is required to the measured spectrum, the spectral convolution is performed on radiance (including Ring effect) and irradiance separately. The sun-normalised radiance used in retrieval simulations is then formed from the ratio of the two, accounting for potential saturation effects in deep Fraunhofer lines. A wavelength miss-registration between the back-scattered radiance and solar-irradiance can be simulated, to allow so-called under-sampling errors to be modelled (subject to the accuracy of the solar reference spectrum used to simulate the spectra).

In Band 1, the simulated, monochromatic, sun-normalised radiance is formed before convolution with the slit-function, without accounting for miss-registration errors (sufficiently accurate for this band).

3.4 Noise model (NM)

The approach adopted to simulate GOME-2 signal-to-noise for each selected scenario is based on data in [3-2] and [3-3].

The signal (in electrons) detected is

$$F_e = F_p.A_f.T_o.\Omega.R.t.Q_e.S_{pr} + I_d.t/e$$

Where

F_p is the incident radiance (averaged over FOV and slit function), in Phot/s/cm2/nm/sr, as output for each scenario by the IM, above.

A_f is the effective telescope area (0.98 cm^2 for Bands 1 and 2; 0.253 for Bands 3 and 4)

T_o is the transmission of the optics

Ω is the view solid angle (defined by slit dimensions to be 2.4e-3sr)

R is the pixel spectral width /nm (defined from [3-1], above)

t is the integration time /s, as defined above

Q_e is the quantum efficiency

S_{pr} is the fraction of energy incident on the pixel, assumed to be 1 to account for contribution of adjacent pixels

I_d is the dark current. Defined in [3-3] to be 3.91e-16 Amps, at detector temperature –38°C.

e is the electron charge / Coulombs

The product $A_f.T_o$ is reported in [3-2] based upon measurements at the individual component level. The tabulated data (for unpolarised light) for each band has been extracted from this report, and is linearly interpolated to each detector pixel in each band, from the reported spectral points.

Q_e is taken from the tabulated values in [3-3], and linearly interpolated to each detector pixel from the reported spectral points.

Noise on each pixel is calculated by

$$\Delta F_e^2 = F_e + \Delta F_r^2$$

Where read-out noise, ΔF_r, is defined in [3-3] to be 1700 electrons rms.

The signal to noise ratio (F_e /ΔF_e) in each spectral element for the backscattered and direct-sun views is then used to determine the random error on the sun-normalised radiance.

3.5 Retrieval model

Retrieval simulations are based on optimal estimation [3-7]. Results are based on a linearisation of the forward model (FM), comprising RTM and IM above, about linearisation points defined by the selected scenarios (see WP131), such that the change in the vector of measurements, *y*, for a given change in the state vector, x, is:

$$\Delta y = K\,\Delta x$$

Where weighting function matrix K, contains elements $K_{ij} = \delta y_j/\delta x_i$, the partial derivatives of measurement *j* with respect to state vector element *i*.

If x represents a set of retrieved quantities for which, the covariance of x after retrieval is given by:

$$\mathbf{S_x} = (\mathbf{S_a}^{-1} + \mathbf{K}^t\mathbf{S_y}^{-1}\mathbf{K})^{-1}$$

Where S_a, the a priori covariance is used to regularise the retrieval problem and describes knowledge of the state before information from the measurements is introduced. $\mathbf{S_y}$ is the measurement covariance matrix. For the GOME-2 simulations this is assumed diagonal, with elements corresponding to the variance of the random error on the measurements, derived from the NM (though note the "noise-floor" discussed below). The precision or estimated standard deviation (ESD) of x after retrieval is given by the square root of the diagonal elements of $\mathbf{S_x}$.

Other diagnostics are the measurement contribution function, $\mathbf{D_y}$, averaging kernel $\mathbf{A_k}$ and a priori contribution function $\mathbf{D_a}$, which describe the derivative of the retrieved state with respect to perturbations in, respectively, the measurement, true state and *a priori* state:

$$\mathbf{D_y} = (\mathbf{Sa} + \mathbf{K}^t\mathbf{S_y}^{-1}\mathbf{K})^{-1}\mathbf{K}^t\mathbf{S_y}^{-1}$$

$$\mathbf{A_k} = \mathbf{D_y}\,\mathbf{K}$$

$$\mathbf{D_a} = \mathbf{I} - \mathbf{A_k}$$

where $\mathbf{I}$ is the identity matrix.

The sensitivity of the retrieved state to perturbations in parameters other than those retrieved can be quantified by the so-called linear mapping approach. Given a measurement simulated with a modified RTM or IM parameter, y', the impact on the retrieved state of neglecting (or having no information about) the change is given by

$$(x'-x) = \mathbf{D_y}\,(y'-y)$$

The covariance in x, associated with a given covariance, $\mathbf{S_b}$, in model parameter vector b is given by

$$\mathbf{S_x}^b = \mathbf{D_y}\mathbf{K}\mathbf{S_b}(\mathbf{D_y}\mathbf{K})^t$$

The retrieval algorithm implemented for this study follows closely the approach adopted by the RAL GOME-1 operational scheme. To cope with differences in field of view and the difficulty of obtaining *absolute* back-scattered radiance spectra of adequate accuracy to exploit temperature dependent structure in the Huggins bands, a 3-step approach is adopted as follows:

1. An O_3 profile is retrieved from sun-normalised radiances in the Hartley band between 265 nm and 307 nm, contributing information mostly in the stratosphere. Small regions within this spectral range are excluded to avoid NO gamma-bands. A retrieval grid of 0, 6, 12 km, then 4 km intervals up to 80 km is used. *A priori* errors of 100% are assumed, with a vertical correlation length of 6 km. (Rows/columns of $\mathbf{S_a}$ have Gaussian shape with 6 km FWHM). Lambertian surface albedo, Ring effect scaling parameter, and wavelength calibration are retrieved jointly with O_3. In contrast to the GOME-1 scheme, leakage current is not retrieved in the GOME-2 simulations. Should the Band 1A/1B boundary lie below 307 nm, and then two sets of auxiliary retrieved parameters (i.e. those other than O_3) are retrieved corresponding to each band.
2. The surface albedo for the Band 2 FOV is retrieved (jointly with Ring scaling parameter) from the window regions 335.3 - 336.2 and 338.2 - 340,0 nm, assuming the ozone profile retrieved from Step 1.
3. O_3 information is extended downwards into the troposphere by fitting measurements in the Huggins bands between 323 nm and 334 nm. The profile from Step 1 is taken as *a priori* and the associated covariance is formed by taking the ESDs output from the Step 1 retrieval and imposing an 8 km correlation length. To enable precise fitting to the temperature dependent structure in the band, the measurement vector is formed by taking the logarithm of the sun-normalised radiance and subtracting a second order polynomial. ($y = \ln(I/I_0) - P_2$, where P_2, is a second order polynomial fit to $\ln(I/I_0)$.). O_3 is

retrieved jointly with Ring effect scaling parameter, radiance spectrum wavelength calibration parameters, column amounts of BrO and NO_2, and surface albedo. The Step 2 retrieval with its associated ESD is used as *a priori* for surface albedo.

The ESD for O_3 from the Step 3 retrieval is reported as the ESD for the overall retrieval.

The linear mapping approach is somewhat complicated by the 3-step retrieval approach since the response of the Step-3 retrieval to perturbations in the measurements used in Steps 1 - 2 must be tracked through their respective contributions to the Step-3 *a priori*. The averaging kernel for the overall 3-step process is:

$$\mathbf{A_k} = \mathbf{D_y^3 K^3} + \mathbf{D_a^3 M_{13}} (\mathbf{D_y^1 K^1}) \mathbf{M_{13}^t} + \mathbf{D_a^3 M_{23}} (\mathbf{D_y^2 K^2}) \mathbf{M_{23}^t}$$

Where the superscripts denote the matrices for each single bands retrieval and $\mathbf{M_{13}}$ is the matrix (consisting entirely of 0s and 1s) which maps the elements of the Step-1 state vector corresponding to O_3 into the appropriate elements of the Step-3 state vector and $\mathbf{M_{23}}$ is the Step-2 to Step-3 mapping of surface albedo. Linear mapping is accomplished by substituting the **K**s in the above by the step-specific measurement-vector perturbations.

To account for a combination of errors in the FM and GOME calibration, limits are set on the fitting precision attempted in the retrieval by defining minimum values for the measurement variances expressed in $\mathbf{S_y}$. Based on GOME-1 experience these minimum random errors (or "noise floors") are 1%, 2% and 0.05% for Steps 1 - 3 respectively.

3.6 References

[3-1] "GO-0006: GOME-2 Optical Design Report. MO-NT-GAL-GO-0006"

[3-2] "GO-0022: GOME-2 EQM Optical Throughput. MO-NT-GAL-GO-0022"

[3-3] "MO-NT-GAL-GO-0023"

[3-4] Chance, K., and R. Spurr, "Ring effect studies, GOME Geophysical Validation Campaign. Workshop Proceedings", ESA WPP-108, pp.69-74, 1996

[3-5] Fortuin, J. P. F., and U. Langematz, "An Update on the Global Ozone Climatology and on Concurrent Ozone and Temperature Trends, Atmospheric Sensing and modelling", R. P. Santer (Ed.) pp. 207-216, Proc. SPIE 2311 Washington, DC, 1994

[3-6] Munro, R., R. Siddans, W.J. Reburn and B.J. Kerridge, "Direct Measurement of Tropospheric Ozone from Space Nature", v392 (6672), pp.168-171

[3-7] Rodgers, C. D., "Characterisation and error analysis of profiles retrieved from remote sounding measurements'', Journal of Geophysical Research, 95(D5), pp.5587-5595, 1990

[3-8] Rozanov, V., D. Diebel, R. Spurr, and J. Burrows, "Gometran: A radiative transfer model for the satellite project GOME", J. Geophys. Res., v102 (D18), pp. 21809-21823

4 WP120: Tracegas Column Algorithm (IUP)

4.1 Introduction

This work package was carried out by IUP.

4.2 Tracegas column retrieval

KVANT, the retrieval algorithm was, which was used in this study, uses the Differential Optical Absorption Spectroscopy (DOAS) method, which applies the Lambert-Beer Law as an approximation of the attenuated solar radiation backscattered from the earth atmosphere. Taking the logarithm of the sun-normalised intensity permits the linear relation between atmospheric optical depth and trace gas amounts to be exploited (Lambert-Beer Law) under certain assumptions. Absorption cross-sections of the trace gases, which are derived from laboratory measurements under different conditions, are fitted to the measured optical depth. Discrimination between fine-scale and broadband spectral features is achieved by subtracting a polynomial, which is simultaneously fitted. Subtracting the polynomial from the spectrum yields the differential spectrum, which mainly contains information about the atmospheric trace gas amounts. The main assumptions in the approximation used are:

- Weak trace gas absorption
- Weak altitude dependence of molecular absorption cross-section (negligible pressure and temperature dependences)
- Weak wavelength dependence of scattering within spectral window

Thus, from the depth of the differential absorption structures, trace gas amounts can be derived using the knowledge about their absorption cross-section and a polynomial fit to derive the differential spectra.

However, it should be noted that of all trace gases targeted by GOME-2, ozone do not fulfil these requirements. Ozone is a strong absorber and thus has strong wavelength dependence on the airmass factor; this makes conversion of slant columns into vertical columns more complex [3-1]. For GOME-1 retrieval, it has been shown that using AMF at the wavelength of largest absorption (here 325 nm for the 325-335 nm spectral window) suffices after regular slant column fitting of ozone [4-1].

Using GOME-2 satellite measurements, wavelength shifts between laboratory cross-sections, solar irradiance and earth radiance spectra may exist. These can be corrected by KVANT using a shift and squeeze correction scheme by applying a non-linear least squares fitting.

KVANT is operating nominally and runs on SUN and Linux PC under Fortran90.

Table 4-1: DOAS Fitting windows

Molecule	Spectral Region [nm]	Polynomial Order	Interfering Species
O_3	325-335	Quadratic	NO_2, Ring, (BrO)
NO_2	425-450	Quadratic	O_3, O_4, H_2O, Ring
OClO	363-393	Cubic	NO_2, O_4, BrO, O_3, Ring
BrO	344-360	Cubic	O_3(T), NO_2, O_4, OClO, H_2CO, Ring
O_3VIS	450-497	Quadratic	O_3(T), NO_2, O_4, H_2O, Ring

By A. Richter - personal communication

Air mass factors (AMFs) will be calculated using GOMETRAN/SCIATRAN [4-3] and CDI [4-4], [4-5] in order to test the plane-parallel atmosphere approximation. In selected cases comparison of AMFs derived from pseudo-spherical and fully spherical CDI are planned.

The Table 4-1 shows the DOAS fitting windows for the absorbers investigated in this study. The recommendations are based on GOME-1 experience.

4.3 Optimisation of RTM and DOAS algorithm

Additional tests have been made for consistency of the Radiative Transfer Model (RTM) and the KVANT retrieval algorithm in a closed-loop. As a result model and retrieval parameters and settings are now optimised for the GOME-2 error analysis. Potential error sources of the test system have been quantified as discrepancies in the retrieval results.

Perfect consistency of the input and output vertical columns can be achieved only if:

- The same O_3 cross-section is used in the modelling and for fitting
- The parameterisation of temperature (altitude) dependence of absorption can not be fully accounted for in the slant column fitting, even if two temperature cross sections are included in the retrieval
- No interpolation has been applied; spectral interpolation can be avoided by using the same wavelength grid for all cross-section spectra
- The same cross-sections and wavelength grids are used in modelling and retrieval.
- The same RTM and identical trace gas climatologies are used for calculation of radiances and AMFs

As an example when using SCIATRAN AMFs, the difference in the vertical column retrieved from CDI and SCIATRAN spectra is about 0.7% for a mid-latitude April MPI scenario.

With the exception of using modified DOAS instead of standard DOAS, the calculation of AMF can be done only for a few specific cases in order to get an estimate for the overall error budget. For adjusting the proper instrumental parameters, errors in the slant column results are the driving and limiting factors.

KVANT, a Fortran 90 code for DOAS retrieval, is currently running on a SUN and Linux PC. It has been thoroughly tested for SO_2 retrieval [4-2] and is currently used for error assessment in the SCIAMACHY Level 1 to 2 processor study.

4.4 Multiple fitting windows for ozone

Spectral fitting of multiple windows is currently not possible with KVANT. The Serco GOME-1 Trace Gas Study (ESA contract 10728/94/NL/CN) remarked in Section 5.6: "The most general conclusion of all is that ... the ultraviolet windows are the preferred choice for the DOAS fitting process." This study also confirmed that 325-335 nm window is an optimum choice.

Error estimates for other UV windows showed similar error statistics. Combining visible and UV fitting windows may enable separation of tropospheric and stratospheric ozone, but it requires development of a new algorithm. This is beyond the scope of this study. Since this provides large merit and represents a novel approach, a new EUMETSAT/ESA study to focus on tropospheric ozone (trace gas) retrieval is proposed.

4.5 References

[4-1] J.P. Burrows, M. Weber, M. Buchwitz, V.V. Rozanov, A. Ladstätter-Weissenmayer, A. Richter, R. de Beek, R. Hoogen, K. Bramstedt, K.-U. Eichmann, M. Eisinger und D. Perner, "The Global Ozone Monitoring Experiment (GOME): Mission Concept and First Scientific Results", J. Atm. Sciences, 56, 151-175, 1999

[4-2] M. Eisinger and J.P. Burrows, "GOME observations of tropospheric sulphur dioxide, European Symposium on Atmospheric Measurements from Space", Proc. ESAMS'99, ESA-WPP-161, 421-424, 1999

[4-3] Rozanov, V. V., Diebel, D., Spurr, R. J. D., and Burrows, J. P., "GOMETRAN: A radiative transfer model for the satellite project GOME - the plane-parallel version". J. Geophys. Res., 102, 16683-16695, 1997

[4-4] Rozanov, A., V. Rozanov, and J. P. Burrows, "Combined differential-integral approach for the radiation field computation in a spherical shell atmosphere: Non-limb geometry", J. Geophys. Res., 105, 22937-22942, 2000

[4-5] Rozanov, A., V. Rozanov, and J. P. Burrows, "A numerical radiative transfer model for a spherical planetary atmosphere: Combined differential--integral approach involving the Picard iterative approximation", J. Quant. Spectrosc. Radiat. Transfer, 69, 491-512, 2001

5 WP130: Acquisition of Input Datasets (RAL)

5.1 Introduction

Thus section describes the acquisition of external input data-sets required to conduct the retrieval simulations in Task 1 and Task 2.

5.2 GOME-1 and ATSR-2 products from delta-validation exercise (WP131)

It was agreed at the kick-off meeting that a limited number of scenarios would be defined to span the GOME-2 observing conditions, and that conclusions would be based on retrieval simulations for these scenarios. GOME-1/ATSR-2 data for the Delta-validation exercise was agreed at the KO meeting to no longer be required for the study. Scenarios have been defined by agreement between University of Bremen and RAL to consist of the following basic cases

- 4 seasons represented by 15 January, April, July, October
- 3 latitudes: 5N, 55N and 75N
- 2 Lambertian surface albedos (0.05 and 0.8)

(12 geographical/temporal scenarios, simulated with 2 surface albedos = 24 basic cases.)

The January 75N case is not observed in daylight by GOME-2, and so this case is replaced by October 75^{o}S (Antarctic spring).

Trace gas and temperature / pressure profiles assigned to each scenario are described in Section 6 and are illustrated in Appendix A in Figures A2.1.

GOME-2 solar / observing geometry was taken from orbit propagator data provided by ESA / M. Eisinger. Geometrical details are indicated in Section 6 and together with the O_3 profile basic retrieval simulation plots.

For O_3 profile retrievals, it is not possible to present results in a compact graphical form for all viewing angles across swath for all 24 scenarios. Results are presented for nadir, and the two extremes of the 1920 km across-track swath to identify the range of conditions across the swath.

5.3 Selected Landsat-TM images (WP132)

A limited number of LANDSAT 7 ETM+ images are available free-of-charge from the NERC Earth Observation Data Centre (NEODC) based at RAL. Most of the images archived at NEODC had been selected to contain large cloud-free areas, and so many are not well suited for the purposes of this study. In addition to the NEODC data, a few extra scenes have been acquired from OhioLINK's Landsat 7 Satellite Data Server (http://dmc.ohiolink.edu/GEO/LS7).

All of images have been reviewed and the most promising selected for further investigation in Task 2. Selected images are shown in Figure A1.1.1 and Figure A1.1.2 in Appendix A.

5.4 ECMWF temperature analyses (WP134)

Access to ECMWF temperature analyses was obtained at RAL. A day on which extensive tropopause folding was observed was selected (26 July 1988) to be used, as extreme example of temperature gradients within the GOME-2 FOV in Task 2.

6 WP130: Acquisition of Input Datasets (IUP)

6.1 Introduction

This work package was carried out by IUP.

6.2 CDI simulation of spectra

Using CDI [6-10] sun-normalized spectra have been calculated for selected twenty-four atmospheric scenarios. CDI calculates the radiation field in a spherical homogeneous atmosphere. Source functions are calculated as a psuedo-spherical approximation, which is considered sufficient for lines-of-sight available to GOME-2. The spectral range encompasses all fitting windows of ozone profiles and trace gas columns (270-394 nm, 425-555 nm). Extension to 555 nm was done to enable O3 visible retrieval in channel 3. The basic configuration for CDI is summarized in the Table 6-1:

Table 6-1: Basic Configuration of CDI

Two spectral windows:

270.00 – 396.00 nm with sampling of 0.12 nm (1051 spectral points)

420.00 – 555.08 nm with sampling of 0.24 nm (554 spectral points)

Absorbing gaseous components:

O_3, NO_2, ClO, OClO, BrO, HCHO, SO_2, Ring, O_2, H_2O,O_4

Aerosol loading:

Boundary layer aerosol type 0 - 2 km

- aerosol type - maritime
- visibility -23 km
- humidity - 80 %

Tropospheric aerosol 2 - 10 km

- visibility -23 km
- humidity - 80 %

Stratospheric aerosol 10- 30 km

- aerosol loading - background
- aerosol type - background

Mesospheric aerosol 30 - 60 km

- aerosol loading - normal mesosphere

Viewing geometry:

zenith line-of-sight angles from - 46.535 deg to 46.535 deg

Scan time τ = 4.5 sec.

Sampling time δ = 0.01875 sec.

Number of line-of-sights τ / δ = 240.

Surface properties:

Wavelength independent Lambertian albedo (BRDF only special cases)

Horizontal homogeneous layering

Simplification:

Cloud-free conditions

Refraction is not included

Pseudo-spherical geometry is used

Zenith and azimuth angles for satellite and sun are taken from representative orbits on January 15, April 15, July 15, and October 15 as shown in Table 6-2 [M. Eisinger, personal communication]. Here, the definition of relative azimuth angle follows the convention in radiative transfer models as explained later in Section 6.5

N	Month	Latitude deg	SZA Deg	Rel. az. Deg (east/west)	Albedo %
1	January	5 N	46.5	23.3/156.7	5
2					80
3		55 N	79.8	46.8/133.2	5
4					80
5	April	5 N	36.7	22.0/158.0	5
6					80
7		55 N	49.5	39.6/140.4	5
8					80
9		75 N	65.0	50.4/129.6	5
10					80
11	July	5 N	40.4	40.0/140.0	5
12					80
13		55 N	39.0	31.8/148.2	5
14					80
15		75 N	53.4	48.5/131.5	5
16					80
17	October	5 N	35.8	10.0/170.0	5
18					80
19		55 N	66.3	49.4/130.6	5
20					80
21		75 N	83.4	54.3/125.7	5
22					80
23		75 S	76.0	55.0/125.0	5
24					80

Table 6-2: Viewing Geometry of twenty-four atmospheric scenarios

Angles are given for a topocentric coordinate system with origin at satellite altitude (824km)

On a SGI Alpha computer calculations take about 40 min for an entire 240 line-of-sight scan simulation and approximately 2.5 hours on a Cray Jedi super computer.

6.3 Graphical presentation of CDI simulated spectra

Figures 5-1 and 5-2 show the spectral and line-of-sight dependence of the sun-normalised radiance for an October 55°N scenario with albedos of 0.05 and 0.80, respectively. Solar zenith angle is 66.3° and the relative azimuth between LOS and sun is 67° (east view). For low albedo scenarios we see only a slight asymmetry in the intensity around the nadir viewpoint. Also the differential structure (see 425-450 nm range) is rather small. As the albedo increases, the differential structures gets more pronounced. A larger asymmetry around the nadir point is observed with high albedos in the UVA and visible spectral range. Only for relative azimuth angles of 90° are the spectra symmetric, which could only be obtained with a local equator crossing time at noon. For the graphical presentation trace gas climatologies were taken from the MPI 2D CTM climatology, which is part of the GOMETRAN/SCIATRAN package [C. Brühl, personal communication].

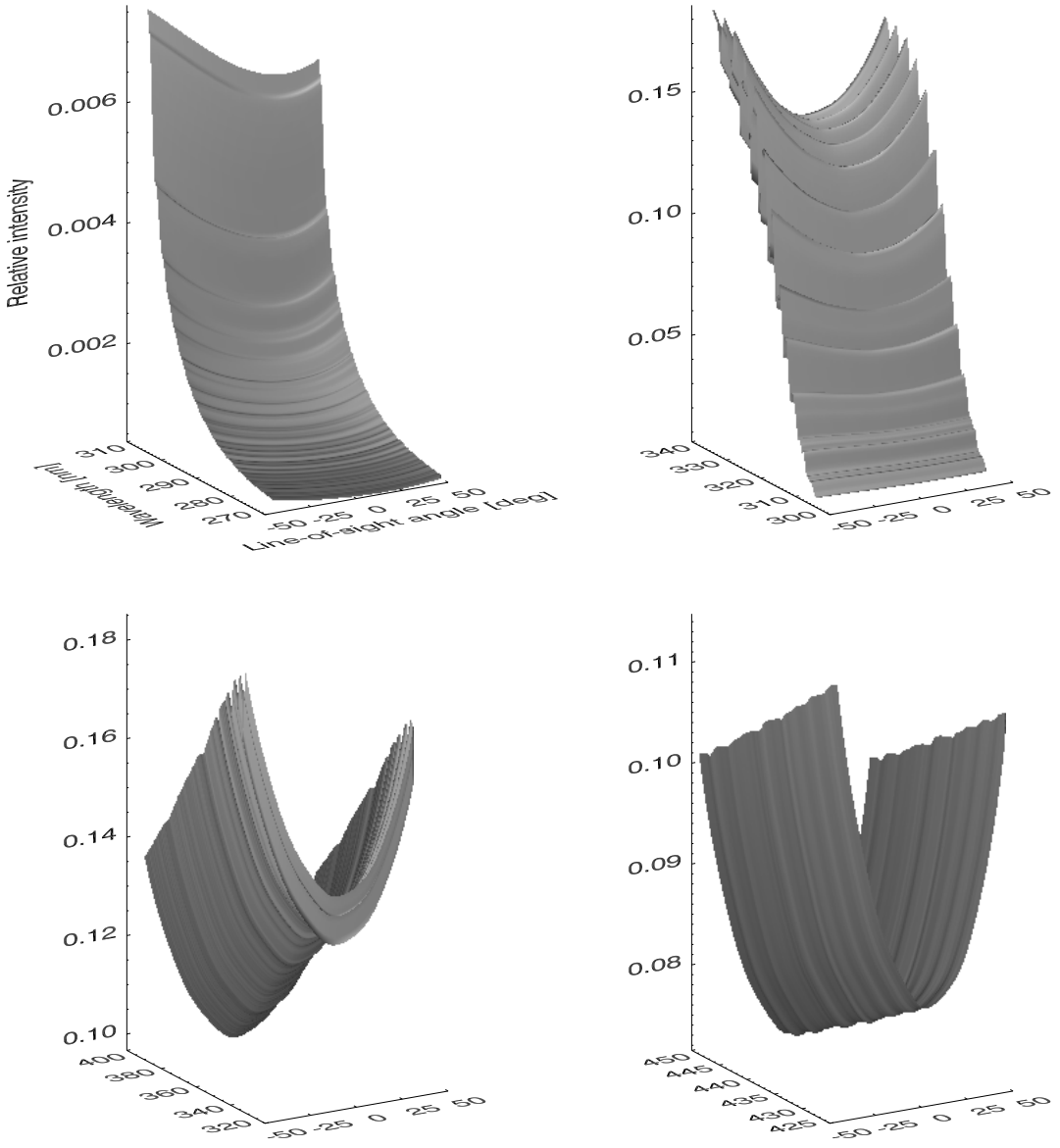

Figure 6-1: CDI intensity spectra for an October scenario at 55°N with albedo of 5%.

Top left: 270-310 nm
Top right: 300-340 nm
Bottom left: 320-400 nm
Bottom right: 425-450 nm
SZA: 66.3°,
Relative azimuth angle between LOS and sun: 67.0°

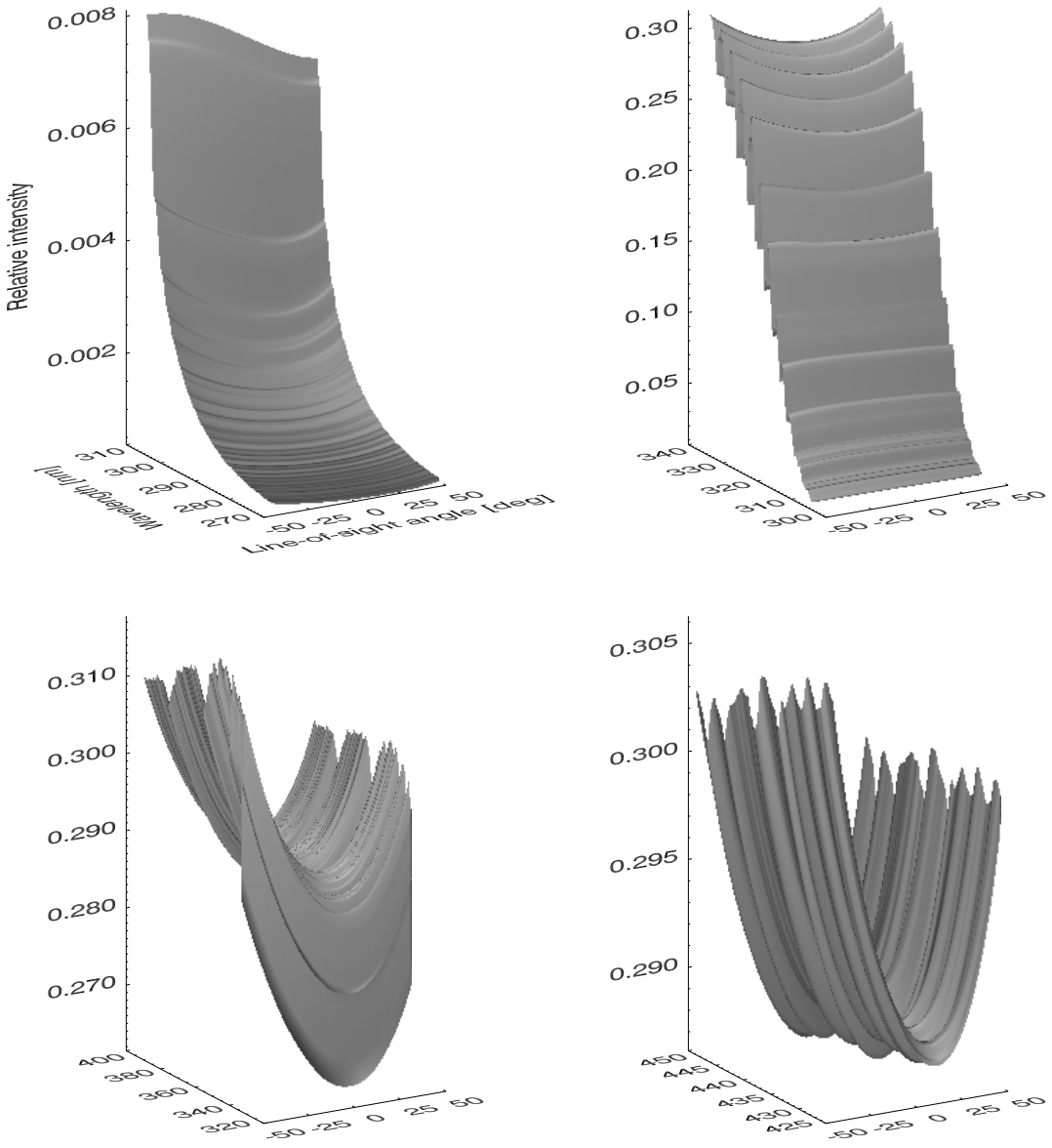

Figure 6-2: **CDI intensity spectra for an October scenario at 55°N with albedo of 80%**

Top left: 270-310 nm,
Top right: 300-340 nm,
Bottom left: 320-400 nm
Bottom right: 425-450 nm.
SZA: 66.3°,
Relative azimuth angle between LOS and sun: 67.0°.

6.4 Generation of spectra with realistic trace gas profiles

Particularly for the minor trace gases (other than ozone), no climatological informattion based upon global observations are available. For sporadic events such as local regional pollution events (industry and biomass burning) statistical information is rather rare and, because of the limited spatial and temporal extent of such events, are not well represented in zonal climatologies.

In preparation for the GOME-2 data processor (Development of trace gas climatologies for the ozone monitoring satellite application facility, contract with FMI, Finland), a new BrO climatology has been prepared based upon SLIMCAT 3D chemical transport model results during the period October 1996 until October 1997 (courtesy Marco Bruns, IUP Bremen). In order to account for photochemical changes, photochemical box model results (BRAPHO) initialised with SLIMCAT were used to account for solar zenith angle dependence of the photochemical species. Data from other trace gas data (NO_2, OClO, O_3) were also extracted from the model calculation. From this database the most suitable scenarios fitting conditions of the GOME-2 scenarios were selected according to Table 6-2. The new SLIMCAT/BRAPHO climatology, however, contains only stratospheric profiles because of lacking observational tropospheric data (also SLIMCAT and BRAPHO are optimised for stratospheric applications). In order to extend this tracegas profiles to 120 km altitude (as required for CDI), the temperature profile from the US standard atmosphere and constant VMR of all gases have been assumed above 58 km.

Those file names, which are colour-marked, have been modified by adding tropospheric profiles as follows:

1) Constant tropospheric O_3 number density profile (all)
2) Biomass burning/ biogenic emission (5N, July)
   - H_2CO 2ppb < 3 km (may affect BrO fit)
   - NO_2 taken from MPI-2D CTM
   - O_3 doubled < 5 km
3) Free tropospheric BrO (55N, April)
   - BrO 1ppt < 10 km (Fitzenberger et al., 2001)
4) PBL BrO explosion (75S, October)
   - BrO 50ppt < 2 km
   - O_3 0ppm < 2 km

In order to obtain elevated OClO amounts, 90° solar zenith angle trace gas profiles were assumed in the Antarctic ozone hole scene (75°S, October). At decreasing SZA, OClO rapidly photolyses. A large difference between MPI-2D and the SLIMCATR/BRAPHO is seen in the estimate of OClO. MPI-2D models a lower stratospheric (PSC chlorine activation) and a broad upper stratospheric maximum (background chlorine level) in the concentration profile, while SLIMCAT/ BRAPHO models only a strong lower stratospheric maximum. This is due to the fact that BrO has only a very weak maximum in the upper stratosphere (Figure 6-3). BrO and OClO are the major source of OClO. Table 6-3 summarises the SLIMCAT/BRAPHO trace gas climatologies, which most closely match the GOME2 scenarios. Differences in albedo cause changes in the total column due to varying photochemical activity.

SLIMCAT/BRAPHO Scenarios (Marco Bruns, private communication)					
			total column		
fitle	O_3 [DU]	NO_2 [10^{19}/m^2]	BrO [10^{18}/m^2]	OClO [10^{16}/m^2]	
9610am_lat18N_lon300_SZA40_a10.tg	252	1.944	0.180	0.095	
9610am_lat18N_lon300_SZA40_a90.tg	250	1.704	0.187	0.088	
9610am_lat55N_lon300_SZA69_a10.tg	276	1.796	0.267	0.249	
9610am_lat55N_lon300_SZA69_a90.tg	275	1.712	0.277	0.245	
9610am_lat77N_lon000_SZA86_a10.tg	262	0.952	0.324	0.498	
9610am_lat77N_lon000_SZA86_a90.tg	262	0.945	0.327	0.495	
9610am_lat77S_lon000_SZA90_a10.tg	152	1.539	3.174	4.261	PBL BrO
9610am_lat77S_lon000_SZA90_a90.tg	151	1.549	3.172	3.947	ozone hole
9701am_lat18N_lon300_SZA50_a10.tg	219	1.844	0.177	0.090	
9701am_lat18N_lon300_SZA50_a90.tg	218	1.647	0.182	0.085	
9701am_lat55N_lon000_SZA80_a10.tg	288	1.136	0.285	0.347	
9701am_lat55N_lon000_SZA80_a90.tg	288	1.114	0.289	0.341	
9704am_lat18N_lon300_SZA40_a10.tg	250	2.016	0.173	0.088	
9704am_lat18N_lon300_SZA40_a90.tg	247	1.781	0.180	0.081	
9704am_lat55N_lon300_SZA49_a10.tg	320	2.478	0.388	0.163	free troposph-
9704am_lat55N_lon300_SZA49_a90.tg	319	2.250	0.414	0.162	BrO
9704am_lat77N_lon000_SZA69_a10.tg	294	2.889	0.211	0.187	
9704am_lat77N_lon000_SZA69_a90.tg	293	2.769	0.229	0.194	
9707am_lat18N_lon300_SZA41_a10.tg	285	2.420	0.197	0.094	biomass
9707am_lat18N_lon300_SZA41_a90.tg	282	2.171	0.206	0.089	burning
9707am_lat55N_lon300_SZA39_a10.tg	311	3.424	0.234	0.117	
9707am_lat55N_lon300_SZA39_a90.tg	309	3.050	0.270	0.118	
9707am_lat77N_lon000_SZA59_a10.tg	292	4.235	0.208	0.077	
9707am_lat77N_lon000_SZA59_a90.tg	290	3.918	0.238	0.077	

Table 6-3: New modified SLIMCAT/BRAPHO scenarios

File name contains information on the month of the year, latitude and longitude, solar zenith angle, and albedo (0.1 and 0.9). Tropospheric modifications have been applied to colour-marked tracegas scenarios. (See text).

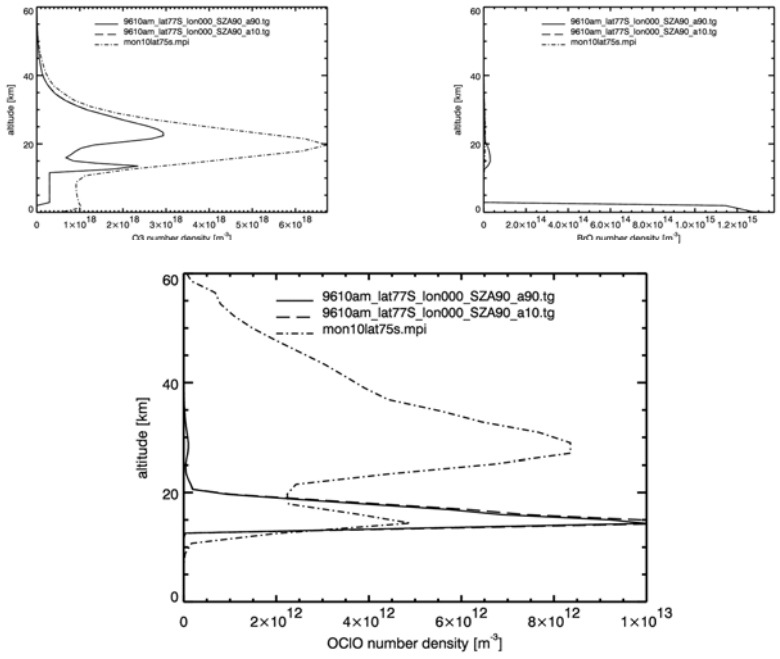

Figure 6-3: Concentration profiles of O_3, BrO, and OClO at 75°S in Oct 1996

This scenario shows a typical Antarctic ozone hole situation. Planetary boundary (PBL) layer BrO explosion of 50 ppt is included, which causes the PBL ozone to be completely depleted ("low ozone event"). Also shown are the corresponding zonal means from the MPI-2D climatology (dash-dotted lines). Note the difference in profiles due to albedo effects (dash: albedo 0.9, solid: albedo 0.1).

6.5 Topocentric coordinate system and relative azimuth definition

Table 6-4shows the relative azimuth angle definition used in GOMETRAN and CDI, which differs from the difference between the azimuth angles of satellite LOS and solar zenith angle in a topocentric coordinate system. Also shown in this figure are possible choices for origins of the topocentric coordinate system at satellite altitude, top-of-atmosphere, and surface (SAT, TOA, and GRD).

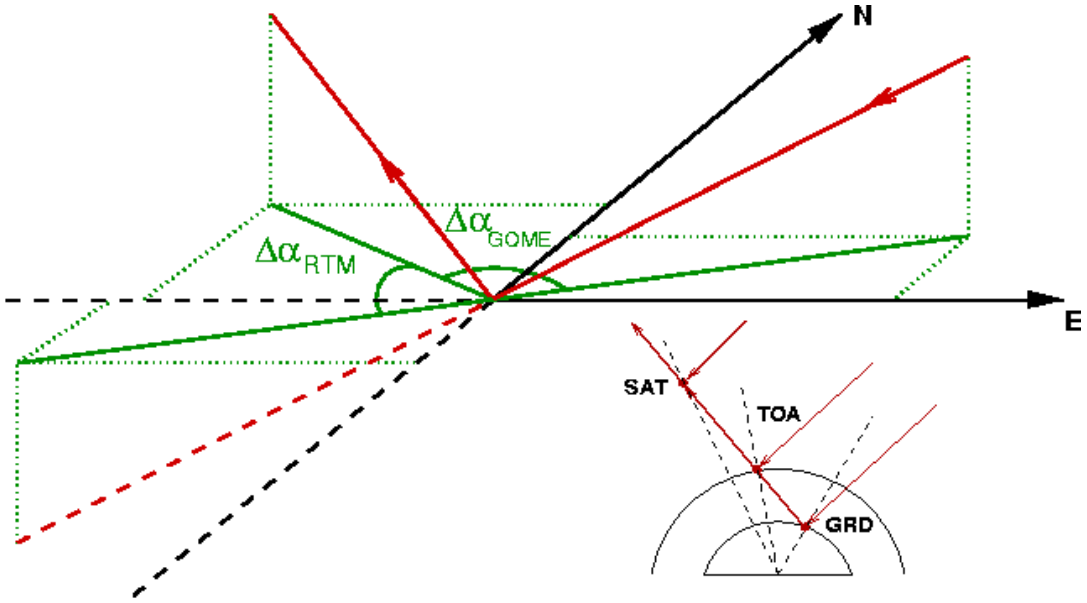

Figure 6-4: Definition of relative azimuth in RTMs ($\Delta\alpha_{RTM}$) in a topocentric coordinate system.

The relationship between the difference in azimuth angles of the GOME-2 LOS and the incident solar angle, $\Delta\alpha_{GOME}$, to the relative azimuth defined in radiative transfer models is $\Delta\alpha_{RTM} = \pi - \Delta\alpha_{GOME}$. Each point along the LOS of the satellite, can serve as an origin of the topocentric coordinate system.

The inset shows the most frequently used centre coordinates at satellite altitude (SAT), at top-of-atmosphere, e.g. 80 km altitude (TOA), and at the surface (GRD). CDI uses angles defined at SAT. For pseudo spherical approximations viewing and solar angles in a GRD and TOA centred coordinate systems have been alternatively used as representative angles in a plan-parallel atmosphere (Section 20, WP250).

6.6 Required number of simulated LOS for swath simulation

For each GOME-2 ground pixel a spectrum is obtained by integrating successive intensity spectra calculated for 10 LOS from the CDI simulations made for 240 LOS along the entire GOME-2 swath (one east-west scan comprises 24 ground pixels). To test the quality of this approximation, spectra calculated using 5 LOS for one ground pixel range have been integrated for comparison. Differences expressed as log-ratios are shown in Figure 6-5. Differences between 10-LOS and 5-LOS simulations of a GOME ground pixel are below 0.3% for all cases. It can be therefore concluded, that a 10-LOS approximation is sufficient for accurate GOME-2 ground pixel intensity simulation.

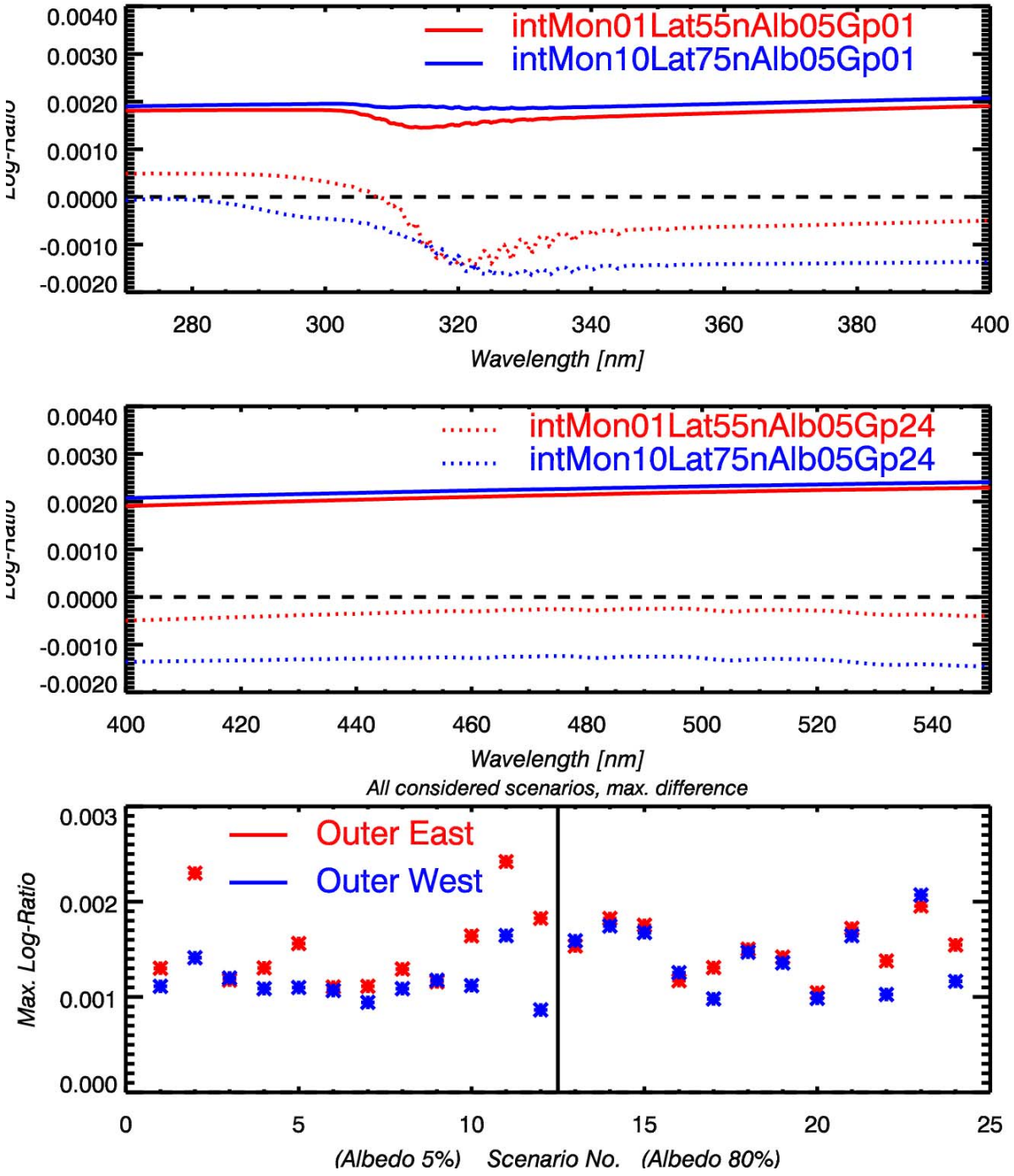

Figure 6-5: Differences of ground-pixel-equivalent intensity spectra (using nominal and equidistant LOS for scenarios)

Blue: extreme east pixel Red: extreme west pixel
Bottom: max absolute differences observed in all scenarios

Differences (log-ratios) of GOME-2 ground-pixel-equivalent intensity spectra are calculated using 10 (nominal) and 5 equidistant LOS for various scenarios and albedo of 0.05

6.7 BRDF parametrisation in CDI

6.7.1 RPV parameterisation

In preparation for WP260 a BRDF parameterisation was implemented in CDI. The goal is to find an optimum parameterisation for the BRDF, which is simple and computationally efficient. Reflected surface radiance usually shows not only a spectral but also a directional dependence. The spectral features can usually be described with a spectral dependent albedo. For describing directional dependence, a bi-directional reflectance distribution function (BRDF) is used. The BRDF has been measured in the last decades using ground and airborne experiments. BRDF effects have been obtained from space with AVHRR, in its vertical across-track plane of observation. Clear directional signatures for all azimuths are obtained from POLDER data. Specific directional effects in the hot spot and specular directions are well observed in these data [3-1].

Currently existing surface BRDF models are principally of three kinds:

1) Geometrically based
2) Radiative transfer theory based
3) Empirical.

Seven BRDF models have been tested by Cabot and Dedieu [6-2]. Their approach relies on fitting BRDF model parameters based up on NOAA AVHRR satellite measurements. The comparison of all models with observed reflectances gave similar results (rms error of reflectance around 0.03 - i.e. 10 %).

Privette et al. (1997) assessed the relative ability of 10 models to predict commonly used remote sensing products (nadir reflectance and albedo). For this purpose data from nine land cover types, ranging from soil to grassland and to forest has been used. It was found that overall the non-linear model of Rahman et al. [6-9] and the linear kernel-driven RossTickLiSparse model [6-11] was most accurate.

Yet another example of a BRDF can be found in [6-1], where the non-linear three-parameter model of Rahman et al. [6-9] has been successfully used for classification of boreal forest with the POLDER instrument aboard a NASA C-130 aircraft.

The BRDF model must have enough flexibility to be applicable over a wide range of surface types, conditions. Wavelengths and at the same time must also be as simple as possible to limit the additional computational cost.

We have selected the three-parameter non-linear RPV model, named after the initials of the authors of the Rahman et al. paper [3-1], which has been extensively tested with satellite and airborne BRDF measurements of various surfaces. Recently the RPV model has been successfully used to derive surface albedo parameters from Meteosat data [6-6], [6-7].

Another advantage of the RPV model is that fit-parameters of this model are available for a large number of surface types covering at least the visible and near-IR spectral range. In Table 5-4 RPV parameters for ten types of vegetation and two types of soil according to Lyapustin [6-5] are summarised. Table 6-5 summarises the equations and parameters used in Table 6-4.

N	Surface	ρ_0	Θ	k	ρ_0	Θ	k
		Visible			near-IR		
1	spruce	0.008	-0.308	0.554	0.050	-0.201	0.581
2	sparse erectophile	0.064	-0.001	1.207	0.278	-0.006	0.725
3	tropical forest	0.012	-0.169	0.651	0.303	-0.034	0.729
4	plowed field	0.072	-0.257	0.668	0.077	-0.252	0.678
5	grasses	0.014	-0.169	0.810	0.242	-0.032	0.637
6	broad leaf crops	0.012	-0.281	0.742	0.204	-0.089	0.658
7	Savannah	0.010	-0.287	0.463	0.219	-0.050	0.673
8	leaf forest	0.022	-0.228	0.633	0.285	-0.060	0.745
9	Conifers	0.018	-0.282	0.364	0.235	-0.095	0.758
10	hardwood forest winter	0.028	-0.175	0.768	0.066	-0.141	0.735
11	loam soil	0.147	-0.096	0.839	0.195	-0.097	0.850
12	irrigated wheat	0.027	-0.078	0.382	0.306	-0.008	0.606

By Lyapustin, 1999

Table 6-4: Best fit parameters of RPV model for different land covers

Table 6-5: RPV Equations for BRDF

$$\rho(\theta_s, \theta_v, \phi) = \rho_0 \; H(g) \; [1 + R(G)] \; \frac{\cos^{k-1}\theta_s \; \cos^{k-1}\theta_v}{(\cos\theta_s + \cos\theta_v)^{1-k}} \tag{1}$$

$\rho(\theta_s, \theta_v, \phi)$: surface bidirectional reflectance
ρ_0, k: empirical parameters
θ_s: sun zenith
θ_v: the line-of-sight zenith
ϕ: the azimuthal angle
$H(g)$: average scattering phase function
$R(G)$: hot spot function

$$H(g) = \frac{1 - \Theta^2}{(1 + \Theta^2 + 2\,\Theta\,\cos g)^{1.5}} \tag{2}$$

Θ: asymmetry factor (ranging from -1 to +1)
g: phase angle

$$\cos g = \cos\theta_s \; \cos\theta_v + \sin\theta_s \; \sin\theta_v \; \cos\phi \tag{3}$$

$$R(G) = \frac{1 - \rho_0}{1 + G} \tag{4}$$

G: geometry factor

$$G = (\tan^2\theta_s + \tan^2\theta_v - 2\tan\theta_s \; \tan\theta_v \; \cos\phi)^{0.5} \tag{5}$$

An example of the BRDF according to the RPV model is presented in Figure 6-6 for loam soil at 550 nm. The radius of the polar diagrams represents the viewing zenith angle θ, and the polar angle is the relative azimuth ϕ between view and sun direction. The lines in the polar diagram are contours of the reflectance in percent.

The general patterns of all the data in Table 6-4 (see also Figure 6-6) are similar. The reflectance shows the largest gradient in the principal plane and only small variations in the perpendicular plane. Only for grass in the near-IR (not shown) is the gradient in the perpendicular plane is larger. The maximum reflectance is always located in the so-called *hot spot* direction, where the viewing direction approaches the solar direction. The minimum reflectance is found in the forward scatter direction.

The reflectance magnitude depends on surface type. Thus, values of 1.8% at 550 nm and 10.4% at 864 nm can be found for spruce at nadir, contrasted with 25.1% at 550nm and 33.2% at 864 nm for loam soil. Grass shows a very strong wavelength dependence of the reflectance magnitude.

$$\rho_S(\theta_s, \theta_v, \phi) = \rho_0 \Big[\ H(g)\ [1 + R(G)]\ \frac{\cos^{k-1}\theta_s\ \cos^{k-1}\theta_v}{(\cos\theta_s + \cos\theta_v)^{1-k}} + \frac{\sigma}{\cos\theta_s}\Big]\ T \qquad (1)$$

$$T = t_1\ \exp[t_2\ (\pi - g)] + 1 \qquad (2)$$

$\rho_0 = 0.728$
$k = 0.946$
$\Theta = 0.042$
$\sigma = -0.003$
$t_1 = 2$
$t_2 = -4$

By Deguenther and Meerkötter, 2000

Table 6-6: RPV Equation for snow

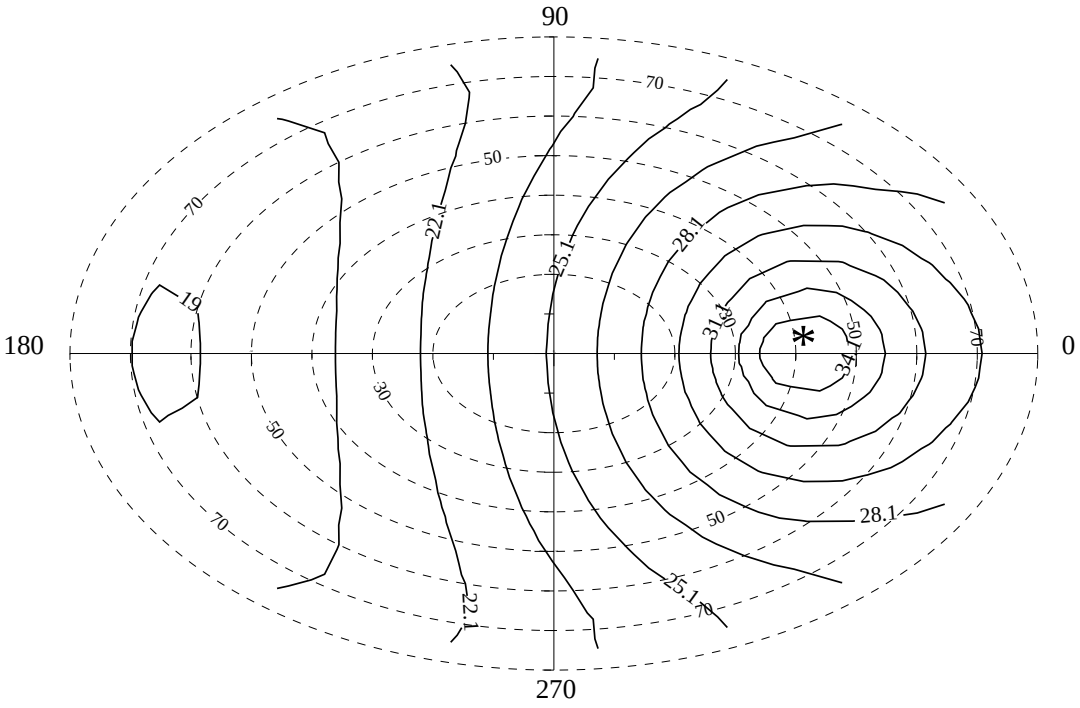

Figure 6-6: BRDF for loam soil at 550 nm (SZA=40°)

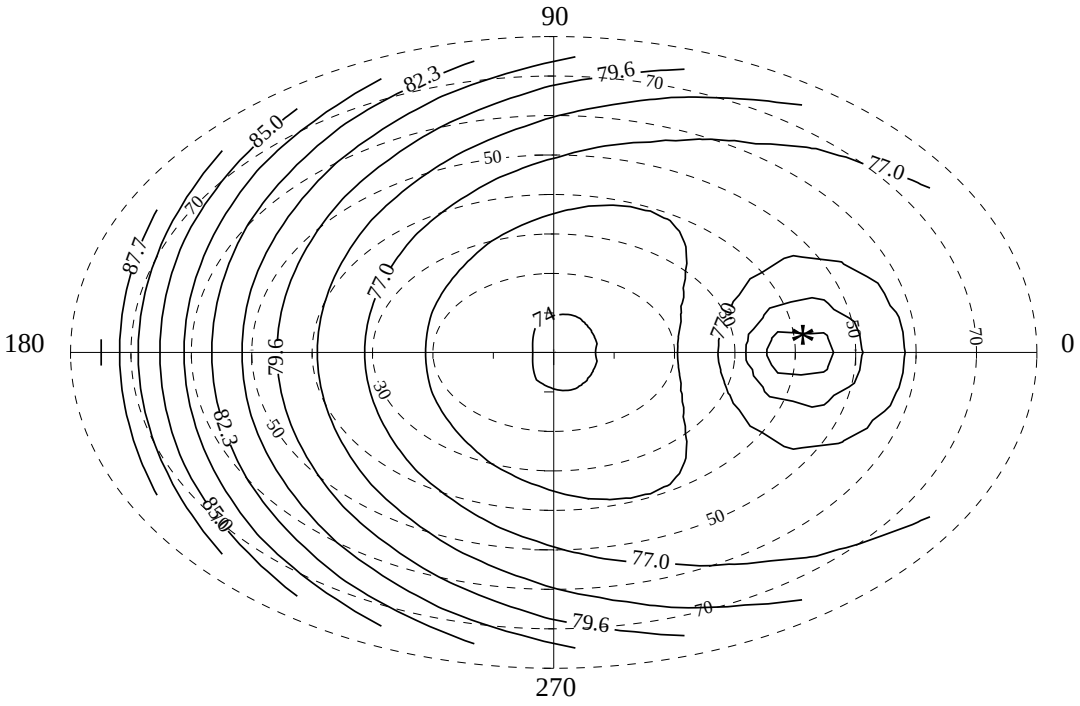

Figure 6-7: BRDF for Snow at 300-330 nm (SZA=40°)

6.7.2 Snow BRDF

For high reflectance surfaces we consider as an specific example snow covered surfaces. The corresponding BRDF has been parameterised on the basis of measurements by Warren et al. [6-12]. To approximate the measured data the four-parametric version of the bi-directional reflectance model by Rahman et al. [6-9] has been applied. An additional multiplicative term allowing a better parameterisation of the strong forward scattering by snow is introduced [6-3], see Table 6-6. A mean deviation of about 5% between the modified RPV model (ρ_o =0.728, k=0.946, Θ=0.042, σ=-0.003, t_1=2, t_2=-4 and normalised by A/π, where A is the cosine weighted upward hemispheric BRDF integral) and the anisotropic reflection factor measured by Warren et al. [6-12] has been obtained. The snow BRDF at 300-330 nm is displayed in Figure 6-7. As can be seen the magnitude of reflectance reaches about 88% in the forward scattering direction and shows large gradients both in the principal and perpendicular planes.

For different soil and vegetation types we have according to Table 6-4 different magnitudes of reflectance and shape parameters for the RPV distribution function. In this study (WP260) we propose two special cases:

1) The dark surface case, represented by ρ_o= 0.047, k=1.0, and Θ=-0.2
2) The bright surface case, represented by ρo=0.270, k=0.82 and Θ=0.0

As was pointed out by Pinty et al. [6-6], these values are representative for tropical forest and desert encountered in central and northern Africa, respectively. These two model BRDFs are displayed in Figure 6-7 and Figure 6-8. Together with snow BRDF and ocean glint we have four selected BRDF scenarios in WP 260.

6.7.3 Ocean Glint

Ocean glint causes strongly intensified hot spot in the bi-directional reflection distribution. They can be observed by GOME in the tropical region, when the relative azimuth between satellite and solar line-of-sight is 0°. The largest contribution under most circumstances is the Fresnel reflection of individual wave facets. The specular reflection of each facet accumulate to a complex pattern. The slope distribution of these facets was measured and parameterised as a function of wind speed by Cox and Munk, 1954. Important parameter is the effective wind speed and the refractive index of water selected. A detailed description of the calculation of the glint effect is given by Watts et al. [6-13]. Ocean glint BRDF was derived for a wind speed of 5 m/s and using the refractive index of pure water at 350 nm. Figure 6-10 shows the corresponding BRDF distribution.

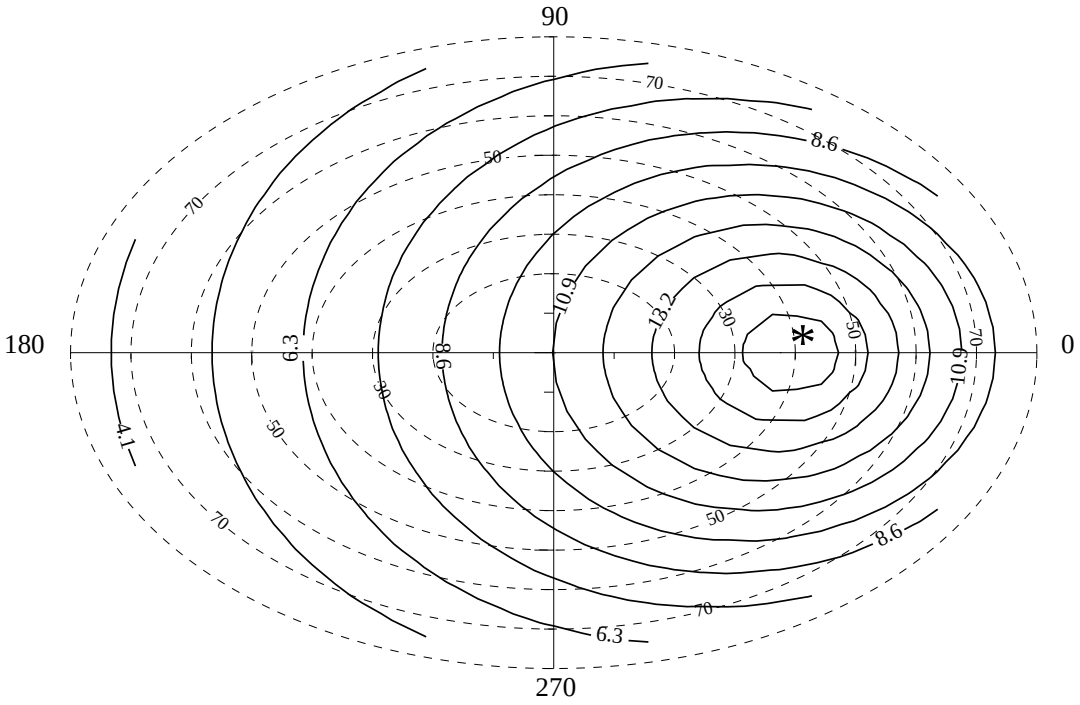

Figure 6-8: BRDF for dark surface (40° SZA)

Figure 6-9: BRDF for bright surface (40° SZA)

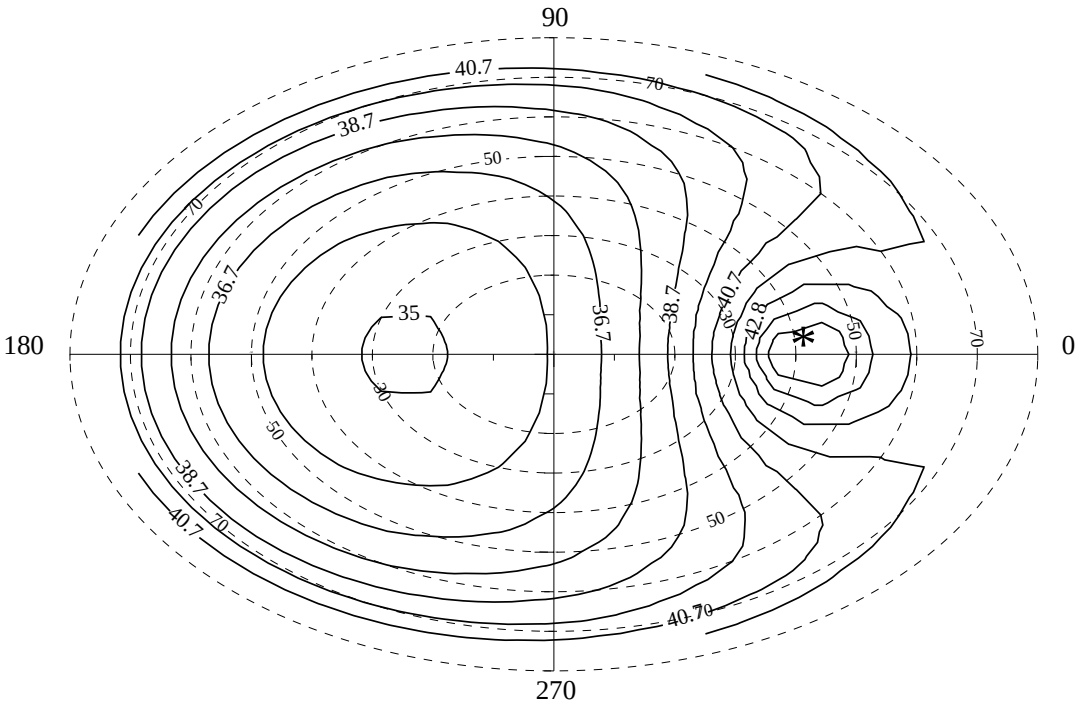

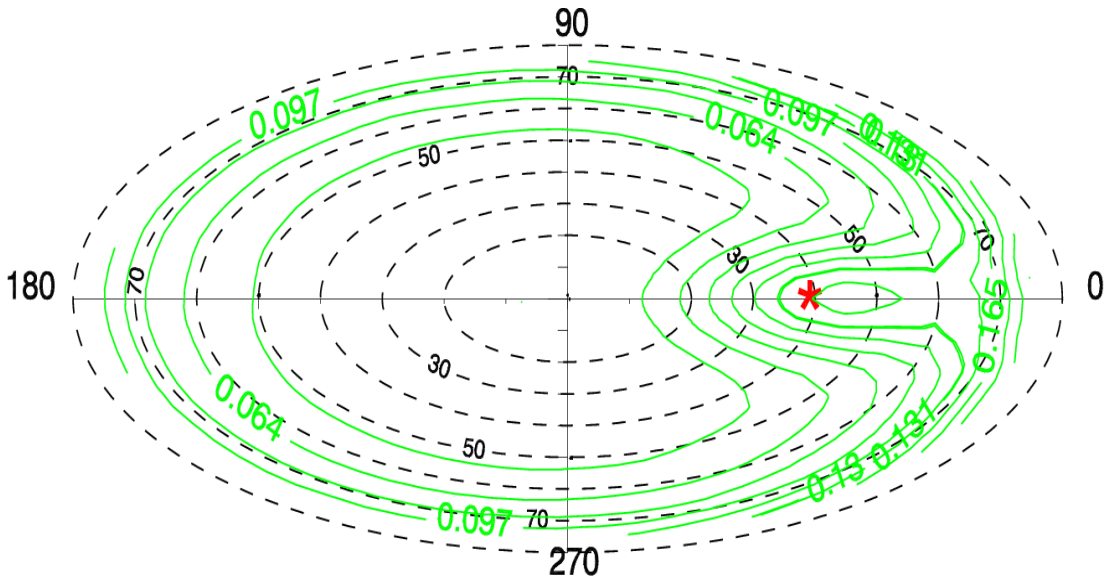

Figure 6-10: BRDF distribution for ocean glint

Effective wind speed of 5 m/s and index refraction for pure water at 350 nm were used in the ocean glint model. Solar zenith angle of 36.7° was selected (April 5°N scenario).

6.8 References

[6-1] Bicheron P., M. Leroy, O. Hautecoeur, and F.M. Breon, "Enhanced discrimination of boreal forest covers with directional reflectances from the airborne polarization and directionality of Earth reflectances (POLDER) instrument", J. Geophys. Res. 102, 29517-29528, 1997

[6-2] Cabot F., and G. Dedieu, "Surface albedo from space: Coupling bi-directional models and remotely sensed measurements", J. Geophys. Res. 102, 19645-19663, 1997

[6-3] Deguenther M. and R. Meerkötter, "Influence of inhomogeneous surface albedo on UV irradiance: Effect of stratus cloud", J. Geophys. Res., 105, 22755-22761,2000

[6-4] Hautecoeur O., and M.M. Leroy, "Surface bi-directional reflectance distribution function observed at global scale by POLDER/ADEOS", Geophys. Res. Lett. 25, 4197-4200, 1998

[6-5] Lyapustin A.I. "Atmospheric and geometrical effects on land surface albedo", J. Geophys. Res. 104, 4127-4143, 1999

[6-6] Pinty B., F. Roweda, M.M. Verstraete, N. Gobron, Y. Govaerts, J.V. Martonchik, D.J. Diner, and R.A. Kahn, "Surface albedo retrieval from Meteosat 1. Theory", J. Geophys Res. 105, 18099-18112, 2000a

[6-7] Pinty B., F. Roweda, M.M. Verstraete, N. Gobron, Y. Govaerts, J.V. Martonchik, D.J. Diner, and R.A. Kahn, "Surface albedo retrieval from Meteosat 2. Applications", J. Geophys Res. 105, 18113-18134, 2000b

[6-8] Privette J.L., T.F. Eck, and D.W. Deering, "Estimating spectral albedo and nadir reflectance through inversion of simple BRDF models with AVHRR/MODIS-like data", J. Geophys. Res. 102, 29529-29542, 1997

[6-9] Rahman H., B. Pinty, and M.M. Verstraete, "Coupled surface-atmosphere reflectance (CSAR) model, 2.Semiempirical surface model usable with NOAA advanced very high-resolution radiometer data", J. Geophys. Res. 98, 20791-20801, 1993

[6-10] Rozanov, A., V. Rozanov, and J. P. Burrows, "Combined differential-integral approach for the radiation field computation in a spherical shell atmosphere: Non-limb geometry", J. Geophys Res., 105, 22937-22942, 2000

[6-11] Wanner W., X. Li, and A.H. Stahler, "On the derivation of kernels for kernel-driven models of bi-directional reflectance", J. Geophys. Res. 100, 21077-21090, 1995

[6-12] Warren S.G., R.E. Brandt, and P. O'Rawe-Hinton, "Effect of surface roughness on bi-directional reflectance of Antarctic snow", J. Geophys. Res. 103, 25789-25807,1998

[6-13] Watts, P.D., M.R. Allen, C.T. Mutlow, C. Levoni, "Aerosol Properties derived from Meteosat Second Generation observations", Phase I and II Report, EUMETSAT Contract, 1999

7 WP140: Definition of GOME-2 Instrumental Errors (SRON)

7.1 Introduction

As GOME-2 relies heavily on GOME-1 heritage, the experience with GOME-1 gives an indication of the possible error sources. The dominant error for GOME-1 sources are here summarised, and in the following section the main differences between GOME-1 and GOME-2 are highlighted. This is the basis for the investigations described later in this report (e.g. spatial aliasing). It also serves as reminder of possible error effects that might be seen in flight by GOME-2.

This work package was carried out by SRON.

7.2 Dominant GOME-1 instrument errors

This section describes the dominant instrument or calibration errors in GOME-1 and to what extent data products are affected. Main error sources are listed first.

a. Diffuser spectral features

The GOME-1 diffuser introduces spectral features, which give rise to similar spectral fitting residuals from year to year. Interference of light reflected on different parts of the diffuser is very likely the cause of this error source. It is the major error source in GOME-1 DOAS retrievals. In the equatorial region errors on the NO_2 column are ~50%, and for BrO the errors are ~75%. For weaker absorbers (such as formaldehyde) the errors are even larger. See [7-1] and [7-2].

b. Dichroic mirror after launch outgassing

Outgassing of the dichroic mirror directly after launch resulted in a very pronounced shift (~10 nm) of the dichroic reflectivity/transmissivity spectrum in Channels 3 and 4. The shift in the differential spectral features of the polarization sensitivity ε (Section 9.3) made it impossible to retrieve O_3 from the GOME-1 DOAS visible spectral window. Also, NO_2 retrievals from the visible are possibly affected. See [7-3], [7-4], [7-5] and [7-6]

c. Scan mirror degradation (scan angle dependence)

Degradation of solar irradiance measurements in the UV was observed in the first months after launch. After January 1998 it became apparent that the degradation in the UV is different for different angles of incidence of the light on the scan mirror, with smooth wavelength dependence. This behaviour is attributed to deposition of a contaminant on the scan mirror. The effect on back-scattered albedo (Earth, Moon) results in errors of the order of 50%, with the largest errors for the most extreme incidence angles (this can be shown for east viewing, north pole and moon albedo, and also it most probably severely affects south polar views) and shortest wavelengths. Errors on retrieved O_3 profiles can be of the order of 100%, and aerosol retrieval is also affected. See [7-7], [7-8] and [7-9].

d. Polarisation correction algorithm in level 0-1 data processing

Due to the broadband nature of the GOME-1 polarisation measurements errors are introduced in the polarisation radiometric correction. Errors are most pronounced when wavelength dependence in the polarisation is strong. This is particularly true for the O_3 absorption 300-320 nm where errors in the radiances are 2-4%. O_3 profile and aerosol retrievals are affected. See [7-10] and [7-11].

***e.* Wavelength calibration, slit-function and undersampling**

Uncertainty on the knowledge of slit function and its variation with wavelength at the short wavelength end is a major error source for O_3 profile retrieval in Channel 2 below 325 nm. In addition, possibly (thermally

induced) differences in wavelength calibration and/or slit function between Earth and Solar spectra, as well as ghost straylight, may lead to additional error sources in this wavelength region. The wavelength region below 325 nm in Channel 2 is therefore often ignored in O_3 profile retrievals (B. Kerridge, private communication). Due to the limited sampling in GOME-1 (0.17-0.33 nm) differential spectral errors are introduced resulting from the Doppler shift of the solar irradiance and (thermally induced) shifts in spectral calibration for Earth and Solar spectra. See [7-12].

f. PMD-1 degradation

Degradation of the UV PMD (PMD-1) has been observed during solar observations. The degradation is much faster than the corresponding main channel degradation and is present also for Earth radiance measurements. This led to errors of about 5% in the Earth radiance after three years of GOME operations.

Analysis has shown that this degradation is very similar for Earth observations indicating that the degradation is common to both Earth and Solar optical path. It was therefore possible to define a correction based on the solar data, which is implemented in the GOME Data Processor. The error, when not corrected, affects O_3 profile and aerosol retrievals, because backscattered sunlight is polarised whereas direct sunlight is not. See [7-13] and [7-14].

g. Solar calibration unit, BSDF Azimuth dependence

The observation of GOME-1 solar spectra over a period of five years showed a periodical error of approximately +/- 1% on solar irradiances, larger for shorter wavelengths. It correlates to the solar azimuth angle (which, as the error, is maximum in July for GOME-1), is attributed to inaccuracies in the calibration of the Bi-directional Scattering Distribution Function (BSDF) of the solar calibration unit. The BSDF determined for GOME-1 assumed a quadratic dependence on the azimuth angle, while the in-flight correction - implemented as a switch in the extractor - adds an additional linear term. The remaining errors will affect O_3 profile and aerosol retrievals. See [7-15] and [7-16].

h. Air-vacuum calibration errors (Channels 1 and 2)

Outgassing of optical coatings, such as the MgF_2 coating on the scan mirror, resulted in a change of GOME-1 optical transmission after launch compared to the on-ground calibration. The difference between the pre-launch calibration in air and the in-flight calibration in vacuum is most pronounced in the UV where a characteristic parabolic deviation can be observed with deviations up to 18% (@ 340 nm). This effect was corrected using pre-flight and in-flight Spectral Lamp Source (SLS) measurements. The accuracy of such a correction is hard to establish, particularly because different optical paths are used for the SLS, Solar and Earth observations. Any remaining errors will affect O_3 profile and aerosol retrievals. However, the error is expected to be small. See [7-17] and [7-18].

i. Spatial aliasing

Spatial aliasing introduces additional noise in the spectra in case of inhomogeneous scenes. Quantification of this effect is given in [7-19]. Not considered a major problem in GOME-1 DOAS retrievals. However, in the event that other factors did not limit fitting precision for GOME-1, this source of quasi-random noise would do so. In addition, spatial aliasing introduces jumps at channel overlaps in case of inhomogeneous scenes. Some quantification is given in [7-20]. This can interfere with O_3 profile retrievals combining Ch. 1 and Ch. 2. However, it is not considered the major error source in this wavelength area. See [7-19] and [7-20]. In addition, it can be shown that spatial aliasing can yield wrong fractional polarisation values for GOME-1 (C. Tanzi, private communication).

j. Etalon

(Changes in) etalon structures are introduced by condensation and evaporation of thin contaminant layers on the detectors. This is not a major problem in GOME-1 except when GOME-1 detector coolers are switched off and on because Earth and Solar data both contain the same etalon feature, which cancels in the ratio. See [7-21].

7.3 Main instrument differences between GOME-1 and GOME-2

This section describes the main instrument differences between GOME-1 and GOME-2 and the implications this may have on the error sources.

a. Polarisation measurements

The GOME-2 polarisation measurements have been improved and in addition the polarisation sensitivity of the main spectrometer is reduced. The two orthogonal linear polarisation components are measured with separate PMDs with 15 spectral bands. A study is performed by SRON to develop the polarisation algorithm for radiometric correction, which includes the definition of the 15 spectral bands and the corresponding radiometric error due to the finite spectral resolution of the PMDs [7-22]. The error in the wavelength region of interest to O_3 profile retrieval is reduced by almost one order of magnitude for 300-310 nm, and by more than 2 orders of magnitude for most wavelengths in the range 310-340 nm[1].

b. Swath width

The GOME-2 swath width will be 1920 km, although the operational swath width is subject of this study. The default swath width of 1920 km means that the swath width is twice the GOME-1 swath width. This has several implications.

As far as radiative transfer modelling is concerned, the extremes of the swath are comparable to limb-viewing geometries and require radiative transfer models using spherical geometry. This is subject of this study and will be addressed in WP240, WP250, and WP260.

The use of a large swath width also has implications for the scan-angle dependences of optical properties (e.g. wavelength-dependence of the polarisation dependence) of the scan mirror and their calibration and, potentially, in-flight degradation in these properties. The effect of degradation will be stronger for scan mirror reflectivities with angles close to grazing incidence. A larger swath width implies a larger incidence angle range and thus reflectivities at more extreme incidence angles.

c. Integration Times

The GOME-2 integration times (IT) will be reduced to 0.1875 sec in Bands 1B to 4, in order to allow smaller ground-pixels (80 or 40 x 40 km^2, depending on whether swath width is 1920 km or 960 km). Although the detector read-out time is reduced to 48 ms, the ratio of read-out time to IT (0.256) is ~4 times larger for GOME-2 than for GOME-1 (for which the read-out time is 93.75 ms and the integration time is 1.5s, giving a ratio of 0.0625). This implies a more pronounced spatial aliasing effect in GOME-2 in case of inhomogeneous scenes. However, the eight-fold reduction in integration time means that the photon-noise for an individual pixel will also be increased by a factor of ~sqrt(8) in relation to GOME-1. The effect of spatial aliasing on GOME-2 retrievals is subject to this study and will be addressed in WP210.

d. Spectral resolution

The spectral resolution in GOME-2 is intentionally degraded (focussing) in order to reduce undersampling effects inherent to spectral structure at much higher resolution present in the solar irradiance. The aimed number of pixels per FWHM is 2.0-2.5 pixels (Channels 1 and 2) and 1.9-1.38 pixels (Channels 3 and 4). The effect of this change, and further spectral resolution degradation (2.7-3.0 px) will be investigated in this study (WP230).

e. On-board white light source

GOME-2 is equipped with an on-board white light source (WLS). This allows for in-flight characterisation of the etalon features introduced by (changing) thickness of the condensation on the main channel detectors. In addition, the WLS will be used for detector Pixel to Pixel Gain, although the LEDs can be used for that purpose as well just as in GOME-1.

[1] This assumes the first useful polarisation measurement at 312 nm for GOME-2.

f. Dichroic mirror change

The coating of the dichroic mirror is deposited on the bare mirror using a different technique. This ensures a much harder coating. In addition, the spectral features (at least at the % level) in the reflectivity/transmission spectrum of the mirror do not fall within the DOAS O_3 or NO_2 spectral window (425-500 nm).

g. Channel 2 slit function

The change in slit function with wavelength at the short wavelength end of Channel 2 in GOME-1 was introduced by a late change in the GOME-2 optical settings to reduce straylight. The error in knowledge of GOME-2 slitfunction shape resulting from either defocusing or 'opening slit' is addressed in Section 16 and Section 25.

Summary

The differences between GOME-1 and GOME-2, notwithstanding some of the error sources listed for GOME-1, cannot be *a priori* excluded for GOME-2. Specifically, the following GOME-1 error sources might also be present in GOME-2: (i) presence of spectral features in the diffuser (7.2 a), (ii) outgassing of the dichroic mirror after launch (7.2 b), (iii) degradation of scan mirror (7.2 c) and (iv) calibration uncertainties in the solar calibration unit (7.2 g).

7.4 Quantification of selected error sources for GOME-2

Two GOME-1/2 error sources were translated into corresponding error spectra on sun-normalised radiance and provided as input to the project partners. In this section information on these error spectra are provided.

Degradation GOME-1 earth reflectivities

In order to determine the degradation of the ratio of backscattered Earth radiance to solar irradiance for GOME-1 (see Sect. 7.3.c above), sun-normalised UV radiances for a given day were averaged over a latitude band where the variation of solar zenith angle is minimal, and were compared over the years. The ozone columns determined by DOAS fitting within Band 2 (a technique expected to be quite robust against degradation in absolute reflectivity) in the selected latitude band vary within only 20 DU. It follows that, for wavelengths shorter than 295 nm, the true Earth reflectivities should be stable over this period and latitude band to within +/-4% (this calculation takes into account variations of ozone profiles, as derived in the Fortuin and Kelder climatology). Although such a comparison is possible only over a limited latitude band, comparisons of measured Earth reflectivities with forward calculations show that the Earth reflectivities over this latitude band are representative for the whole orbit [7-26].

The data obtained for 14 (or 15) August over 1995 to 2000 (total integration time of 12s, thus a sweep of 30 deg of the GOME-1 scan mirror) have been provided, together with the standard error of the mean, as an indication of possible degradation for GOME-2 (Figure 7-1). For the years 1998 to 2000, averages above 282.9 nm (Band 1B sampled at 1.5s instead of 12s for Band 1A) are also provided for east and west viewing. As the differences over the years are greater for east viewing, the data relative to 12s integration time only give indication of an average degradation.

Above 295 nm the variation in ground albedo and ozone columns make the determination of degradation rates of albedos very difficult. See [7-24] and [7-25].

Error spectrum resulting from the polarisation correction algorithm

We have calculated earth radiances using a doubling-adding code, which accounts for multiple scattering and polarisation of the radiance. The code accounts for Raleigh scattering and absorption by the ozone Huggins and Chappuis bands (~322 Dobson Units) and the O_2-A band. Aerosols are not included in the calculations.

12 viewing geometries are selected which include extreme east, nadir and extreme west scanning angles. The geometries cover representative satellite locations during different times of year.

It should be noted here that the radiative transfer code assumes plane-parallel geometries. This assumption is less valid for low (<15 degrees) solar and satellite elevations. For some of the solar elevations considered here this is actually the case, and some caution should be taken in the interpretation of the modelling results.

The Lambertian surface albedo is constant in wavelength at values of 0.05 and 0.8. The spectral range is set between 260-340 nm at a constant spectral resolution of 0.2 nm.

The radiance and polarisation are input to calculations of the percentage radiance error as a result of application of the polarisation correction algorithm (MO_TN_DLR_GO_0006). GOME-2 instrument sensitivity parameters for nadir scan angles, given in MO_NT_GAL_GO_0022 and MO_NT_GAL_GO_0023, are used. Scan angle dependences at the extreme east and west geometries are accounted for by theoretical approximations of the scan mirror polarisation sensitivity [Slijkhuis, private communication].

An integration time of 0.1875s is applied for the main channels above 283 nm in agreement with the Channel 1A/B boundary. PMD readouts are co-added to match the integration times of the main channels.

Radiance errors are calculated for each main channel individually. Read-out noise and dark current noise, specified in MO_NT_GAL_GO_0023, are included as well as signal and stray-light shot noise. Straylight is estimated as 1 percent of the signal at 312 nm and constant over wavelength. The applied PMD spectral bands are specified in the PMD band selection document (MO_TN_ESA_GO-0203). A typical result is shown in Figure 7-2.

The largest error occurs at wavelengths between the single scattering region (shortest wavelengths) and the first measured data point. This is mainly due to a combination of the interpolation between single scattering point (fixed at 300 nm) and the data points, and the steep slope of the polarisation curve around ~310 nm.

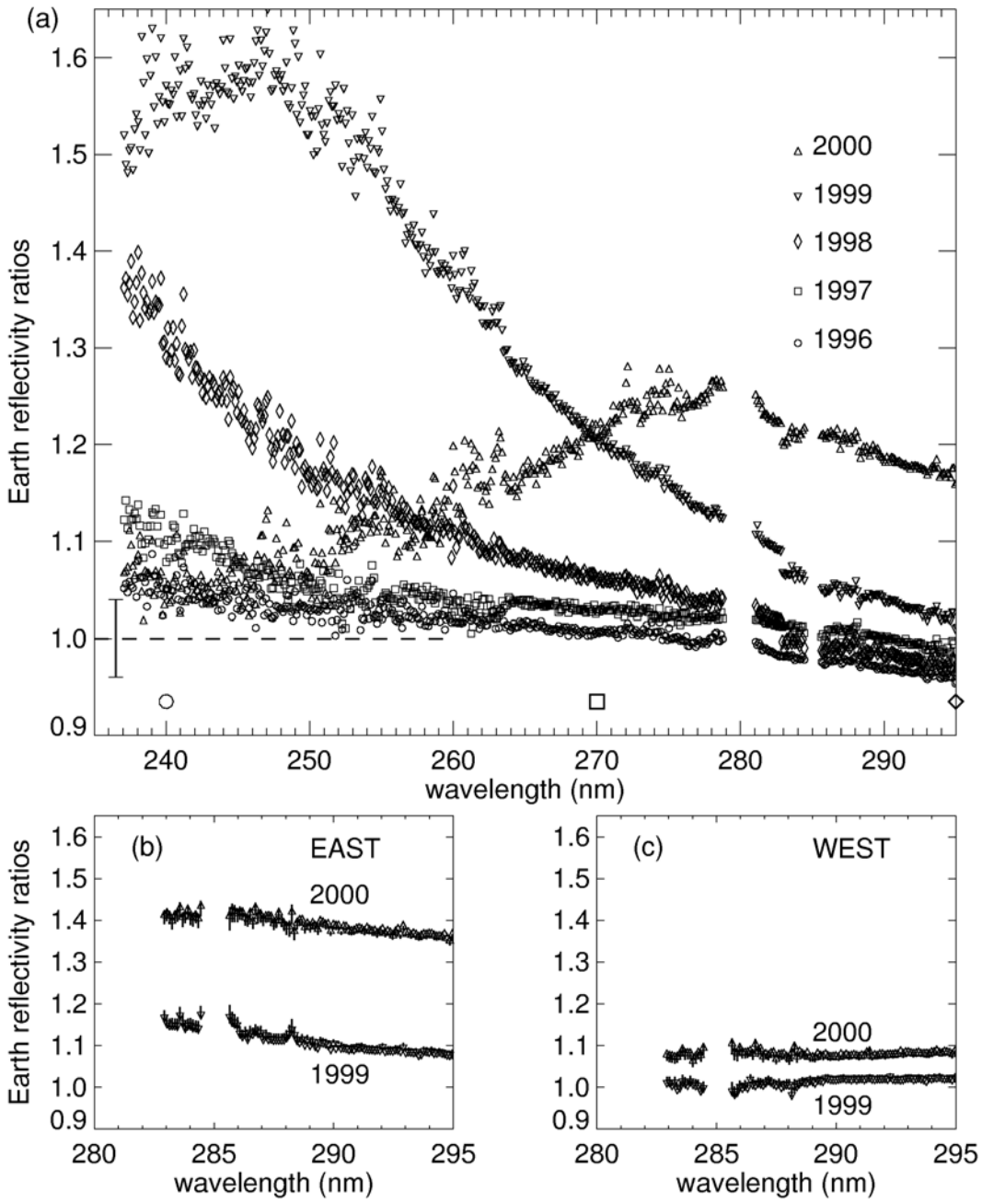

Figure from Tanzi et al, 2002 [7-27]

Figure 7-1: Average Earth Reflectivities

a) Average over 10-20° N of all Earth reflectivities measured on 13/14 August +/- 30° scans (960*80 km^2), ratioed to the 1995 average. The solar zenith angle is 20.9° +/- 0.3° and ozone columns from GOME 273 +/- 17 DU (corresponding to +/- 4% reflectivity). Any significant variation from unity is caused by different degradation of Earth and solar optical paths. The standard error of the mean (not shown) is of the same order of the scatter of the data (Fraunhofer lines, with low S/N, are not shown).

b, c) same as (a) but over scans of +/- 10-30° (320*40 km^2), east and west of track, ratioed to 1998. The standard error of the mean is also shown.

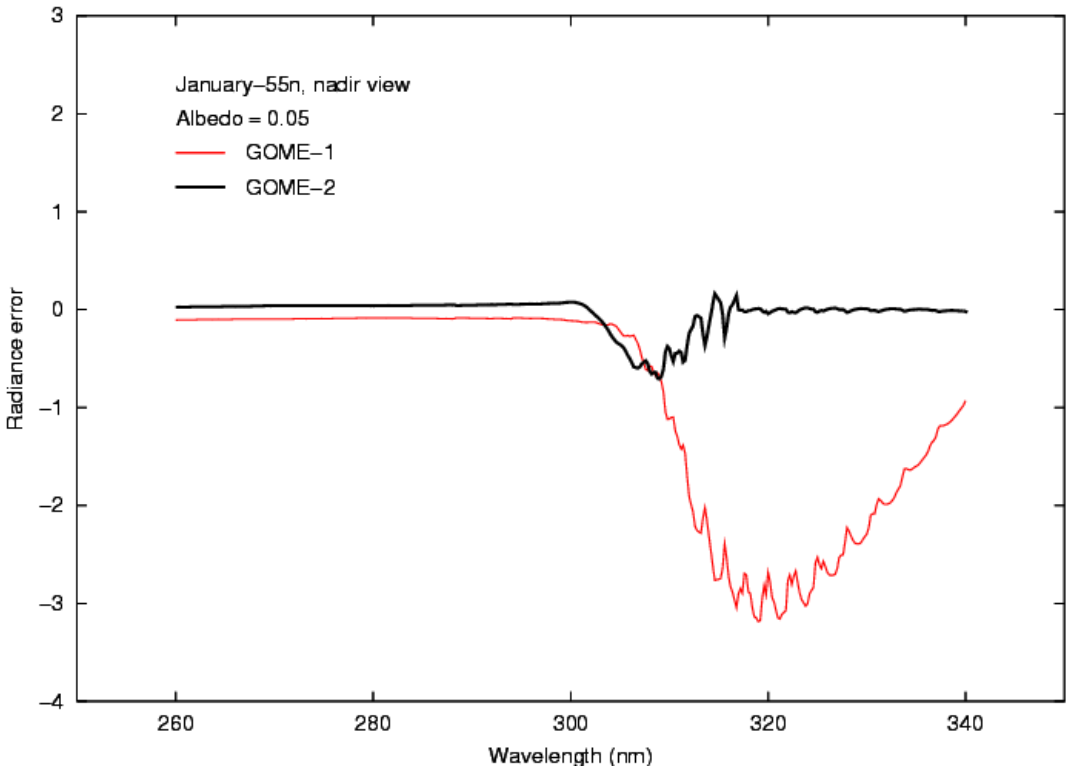

Figure 7-2: Resulting GOME-2 radiometric error spectrum for a typical case

The resulting GOME-2 radiometric error spectrum for a typical case - For comparison the GOME-1 error for the same case is also shown. The latter is much bigger because the instrument polarisation sensitivity is higher, and the polarisation is only measured at 3 wavelengths across the entire wavelength range (300-800 nm).

7.5 References

[7-1] A. Richter and T. Wagner, "Diffuser plate spectral structures and their influence on GOME slant columns", Technical note, Jan. 2001

[7-2] M. Eisinger, J.P. Burrows and A. Richter, "Studies on the Precision of GOME Irradiance and Radiance Products and GOME Measurements of OClO and BrO over Antarctica", GOME Geophysical Validation Campaign in Frascati, ESA WPP-108, pp.93-108, Jan. 1996

[7-3] M. Eisinger, J.P. Burrows and A. Richter, "Studies on the Precision of GOME Irradiance and Radiance Products and GOME Measurements of OClO and BrO over Antarctica", GOME Geophysical Validation Campaign, ESA WPP-108, pp.93-108, Jan. 1996

[7-4] M. Eisinger et al., "In-orbit monitoring of GOME polarisation sensitivity", ESAMS Workshop in ESTEC, ESA WPP-161, Vol. 2, pp. 665-668, March 1999

[7-5] I. Aben et al., "GOBELIN - GOME BBM instrument characterization – final report", Tech. Rep., RP-GOB-001SR/99, SRON 1999

[7-6] I. Aben et al., "GDAQI Final Report (GOME Data Quality Improvement)", TN-GDAQI-003SR/2000 (Sect. 7), Sep 2000

[7-7] C.P. Tanzi, R. Snel, O. Hasekamp, I. Aben, "Degradation of UV earth albedo observations by GOME", ERS-ENVISAT Symposium, Gothenburg, 16-20 October 2000, ESA SP-461, on CD-ROM, Jan 2001

[7-8] C.P. Tanzi, R. Snel and I. Aben, "Degradation of Observations in the UV of the Global Ozone Monitoring Experiment (GOME)", in IRS 2000: Current Problems in Atmospheric Radiation, Deepak, 2001, pp. 181-184

[7-9] R. Snel, "In-orbit optical path degradation: GOME experience and SCIAMACHY prediction", Proc. ERS-Envisat Symposium, Gothenburg, ESA SP-461, on CD-ROM, Jan. 2001

[7-10] N.A.J. Schutgen and P. Stammes, "Improving the polarisation correction algorithm for GOME (Global Ozone Monitoring Experiment)", Proc. SPIE, Vol. 3754, pp. 411-422, 1999

[7-11] N.A.J. Schutgen and P. Stammes, "A parameterisation of UV polarisation of the Earth's atmosphere", IRS 2000: Current Problems in Atmospheric Radiation, Deepak, 2001, pp. 333-336

[7-12] K. Chance, "Analysis of BrO measurements from the GOME", Geophys. Res. Lett., 25, 3335-3338, 1998

[7-13] C.P. Tanzi, I. Aben, S. Slijkhuis, "Influence of GOME in-flight degradation on earth radiance measurements", ESAMS Workshop in ESTEC, ESA WPP-161, Vol. 1, pp. 681--685, March 1999

[7-14] I. Aben et al., "GDAQI Final Report (GOME Data Quality Improvement)", TN-GDAQI-003SR/2000 (Sect. 5), Sep 2000

[7-15] H. Hegels and S. Slijkhuis, "GOME: Correction of Degradation and Update of Key Data", ESAMS Workshop in ESTEC, ESA WPP-161, Vol. 2, pp. 695-700, March 1999

[7-16] I. Aben et al., "GDAQI Final Report (GOME Data Quality Improvement)", TN-GDAQI-003SR/2000 (App. B), Sep 2000

[7-17] R. Hoekstra, C. Olij, E. Zoutman and M. Le Kluse", "Validation of in-orbit calibration of GOME", GOME Geophysical Validation Campaign in Frascati, ESA WPP-108, pp.21-32, Jan. 1996

[7-18] I. Aben et al., "GDAQI Final Report (GOME Data Quality Improvement)", TN-GDAQI-003SR/2000 (Sect. 3), Sep 2000

[7-19] Diebel et al., "Detailed analysis of the retrieval algorithms selected for the level 1-2 processing of GOME data", October 1995.

[7-20] P. Stammes, memo AO-00-01, "Statistical analysis of channel-to-channel jumps in GOME spectra", May 2000

[7-21] I. Aben et al., "GDAQI Final Report (GOME Data Quality Improvement)", TN-GDAQI-003SR/2000 (Sect. 8), Sep 2000

[7-22] Hartmann & Aben, "GOME-2 polarisation study", RP-GOME-2-002SR/00, Jan. 2001

[7-23] "GOME-2 Critical Design Review Data Package", Galileo, 18/5/2001

[7-24] C.P. Tanzi, R. Snel, O. Hasekamp and I. Aben, "Degradation of UV Earth Albedo Observations by GOME", ERS-Envisat Symposium "Looking down to Earth in the New Millennium, on CD-ROM, Jan 2001

[7-25] C.P. Tanzi, R. Snel and I. Aben, "Degradation of Observations in the UV of the Global Ozone Monitoring Experiment (GOME)", in IRS 2000: Current Problems in Atmospheric Radiation, Deepak, 2001, in press

[7-26] van der A et al, "Ozone profile retrieval from recalibrated GOME data", J. Geophys. Res., 2001, in press

[7-27] Tanzi et al, "In flight degradation of UV observations by GOME", in preparation, 2002

8 WP150: Retrievals and Instrument-Induced Errors (RAL)

8.1 Introduction

This section describes work carried out to define the baseline errors budget against which the significance of results in Task 2 can be judged.

8.2 Retrieval Scheme configuration

The O_3 profile retrieval scheme selected for use in this study, described under WP110 is based on that developed at RAL to analyse GOME-1 flight data. This scheme has been optimised to be robust to (a) measurement errors at the level experienced with GOME-1 and (b) intrinsic variations in information content with varying geophysical conditions. The presentation of the information content available from GOME spectra is sensitive to retrieval algorithm choices. In particular, estimated retrieval errors will depend upon:

- Vertical resolution at which the retrieval is attempted
- Choice of *a priori* constraint.

For the purposes of this study, which focuses on revealing the impact of operational settings on retrieval quality, it has been decided to adopt a relatively weak a priori constraint, whereas in an operational scheme good *a priori* knowledge of the stratosphere might be exploited.

To facilitate the comparison and interpretation of results from this study with diagnostics reported elsewhere by other retrieval groups, a set of diagnostics have been computed as follows:

- Retrieval grids (altitudes at which O_3 retrieved)
  1. 0, 6, 12 then 4 km intervals to 80 km (as RAL standard scheme)
  2. Uniform spacing at 6 km intervals from 0 to 78 km
  3. Uniform spacing at 6 km intervals from 6 to 78 km, where 6 km level defines the sub-column from 0-6 km.
  4. Uniform spacing at 6 km intervals from 12 to 78 km, where 12 km level defines the sub-column from 0-12 km
- *A priori* options
  1. *A priori* error defined to be 100% of the a priori mixing ratio profile at each retrieval grid point, as implemented in the RAL standard scheme. The *a priori* covariance matrix is defined with a Gaussian correlation length of 6 km for the Band 1 retrieval, and 8 km for the Band 2B retrieval
  2. Errors defined to be 100% as above, but with diagonal covariance matrix (no correlations)
  3. Errors defined to be 30% at and above 16 km and 100% below, with correlations (to show the impact of more tightly constraining the stratosphere).
  4. Errors defined to be 300%, with correlations

Diagnostics are shown for the range of geo-temporal / albedo scenarios in Figures A2.2 in Appendix A. Examples for the July 5N and April 55N cases (at albedo 0.05) are shown in Figure 8-1. Averaging kernels shown are for the 100% uncorrelated error case, at the nominal grid. Note that tropospheric precisions can be high depending on retrieval option and in particular for the 0 - 12 km column retrieval with 30% stratospheric constraint (best case 5% for July 5N). One should however note, that the retrieval of a column implies an assumption within the retrieval model that the profile shape is known within the defined column and although the precision estimated based on instrument noise is improved, errors due to the representation of profile shape will increase.

All retrieval simulation results reported elsewhere in this report are based on the RAL operational scheme settings i.e. retrieval grid option 1 and a priori option 1 (above).

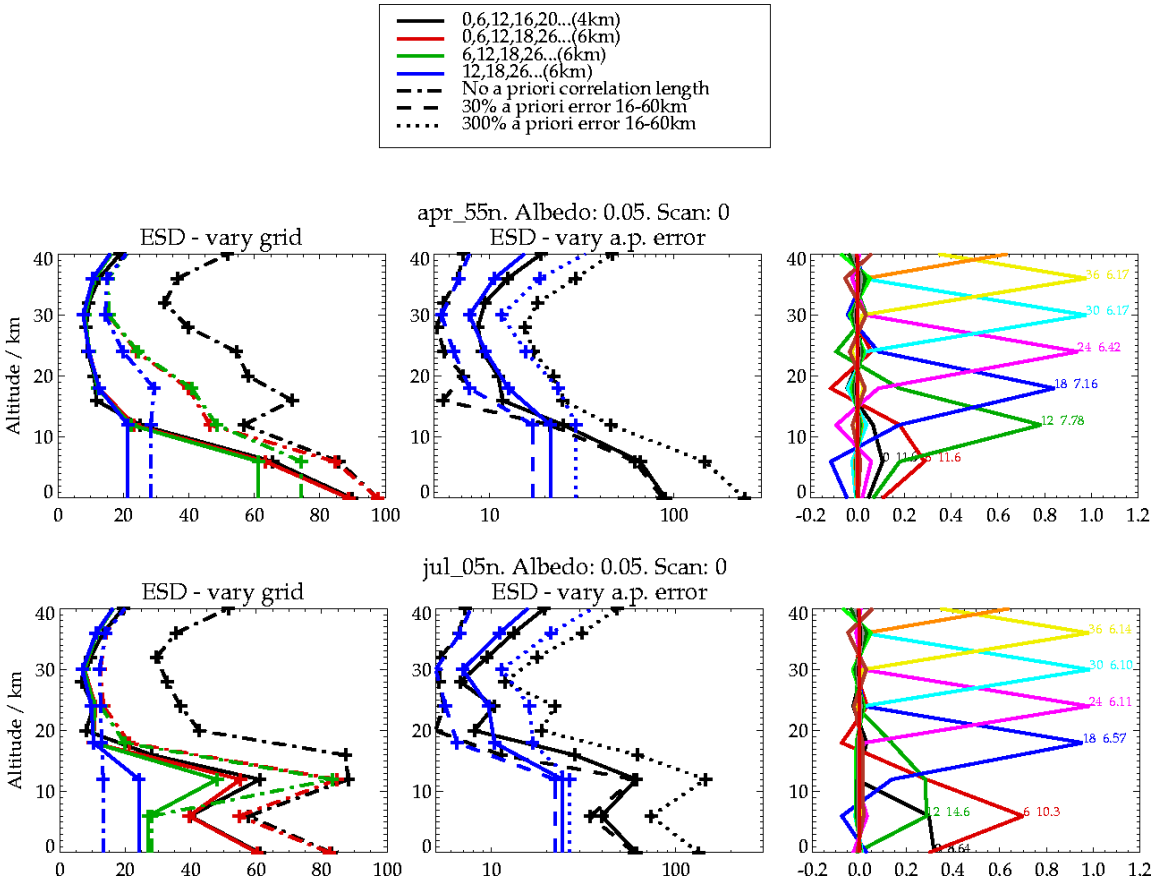

Figure 8-1: Impact of retrieval model options for scenarios April, 55°N and July 5°N scenarios.

8.3 Basic errors

In addition to the retrieval ESD, a number of other "basic" error sources have been simulated to provide a reference error budget by which to judge the significance of the specific errors quantified in Task 2. These errors, quantified by the linear mapping approach described above, are described below. Text in square brackets denotes the annotation used for the error in the retrieval simulation plots discussed below.

8.3.1 Forward model errors [FME]

Aerosol

Errors in retrieved ozone introduced by deviations in the aerosol profile from the background case assumed in the FM are simulated by mapping measurement perturbations based on the following cases. All scenarios are based on the MODTRAN aerosol models [Anderson].

Case	Season	Boundary Layer (0-2km)			Troposphere (2-10km)		Stratosphere (10-35km)		Mesosphere
		Type	Visibility	Humidity	Visibility	Humidity	Load	Type	Load
BKG	Fall/Winter	rural	50km	0%	50km	0%	background	background	normal
HIGH	Spring/Summer	urban	5km	80%	23km	80%	moderate volcanic	aged volcanic	normal
SUM	Spring/Summer	rural	50km	0%	50km	0%	background	background	normal
MODVOL	Fall/Winter	rural	50km	0%	50km	0%	moderate volcanic	aged volcanic	normal
BL10	Fall/Winter	rural	10km	0%	50km	0%	background	background	normal

Notes: [BKG] is the background case assumed in the standard retrieval model.

[HIGH] represent a maximum boundary layer / troposphere optical depth case from the MODTRAN scenarios, with a moderate volcanic stratosphere.

[BL10], [SUM] and [MODVOL] are close to the background case except in the boundary layer, troposphere and stratosphere respectively, where they are close to the [HIGH] scenario. The aerosol optical properties of the 5 scenarios are illustrated in Figure 8-2.

[PRESSURE] Effect of a 1% perturbation in surface pressure on scattering profile and hence retrieval (absorber number density not perturbed)

[TEMP-2KM] Effect of 1K error in assumed temperature profile on 2 km grid. Both temperature errors are propagated through the absorption cross-section *only* (i.e. not via number density profile)

[TEMP-10KM] As, above but assuming a Gaussian correlation with 10km half-width

[TEMP-FCBKG] As above, but taking the covariance matrix from a numerical weather prediction background error covariance matrix. Previous retrieval simulations conducted by A. Collard (Met Office, private communication) for IASI were taken as a baseline. In these simulations an ECMWF background covariance matrix was used an *a priori* for an IASI retrieval in which temperature and specific humidity were retrieved at the 43 model levels (the spacing of which varied as a function of height), together with surface pressure. The *a priori* covariance matrix contained correlations in the vertical for both temperature and humidity, but no cross-correlations between temperature and humidity. The simulation included IASI random noise together with a simple estimate of forward model error (0.2K, wavelength independent). In this case the ECMWF model background covariance matrix is used as the temperature error covariance mapped onto the GOME-2 ozone retrieval.

[TEMP-IASI] As [TEMP-FCBKG], but using the estimated covariance after assimilation of IASI information. The matrices used are illustrated in Figure 8-3

8.3.2 Instrumental errors (INST)

[POLERR] Estimated effect of error in polarisation correction given GOME-2 correction scheme, based on the SRON analysis of this study (see section WP140).

[RADCAL] 2% Gain error, i.e. mapping of a 2% of the nominal back-scattered radiance is mapped as a systematic error, to represent radiometric calibration errors. The magnitude of the error is chosen to be consistent with that of the estimated radiometric calibration error budget for unpolarised sun-normalised radiance reported in [MO-RS-TPD-GO-0016.iss.2]. Note that the effect of radiometric-offset errors (e.g. induced by uniform stray-light or dark current) is included through the retrieval of "dark signal" in Band 1 (A and B).

8.3.3 Instrumental errors based on GOME-1 performance ([G1-INST])

[MIRROR] Errors, which would be caused in GOME-2 measurements, were the scan mirror to degrade in the same way as GOME-1 and the degradation remains uncorrected. This result is based on a second order polynomial fit to the 1998 GOME-1 curve in the section on WP140 (SRON), constrained to be close to 1 at 310 nm. The result is illustrative of the effect of increasing optical degradation towards the UV.

[POLERR-G1] Estimated effect of error in polarisation correction given GOME-1 correction scheme (and PMD data). *Error-spectra mapped have only been calculated (by SRON) for albedo 0.05 – results for albedo 0.8 should therefore be treated with extreme caution.*

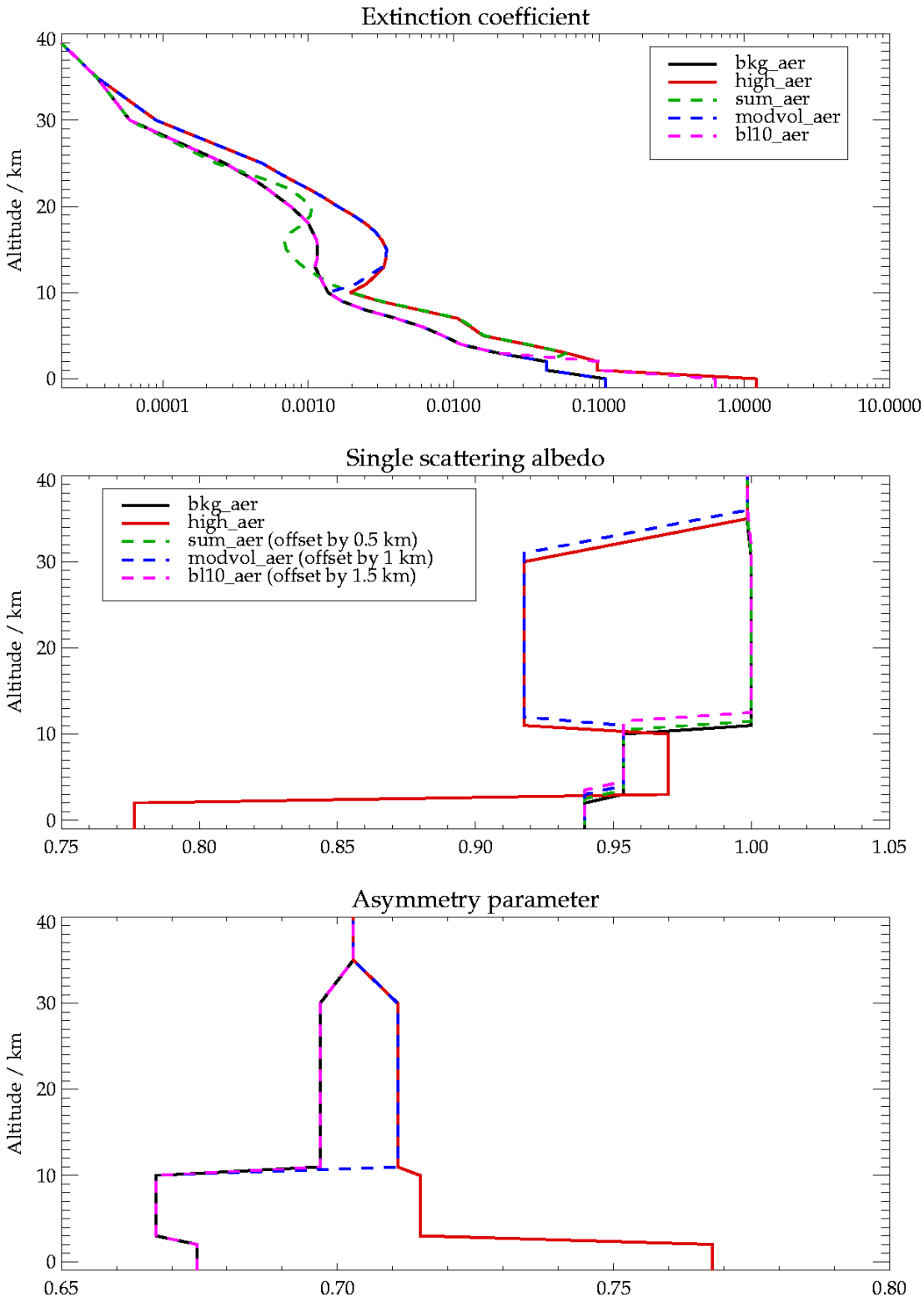

Figure 8-2 : Aerosol profiles used for ozone profile retrieval simulations

Top panel: Extinction coefficients at 320 nm,
Middle panel: Single scattering albedos (ratio of scattering to extinction coefficient)
Bottom panel: Phase-function asymmetry parameter.

For clarity, in bottom two panels some profiles are offset in altitude.
Also, in all panels, value at 0 km is extended to –1 km

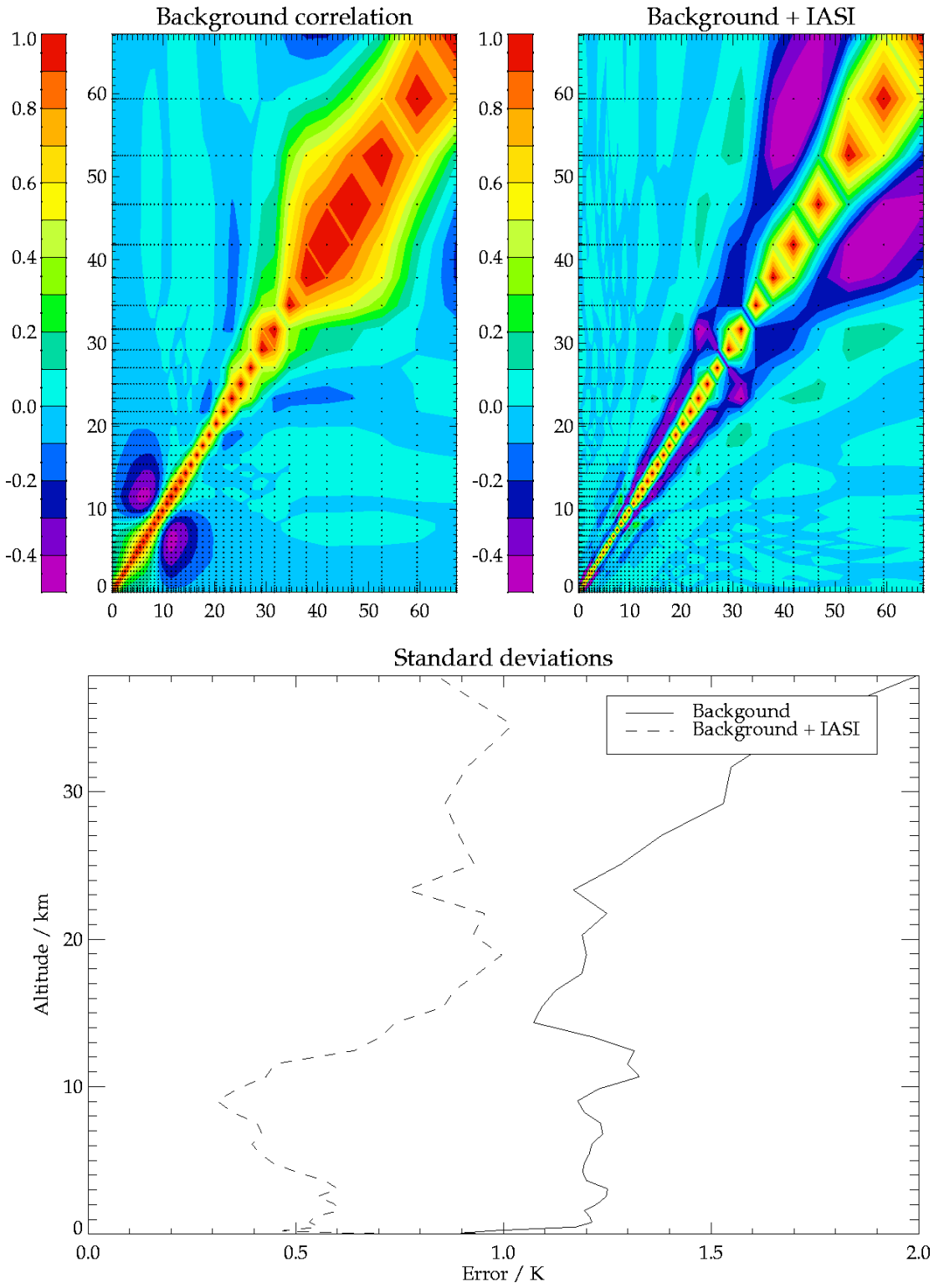

Figure 8-3: Temperature covariance matrices used in basic error budget from A. Collard (UKMO)

Bottom panel shows standard deviations (square root of the diagonal elements) of an ECMWF background covariance matrix and the corresponding matrix after assimilation of information from METOP IASI.

The top two panels show the associated correlation matrices.

Small + symbols indicate the 43 levels at which the covariances are represented

8.3.4 Combination of basic errors into base-line error budget

Figure 8-8 shows the ESD and each mapped error for April 55°N. (Versions of the plot for all geo-temporal scenarios are included in the Appendix A, Figures A2.9 - A2.10).

These mapped errors are intended to be used as a reference by which the significance of the specific errors assessed in Task 2 are judged. To facilitate this comparison the root-sum-squared (RSS) combination of the following errors is taken:

[PRESSURE] 1% error in surface pressure is considered a conservative estimate of the accuracy of NWP model errors.

[TEMP-IASI] i.e. where it is assumed that information from IASI will be used to constrain the temperature profile used in the GOME-2 retrieval.

[POLERR]

[RADCAL]

[HIGH_AER]

This RSS error is included in retrieval diagnostic plots to provide, together with the ESD, a measure by which to judge the significance of other error sources or impacts of retrieval model modifications.

Note that the mirror degradation error is not included. As can be seen in the Figure 8-8, were this error to occur as in GOME-1 and remain uncorrected it would be a dominant error source, but it has not been possible within the scope of this study to adequately predict the extent to which the error can mitigated in GOME-2, possibly by use of the white light source (and in any case the error will not be present initially).

Since the aerosol error is (a) a rather extreme case, (b) will occur with non-random geographical distribution and (c) may well be mitigated using information from GOME-2 itself or other sensors, an alternative RSS error, not including this error is included in retrieval diagnostic plots.

It should be noted that errors in spectroscopy are also likely to be significant contributors to the overall budget, but have not been possible to quantify by retrieval simulation to date within the context of this study.

8.3.5 Diagnostic plots

Retrieval simulations including all mapped errors described above for all 24 geo-temporal scenarios and three view angles (nadir + extremes of 1920 km swath) have been computed for a range of retrieval model options. Selected results are presented below, as required to address the specific retrieval model issues. All results are included for the specific retrieval model configuration taken forward to Task 2. The following plots are included in Appendix A:

A2.3-4	To illustrate the impact of B1 and B2 spectral coverage options (see below). ESDs+ of RSS baseline errors for the 24 scenarios but nadir geometry only
A2.5-6	ESDs + individual baseline errors + RSS combinations for nadir + extreme 920 km swath viewing angles for selected wavelength coverage options. 1 page per geo-temporal scenario
A2.7-8	ESDs + RSS errors as in A2.5-6, all viewing geometries on 1 panel, no individual mapped errors.
A2.11-2.12	Averaging kernels

Note that in the panels of Figures A2.3 - A2.8, the x-axis is split and the scale changes to allow details at low values to be seen more clearly. Plots are discussed in more detail below.

8.4 Spectral coverage selection

The RAL operational GOME-1 scheme uses restricted wavelength ranges in GOME Bands 1 and 2 due to limitations in the level 1 data. The following simulations have been conducted to investigate possible options for extending Bands 1 and 2 spectral coverage for ozone profile retrieval beyond the ranges used in the operational scheme, in order to increase the available information content. The following options have been considered:

For Band 1:

1. 240 - 314 nm (maximum coverage)
2. 265 - 307 nm (nominal case)
3. 240 - 307 nm (extending to short-wave)
4. 265 - 314 nm (extending to long-wave)

For Band 2:

1. 312.0 - 340.0 nm (maximum coverage considered)
2. 323.5 - 334.6 nm (nominal)
3. 315.0 - 334.6 nm (extending to short-wave)
4. 315.0 - 340.0 nm (extending to long-wave)

Retrieval simulations results for each geo-temporal/albedo scenario are shown in Figures A2.3 in Appendix A, for varying Band 1 option, assuming Band 2 range 2 (Figure 8-4 shows the April 55N example) and in Figures A2.4, for varying Band 2 option, assuming Band 1 range 2 (Figure 8-5 shows the April 55N example). Results for nadir geometry only are presented.

In general, extending Band 2 coverage above 334.6 nm or extending Band 1 below 265 nm does not offer significantly enhanced retrieval performance (other than above 40 km in the latter case and very marginally for high solar zenith scenarios in the former). There are apparent benefits to Band 1 option 4 (extending to 314 nm) and Band 2 option 3 (extending down to 315 nm), although note that these options have generally increased sensitivity to mapped errors, with respect to the nominal case.

For Task 2 simulations, Band 2 option 3 is selected and both Band 1 options 2 and 4 are carried forward.

8.5 Baseline retrieval simulations

Diagnostics for the retrieval model configuration to be used in Task 2 (two options corresponding to the two Band 1 spectral coverage cases) are illustrated in Figures A2.5-A2.12 in Appendix A. Figure 8-6 and Figure 8-7 contain summarised versions of the ESD and RSS errors, for the two albedo options.

Figures A2.5-2.6 and A2.9-A2.10 in illustrate the contributions to the RSS mapped errors and sensitivity to the other T1 errors, and Figures A2.11-A2.12 illustrate the averaging kernels.

8.6 References

[8-1] Anderson, G.P. et al. FASCODE/MODTRAN/LOWTRAN: Past/Present/Future.18th Annual Review Conference on Atmospheric Transmission Models, 6-8 June 1995

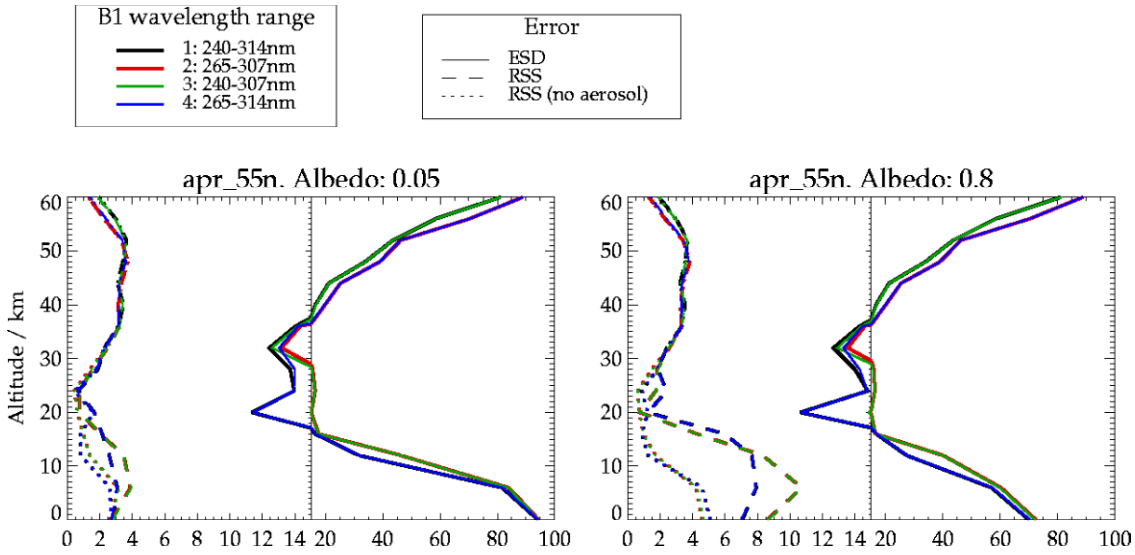

Figure 8-4: Impact of Band 1 spectral coverage options for April 55°N scenarios

Assuming Band 2 coverage option 2 (232-334.6nm). Nadir geometry only

.

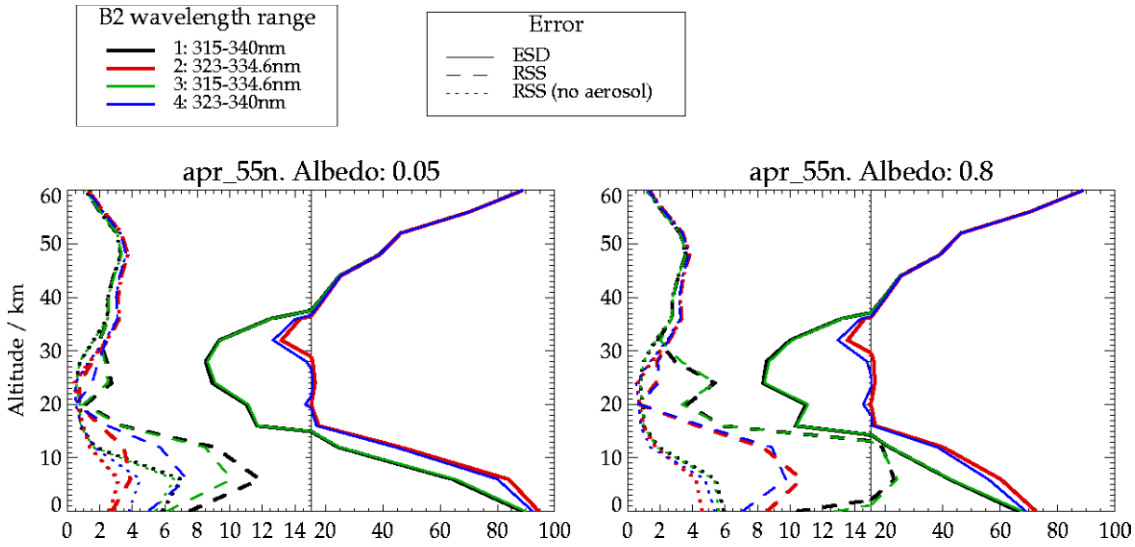

Figure 8-5: Impact of Band 2 spectral coverage options for April 55°N scenarios

Assuming Band 2 coverage option 2 (232-334.6nm). Nadir geometry only

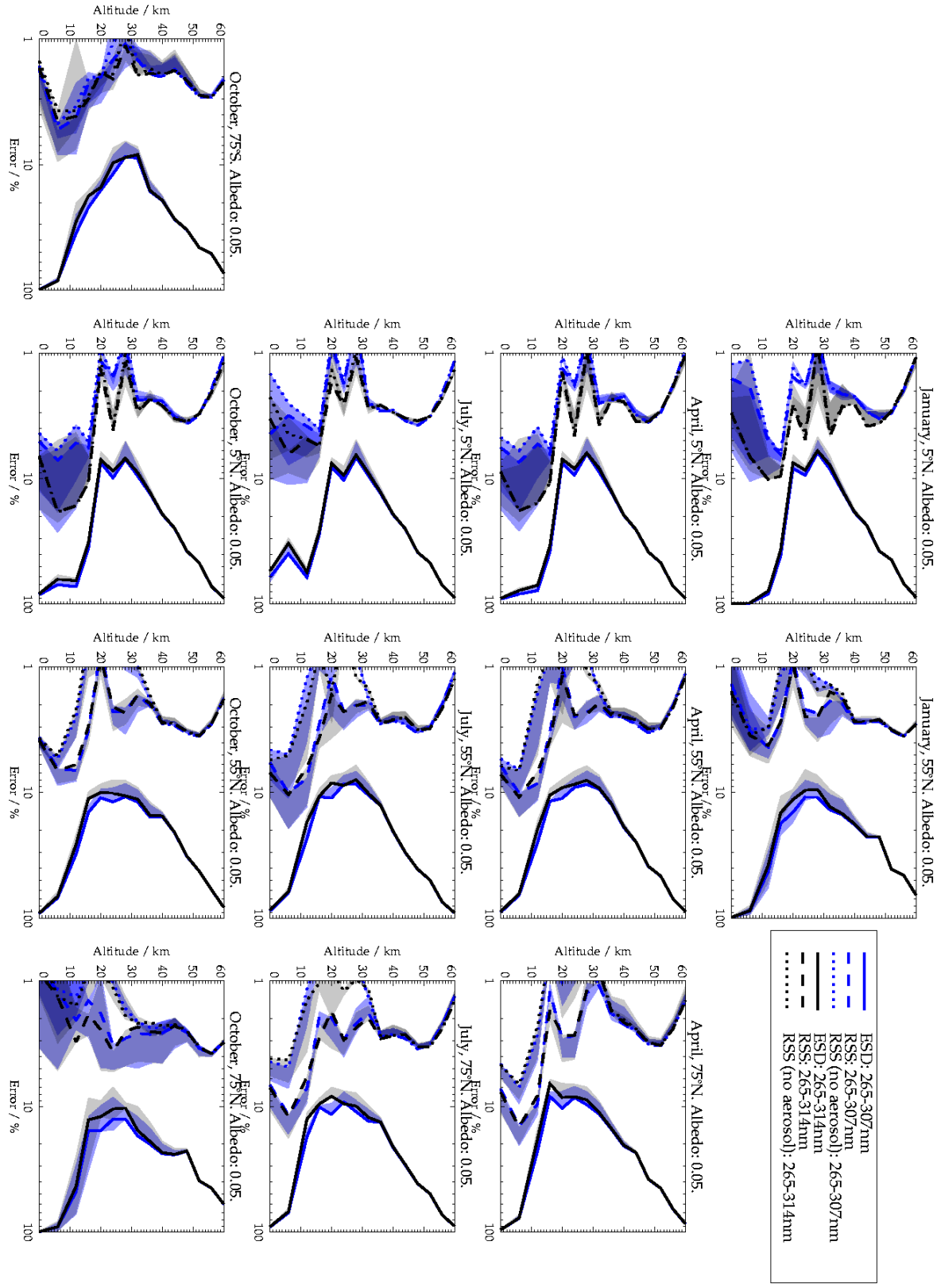

Figure 8-6: Comparison of ESDs, RSS baseline errors for both B1 coverage options: - surface albedo 0.05

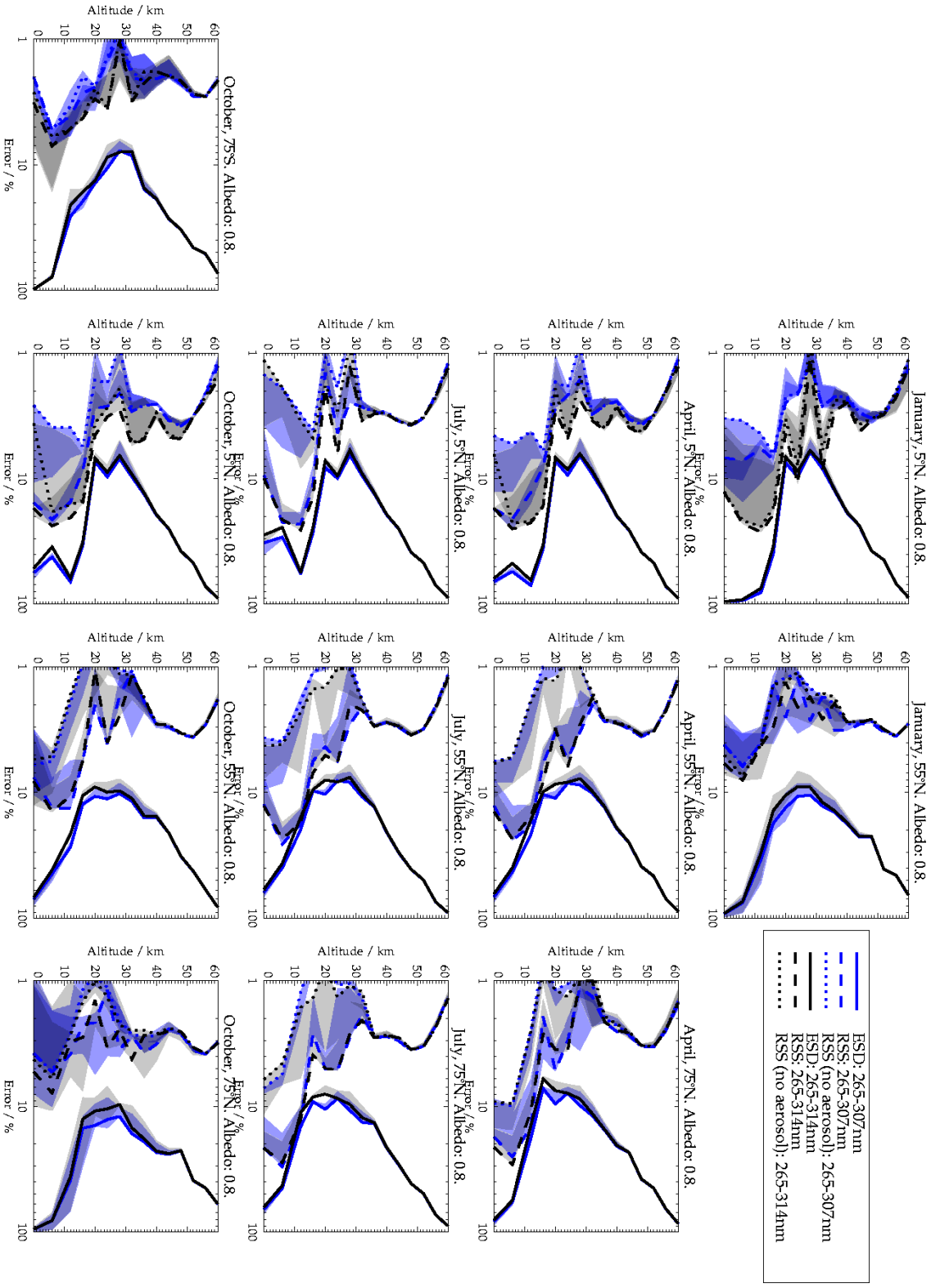

Figure 8-7: Comparison of ESDs, RSS baseline errors for both B1 coverage options: - surface albedo 0.8

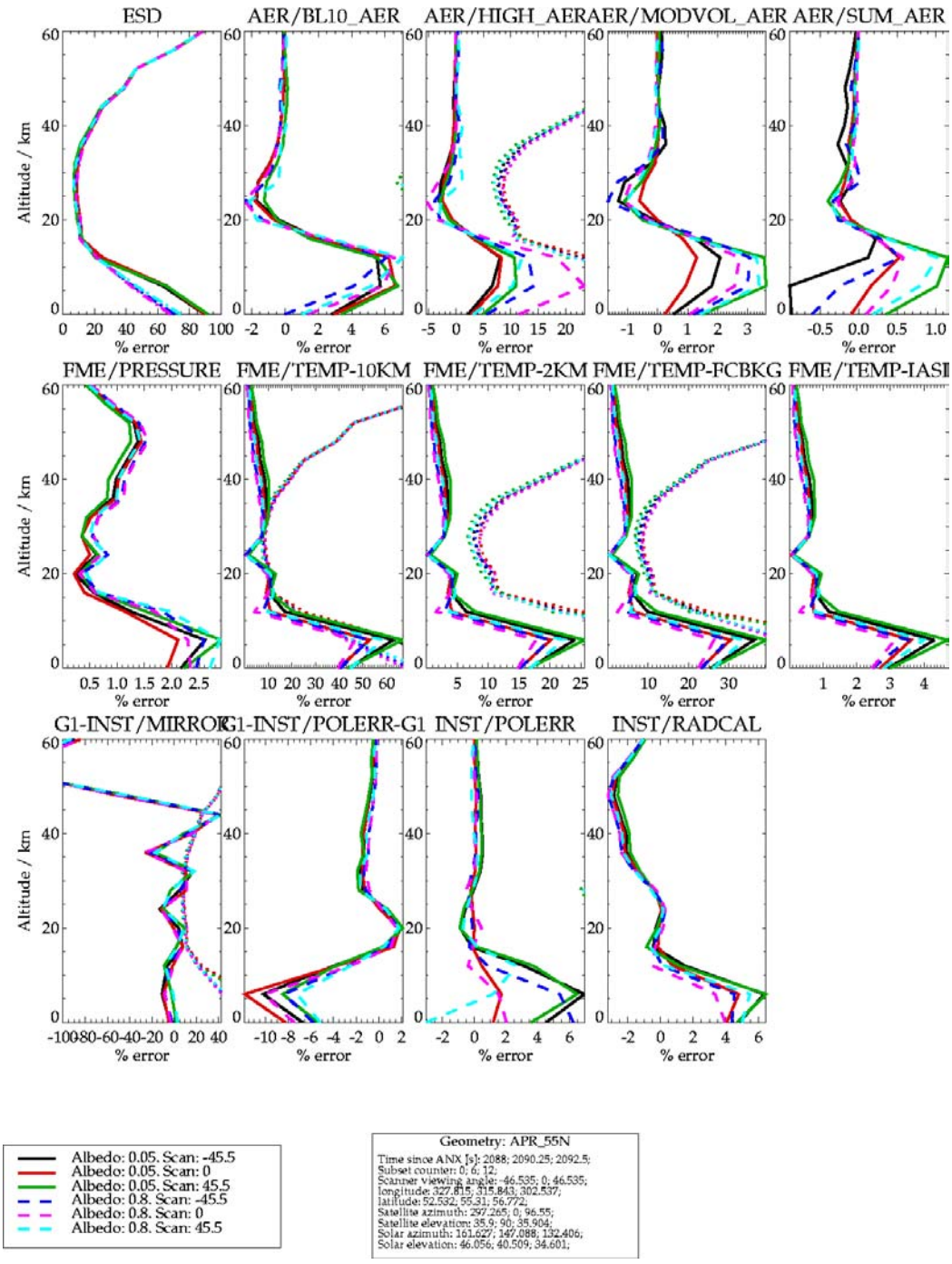

Figure 8-8 **Estimated standard deviations and mapped errors for April, 55°N scenario:**
- Band 1 wavelength range 265-306 nm

9 WP150: Use of Proper Ozone Cross-Sections beyond 340 nm (IUP)

9.1 Summary

Figure 9-1 shows SCIATRAN top-of-atmosphere spectra calculated with Bass-Paur and GOME FM ozone cross-section. Calculations are based upon MPI-2D 75°S October trace gas profiles. Bass-Paur measurements only extend up to 343 nm, see [9-1] and [9-2]. The change in cross-section is clearly visible in the residual (bottom).

Beyond 340 nm GOME FM clearly has the best signal-to-noise ratio and weak ozone bands are still detectable up to 355 nm. The origin of the low-resolution ozone cross-section used to extend Bass-Paur beyond 340 nm is unknown. In SCIATRAN the Bass-Paur spectra are only used up to 340 nm (see Figure 9-1).

The following conclusion and recommendation can be drawn:

a) > 340 nm GOME FM best spectra available

b) 330-340 nm bias of ~1% in relative intensity between Bass-Paur and GOME FM

c) Profile retrieval up to 340 nm can be done using either Bass-Paur or GOME-FM

9.2 References

[9-1] R.J. Paur, A.M. Bass, The ultraviolet cross-sections of ozone, II, Result and temperature dependence, in Atmospheric Ozone, ed. C.S. Zerefos and A. Ghazi, p. 611-616, D. Reidel, Norwell, Mass., 1985.

[9-2] A.M. Bass, R.J. Paur, The ultraviolet cross-sections of ozone, II, The measurements, in Atmospheric Ozone, ed. C.S. Zerefos and A. Ghazi, p. 606-610, D. Reidel, Norwell, Mass., 1985.

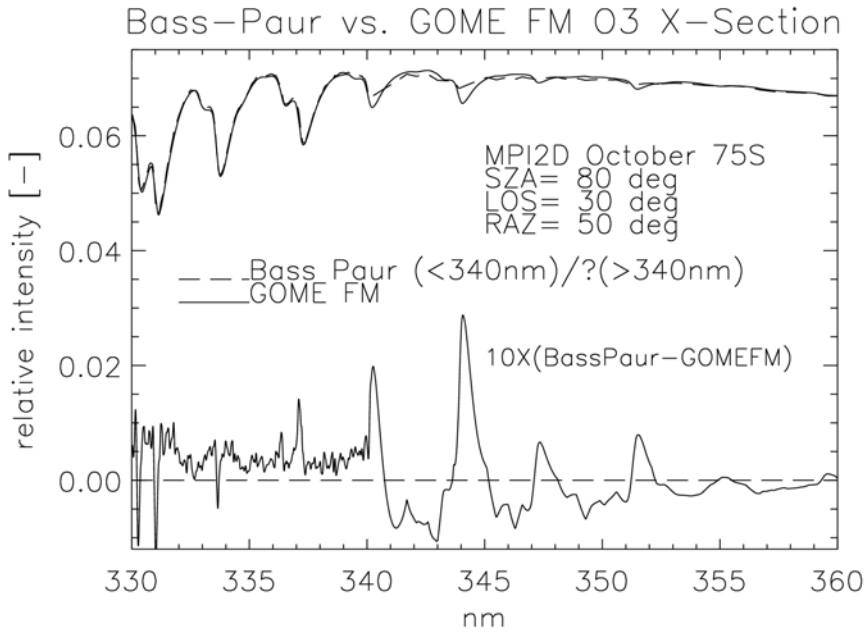

Figure 9-1: SCIATRAN relative intensity calculation using Bass-Paur and GOME FM O_3 cross-sections

Dashed line: Bass-Paur Solid line: GOME FM

10 WP 150: Column Retrievals and Instrument-Errors (IUP)

10.1 Introduction

This part of the work package was carried out by IUP, University of Bremen. In discussion with SRON a preliminary assessment of possible instrument related error sources with respect to DOAS retrieval is summarised below. More details on the instrumental effects have been already given in Section 7.

10.2 Diffuser plate spectral structures

The sanding of the Aluminium coating on the diffuser plate introduces some regular features, which result in spectral features in differential spectra that strongly correlate with absorption features Seasonal patterns that are seen in time series of NO_2 and BrO in the tropics (see Figure 4, Figure 5 and the Appendix of [10-2]). Large jumps repeating in subsequent years at almost the same time cannot be the results of tropospheric events (biomass burning, urban emission), which are rather random. This is related to the annual cycle in the elevation and azimuth angles of the incoming solar radiation [10-2]. A smaller signature is expected for strong absorbing ozone. Because of the large dynamic variability of ozone in the course of a year a discovery of such a signature may be more difficult. Stratospheric ozone is more stable in the tropics, but clouds can be very variable and modulation due to tropospheric ozone or diffuser plate characteristics may be difficult to be distinguished. Another way to highlight the diffuser plate error in the DOAS retrieval is to plot the difference between DOAS fit using the daily solar irradiance and fit using a fixed solar reference spectrum. A similar recipe could be applied to ozone retrieval, by looking at time series of ozone profiles using fits with fixed and daily variable solar reference spectra.

The diffuser plate error severely affects DOAS retrievals with 50% error in NO_2 and larger errors for weaker absorbers. To limit this impact, a second diffuser plate has been added to SCIAMACHY. To our knowledge, GOME-2 uses a diffuser plate similar to that of GOME-1. Of all possible error sources this is believed to be the largest contribution to the instrument-induced error. However, diffuser plate effects are not investigated as part of this study.

Although the error due to the diffuser plate may be quite small for total ozone, it might be nevertheless non-negligible. This was tested using total ozone derived from FURM ozone profile retrieval using FURM [10-9]. The daily GOME solar spectrum is a mean of about 17 individual measurements taken in sequence during full solar disc viewing [10-10]. Using different solar spectra in the FURM retrieval from this sequence one can study the effect of varying elevation angles on the diffuser plate [10-8]. Figure 10-1 shows the FURM total ozone from the individual solar spectra. Remarkable is the smooth variation of total ozone value by changing incident or elevation angle. A small effect on the order of 0.3% is observable. During this sequence of sun measurements the zenith angle at the diffuser plate varies, whereas in the course of the year the azimuth angle in addition varies, so that the error due to the diffuser plate could be even larger. Therefore, a quantitative statement about the amplitude of a seasonal effect cannot be derived, but it may be larger than 0.3%.

The following additional References to diffuser plate characteristics and its influence on NO_2 retrieval are given at the end of this section: [10-5], [10-6] and [10-7].

10.3 Dichroic features in Channel 3 and Channel 4

Outgassing of the dichroic mirror after launch of GOME-1 resulted in strong wavelength shifts in the calibration parameters. This introduces sharp structures in the differential spectra making it difficult to retrieve ozone in the visible Chappuis band [10-1]. The NO_2 window for DOAS retrieval has also been shifted in the operational GOME-1 retrieval. The change of the window to 425-450 nm leads to larger O_3 contribution in the optical depth spectra.

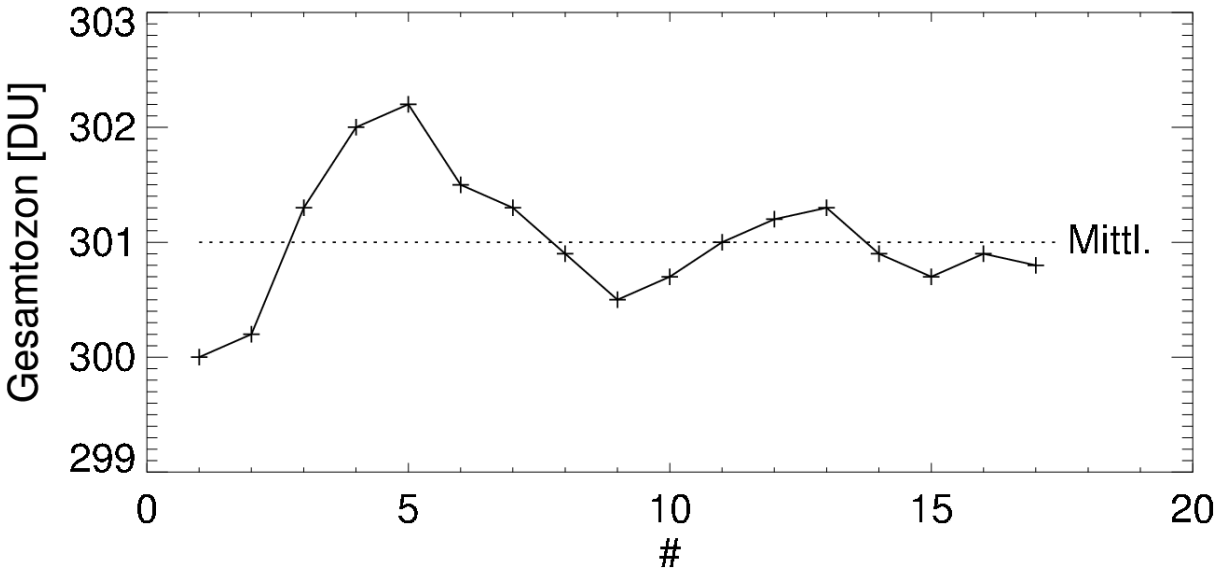

Figure 10-1: Total ozone from different GOME1 solar spectrum during full solar disc viewing at a given day

10.4 Scan mirror dependent optical degradation

The scan angle dependence of the optical degradation can lead to (differential) degradation observed in sun-normalised radiances (see references in Section 6). As long as this is a broadband effect, this is removed by the fitted polynomial subtracted from the optical depth spectra. One should also note here that no reliable information on differential degradation is available for wavelengths longer than 295 nm.

10.5 Polarisation correction / PMD degradation

Polarisation sensitivity is a rather smooth function of wavelength and any error will be taken care of by the fitted polynomial. However, errors in the Eta key parameters (ratio of polarisation sensitivity perpendicular to parallel instrument defined angle) can lead to artificial residual structures (for instance due to dichroic features). This currently inhibits the possible O_3, IO, and OIO retrieval from GOME-1.

For the different scenarios as listed in Table 10-1, polarisation correction errors spectra were provided from SRON. These error spectra exhibit very weak ozone structure (less than 0.1% of the radiance) in the wavelength region beyond 325 nm (Figure 7-2). All error spectra were directly fitted to obtain ozone slant columns. For all scenarios the errors in the ozone slant columns were less than 0.6% (Figure 6-5). No differences in the error statistics were found between the two-albedo values. In reality, clouds with high albedos tend to depolarise the radiance and thus even lower errors should be expected for cloudy scenes.

10.6 Wavelength calibration

Differences in the wavelength scales of cross-section spectra and between solar irradiance and nadir radiance spectra can be corrected using shift and squeeze to match the various spectra with respect to a selected reference. Spurious effects can still occur due to changing slit-widths with wavelength and due to noise introduced by interpolation of nearly under-sampled spectra.

10.7 Undersampling

The limited sampling of GOME-1 (~1.5 detector pixel spectral resolution) leads to larger errors in the Doppler correction of the solar spectrum with respect to the radiance measurements. This adds differential structure to the sun-normalised spectra. A solar spectrum measured at a much higher spectral resolution than GOME-1 can be used for an undersampling correction

This reduces the residual noise considerably but adds no new information to the retrieval [10-3]. The 2.1 - 2.3 detector pixel spectral resolution means that GOME-2 is slightly over-sampling the spectrum. Larger over-sampling (~0.5 nm spectral resolution) improves significantly the signal-to-noise ratio and reduces residual noise from interpolation. Part of this study will be devoted to the undersampling issue (WP230).

10.8 Air-vacuum calibration correction

Since this correction is slowly varying with wavelength, this should not affect column retrieval.

10.9 Spatial aliasing

Spatial aliasing due to the finite readout time of the detector introduces slopes in the radiance spectra and jumps in the overlap region between channels. This slope can be removed by the polynomial fitted to the optical depth spectrum. Changing cloud conditions as a function of wavelengths can lead to differences in achieved signal-to-noise ratio, indirectly affecting DOAS retrieval. It is also possible that hidden planetary boundary layer trace gas column amounts below the cloud change with wavelength. However, this is a desired effect to retrieve tropospheric columns using cloud-slicing techniques. This study investigates this aspect in greater detail in WP 210.

10.10 Summary

Possible major instrument induced error sources for trace gas column retrieval are related to spectral features induced by the diffuser plate (presumably the same diffuser plate is used for GOME-2) and by dichroic features, which will be strongly reduced by improved coating techniques. These error sources are not investigated as part of this EUMETSAT study. Many instrumental artefacts, including those not listed here (see Section 7.2), can be removed by the fitted polynomial, if they are fairly slowly varying with wavelength. An indirect effect comes from changes in signal-to-noise ratio. The issue related to the optimum balance between over-sampling (spectral resolution) and signal-to-noise ratio, and its impact on DOAS retrieval, is investigated in WP230. Spatial aliasing is investigated in WP 210.

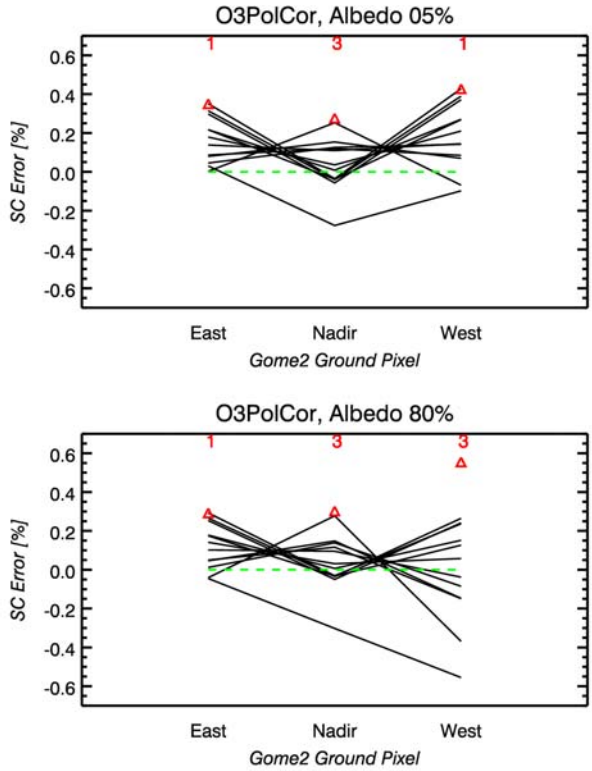

Figure 10-2: Slant column errors due to polarisation correction error

Top: albedo 0.05% Bottom: albedo 0.8%

Red triangles indicate maximum error observed in all scenarios. The numbers at the top of the figure correspond to the scenario number having the largest error.
(See Table 10-1 below.)

Number	*Month/Latitude*
1	Mon01Lat05n
2	Mon01Lat55n
3	**Mon10Lat75s**
4	Mon04Lat05n
5	**Mon04Lat55n**
6	Mon04Lat75n
7	Mon07Lat05n
8	Mon07Lat55n
9	**Mon07Lat75n**
10	Mon10Lat05n
11	Mon10Lat55n
12	Mon10Lat75n

Table 10-1: Numbering of the tracegas scenarios used in plots

Colour coded entries are scenes for Antarctic ozone hole (3, blue), free tropospheric BrO (5, yellow), and biomass burning (9, red) conditions.

For more details see Tables 6-1, 6-2, 6-3.

10.11 References

[10-1] Eisinger, M., J.P. Burrows and A. Richter, "Studies on the Precision of GOME Irradiance and Radiance Products and GOME Measurements of OClO and BrO over Antarctica", GOME Geophysical Validation Campaign, ESA WPP-108, pp.93-108, 1996

[10-2] A. Richter and T. Wagner, "Diffuser Plate Spectral Structures and their Influence on GOME Slant Columns", Technical, January 2001

[10-3] Slijkhuis, S., A. von Bargen, W. Thomas, and K. Chance, "Calculation of ´Undersampling correction spectra' for DOAS fitting", European Symposium on Atmospheric Measurements from Space, Proc. ESAMS'99, ESA-WPP-161, 563-569, 1999

[10-4] C.P. Tanzi, R. Snel, O. Hasekamp, I. Aben, "Degradation of UV earth albedo observations by GOME", ERS-ENVISAT Symposium, Gothenburg, 16-20 October 2000, ESA SP-461, on CD-ROM, Jan 2001

[10-5] Richter, A. and J.P. Burrows "A multi wavelength approach for the retrieval of tropospheric NO_2 from GOME measurements, in proceedings of the ERS / ENVISAT symposium", Gothenburg October 2000, ESA-SP 461, 2000 (CD-ROM)

[10-6] Richter, A. and J.P. Burrows, "Retrieval of Tropospheric NO2 from GOME Measurements", accepted for publication in Adv. Space Res., 2000

[10-7] Elders, G. J. M.; C. Grainer, R. W. Portmann, K. Pfeilsticker, M. Wenig, T. Wagner, U. Platt, A. Richter, and J. P. Burrows, "Global tropospheric NO_2 column distributions: Comparing 3-D model calculations with GOME measurements", JGR, D 106, 12643-12660, 2001

[10-8] K. Bramstedt, J. Gleason, D. Loyola, A. Bracher, M. Weber, and J.P. Burrows, "Comparison of total ozone from the satellite instruments GOME and TOMS with measurements from the Dobson network 1996–2000", manuscript in preparation

[10-9] R. Hoogen, V.V. Rozanov and J.P. Burrows, "Ozone profiles from GOME satellite data: Algorithm description and first validation", J. Geophys. Res. 104, 8263-8280, 1999

[10-10] M. Weber, J.P. Burrows and R.P. Cebula, "GOME Solar UV/VIS Irradiance Measurements between 1995 and 1997 - First Results on Proxy Solar Activity Studies", Solar Physics 177, 63-77, 1998

11 WP 150: Basic SNR for DOAS Retrievals (IUP)

11.1 Introduction

Using the output from the noise model (Section 8.3) Gaussian distributed random noise was added to the CDI spectra (see Figure 11-1). It was assumed that the modelled SNR is representing the 1σ level of the Gaussian distribution. Outliers above twice that value were excluded to avoid spurious spikes in the spectra. SNR were determined by assuming 0.1875 sec integration time for each GOME pixel and 30 sec integration for solar irradiance. Each GOME pixel spectra is obtained by integrating ten successive LOS spectra from the CDI simulations (one east-west scan comprises of 24 ground pixels) before adding the noise.

For all calculations and all input cross-section spectra, identical wavelength grids were used to avoid wavelength interpolation effects. Two ground albedos have been investigated in order to obtain slant column SNR errors for O_3, NO_2, BrO, and OClO. This amounts to 2304 case scenarios.

11.2 Error statistics and linear error mapping

Two approaches have been applied to achieve slant column (SC) error estimates for the considered trace gases. First, slant column errors were obtained from all individual cases by adding random generated Gaussian noise to each set of spectra. Secondly, SNR were included in the covariance matrix and slant column errors were determined using a linear mapping approach. SC retrieved from "clean" spectra (not noise corrupted) were taken as reference values (perfect fit) to determine SC errors in percent.

Linear Mapping (LM) is based on the following equations: Having Matrix A, constructed as

$$A = \begin{bmatrix} \sigma_{11} & \sigma_{12} & \dots & \sigma_{1M} & 1 & \lambda_1 & \lambda_1^2 & \dots & \lambda_1^P \\ \sigma_{21} & \sigma_{22} & \dots & \sigma_{2M} & 1 & \lambda_2 & \lambda_2^2 & \dots & \lambda_2^P \\ \dots & \dots & \dots & \dots & \dots & \dots & \dots & \dots & \dots \\ \sigma_N & \sigma_N & \dots & \sigma_{NM} & 1 & \lambda_N & \lambda_N & \dots & \lambda_2^P \end{bmatrix}$$

where the absorption cross-sections σ_{ij} of the j-th trace gas at each wavelength λ_i are taken into account. A polynomial of degree P is implicitly applied as for DOAS. The matrix

$$T = \left(A^t \Sigma^{-1} A\right)^{-1}$$

then gives the covariances calculated using the spectral covariance matrix Σ, which diagonal elements are variances according to the modelled noise. The standard deviation error for the j-th trace gas is then

$$\epsilon_j^{SC} = \left(\sqrt{T_{jj}} / SC_j^{perf}\right) \times 100\%$$

expressed as percentage error w.r.t. the perfect fit result SC_j^{perf}, which has been achieved fitting the un-corrupted (clean) spectrum. Some errors, which are larger than 2-sigma (e.g. ground pixel 12 and 13, April 5N), can be explained by correlations of cross-sections fitted including Ring with the noise pattern and for the case of O_3 by the use of two cross-sections (two temperatures) for the fitting, whereas for the modelling, temperature dependencies were taken into account using Bass-Paur polynomial approximations. For similar reasons such cases occur also for NO_2 (e.g. Figure 11-10 bottom right, ground pixels 1, 21 and 23).

Figure 11-1 shows fitted Ring amplitudes for all scenarios and ground pixel when using noisy intensities. Maximum values of RMS and correlation coefficients are indicated for O_3 and NO_2. For the fitting, the Ring spectrum added onto the modelled intensity has been used, thus for the ideal (noise free) case an amplitude of one is expected. Noise and correlations with cross-sections lead to errors on the Ring amplitude as well as

on the trace gas fit-results. From this, largest errors due to Ring interferences can be expected for NO_2 (red). Although the largest correlation is observed for O_3 for 80% albedo the Ring impact should be small due to the dominance of O_3.

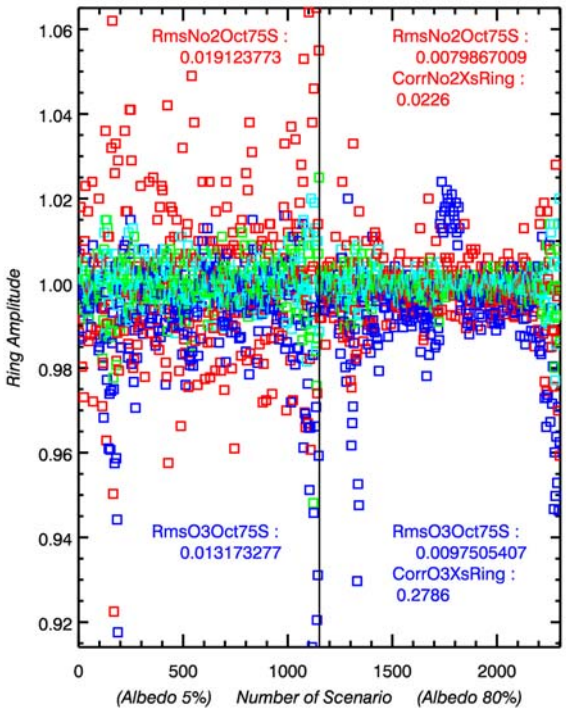

Figure 11-1: Ring amplitudes for all scenarios and ground pixels when fitting noisy intensities.

Numbers: root-mean-squares and correlation coefficients for NO_2 (red) and O_3 (blue).

Symbols: indicate Ring amplitudes, when fitting in the (a) BrO window (green) (b) OClO window (light blue)

Although specific examples of noise corruptions are not sufficient for statistically representative error statements, results for such cases are shown. It is considered useful to include them in the figures together with standard deviation estimates, to emphasize the meaning of the statistical parameters and to illustrate what has to be expected for single cases.

Starting with O_3, the following description is split into four paragraphs each related to one of the considered trace gases. The structure is similarly repeated for NO_2, BrO and OClO.

11.3 Ozone in the UV

Detailed results of percentage errors from the O_3 SNR error analysis are shown in Figure 11-3 to Figure 11-6 for January, April, July and October.

Figure 11-7 gives errors for East, West and Nadir GOME-2 ground pixel as a function of SZA.

Before presenting error numbers, an example of differential optical depth spectra for each trace gas considered in the O_3 fit window is depicted in Figure 11-2. It illustrates the depth of the absorption structures compared to the noise level, which has been translated into percentage units.

It is shown that for the selected Scenario 1 the 221K O_3 absorption structure spreads from - 6% to almost 9% relative to the intensities at 326.8 nm and 328 nm, respectively. The structures are therefore visible by eye even on the intensity scale. The 241K O_3 structure is about 20 times smaller. The BrO, NO_2 and noise (dotted lines) are barely visible (Figure 11-2). Ring is clearly visible but with low correlation to other structures. Small errors are therefore expected for O_3 in the UV.

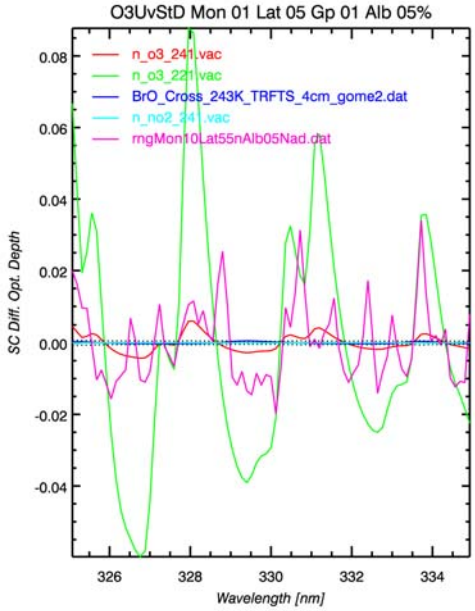

Figure 11-2: Differential optical depth calculated using slant columns from fitting a noise free spectrum

Each fitted slant column from scenario 1 with albedo 0.05 has been multiplied by the differential cross-section used in the O_3 UV fitting window.

- BrO (blue), NO_2 (light blue).
- Noise (dotted line) is barely visible.
- Ring is also included (pink line).

January

In the January scenarios (Figure 11-3), the LM SC errors are maximal near nadir for both albedos considered. For 5% albedo in the tropical scenario, the maximum error is about 0.4% for the tropical located slightly east of nadir. This is observed in many cases due to the westerly-orientated satellite orbit. GOME-2 is therefore directed to the sun when looking easterly (smaller slant path) and away from the sun when looking to the west (larger slant path). For northern mid-latitude the error is about 0.3% in the maximum. The errors decline to about 0.3% and 0.2%, respectively, on the east side and in the west. Decreasing errors to the sides are expected for stratospheric absorbers as the slant path of the light increases with LOS. However, it has to be kept in mind that longer light paths also go along with low light conditions and increasing SNR. For 80% albedo the maximum errors are 0.2% except for the Worst Case (S/N ceiling, errors up to >0.35%), the LOS dependency is relatively similar, except of the maximum, which tends to be westerly from nadir.

April

In the April scenarios (Figure 11-4), the maximum errors again occur for the tropical scenario, especially for 5% albedo (0.3%, nadir, 0.25% and 0.2% for east and west, respectively). For the northern mid-latitude and polar scenarios similar errors occur (<0.2%, 0.25%, <0.2% for east/nadir/west). The errors are lower for the 80% albedo (0.15% and below), and the LOS dependency is weak.

July

The July scenarios (Figure 11-5) give results very similar to April. The maximum for the tropical scenario is not as much emphasized as for April because the sun is now on the northern hemisphere. However, the maximum remains due to the low tropical ozone amount. For 80% albedo, the errors are even smaller than for April.

October

For October (Figure 11-6), a southern ozone hole scenario is also considered. For this case the errors for 75S and 75N rise up to 0.5% and 0.4%, respectively, for 5% albedo. This is because for both, the light intensities are low, and in the case of the Antarctic, ozone is very low; however, a low Antarctic ground albedo is unrealistic. For 80% albedo the situation is similar, but with errors below 0.3%. In any case errors remain low in general for ozone when retrieved in the UV.

SZA

Figure 11-7 shows O_3 SC errors selected for East, Nadir and West ground pixels over solar zenith angle (SZA). For all cases, errors are smaller for East and West pixels due to the longer light paths by sufficient SNR. For 5% albedo and SZA below 50 degrees, the errors are larger for East than for West pixels.

For the large SZA of 76 and 80 degrees it is the other way round, which is also valid for the 80% albedo cases. Errors are maximal for SZA=76 degrees as for this scenario (Oct 75S) ozone hole conditions are present. For the Jan 55N scenario (SZA=80 degrees) the error for the West pixel is almost as large as for Nadir due to the very low light, where the SNR aspect comes into play even for O_3.

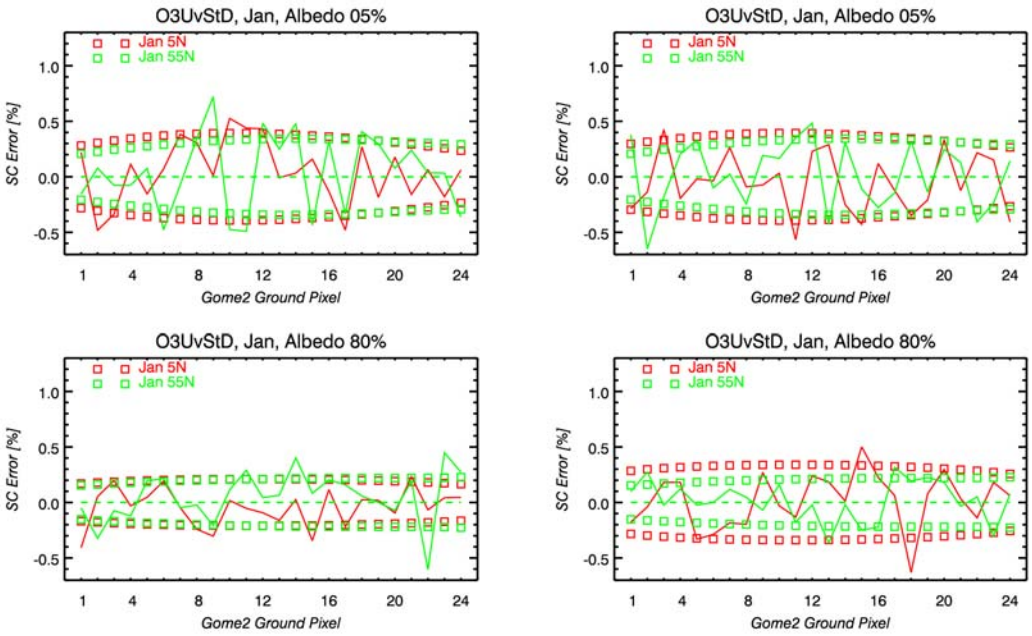

Figure 11-3: O_3 slant column errors w.r.t. perfect fit using uncorrupted spectra (January)

The standard deviations for each GOME-2 ground pixel calculated using linear mapping are indicated by squares for latitudes 5N and 55N. Individual noise corruption results are plotted as solid lines, which apparently correspond to the LM findings as expected.

Top: Albedo 5% Bottom: Albedo 80%

Left: Model noise Right: S/N ceiling at 2000

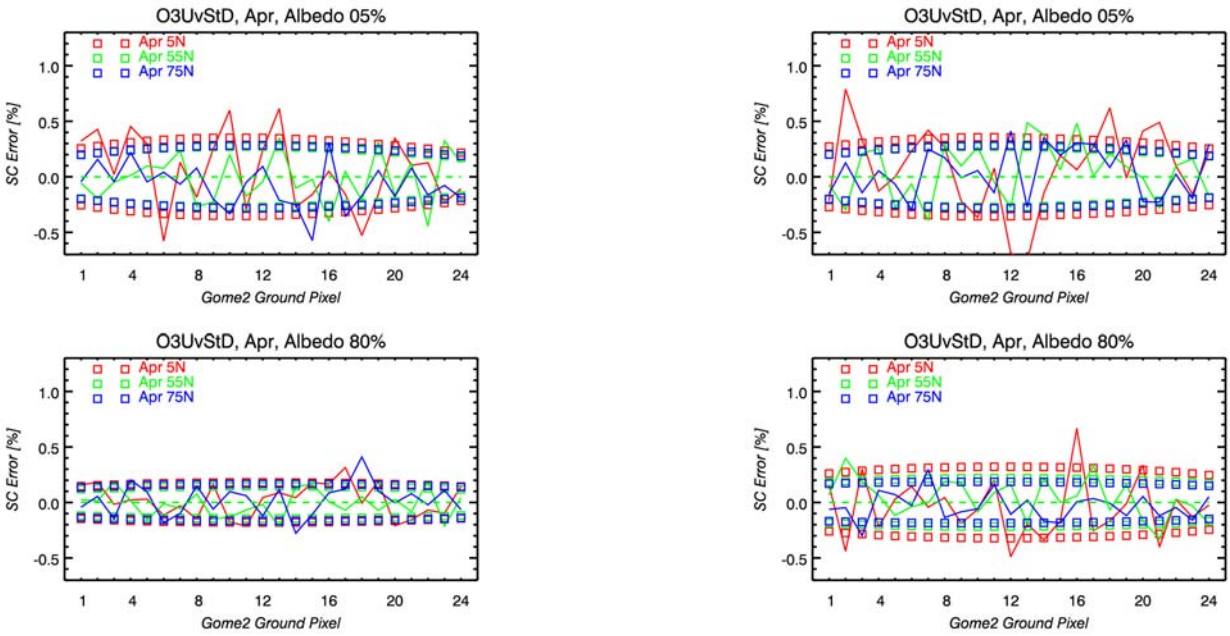

Figure 11-4: O_3 slant column errors w.r.t. perfect fit using uncorrupted spectra (April)

The standard deviations for each GOME-2 ground pixel calculated using linear mapping are indicated by squares for latitudes 5N, 55N and 75N. Individual noise corruption results are plotted as solid lines, which apparently correspond to the LM findings as expected.

Left: Model noise Right: S/N ceiling at 2000
Top: Albedo 5% Bottom: Albedo 80%

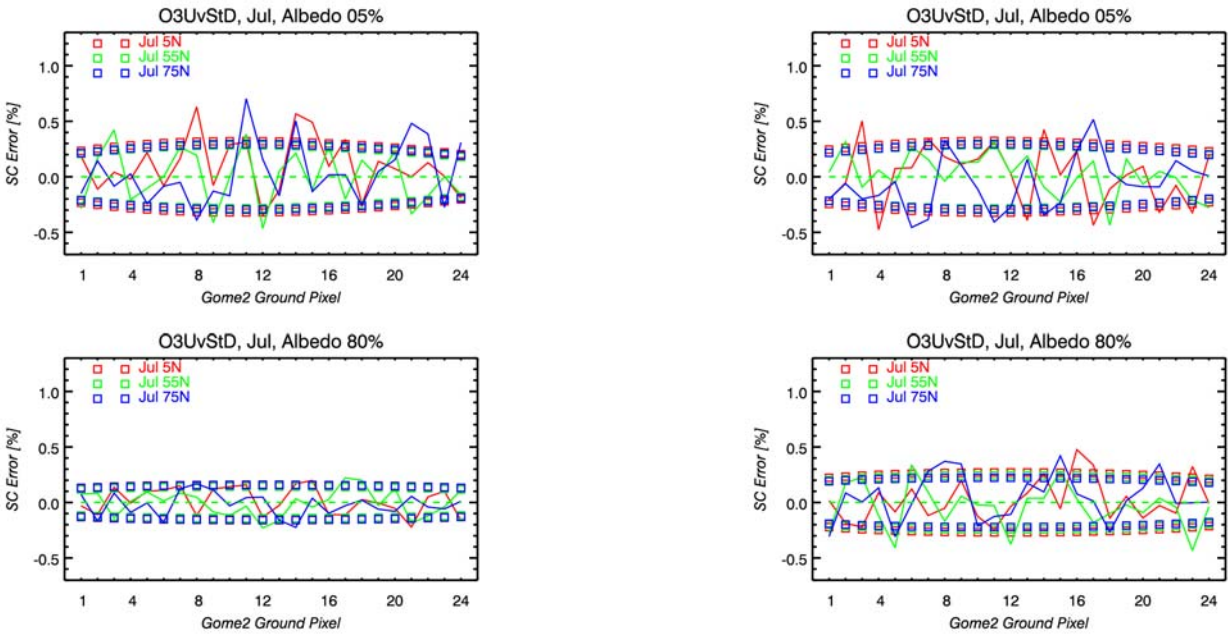

Figure 11-5: O_3 slant column errors w.r.t. perfect fit using uncorrupted spectra (July)

The standard deviations for each GOME-2 ground pixel calculated using linear mapping are indicated by squares for latitudes 5N, 55N and 75N. Individual noise corruption results are plotted as solid lines, which apparently correspond to the LM findings as expected.

Top: Albedo 5% Bottom: Albedo 80%
Left: Model noise Right: S/N ceiling at 2000

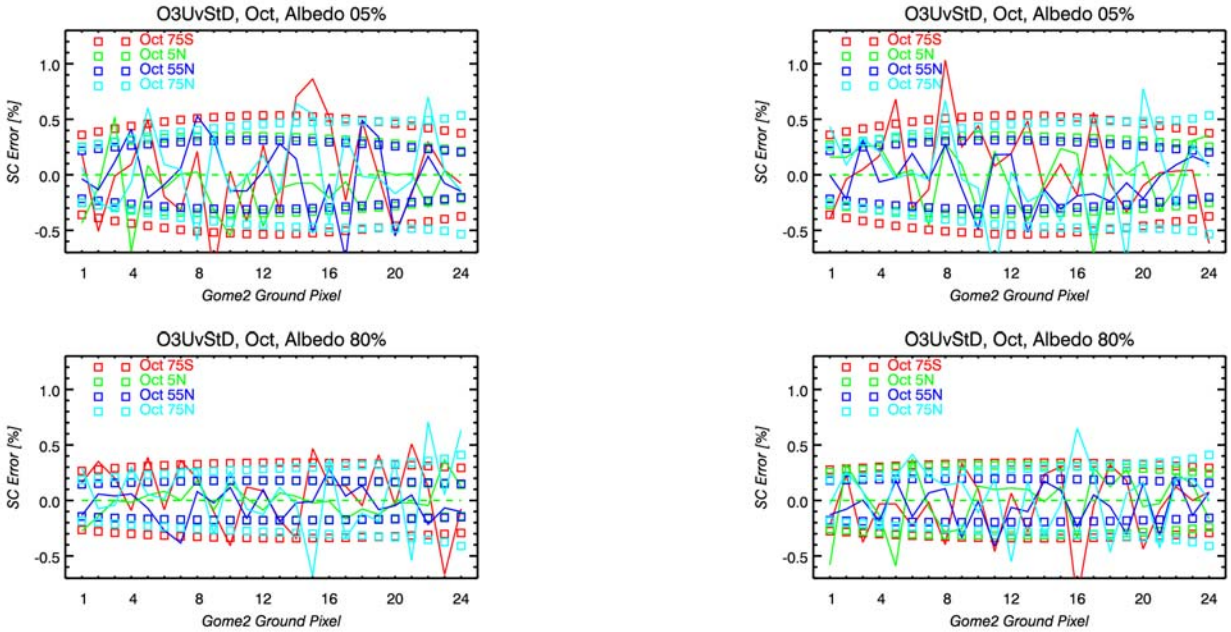

Figure 11-6: O_3 slant column errors w.r.t. perfect fit using uncorrupted spectra (October)

The standard deviations for each GOME-2 ground pixel calculated using linear mapping are indicated by squares for latitudes 75S, 5N, 55N and 75N. Individual noise corruption results are plotted as solid lines, which apparently correspond to the LM findings as expected.

Top: Albedo 5% Bottom: Albedo 80%
Left: Model noise Right: S/N ceiling at 2000

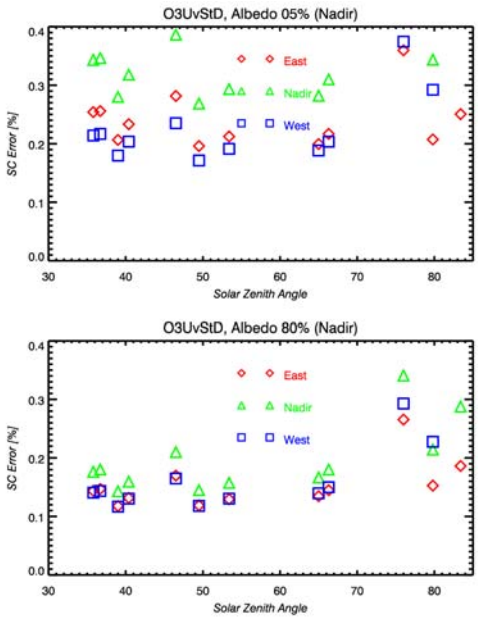

Figure 11-7: O_3 slant column errors for East, Nadir and West pixels as function of SZA

(GOME-2 model noise applied)

11.4 Nitrogen dioxide

The NO_2 fitting window used reaches from 425 nm to 450 nm in GOME-2 Channel 3. Differential optical depth spectra calculated for Scenario 1 (Table 10-1) for the species fitted in this window to obtain NO_2 are shown in Figure 11-8. Detailed results of percentage errors from the NO_2 SNR error analysis are shown in Figure 11-9 to Figure 11-12 for January, April, July and October, respectively. Figure 11-13 gives errors for East, West and Nadir GOME-2 ground pixel as a function of SZA.

From Figure 11-8 it can be seen that, in contrast to the O_3 fitting window, the noise level (dotted lines) in Channel 3 is lower but perturbs the NO_2 retrieval (small absorption) more strongly. In addition, Ring structures lead to large errors in NO_2 columns.

January

The NO_2 SC errors for January are given in Figure 11-9. For the low albedo, errors for 55N are between 12% and 22% for East/West and Nadir, respectively. For the tropical scenario, an asymmetry w.r.t. nadir occurs with errors of 12%, 16% and 10% (East/easterly near Nadir / West). For the high albedo the LOS dependency is small: errors are between 5% and 10% (10% and 12% for worst case noise). For both albedos, errors are larger for the northern mid-latitude scenario compared to the tropical scenario. This is in contrast to O_3 (Figure 11-3) and BrO (Figure 11-15), where for January the tropical scenarios give maximum errors. The reason for this may be related to the January northern mid-latitude low light conditions in conjunction with a high SNR sensitivity of NO_2 (Figure 11-8). Additionally it has to be kept in mind that NO_2 has a strong seasonal variation with minimum vertical columns in January, therefore the percentage errors are larger (see details on modified SLIMCAT / BRAPHO scenarios).

April

For April (Figure 11-10) the tropical scenario gives the maximum errors: for 5% albedo they are between 10% and 17% (West/East and Nadir, respectively). The Polar scenario errors are minimal and about a factor of 2 smaller. The same holds for 80% albedo, but with a tropical maximum error of 5% and weak LOS dependency.

July

The July case (Figure 11-11) is very similar to April. For the tropical biomass-burning scenario, the NO_2 is significantly enhanced in the troposphere. The errors are slightly smaller than for the other month considered. Compared to northern polar and mid-latitude, the errors are larger for the tropical biomass-burning scenario (up to about 15% and 5% (10%) for 5% and 80% albedo (worst case noise), respectively).

October

In October (Figure 11-12), the situation is different, as maximum values occur for the polar scenario (up to 27% for low albedo). For the other latitudes, including Antarctica, the errors are similar and about a factor of 1.5 lower than for the Arctic. The 80%-albedo situation is also similar, but with a maximum error of about 10% (75N), and errors smaller by a factor of about 2 elsewhere.

SZA

Figure 11-13 shows percentage errors for slant columns retrieved for East, Nadir and West GOME-2 ground pixels over SZA. A relatively strong dependence on solar zenith angle can be seen for low albedo with larger errors for low SZA (about 12%, 16%, 10%, respectively) and maxima for high SZA (15% / 19% for East / West, and 27% for Nadir).

Minima were achieved for 53.4 degrees SZA (about 5% for East/West and about 8% for Nadir). For the high albedo these errors are reduced by about a factor of 2. The biomass-burning scenario (SZA 40.4 degrees) does not significantly contrast.

Generally, low slant paths (small SZA) and low intensities (large SZA) induce enhanced errors, thus a trade-off around 55-60 degrees SZA can be estimated.

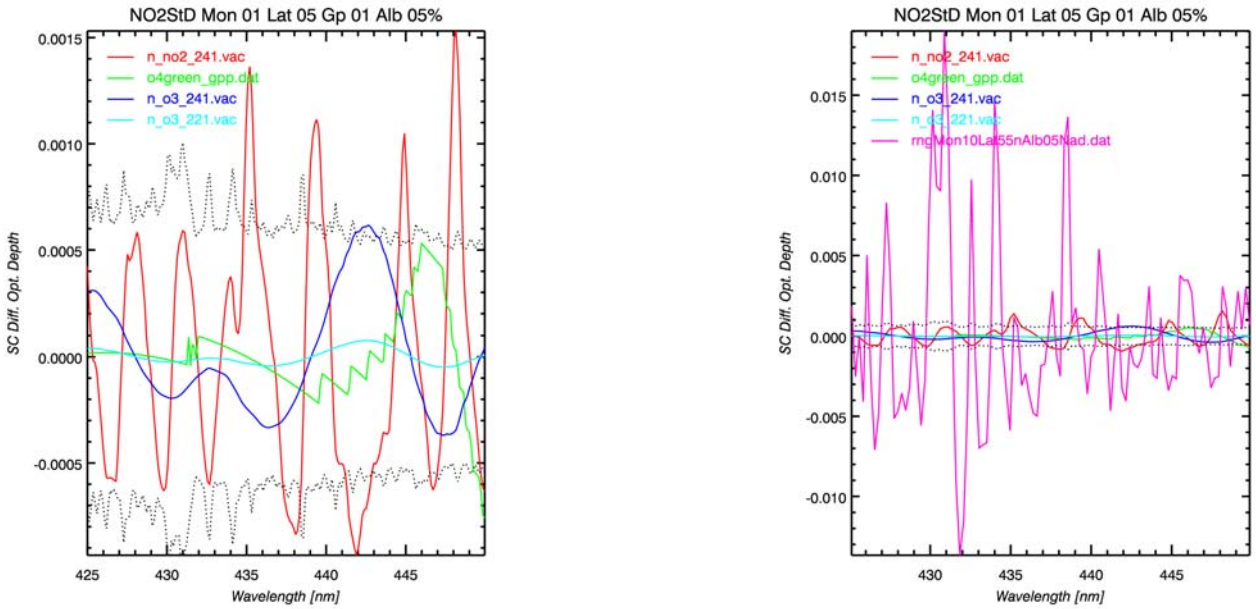

Figure 11-8: Diff Optical Depth calculated using slant columns from fitting a clean spectrum

As an example for illustration, a spectrum similar to trace gas Scenario 1 (Table 10-1) has been used for fitting. Each fitted slant column has been multiplied by the according differential cross-section used for the NO_2 fitting window. The applied noise level (1 sigma confidence) is indicated by dotted lines.

Left: Ring included Right: No Ring considered

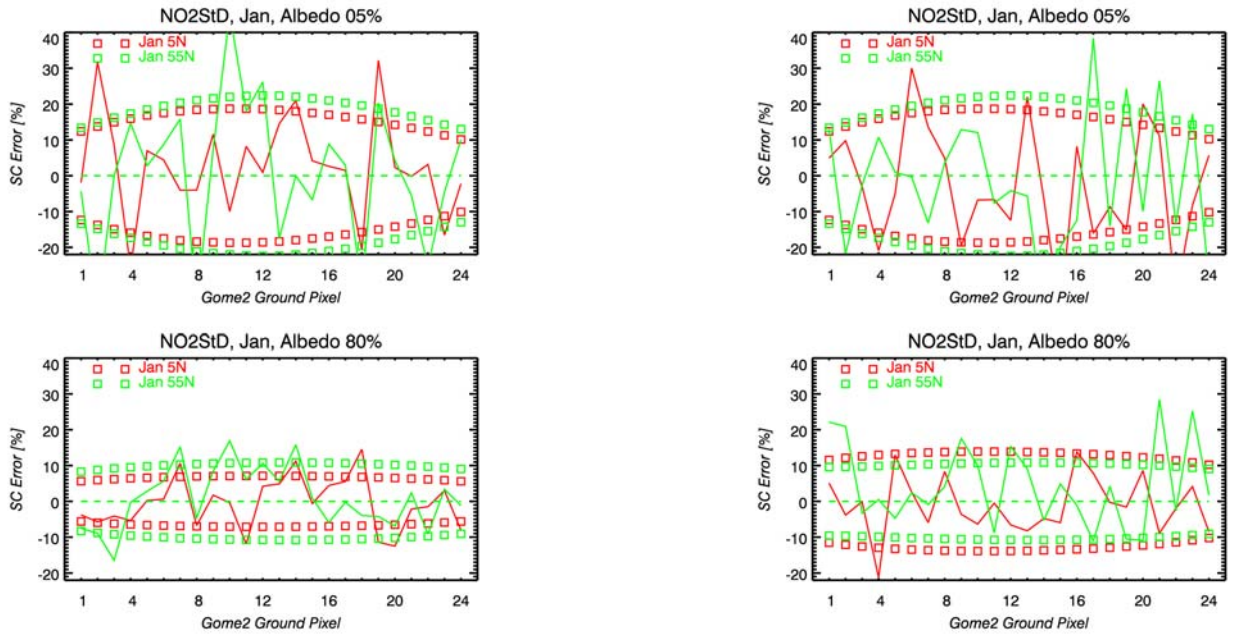

Figure 11-9: NO_2 slant column errors w.r.t. perfect fit using uncorrupted spectra (January)

The standard deviations for each GOME-2 ground pixel calculated using linear mapping are indicated by squares for latitudes 5N and 55N. Individual noise corruption results are plotted as solid lines, which apparently correspond to the LM findings as expected.

Top: Albedo 5% Bottom: Albedo 80%
Left: Model noise Right: S/N ceiling at 2000

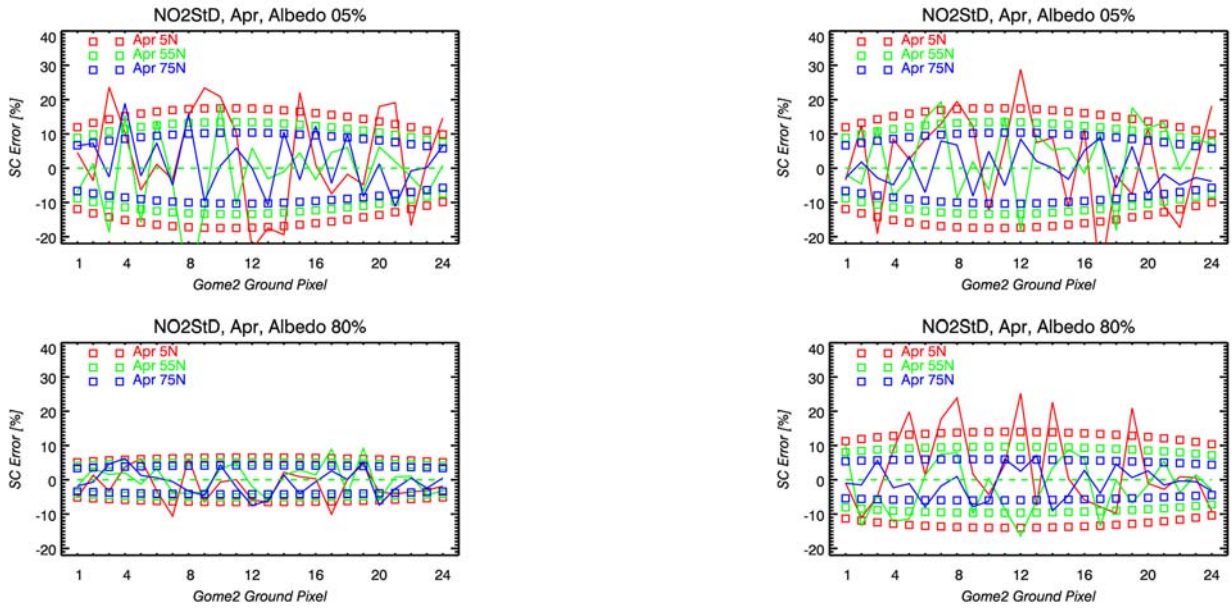

Figure 11-10: NO_2 slant column errors w.r.t. perfect fit using uncorrupted spectra (April)

The standard deviations for each GOME-2 ground pixel calculated using linear mapping are indicated by squares for latitudes 5N, 55N and 75N. Individual noise corruption results are plotted as solid lines, which apparently correspond to the LM findings as expected.

Top: Albedo 5% Bottom: Albedo 80%

Left: Model noise Right: S/N ceiling at 2000

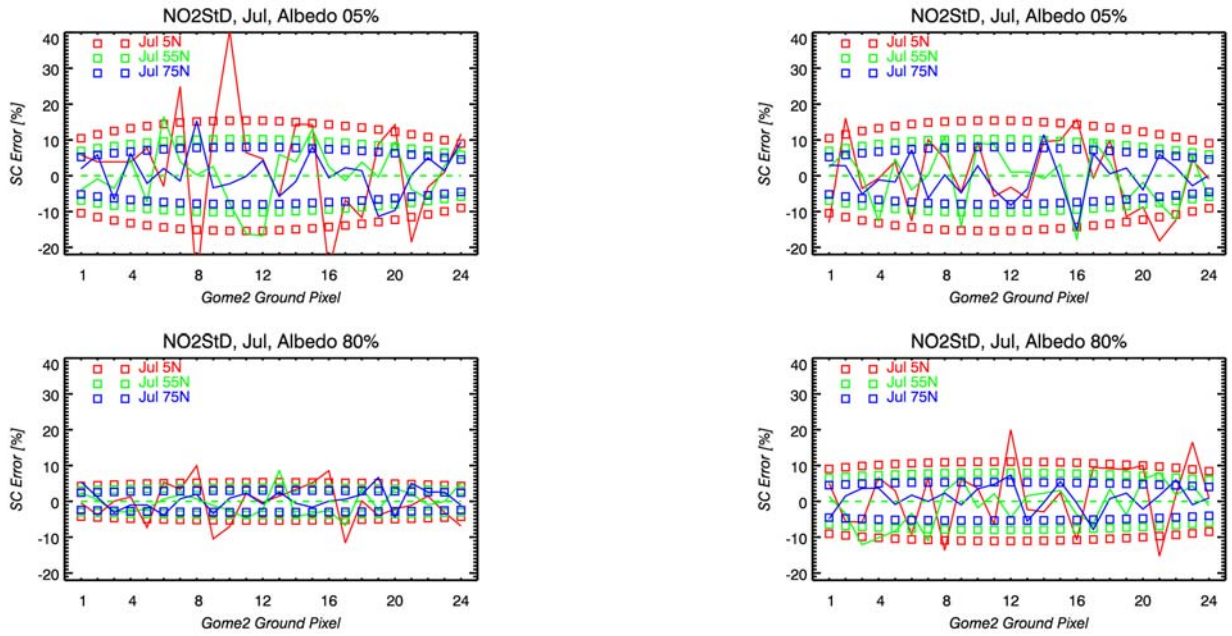

Figure 11-11: NO_2 slant column errors w.r.t. perfect fit using uncorrupted spectra (July)

The standard deviations for each GOME-2 ground pixel calculated using linear mapping are indicated by squares for latitudes 5N, 55N and 75N. Individual noise corruption results are plotted as solid lines, which apparently correspond to the LM findings as expected.

Top: Albedo 5% Bottom: Albedo 80%

Left: Model noise Right: S/N ceiling at 2000

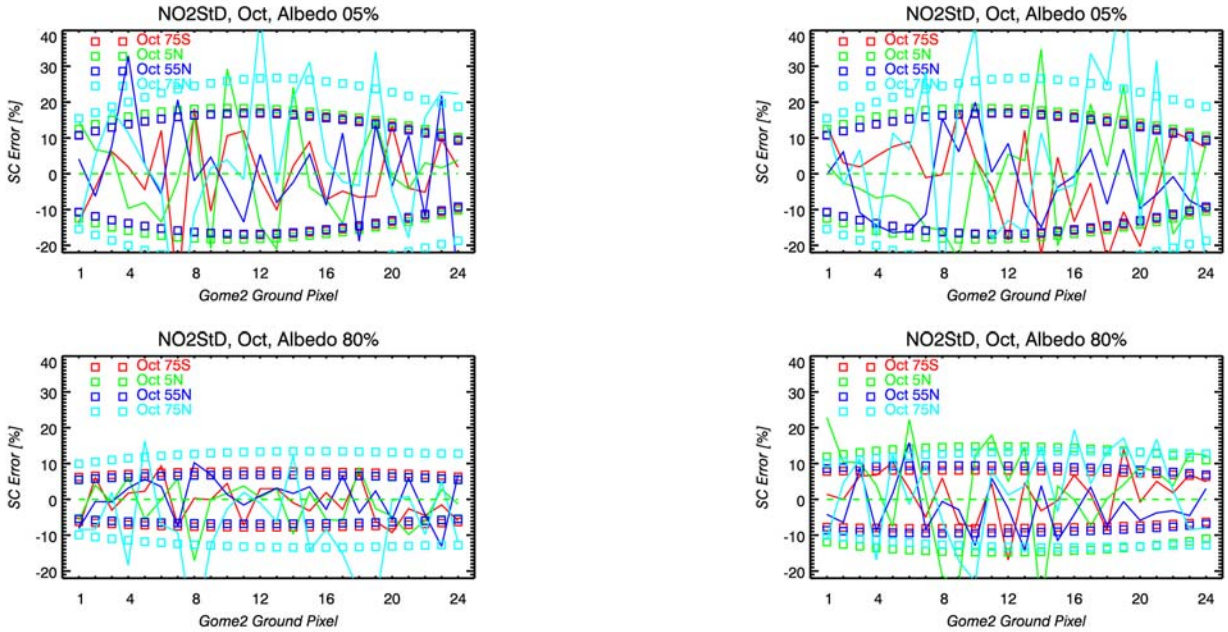

Figure 11-12: NO_2 slant column errors w.r.t. perfect fit using uncorrupted spectra (October)

The standard deviations for each GOME-2 ground pixel calculated using linear mapping are indicated by squares for latitudes 75S, 5N, 55N and 75N. Individual noise corruption results are plotted as solid lines, which apparently correspond to the LM findings as expected.

Top: Albedo 5% Bottom: Albedo 80%
Left: Model noise Right: S/N ceiling at 2000

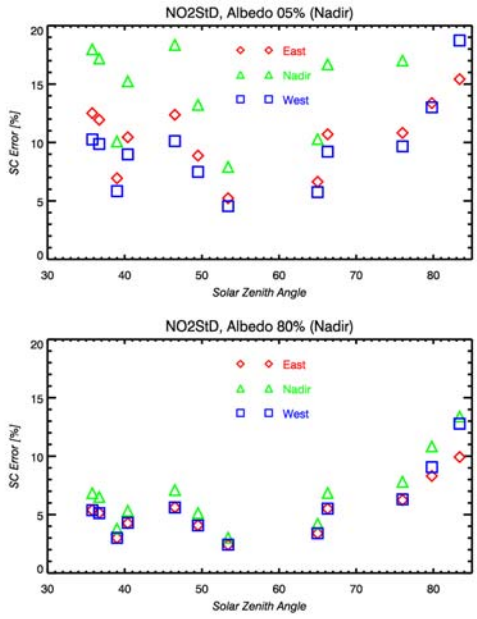

Figure 11-13: NO_2 slant column errors for GOME-2 East, West and Nadir pixel over SZA

11.5 Bromine oxide

In the fitting window between 344 nm and 360 nm, BrO and five other species including Ring are fitted. The resulting differential optical depths of each of the species are shown in Figure 11-14. Detailed results of percentage errors from the BrO SNR error analysis are shown in Figure 11-15 to Figure 11-18 for January, April, July and October, respectively. Figure 11-19 gives errors for East, West and Nadir GOME-2 ground pixel as a function of SZA.

January

For January (Figure 11-15) the tropical scenario gives maximum errors of about 60% and 30%, for 5% and 80% albedo respectively. The results for northern mid-latitudes are smaller, by about a factor of between 1.5 and 2. The LOS dependency is stronger for low albedos than for high albedos

April

Results for April (Figure 11-16) are similar for the tropical scenario, whereas the northern mid-latitude errors are smaller by factors of more than 2 for 5% albedo, and almost 3 for 80% albedo. This is partially due to the free tropospheric enhancement of BrO. Arctic results are in between.

July

For July scenarios (Figure 11-17) the maximum errors are between 40% and 50% for low albedos, and around 20% for high albedos.

October

A stronger variation of errors can be found for October (Figure 11-18), where for low albedos the maximum error spreads from <20% (West, 75S) to 60% (Nadir, 5N). 55N and 75N are similar (maximum <40%, Nadir).

As said, for the Antarctic ozone hole scenario the error rises from <10% (East) via 15% (Nadir) to 20% (West). This LOS dependence is as unusual as an Antarctic 5% albedo and can be therefore neglected. However, a similar LOS dependency is seen for high albedos for 75S, with very small errors below 5% (BrO explosion in PBL). For the other latitudes the errors are between 20% and 30%.

SZA

The BrO SC errors over SZA are shown in Figure 11-19. Minimum errors are for 49.5 degrees SZA (April, 55N, free troposphere BrO) and 76 degrees SZA (Oct 75S, ozone hole). The SZA dependency is stronger for low albedos with decreasing errors from small to large SZAs.

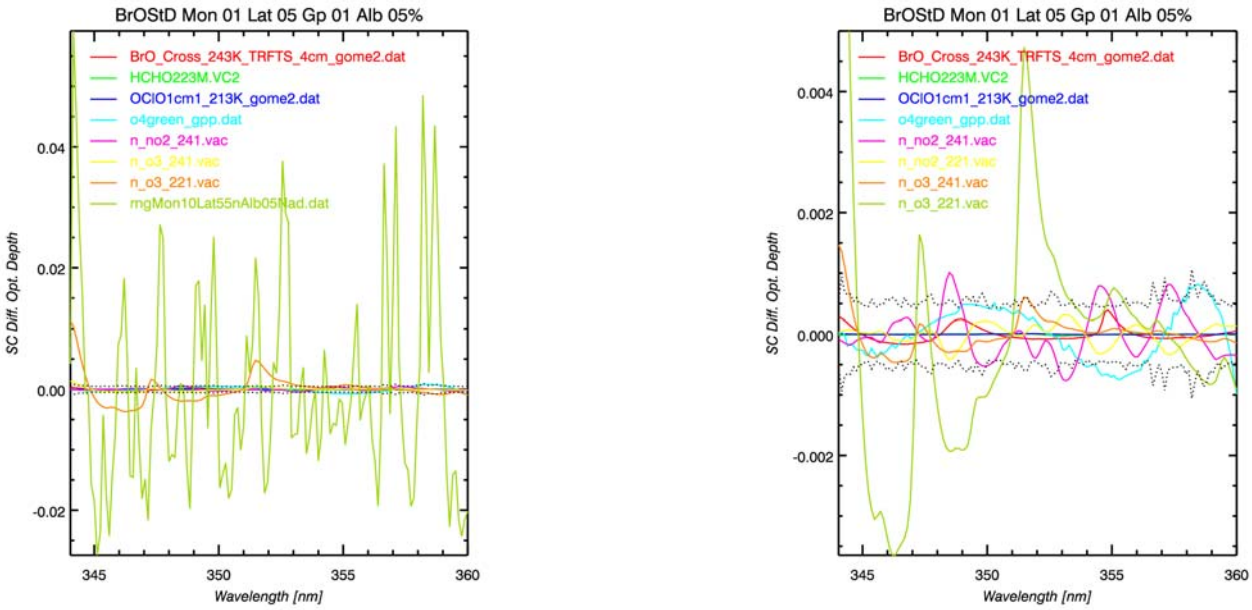

Figure 11-14: Diff Optical Depth calculated using slant columns from fitting a clean spectrum.

As an example the spectrum for trace gas scenario 1 (see Table 10-1) has been used for fitting. Each fitted slant column has been multiplied by the according differential cross-section used for the BrO fitting window. The applied noise level (1-sigma confidence) is indicated by dotted lines.

Left: Ring included Right: No Ring considered

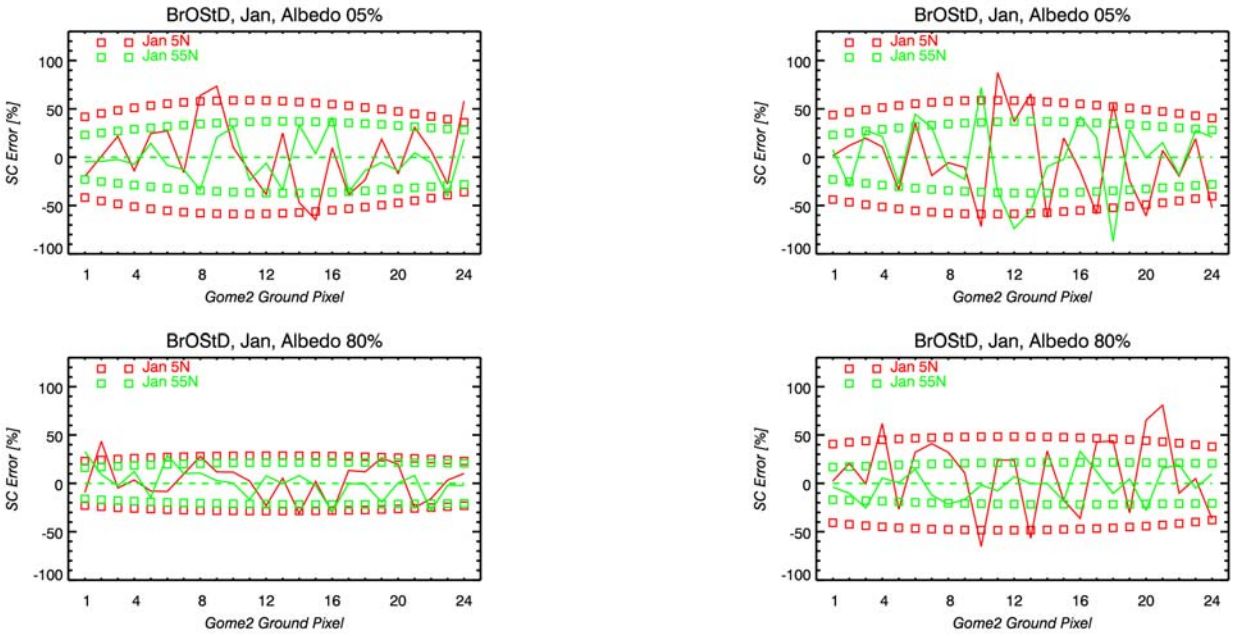

Figure 11-15: BrO slant column errors w.r.t. perfect fit using uncorrupted spectra. (January)

The standard deviations for each GOME-2 ground pixel calculated using linear mapping are indicated by squares for latitudes 5N and 55N. Individual noise corruption results are plotted as solid lines, which apparently correspond to the LM findings as expected.

Top: Albedo 5% Bottom: Albedo 80%
Left: Model noise Right: S/N ceiling at 2000

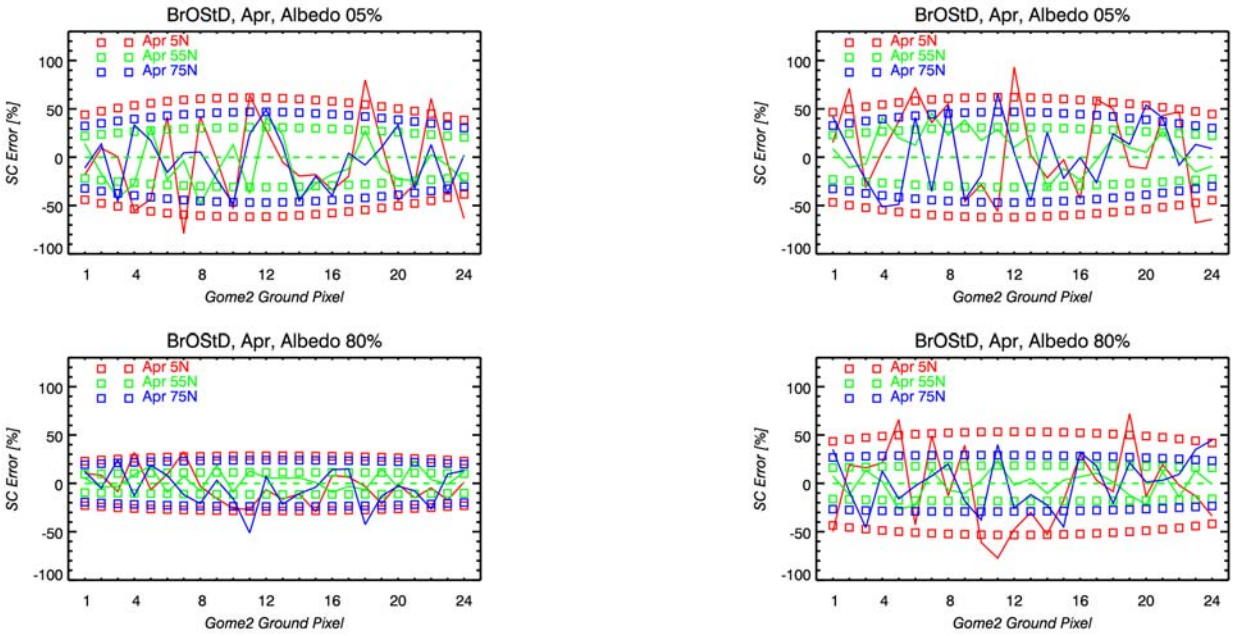

Figure 11-16: BrO slant column errors w.r.t. perfect fit using uncorrupted spectra. (April)

The standard deviations for each GOME-2 ground pixel calculated using linear mapping are indicated by squares for latitudes 5N, 55N and 75N. Individual noise corruption results are plotted as solid lines, which apparently correspond to the LM findings as expected.

Top: Albedo 5% Bottom: Albedo 80%
Left: Model noise Right: S/N ceiling at 2000

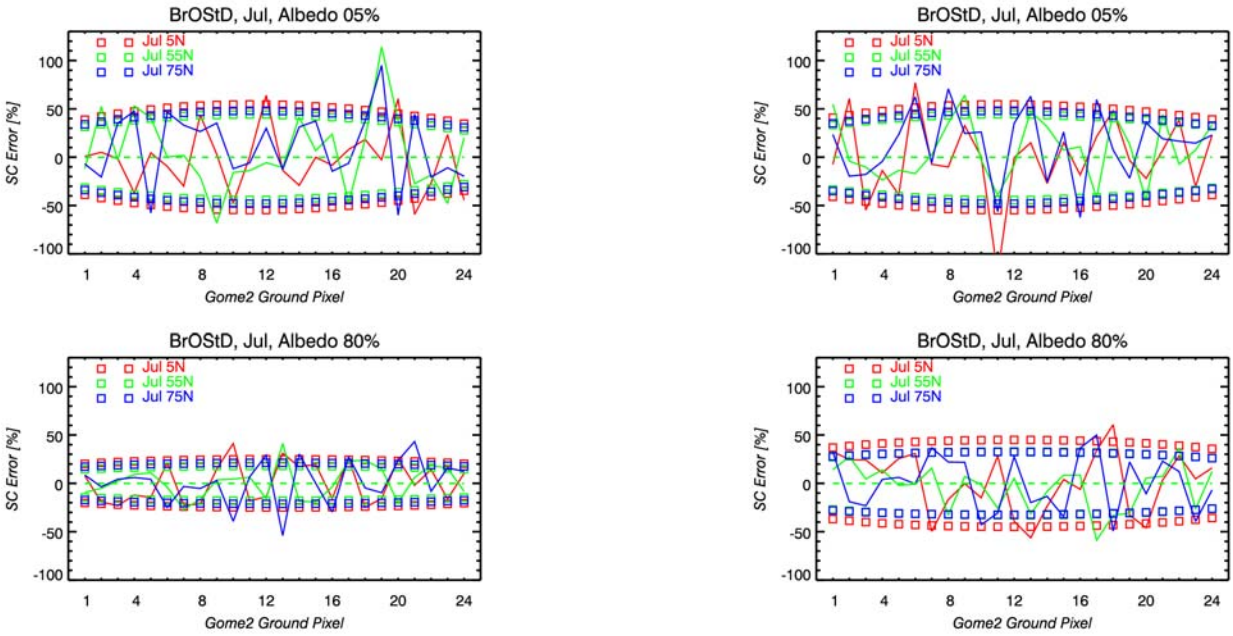

Figure 11-17: BrO slant column errors w.r.t. perfect fit using uncorrupted spectra. (July)

The standard deviations for each GOME-2 ground pixel calculated using linear mapping are indicated by squares for latitudes 5N, 55N and 75N. Individual noise corruption results are plotted as solid lines, which apparently correspond to the LM findings as expected.

Top: Albedo 5% Bottom: Albedo 80%
Left: Model noise Right: S/N ceiling at 2000

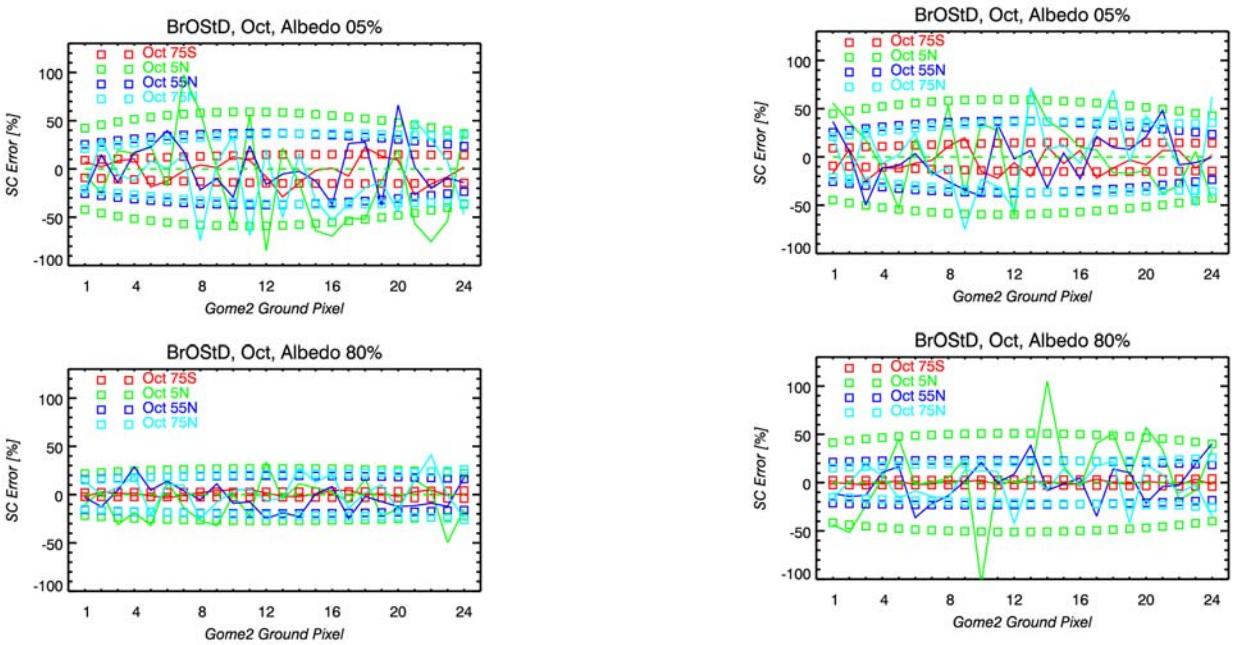

Figure 11-18: BrO slant column errors w.r.t. perfect fit using uncorrupted spectra. (October)

The standard deviations for each GOME-2 ground pixel calculated using linear mapping are indicated by squares for latitudes 75S, 5N, 55N and 75N. Individual noise corruption results are plotted as solid lines, which apparently correspond to the LM findings as expected.

Top: Albedo 5% Bottom: Albedo 80%
Left: Model noise Right: S/N ceiling at 2000

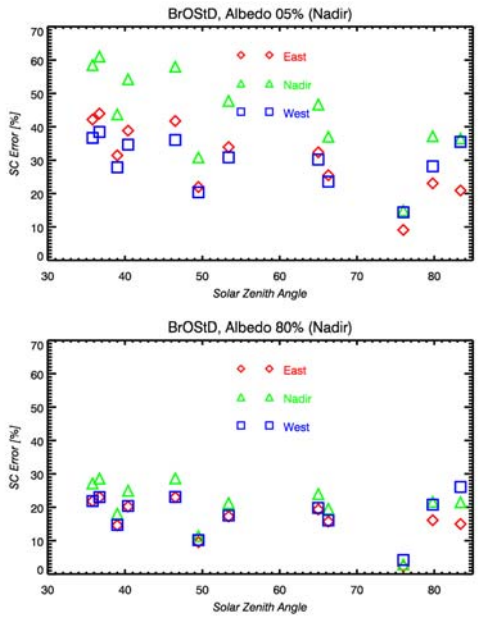

Figure 11-19: BrO SC error as a function of solar zenith angle

11.6 Chlorine dioxide

Figure 11-20 gives differential optical depth spectra and according noise for the OClO fitting window (Jan., 5N, East, 5% albedo). For this case the spectral feature of the driver of this window, OClO is barely visual. For the noise level modelled therefore successful retrievals could not be achieved.

October

In Figure 11-21 it can be seen, that on a 500% scale only the Antarctic ozone hole scenario results are visible, with errors of 200% (100%, albedo 0.8) at nadir and slightly smaller errors at the swath edges. Co-adding is needed to improve OClO retrieval under ozone hole condition.

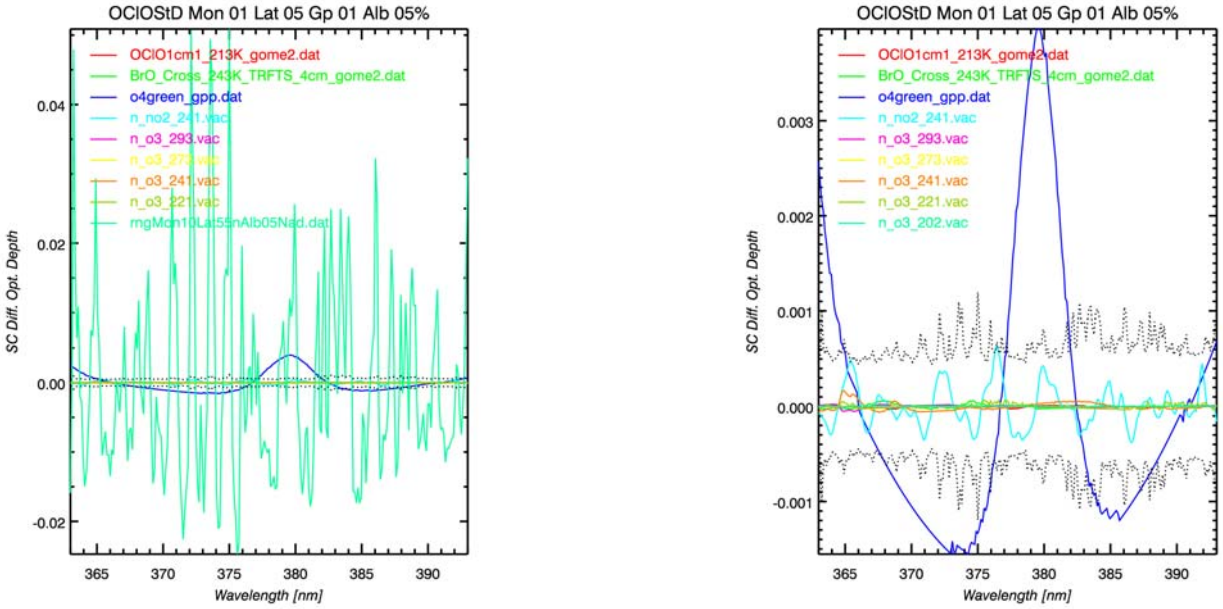

Figure 11-20: Diff Optical Depth calculated using slant columns from fitting a clean spectrum

As an example the spectrum for trace gas scenario 1 (see Table 10-1) has been used for fitting. Each fitted slant column has been multiplied by the according differential cross-section used for the OClO fitting window.

The applied noise level (1 sigma confidence) is indicated by dotted lines.
Left: Ring included Right: No Ring

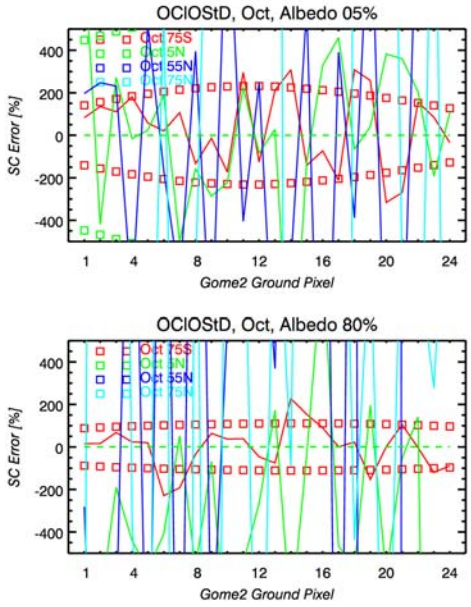

Figure 11-21: OClO slant column errors w.r.t. perfect fit using uncorrupted spectra (October)

The standard deviations for each GOME-2 ground pixel calculated using linear mapping are indicated by squares for latitudes 75S, 5N, 55N and 75N. Individual noise corruption results are plotted as solid lines, which apparently correspond to the LM findings as expected.

Top: Albedo 5% Bottom: Albedo 80%
Left: Model noise Right: S/N ceiling at 2000

11.7 Ozone in the visible

Ozone slant columns have been also investigated when fitting between 450nm and 497nm (GOME-2 channel-3). Results are shown in Figure 11-22 to Figure 11-25, which are for January and October, respectively. Again, normal noise levels (left sides) and the S/N ceiling case (right sides) have been considered for all GOME-2 ground pixels and both 5% (top) and 80% ground albedo (bottom).

Errors are about a factor of 10 larger than from fittings in the UV spectral window due to the small absorption signature of the Chappuis-bands compared to the Huggins-bands.

Again, the tropical scenarios give largest errors except for October (75S). The sensitivity to slant path variations is larger than for the UV (January, April). For Albedo 80%, errors are significantly larger when using the worst-case noise scenario.

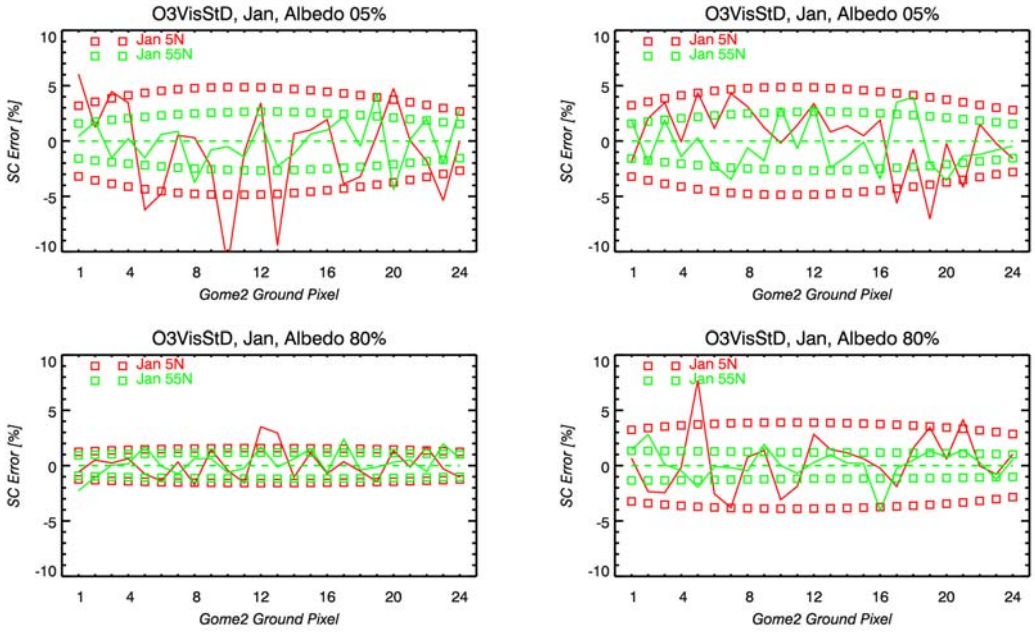

Figure 11-22 O_3 slant column errors from visible fit window w.r.t. perfect fit using uncorrupted spectra (January)

The standard deviations for each GOME-2 ground pixel calculated using linear mapping are indicated by squares for latitudes 5N and 55N. Individual noise corruption results are plotted as solid lines, which apparently correspond to the LM findings as expected.

Top: Albedo 5% Bottom: Albedo 80%
Left: Model noise Right: S/N ceiling at 2000

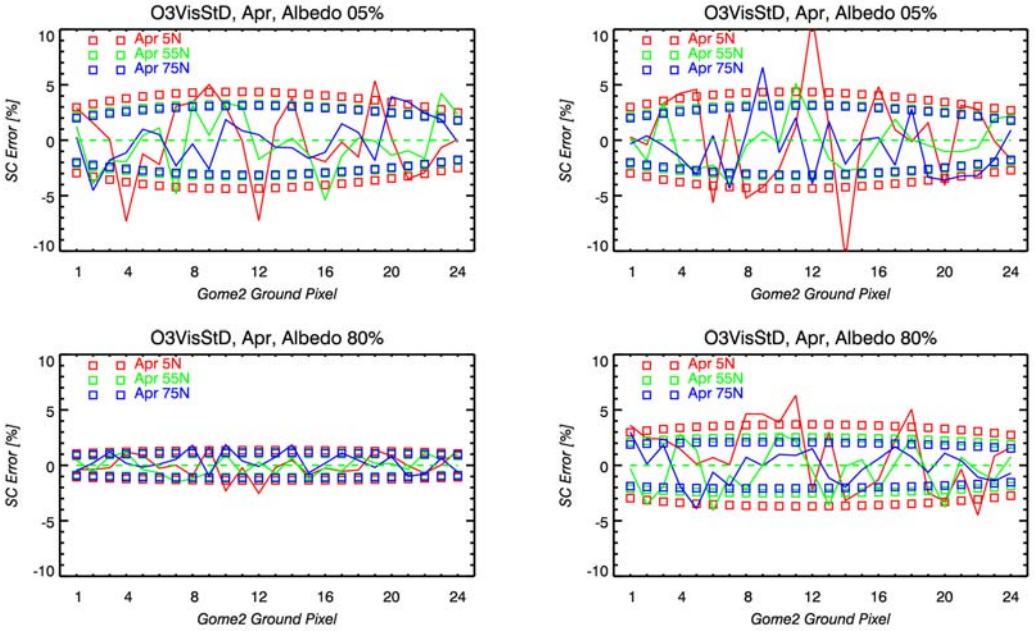

Figure 11-23: O_3 slant column errors from visible fit window w.r.t. perfect fit using uncorrupted spectra (April)

Top: Albedo 5% Bottom: Albedo 80%
Left: Model noise Right: S/N ceiling at 2000

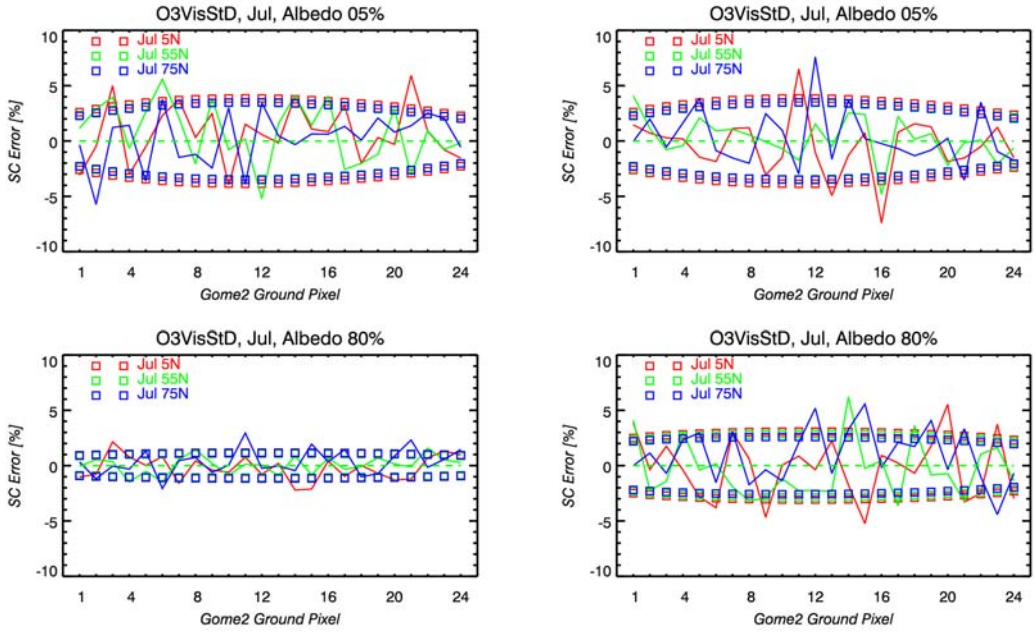

Figure 11-24: **O_3 slant column errors from visible fit window w.r.t. perfect fit using uncorrupted spectra (July)**

Top: Albedo 5% Bottom: Albedo 80%
Left: Model noise Right: S/N ceiling at 2000

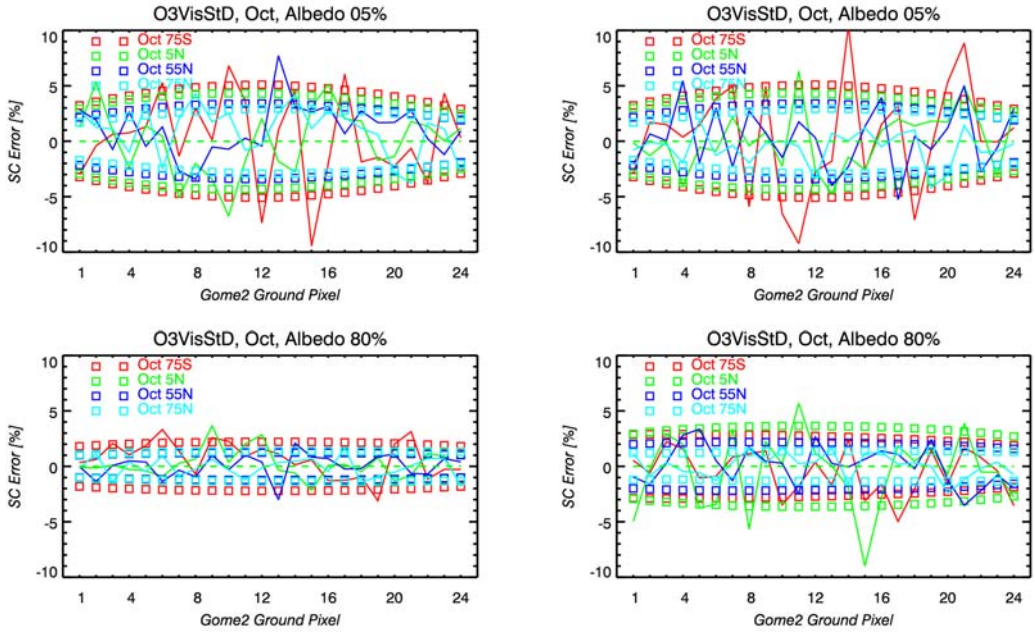

Figure 11-25: **O_3 slant column errors from visible fit window w.r.t. perfect fit using uncorrupted spectra (October)**

Top: Albedo 5% Bottom: Albedo 80%
Left: Model noise Right: S/N ceiling at 2000

11.8 Summary

Ozone slant column errors (1-sigma SD) are generally less than 0.5% for all scan angles and trace gas scenarios when fitting in the UV. On average the errors are on the order of 0.2% (high albedo) and 0.3% (low albedo). For the visible fitting window, errors are about a factor of 10 larger, being on average 2 % and 3% respectively, with a maximum about 5%.

For NO_2 the SC error goes up to 30%. On average the error is about 8% (high albedo) and 10% (low albedo). One has to note here that these numbers are accuracy estimates for mostly purely stratospheric NO_2 columns. Errors may be smaller for strongly enhanced NO_2 emissions.

BrO SC errors are below 60%, with average errors of about 20% (high albedo) and 30% (low albedo). This is also representative for stratospheric BrO.

OClO could not be detected even for the ozone hole scenario. However, under twilight conditions and under ozone hole condition, when chlorine is strongly activated, co-adding may be used to achieve better signals. For the ozone hole scenario the slant column error is below 100% at the swath edges (high albedo).

For ozone, the error increases slightly at larger solar zenith angles, which is due to the fact that the intensity decrease (more noise) compensates the advantage of slant column enhancement. At low albedo NO_2 SC error are becoming larger at both low SZA (low slant column) and high SZA (noise). Best results are obtained at intermediate solar zenith angles and high albedo.

Error budgets for the nominal noise model are summarised in Table 11-1.

Table 11-1: Basic SNR Error budget of slant columns for nominal model noise

Species	Slant Column Errors (1σ %)		
	Maximum	Mean	
		Albedo 5%	Albedo 80%
O_3 (UV)	<0.5	≈0.3	≈0.2
O_3 (vis.)	5	≈3	≈2
NO_2	<30	≈15	≈8
BrO	<60	≈30	≈30
OClO		≈200	≈100

11.9 Conclusions

If the Ring spectrum is included in both spectral simulations and DOAS retrievals errors become significantly larger for NO_2 due to strong correlations, but are negligible for other trace gases.

- O_3 slant column S/N errors are below 0.5% when using the UV fitting window and, for the visible fitting window, about 5% at the maximum.
- O_3 Errors are minimal for low and medium SZA and reach maxima at high SZA.
- NO_2 slant column S/N errors are on the order of 15% to 20% and reach up to 27% (Oct 75N).
- NO_2 errors are minimal for medium SZA, rise up for low SZA and reach maxima at high SZA.
- BrO slant column S/N errors are around 50% to 60% at maximum.
- BrO errors are minimal for high SZA and rise up to low SZA due to photochemical activity.

OClO SC errors under ozone hole are on the order of 100% and higher.

TASK 2: ANALYSIS OF ERROR SOURCES

12 Introduction to Task 2

12.1 Overview

This report describes work conducted in Task 2 of the GOME-2 Error Assessment study. In this task, the impact on trace-gas column and ozone profile retrievals of a range of specific error sources and operating conditions are evaluated.

The report addresses the following sub-tasks:

WP210:	Spatial Aliasing
WP220:	Processing Options for Band 1A
WP230:	Reduction of Spectral Resolution
WP240:	Atmospheric Profile Related Effects
WP250:	Radiative Transfer Model Assumptions and Earth Curvature
WP260:	Non-Lambertian Surface Reflectance BRDF
WP270:	Pointing and Geolocation

TASK 2: ANALYSIS OF ERROR SOURCES
Introduction

13 WP210: Spatial Aliasing (RAL)

13.1 Introduction

Due to the across track scan and finite readout time of the detector arrays, the scene viewed by each spectral pixel is different. Landsat 7 ETM+ images have been used to generate a realistic variation in surface albedo due to viewing different scenes.

13.2 Selected Landsat-ETM+ images

A number of Landsat 7 ETM+ images available free-of-charge from the NERC Earth Observation Data Centre (NEODC) based at RAL and from OhioLINK's Landsat 7 Satellite Data Server (http://dmc.ohiolink.edu/GEO/LS7). The images selected for analysis in the WP are shown in Figure 13-1.

13.3 Landsat calibration problems

The images are provided in a byte scaled format (0-255) representing a linear variation from the minimum to maximum radiance measured in each band. Two problems arose with calibrating the Landsat images:

- Calibration information was only available for two of the images
- The Landsat Band 1 detectors were saturated by reflectance from cloud.

It was therefore decided to use the images in a more simplistic way by scaling each scene from 0 to 1 (water to cloud). The spatial structure, and therefore the spectral error structure, will be correct but the absolute magnitude of the variation will be slightly in error. Due to the variability in the spectral structure seen, it is believed this is a negligible error.

No wavelength dependence of the surface albedo has been included. Originally, it was intended to integrate between Landsat bands to provide some spectral variation. The spectral resolution of the Landsat data this would introduce no spectral structure on the scales of interest here, and so has been omitted.

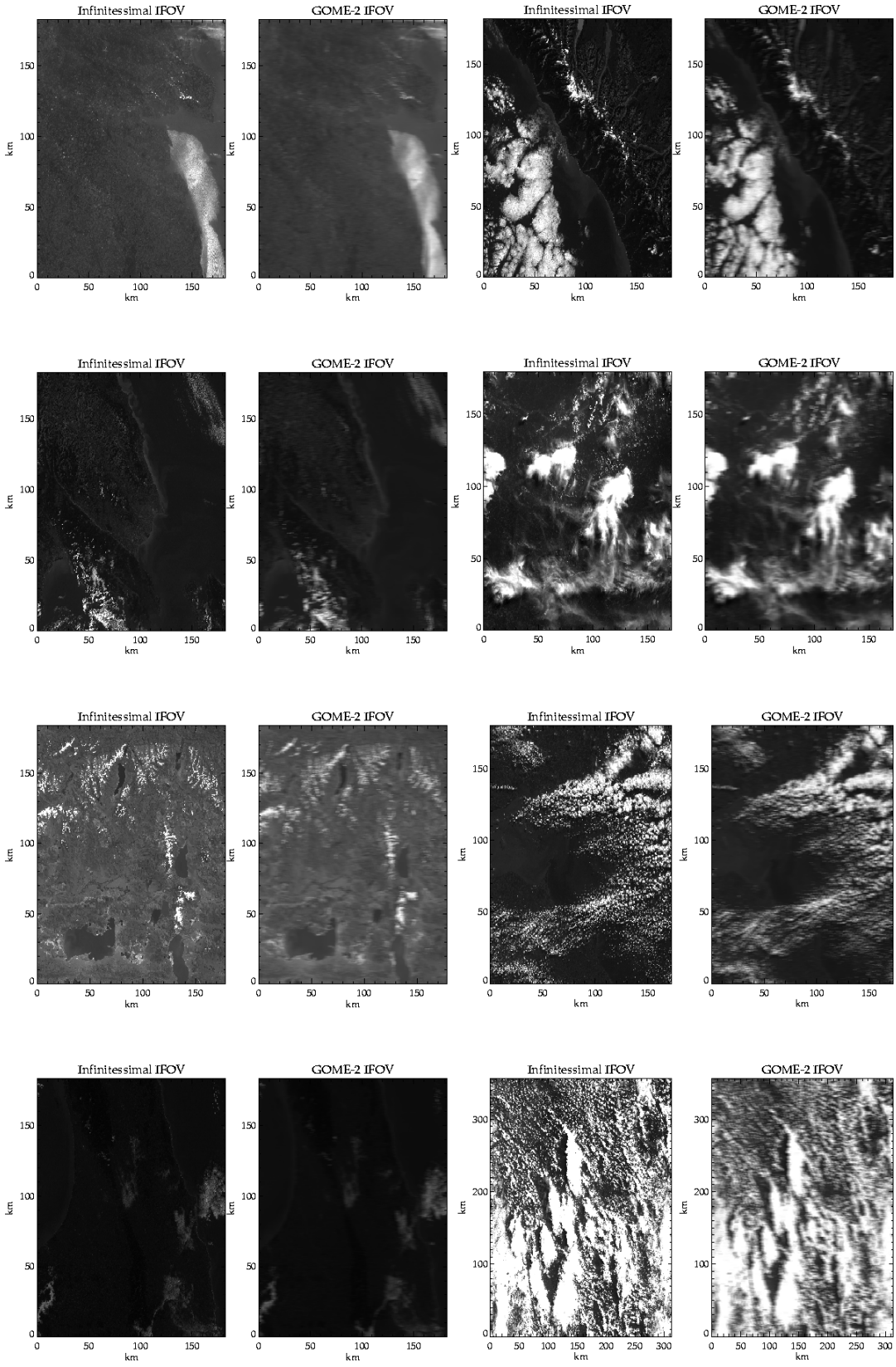

Figure 13-1: LANDSAT 7 images used for calculating spatial aliasing signatures

Left panel of each pair (i.e. panels 1 and 3): original image.

Right panel of each pair (i.e. panels 2 and 4): corresponding image convolved with the GOME-2 Instantaneous Field of View

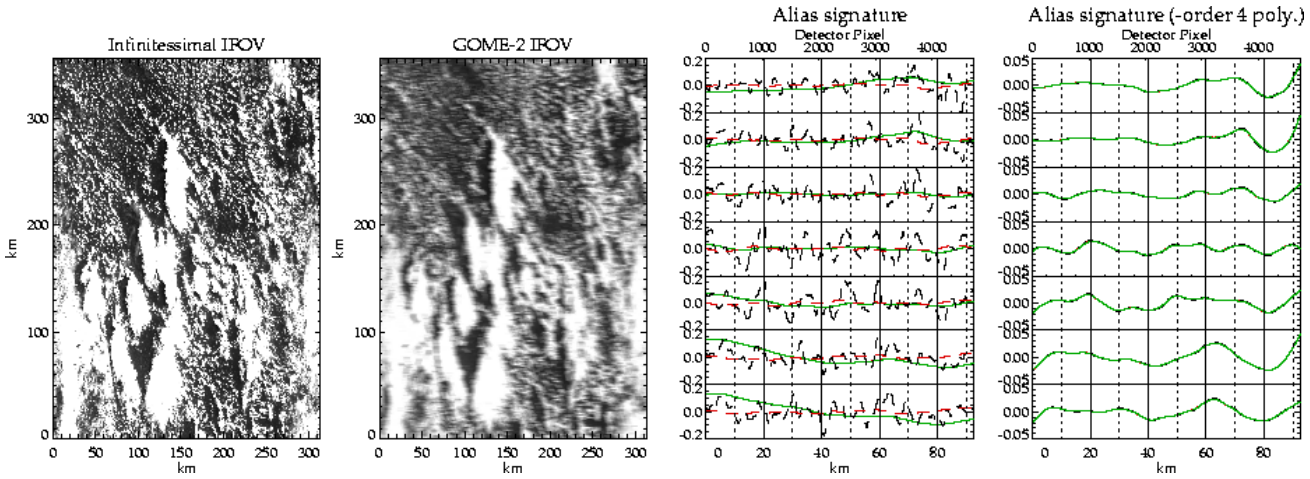

Figure 13-2: Landsat 7 - original images and convolved images, and their corresponding aliasing signature

Left two panels: Landsat 7 (a) original images (b) images convolved with IFOV.

Right two panels: Corresponding aliasing signature, which would be measured from each image after integrating the signal for the nominal integration time.
(Vertical solid/dashed lines indicate 1024 pixel interval bands.)

13.4 Spatial Aliasing Generation

The spatial offset of scenes viewed by the first and last detector elements is calculated as shown in Figure 13-4. With the current nominal configuration, integration time (Ti), readout time (Tr) and pixel size (L), the integrated pixel size is 80 km and the first and final viewed scenes are displaced by 20 km. Neighbouring detector elements scenes are therefore displaced by approximately 20 m.

To simulate the effect on GOME-2 measurements, the instantaneous field of view (IFOV) must also be considered (NOTE: this was not done in the previous analogous GOME study [13-1]. The LANDSAT image is therefore sampled at the approximately 20 m spacing by convolving with the GOME-2 IFOV (approximately a box-car of width 4.6 km - taken from [13-2].

The resampled data are then averaged over the required GOME-2 time integrated pixel size for each detector pixel (i.e. offsets of 1 resampled pixel). This averaged value then shows the effective "surface albedo", or aliasing spectra, seen by each detector pixel. Any 1024 consecutive spectral points represent the possible variation, which would be seen across a GOME-2 band.

In Figure 13-2 (an in all cases in B4.1), the simulation of aliasing signatures and impact of the IFOV convolution is illustrated. The first panel in each row shows the original image. The second panel shows the image after convolving with the GOME-2 instantaneous field of view (IFOV). The third panel shows the spectral aliasing signature for 3 different hypothetical IFOVs: black = 1 m resolution, green = GOME-2 (from CDR), red = boxcar of width equal to the GOME-2 IFOV full-width half-height. Also shown in this panel are the differences in the signature introduced by the IFOV:

- Black dashed line: Difference between the signatures evaluated with and without GOME-2 IFOV. Difference multiplied by 100. This illustrates the additional structure, which would be simulated if the IFOV were to be neglected (as was the case in [13-2]).
- Red dashed line: Difference between signatures evaluated with full GOME-2 IFOV and with boxcar. Again, the difference is multiplied by 100 for plotting. This illustrates the relative unimportance of the precise IFOV shape compared to its width.

The fourth panel shows the signatures after subtraction of a 4th order polynomial across the width of the image, to emphasise the amplitude of higher order structure in the signatures. There is still some variation over the width equivalent to a complete GOME-2 band (1024 pixels). After fitting a 4th order polynomial across just the GOME-2 band, the remaining structure is seen to be of magnitude <0.1 %(see Section 13.6

below). The O_3 profile retrieval system chosen for this study makes use of only sub-intervals of GOME-2 Band 1 and Band 2. In particular, the Bands 1 and 2 are considered separately, with a 2nd order polynomial fit applied in the Band 2 sub-interval. This further reduces the magnitude of aliasing structures on scales likely to impact profile retrieval.

The vertical lines in panels 3 and 4 indicate the extent of a GOME band as it maps onto the spatial dimension. The interval between pairs of vertical lines of the *same* line style (solid or dashed) is 1024 detector pixels.

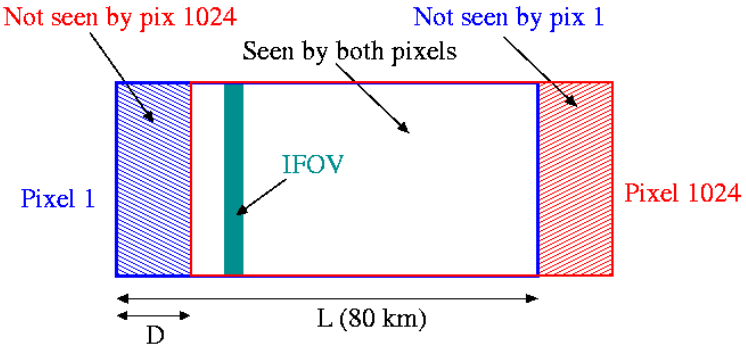

Figure 13-3: Offset of scene viewed due to scan and readout time

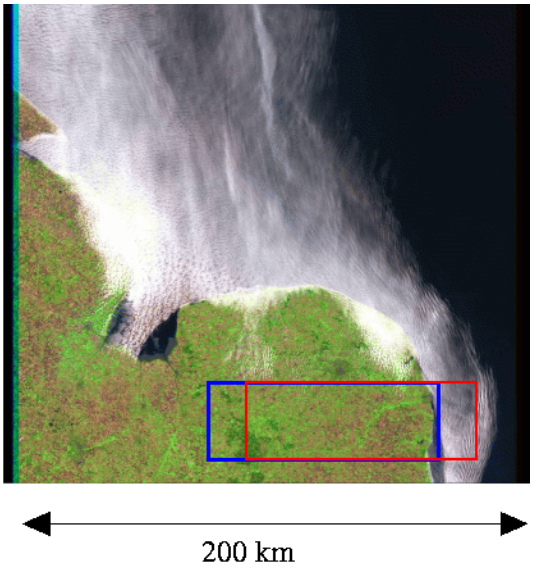

Figure 13-4: Change in scene viewed causing spatial aliasing

Boxes indicate scene viewed by first/last detector elements due to scanning and readout time.

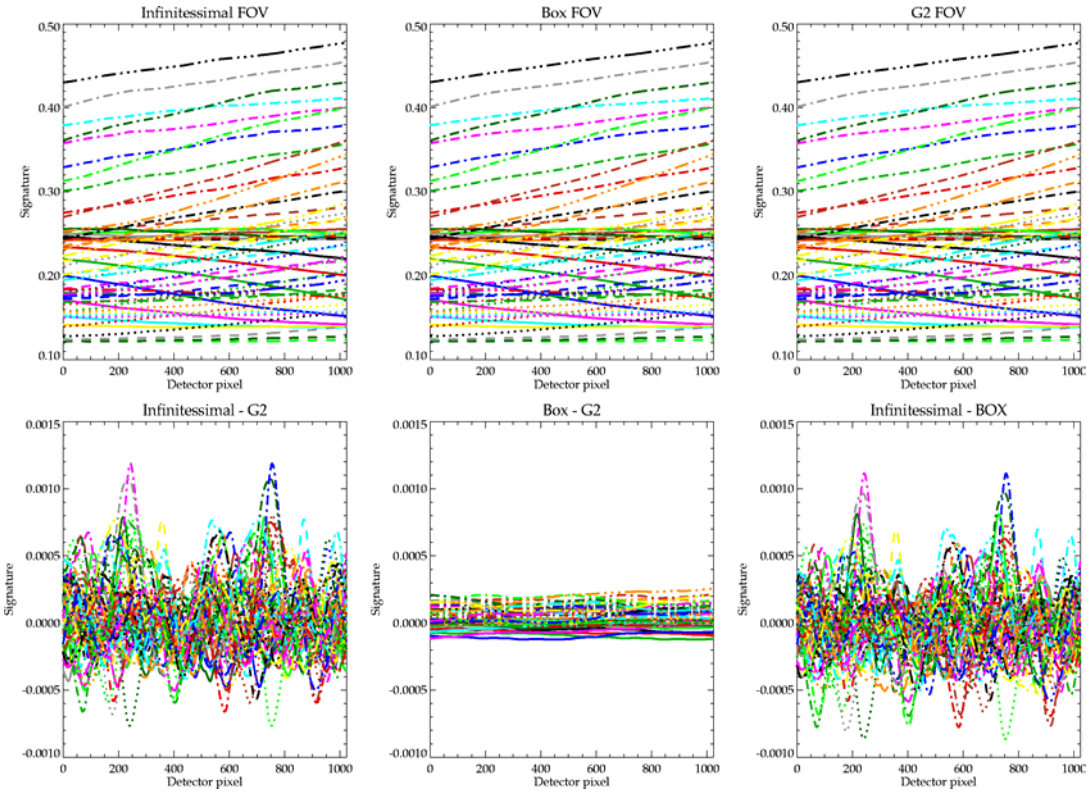

Figure 13-5: Aliasing signatures for Landsat 7 image 10.

Top panels: Signatures computed with infinitesimal boxcar and = GOME-2 field of view (FOV) functions

Bottom panels: Differences in the signatures arising from FOV

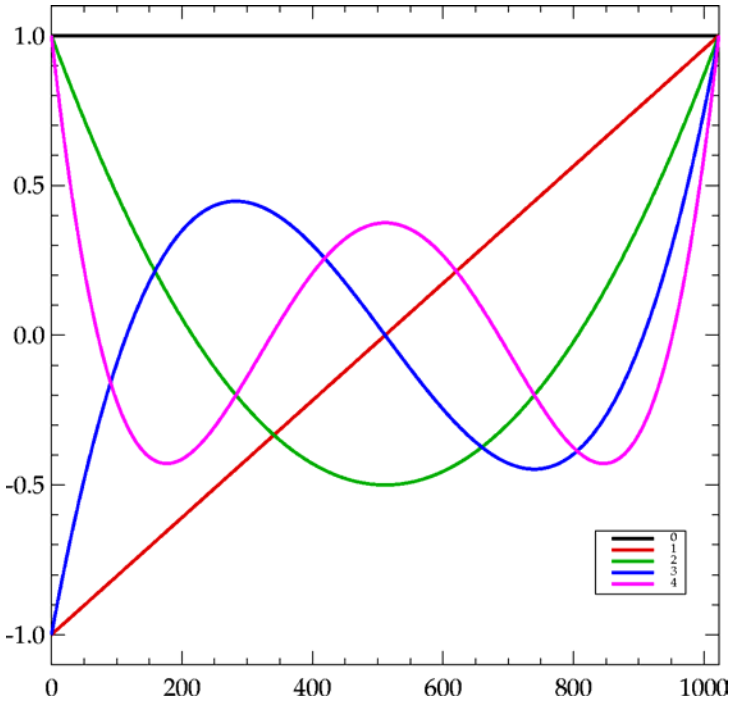

Figure 13-6: Legendre polynomial functions fitted to the aliasing signatures

Legendre polynomial functions fitted to the aliasing signatures to analyse structure at varying polynomial scales

13.5 Synthetic Simulations

A number of theoretical images have been considered to aid in understanding how the scene can affect the spectral signature. These also show the maximum errors, which are possible. The scenes consist a number of regions, which can clearly be seen in Figures B1.1 in Appendix B. Three "albedos" are used grey = 0.5, white = 1.0 (Clouds) and black = 0 .0 (Sea). The scene is divided into a number of regions. The extreme left and right are padding produce understandable convolutions at the edges. The central region is viewed by both the first and last detector pixel. The remaining regions are those viewed differently by each detector element; the left is viewed completely by the first element and not at all by the final one and vice versa for the right.

The spatial aliasing structure for various synthetic images, which contain structure of various scales, are shown in 3rd and 4th panels of Figures B1.2 in Appendix B. In each case, the first plot shows a cross-section of the image after sampling with both a 1 m (black) and GOME-2 (green) IFOV (before integration). The second plot shows the variation in "albedo" after integration due to the changing scene. Any consecutive 1024 detector pixels show the variation, which would be seen across a GOME-2 band. As before, the solid lines indicate the "albedo" scene with various IFOV functions: black = 1 m resolution, green = GOME-2 (from CDR), red = boxcar of width equal to GOME-2 IFOV full-width half-high. The dashed lines indicate 100 times the difference between GOME-2 and the 1 m resolution (black) and boxcar (red) IFOVs.

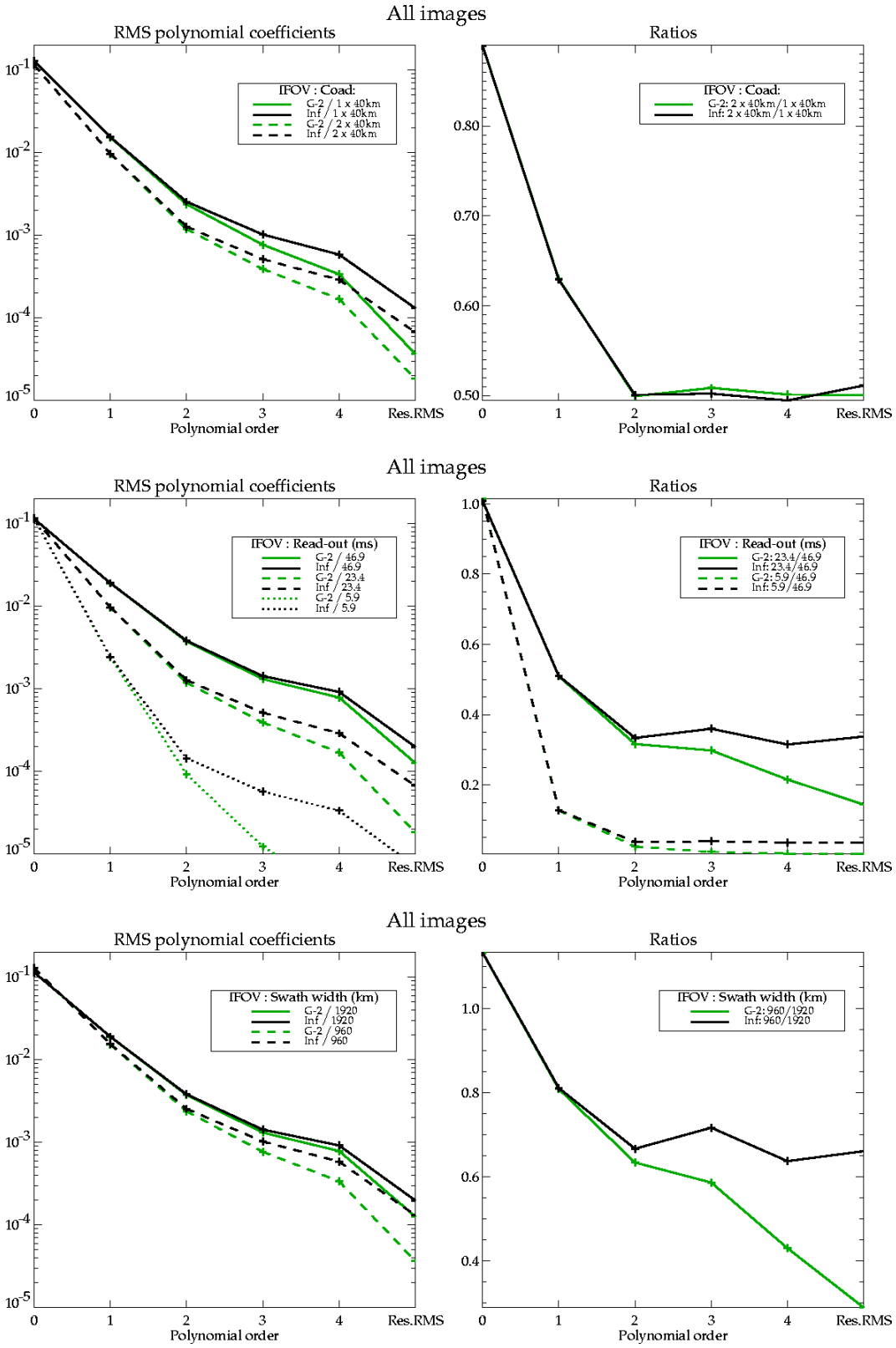

Figure 13-7: Analysis of polynomial coefficients for various sampling options – all images

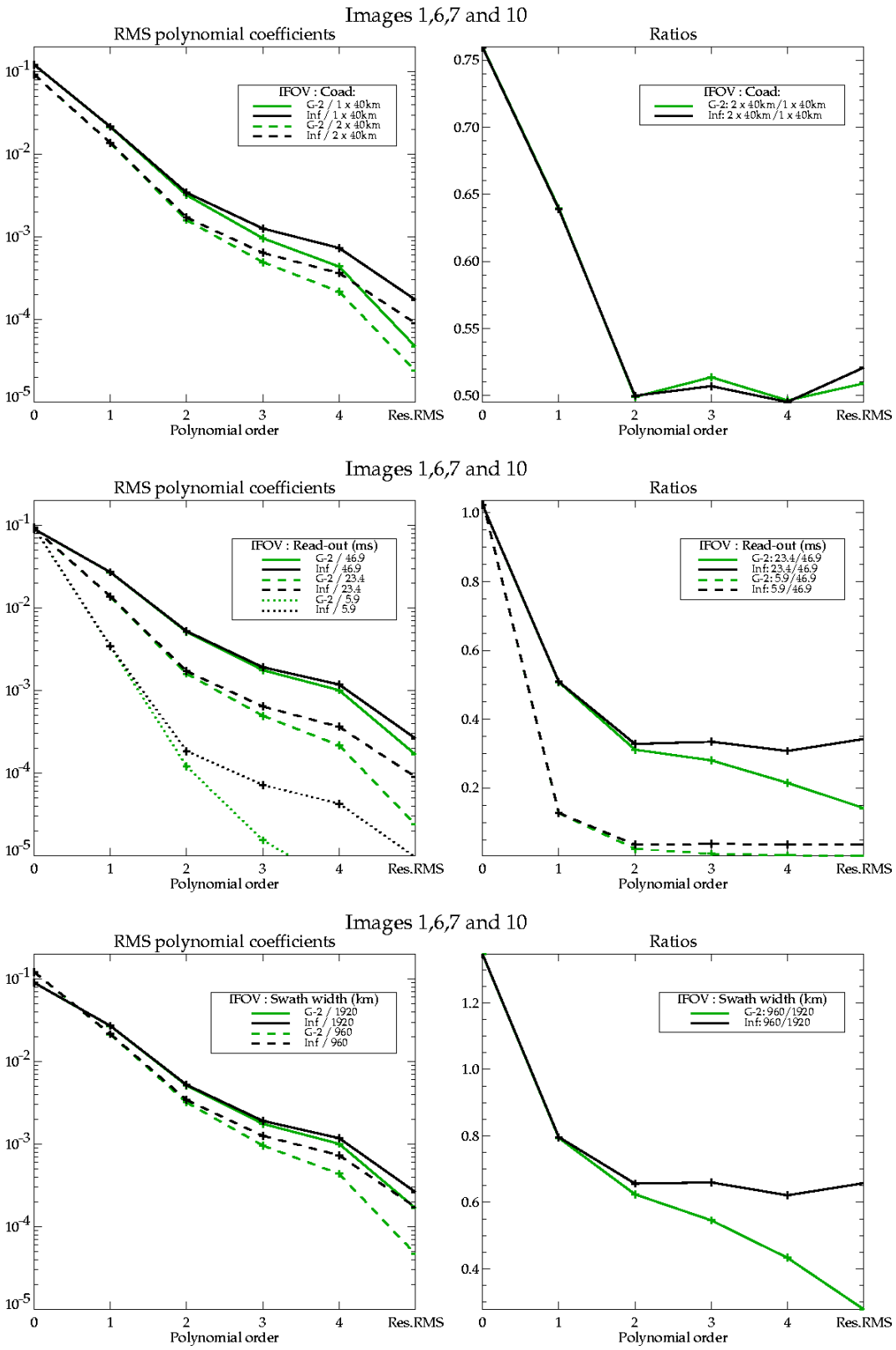

Figure 13-8: Analysis of polynomial coefficients for various sampling options – images 1,6,7 and 10

13.6 Analysis of Signatures

As described above, a single aliasing signature applicable to a GOME band is simulated by any consecutive 1024 pixels of the signatures illustrate in Figure 13-5. To concisely represent the range of possible signatures arising from each image, all spectra delimited either the dotted or full the vertical lines in the figures are selected, i.e. blocks of 1024 detector pixels are selected every 512 pixels, such that the aliasing signature in detector pixels 0 - 511 is the same as that seen in detector pixels 512 - 1023 of the previous signature along the row.

All such signatures for image 10 (with highly variable cloud) are shown in Figure 13-5, for three IFOV options:

a) GOME-2 ("G-2"): IFOV as plotted in MO-RP-GAL-GO-0006
b) Box-car ("Box"): Box-car IFOV with same width (~4 km) as GOME-2
c) Infinitesimal ("Inf"): No IFOV convolution simulated

It is noted that "Box" and "G-2" spectra are very similar (smooth over the band with differences less than 5e-4 - i.e. in general comparable to, or smaller than, photon noise in Band 2). Hence the precise shape of the GOME-2 IFOV does is unlikely to be an important issue with respect to the spatial aliasing analysis. The IFOV width is, however, critical, as illustrated by the difference "Inf"-"G-2" (or "Inf"-"Box") which shows structured differences at a potentially significant level (up to 1e-3).

In [13-2], an FFT approach was used to investigate the level of structure in the aliasing signatures at varying spectral scales. A comparable analysis is performed here, not using FFTs, but fitting normalised Legendre polynomials (illustrated in Figure 13-6) to the signatures.

Given an original signature $s(\lambda)$, a 4th order fit is given by:

$$s_{fit}(\lambda) = a_p.L_o(\lambda) + a_1L_1(\lambda) + a_2.L_2(\lambda) + a_2.L_2(\lambda) + a_3.L_3(\lambda) + a_4.\ L_4(\lambda)$$

Coefficients of a_i of the i-th Legendre polynomial, Li(λ), are found which minimise the root-mean square (RMS) of the residual $s(\lambda)-s_{fit}(\lambda)$.

The RMSs of the coefficients a_0 to a_4 over all signatures provide a measure of the mean amplitude of the associated polynomial structure over all signatures. The mean of the RMS residual (after the fit), Q, over all signatures provides a measure of the amplitude of structures at higher than 4th order.

These measures provide a concise way of representing the amplitude of structures in the aliasing signatures and of comparing the effect of modifying the GOME-2 spatial and/or spectral sampling strategy.

Figure 13-7 and

Figure 13-8 show plots of the RMS polynomial coefficients over all images. Each line in the left hand panels represents the vector $\{RMS(a_0,a_1,a_2,a_3,a_4), mean(Q)\}$, for a specific GOME-2 option.

The right hand panel presents ratios of the lines in the corresponding left hand panel. Throughout, green lines show results for the GOME-2 IFOV (box-car IFOV produces almost identical results), and black lines show results for no (Infinitesimal) IFOV. Different line-styles provide comparisons of the following GOME-2 sampling options:

- Top panel: Effect of co-adding across track ground pixels.
  - Solid lines: 40 km ground pixel (960 km swath, integration time 187.5 ms, read-out time 46.875 ms).
  - Dashed lines: 2 co-added 40 km ground pixel (otherwise as above)

  NB. The effect of co-adding across track pixels cannot be simulated at full swath due to the limited across track extent of the Landsat images.

- Middle panel: Effect of changing readout time
  - All lines are for 80 km ground pixel (1920 km swath, integration time 187.5 ms)
  - Line-styles indicate effect of decreasing the read-out time by factors 1 (solid), 2 (dashed) and 8 (dotted)
- Bottom panel: Effect of reducing swath-width.
  - Integration time and read-out time are kept as nominal.
  - Solid line shows results for 1920 km swath
  - Dashed line shows results for 960 km swath

Note the following:

1. For GOME-2 IFOV spectra, RMS residuals remaining after 4th order polynomial fit, *over the entire GOME band*, are of order 1e-4 even for nominal read-out and swath, i.e. "Noise" at a level likely to influence the profile Band 2 retrieval (or DOAS retrievals) is not seen (at least on the average case). Gradients occur at larger amplitude and might be expected to influence the Band 1 retrieval (and any attempt at retrieving from a combined Band 1 and 2 without subtracting a polynomial from Band 2 measurements). A 6 ms read-out time results in negligible structure beyond the gradient term across the entire GOME band.
2. Co-adding two 40 km pixels results in signatures with factor 2 less structure at orders 2 and higher, relative to a single 40 km pixel. Variability in the (DC) 0th order term is also reduced due to reduced occurrence of uniformly cloudy/cloud-free pixels. Amplitude of 1st order (linear gradient) is also reduced, but by less than factor of two, gradients being introduced by scene structures larger than the pixel size (i.e. these structures are correlated between the co-added signatures).
3. When the swath width is reduced, the IFOV-width has a larger effect towards higher orders, due to the increased size of the IFOV relative to the spatial scales being aliased (one detector pixel corresponding to 10m on the ground for 960 km swath vs. 20 m for 1920, relative to 4 km IFOV).
4. Images 1, 6, 7 and 10 have been selected for retrieval simulation purposes as they contain the most cloud, with varying structure. Polynomial fit results for these images only are shown in Figure 13-8.

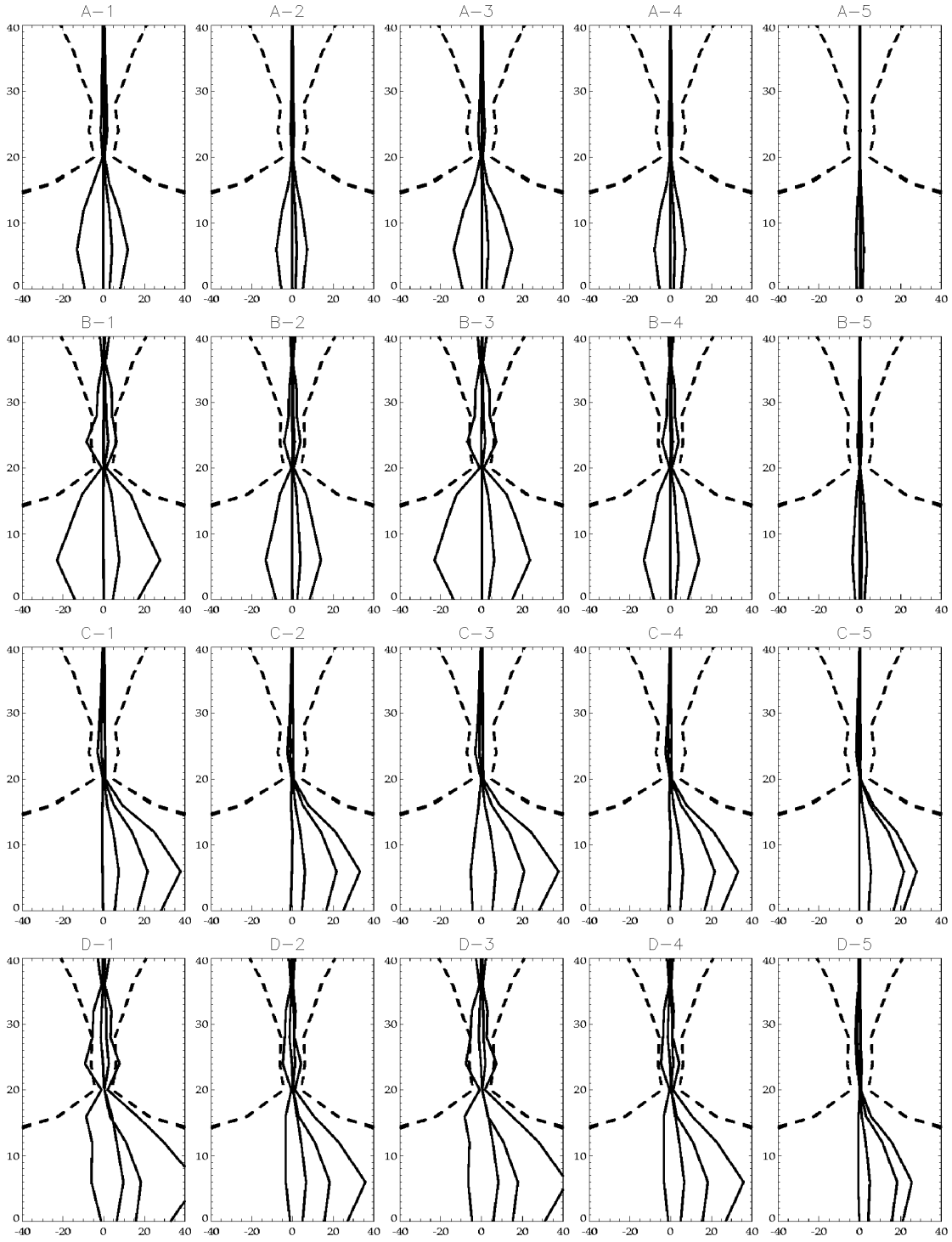

Figure 13-9: Spatial aliasing results for scenario April 5N.

Rows: (A) = Band 1 (265-307 nm) quasi-homogeneous albedo
(B) = Band 1 (265-314 nm) quasi-homogeneous albedo
(C) = Band 1 (265-307 nm) extreme sub-pixel albedo variability
(D) = Band 1 (265-314 nm) extreme sub-pixel albedo variability

Columns: (1) = nominal case (80 km pixel, 1920 km swath, 187.5 ms integration, 46.875 read-out)
(2) = 80 km pixel formed by co-adding 2 pixels from 960 km swath (nominal integration and read-out)
(3) = swath reduced by factor 2 (40 km pixel)
(4) = read out reduced by factor 2
(5) = read out reduced by factor 8

13.7 Ozone profile retrieval simulations

All aliasing signatures from images 1, 6, 7, 10 and 13 have been mapped through the ozone profile retrieval scheme. Note that to realistically simulate the effects of spatial aliasing, the two standard albedo scenarios are no longer relevant, since each signature defines the (spectrally varying) surface albedo for the given ground pixel. Errors introduced in the ozone retrieval by the inability of the retrieval algorithm to cope with the spectrally varying surface albedo implied by the aliasing signatures is quantified as follows:

1. Full radiative transfer calculations are performed for each geo-temporal scenario to provide spectra and weighting functions for albedos 0.01, 0.05, 0.1 and intervals of 0.1 up to 1.
2. Aliasing signatures in the used detector pixels are generated and interpreted as spectrally dependent surface albedos at each associated wavelength.
3. A measured spectrum is synthesised for each aliasing signature by interpolating the full radiative transfer calculations (on a detector pixel by detector pixel basis) to the spectrally dependent albedo defined by the aliasing signature.
4. A retrieval linearisation point (comprising measurement vector and weighting functions) is formed for each signature by interpolating the full RT calculations to the mean albedo over the used pixels in Bands 1 and 2 (i.e. the mean albedo is band dependent).
5. The difference between the measurement vector for the full signature (from Step 3) and that for the (intra-band) wavelength-independent albedo at the linearisation point (Step 4) is mapped to obtain an estimated error in O_3.

I.e. linear mapping is performed about the state in which the retrieval is considered to have correctly fitted the mean albedo associated with the aliasing signature. The spectral dependence about this mean that cannot be accommodated by the spectrally independent (within a band) albedo retrieval is mapped into errors in O_3.

The errors (from all 5 images) for all scene and albedo conditions, for nadir geometry are shown in the following figures in Appendix B:

B1.4: Band 1 wavelength range 265-307 nm.

B1.5: Band 1 wavelength range 265-314 nm.

Within each series of plots, the following viewing geometry options are presented.

1. Nominal viewing geometry (80 km ground pixel, 1920 km swath, integration time 187.5 ms, read-out 47 ms)
2. Two 40 km ground pixels from 960 km swath co-added (integration time 187.5 ms, read-out 47 ms).
3. Nominal for 960 km swath.
4. Nominal except read-out time reduced by factor 2 to 24 ms.
5. Nominal except read-out time reduced by factor 8 to 6 ms.

Figure 13-9 shows the results for the April 5N case, which is approximately a worst case over all geo-temporal scenarios.

Solid lines show (from left to right) the envelope-minimum, mean error (bias), RMS error and envelope maximum of the mapped errors from all images / signatures. Dashed lines show (from left to right) the envelope-minimum, mean and envelope-maximum (again over all images/signatures) of the retrieval ESD for comparison (ESD being a function of the albedo associated with each aliasing signature).

The approach has also been tested by performing partially non-linear retrieval simulations. The forward model for these simulations is linear for all state parameters other than albedo (i.e. the calculated O_3 weighting functions are used directly to calculate measurement vector perturbations as the O_3 state is varied). For albedo, the FM interpolates the pre-calculated cases defined above. The measurement used in these

retrievals is that calculated based on the aliasing signature (Step 3 above), and the retrieval starts at a priori albedo 0.5, with a priori error 1. The retrieval then iterates updating albedo, O_3 and other parameters as appropriate until convergence is reached. These simulations are too slow to by applied to all simulations, but illustrate the validity of the mapping approach as described above. These simulations are shown in Appendix B in Figures B1.8 and B1.9 (for nominal geometry only).

A further test has been performed in which the measurements being mapped are synthesised purely by interpolating the albedo 0.01 and 1 cases to obtain the appropriate spectrally varying albedo. The same linear and non-linear retrieval scheme is used to fit this different measurement. The aim is to simulate the case in which the scene-averaged albedo arises from high sub-pixel scale spatial structure (e.g. variable cloud over ocean), while the forward model used in the retrieval represents the scene as homogenous, with intermediate albedo.

The additional error introduced by modelling the scene averaged albedo as quasi-homogenous in this way is not specific to spatial aliasing and arises from the non-linearity of the radiative transfer with respect to albedo - multiply scattered photon path lengths involving the surface increase non-linearly with surface albedo, causing a systematic positive retrieval bias at low altitudes. This component of the error remains even in the read-out/8 case. These results are shown in Appendix B in Figures B1.6, B1.7 (linear scheme) and B1.10, B1.11 (quasi non-linear scheme). For April 5N, results are shown in the bottom 2 rows (C, D) of Figure 13-9.

13.8 Conclusions

The GOME IFOV would appear to have the effect of removing high frequency structure from the aliasing residuals such that structure remaining after 4th order polynomial fit across a GOME band is of negligible amplitude.

The principle effects of spatial aliasing arise from lower order terms, which may not be well fitted in retrieval schemes seeking to make use of absolute sun-normalised radiance measurements across wide spectral regions.

Some significant effects are noted in the ozone profile retrieval especially when Band 1 is used up to 314 nm, at nominal viewing geometry. It should also be noted that the quasi-DOAS treatment of Band 2 in the profile scheme adopted for this study leads to a mitigation of some of the low-order effects of spatial aliasing. Other retrieval schemes may be more seriously affected.

If read-out time is reduced by a factor of 8, then errors introduced by spatial aliasing are negligible. Radiative transfer non-linearities due to sub-pixel albedo variations (not spatial aliasing) then potentially introduce larger (though still small relative to the ESD) errors.

Given the identified effect of the IFOV, it is clear that further work further work to address the effect of spatial aliasing could be adequately conducted using images of resolution coarser than Landsat but finer than the IFOV width (e.g. ATSR-2 1 km resolution data). The more ready availability of such imagery would permit a much larger and more representative set of imagery to be considered than possible in the current Landsat-based study. ATRS-2 data could also be readily obtained radiometrically calibrated over a larger dynamic range than the current Landsat data set.

13.9 References

[13-1] GO-0006: GOME-2 Optical Design Report. MO-NT-GAL-GO-0006

[13-2] Burrows, J., D. Diebel, H. Frank, K. Muirhead, R. Munro, B.J. Kerridge, D. Pemberton, U. Platt, "A Study of Methods for the Retrieval of Atmospheric Constituents", Final Report, ESA Contract 9687/91/NL/BI

14 WP210: Spatial Aliasing Effects on SC Retrieval (IUP)

14.1 Statistics on radiance error

From the albedo sequences derived from the LANDSAT image worst-case albedo variations were sought by looking at standard deviations of the differential albedo error spectra, defined as:

$$\Delta I(\lambda) - P(\lambda) = W_a(\lambda)\cdot(\Delta a(\lambda)/a) - P(\lambda) \qquad \text{Eq. 14-1}$$

where $\Delta I(\lambda)$ is the albedo error spectrum, and $P(\lambda)$ the subtracted polynomial from best fit.

The albedo error spectra have been calculated using SCIATRAN albedo weighting functions $W_a(\lambda)$ from a standard scenario with solar zenith angle of 49.5°, relative azimuth of 57°, nadir viewing, and albedo of 0.5. a is the average albedo for successive albedo values, and $\Delta a(\lambda)$ represents the variation of albedo around the mean as determined from the Landsat images and from synthetic spectra provided by RAL (Spectra_011024.tar). The standard deviation is here defined as the square root of Sum Square of Eq. 14-1 (summing over wavelengths). Differential albedo error spectra were calculated for all possible albedo sequences contained in the images. The statistics has been carried out for each DOAS fitting window separately, since each spectral windows consists of different number of wavelengths, which are well below 1024 in number.

The database is limited to total of 15 selected scenes from Landsat, thus the data cannot be considered to be representative for global observations. Therefore, statistical properties are difficult to derive from this analysis. For this reason, the slant column error analysis will be entirely based upon worst case scenarios derived from the limited dataset. In Table 14-1 the various categories are summarised for which worst cases were searched:

Table 14-1: Categories for which worst case scenarios were identified

File identifier	Category
1m_box_80	40 x 80 km² GOME pixel (IT=0.1875s), no IFOV convolution
1m_box_40	40 x 40 km² GOME pixel (reduced swath width), no IFOV convolution
gome2_box_80	40 x 80 km² GOME pixel, IFOV GOME2 boxcar convolution
gome2_box_40	40 x 80 km² GOME pixel, IFOV GOME2 boxcar convolution
gome2_80	40 x 80 km² GOME pixel, IFOV GOME2 slit function convolution
gome2_40	40 x 40 km² GOME pixel, IFOV GOME2 slit function convolution

The search results regarding worst case scenarios are summarised in Table 14-2 to Table 14-5 for the trace gases O_3, NO_2, BrO, and OClO. In these tables separate statistics are provided for Landsat images and for synthetic spectra.

Convolution of the albedo sequences with the IFOV (boxcar or bell shape) reduces the standard deviation significantly except for ozone. Synthetic images generally have maximum standard deviations, which are a factor of 2 - 5 higher than achieved with the Landsat images. An exception is ozone, where the maximum standard deviations are on the same order as observed with the Landsat images. The smaller pixel size (40 km x 40 km) leads to higher maximum standard deviations by roughly a factor of two with the exception of BrO, where the error is on the same order. The error statistics delivers similar results for different shapes of the GOME-2 slit function (bell shape or boxcar) as long as the full width half maxima are identical.

LANDSAT IMAGES			(black ROT = 46 ms, blue ROT = 6 ms)	
Position	Scan	SD	albedo mean	albedo sequence file
3585	1	3.87e-04	0.124	img6/l71075090_09020000413_10_1m_box_40
3575	1	3.57e-04	0.127	img6/l71075090_09020000413_10_gome2_box_40
3578	1	3.57e-04	0.127	img6/l71075090_09020000413_10_gome2_40
3318	1	2.55e-04	0.135	img6/l71075090_09020000413_10_1m_box_80
3344	1	2.33e-04	0.132	img6/l71075090_09020000413_10_gome2_box_80
3345	1	2.33e-04	0.132	img6/l71075090_09020000413_10_gome2_80
3360	1	0.29e-04	0.135	img6/l71075090_09020000413_10_gome2_80
SYNTHETIC IMAGES				
Position	Scan	SD	mean albedo	albedo sequence file
536	0	4.98e-04	0.466	syn3/pix80_nd3_p1_10_1m_box_80
1131	0	1.38e-04	0.403	syn1/pix80_nd1_p1_10_gome2_box_80
1133	0	1.37e-04	0.403	syn1/pix80_nd1_p1_10_gome2_80

Table 14-2: Worst case statistics for ozone

ROT stands for read-out-time of detector pixel. Results for ROT of 6ms are shown in blue. Categories are indicated by the endings in the file name (see Table 14-1)

Table 14-3: Worst case statistics for nitrogen dioxide

ROT stands for read-out-time of detector pixel. Results for ROT of 6ms are shown in blue. Categories are indicated by the endings in the file name (see Table 14-1)

LANDSAT IMAGES			(black ROT = 46 ms, blue ROT = 6 ms)	
Position	Scan	SD	albedo mean	albedo sequence file
3852	7	1.44e-03	0.079	img5/l71075091_09120000413_10_1m_box_40
3978	6	4.77e-04	0.071	img5/l71075091_09120000413_10_gome2_box_40
3980	6	4.75e-04	0.071	img5/l71075091_09120000413_10_gome2_40
1805	7	7.56e-04	0.074	img5/l71075091_09120000413_10_1m_box_80
1930	6	2.49e-04	0.070	img5/l71075091_09120000413_10_gome2_box_80
1933	6	2.48e-04	0.070	img5/l71075091_09120000413_10_gome2_80
3618	1	0.02e-04	0.101	img6/l71075090_09020000413_10_gome2_80
SYNTHETIC IMAGES				
Position	Scan	SD	mean albedo	albedo sequence file
509	0	2.67e-03	0.514	syn10/pix80_nd10_p0_10_1m_box_80
664	0	7.70e-04	0.501	syn5/pix80_nd5_p1_10_gome2_box_80
666	0	7.64e 04	0.501	syn5/pix80_nd5_p1_10_gome2_80

LANDSAT IMAGES			(black ROT = 46 ms, blue ROT = 6 ms)	
Position	Scan	SD	albedo mean	albedo sequence file
275	3	2.50e-04	0.062	img5/l71075091_09120000413_10_1m_box_40
3608	0	5.51e-05	0.206	img6/l71075090_09020000413_10_gome2_box_40
3134	2	5.75e-05	0.186	img6/l71075090_09020000413_10_gome2_40
1221	3	1.88e-04	0.103	img15/p18r32_19991122_10_1m_box_80
3348	1	4.60e-05	0.127	img6/l71075090_09020000413_10_gome2_box_80
3352	1	4.60e-05	0.127	img6/l71075090_09020000413_10_gome2_80
3338	1	0.54e-05	0.137	img6/l71075090_09020000413_10_gome2_80
SYNTHETIC IMAGES				
Position	Scan	SD	mean albedo	albedo sequence file
529	0	5.85e-04	0.467	syn3/pix80_nd3_p1_10_1m_box_80
728	0	7.61e-05	0.497	syn5/pix80_nd5_p1_10_gome2_box_80
730	0	7.25e-05	0.497	syn5/pix80_nd5_p1_10_gome2_80

Table 14-4: Worst case statistics for bromine oxide

ROT stands for read-out-time of detector pixel. Results for ROT of 6ms are shown in blue. Categories are indicated by the endings in the file name (see Table 14-1)

Table 14-5: Worst case statistics for chlorine dioxide

ROT stands for read-out-time of detector pixel. Results for ROT of 6ms are shown in blue. Categories are indicated by the endings in the file name (see Table 14-1).

LANDSAT IMAGES			(black ROT = 46 ms, blue ROT = 6 ms)	
Position	Scan	SD	albedo mean	albedo sequence file
3876	7	8.21e-04	0.081	img5/l71075091_09120000413_10_1m_box_40
7029	7	1.70e-04	0.105	img5/l71075091_09120000413_10_gome2_box_40
7031	7	1.66e-04	0.105	img5/l71075091_09120000413_10_gome2_40
1829	7	4.36e-04	0.075	img5/l71075091_09120000413_10_1m_box_80
464	2	9.45e-05	0.118	img15/p18r32_19991122_10_gome2_box_80
466	2	9.33e-05	0.118	img15/p18r32_19991122_10_gome2_80
3332	1	0.24e-05	0.137	img6/l71075090_09020000413_10_gome2_80
SYNTHETIC IMAGES				
Position	Scan	SD	mean albedo	albedo sequence file
437	0	1.72e-03	0.512	syn10/pix80_nd10_p0_10_1m_box_80
391	0	2.82e-04	0.497	syn5/pix80_nd5_p1_10_gome2_80
801	0	2.87e-04	0.498	syn5/pix80_nd5_p1_10_gome2_box_80

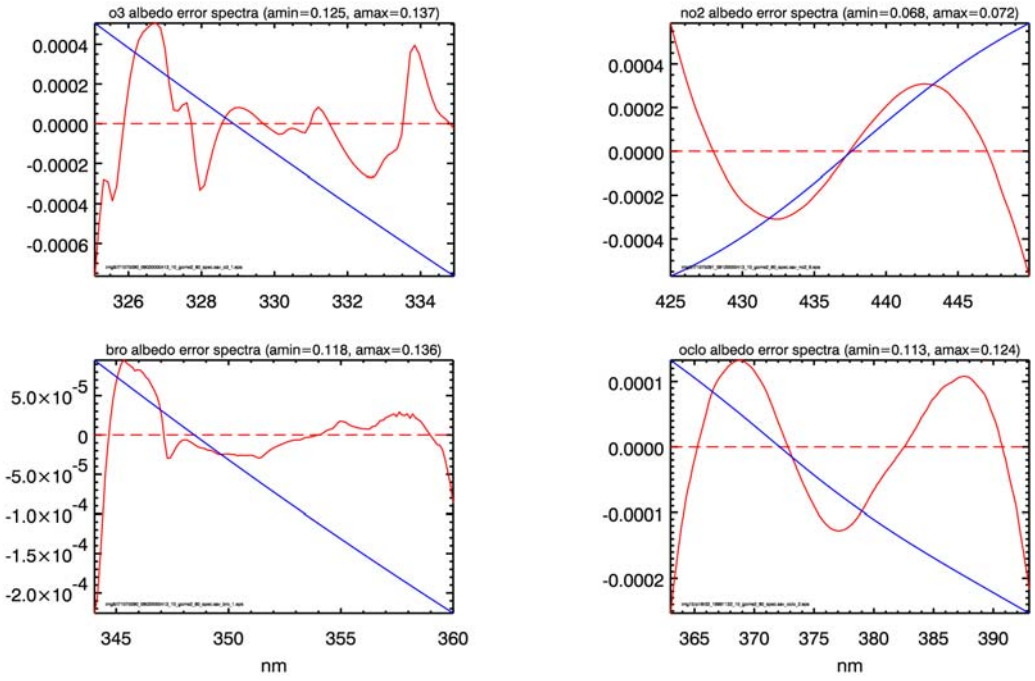

Figure 14-1: Worst case differential albedo error spectra and albedo sequences

Worst case differential albedo error spectra (red) and albedo sequence (blue, without units) based upon analysis of Landsat images (category gome2_80) for:

Top left:	O_3	Top right:	NO_2
Bottom left:	BrO	Bottom right:	OClO

Max and min albedos of the sequences are indicated at the top of each of the graphics (amin, amax)

One should note that the variation of the albedo across the spectral windows are very small and rarely exceeds 0.02. Highest standard deviations in the intensity perturbation, based upon the Landsat image sequences, are mostly found at small mean albedo values ranging between 0.07 and 0.14. Reduction of the detector-read-out time from 46 ms to 6 ms leads to maximum standard deviation being lower by about a factor of about 10.

Figure 14-1 shows the differential albedo error spectra for the corresponding worst-case scenario identified in the case where the GOME ground pixel has a width of 80 km and where the GOME2 slit function convolution on the Landsat albedo sequences has been applied. Also shown in blue are the albedo sequences (without units) as a function of wavelength.

14.2 Slant column error analysis

In the error analysis worst case scenarios for the nominal swath width were investigated using read-out-times of 6 ms and 46 ms. Investigations were limited to the nominal case of IT=0.1875sec and full swath width (40 x 80 km² pixel size, category: gome2_80). For each trace gas the worst-case albedo sequence from the Landsat images as identified in Table 14-2 to Table 14-5were used. Intensity perturbations were recalculated using the appropriate mean albedo. The analysis was carried out for LOS of 44° (east, pixel 1), 0° (nadir, pixel 12) and 44° (west, pixel 24) and for four tracegas scenarios: (1) January 55N, (2) free tropospheric BrO scenario, April 55N, (3) biomass burning scenario, July 5N, and (4) BrO plume and ozone hole scenario, October 75S. No instrument noise was added. Slant column error estimates are shown in Figure 14-2 to Figure 13-3 for each of the DOAS trace gases.

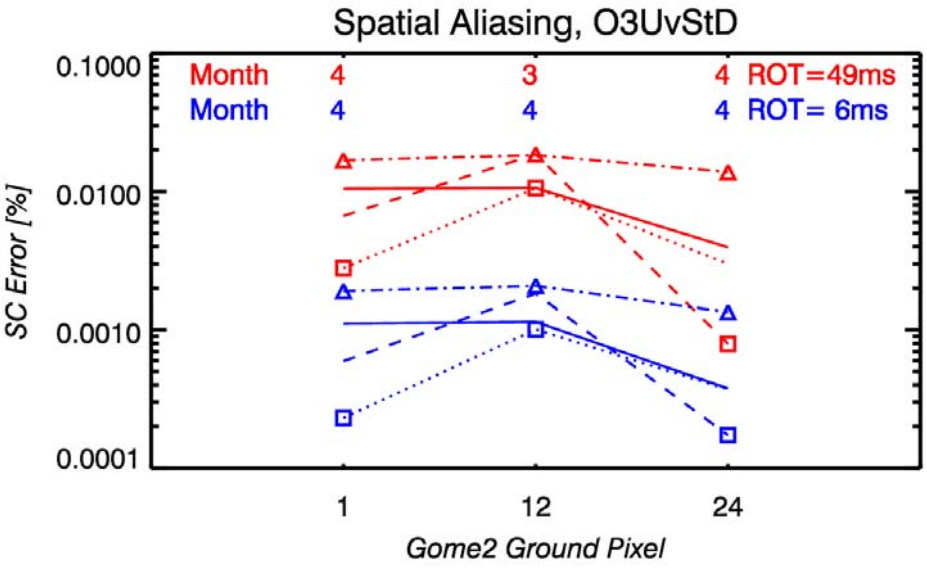

Figure 14-2: Slant column error for O_3 in percent

Number at top is trace gas scenario number (1-4) for which max error is observed.

	Squares: min error	Triangles: max error
Trace gas scenarios	Solid lines: Jan 55N	Dotted lines: Apr 55N
	Dash lines: July 5N,	Dash-dot lines: Oct 75S
Conditions	Blue: ROT 6 msec	Red: ROT of 46 msec

Figure 14-3: Slant column error for NO_2 in percent

Number at top is trace gas scenario number (1-4) for which max error is observed.

	Squares: min error	Triangles: max error
Trace gas scenarios	Solid lines: Jan 55N	Dotted lines: Apr 55N
	Dash lines: July 5N,	Dash-dot lines: Oct 75S
Conditions	Blue: ROT 6 msec	Red: ROT of 46 msec

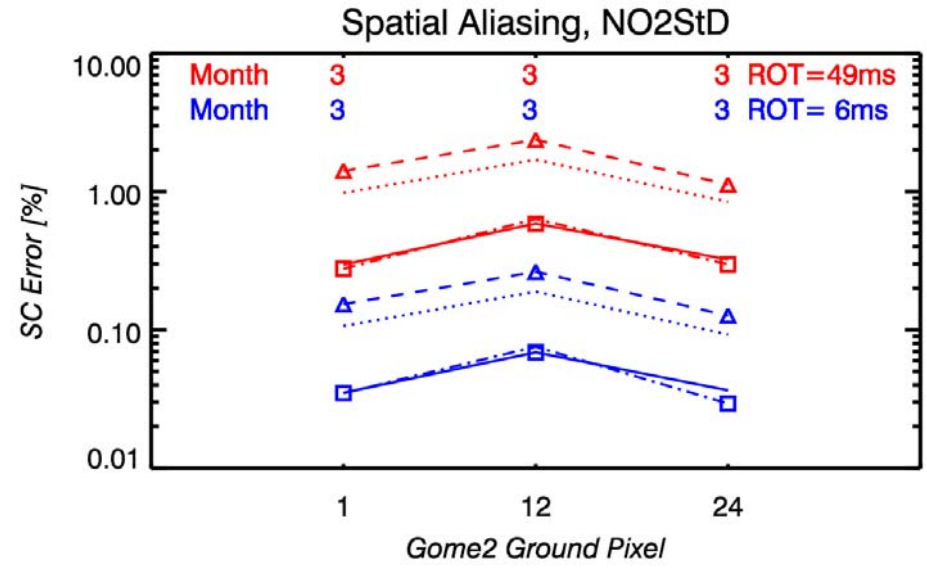

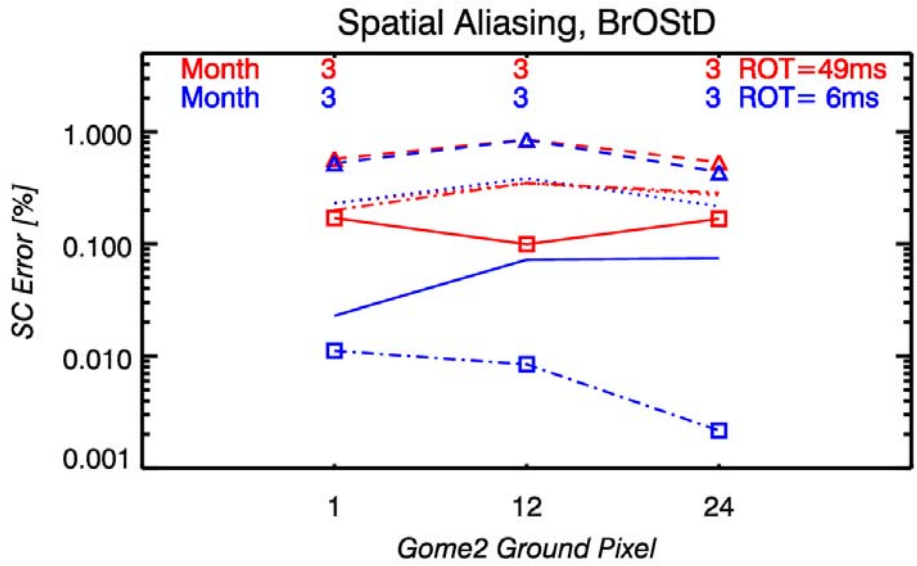

Figure 14-4: Slant column error for BrO in percent

Number at top is trace gas scenario number (1-4) for which max error is observed.

	Squares: min error	Triangles: max error
Trace gas scenarios	Solid lines: Jan 55N	Dotted lines: Apr 55N
	Dash lines: July 5N,	Dash-dot lines: Oct 75S
Conditions	Blue: ROT 6 msec	Red: ROT of 46 msec

Figure 14-5: Slant column error for OClO in percent

Number at top is trace gas scenario number (1-4) for which max error is observed.

	Squares: min error	Triangles: max error
Trace gas scenarios	Solid lines: Jan 55N	Dotted lines: Apr 55N
	Dash lines: July 5N,	Dash-dot lines: Oct 75S
Conditions	Blue: ROT 6 msec	Red: ROT of 46 msec

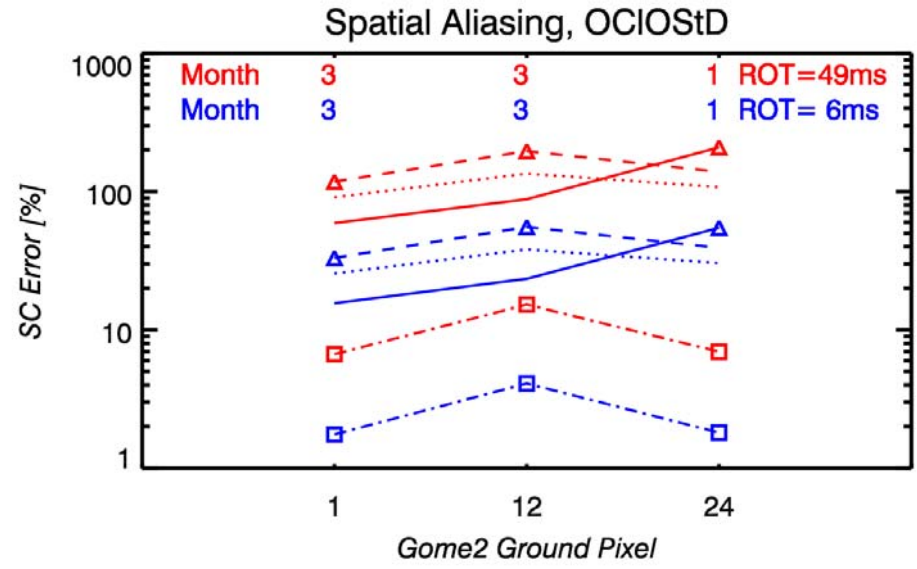

14.3 Conclusion

The slant column errors due to spatial aliasing are generally small. For the worst case Landsat image sequences a maximum error of 0.02% for ozone, 2% for NO_2, 1% for BrO, and 10% for OClO (ozone hole scenario only) were found for full swath width and integration times of 0.1875 sec. These error estimates are generally well below the error from instrumental noise. A reduction of the detector read-out-time is not needed for the DOAS analysis. The comparison of error ratios from the two read-out-times is comparable to the corresponding standard deviation ratio from the earlier statistics, meaning that a reduction of the worst case standard deviation is proportional to the reduction in maximum slant column error (idea of linear relationship between intensity errors and slant column error). As a thumb of rule the maximum slant column errors are reduced by a factor of 8 by using 6 ms read-out-time. In a similar fashion the smaller swath width resulting in a 40 x 40 km GOME ground pixel will increase the slant column error by a factor of up to two.

The slant column errors increase with lower solar zenith angle (maximum error in tropical scenario). The overall small error due spatial aliasing is explained by the combination of fairly narrow spectral windows (much less than 1024 detector pixels) and the finite width of the IFOV of 4 km (0.29°) at the ground. The albedo variation on the order of less than 0.02 across the DOAS fitting windows will not appreciably alter the instrument noise dependence as a function of wavelength.

15 WP220: Processing options for Band 1A (RAL)

15.1 General

The wide swath and 12s integration time base lined for Band 1A, leads to a pixel size of 1920 km x 80 km. It is certain that integrating the pixel over such a large footprint in the across track direction will lead to (a) computational difficulties in representing the radiative transfer across the pixel; (b) radiative transfer model errors due to high view angles affecting all Band 1A data; (c) ozone profile representation errors (O_3 varies significantly over 2000 km scales, even at altitudes influencing the Band 1A wavelengths).

It is therefore desirable to mitigate these problems by increasing the read-out of Band 1A, so that less asymmetric pixels can be constructed by co-adding after read-out. It was proposed to investigate the particular case of reading-out at 1.5s, to obtain 640 km x 40 km pixels, which could be co-added along track to 640 x 320 km (retaining the 12s total integration time) or the symmetric 640 km x 640 km.

The clear disadvantage of post read-out integration is that the read-out noise contribution to the measurement noise is increased. This work packages investigates whether or not this increase in read-out noise has significant consequences for the ozone profile retrieval.

15.2 Noise model

The signal to noise of GOME-2 is modelled based on CDR Optical Throughput [GO22] and Photometric Budget [GO23] documents as described under task WP110:

It is important to note that, based on GOME-1 experience, in the ozone profile retrieval algorithm so-called "noise-floors" are imposed as a means of representing forward model errors (to prevent over-fitting or imperfectly modelled spectra to high signal-to-noise measurements). These floors are set at 1% of sun-normalised radiance in Band 1 and 0.05% in Band 2. I.e. signal to noise degradation due to read-out changes in Band 1A will, by definition, have *no effect* on profile retrievals (*with this algorithm*) where the signal to noise is better than 100 (error 1%) after the modification.

15.3 Noise simulations

The behaviour of the GOME-2 noise model is illustrated for each geo-temporal/albedo scenario in Appendix B in Figures B2.1. An example for April 55N is shown in Figure 15-1. Three integration times are considered: 12s (nominal for Band 1A), 1.5s (required to produce the proposed 640 km x 320 km and 640 km x 640 km pixels), 0.1875s (nominal for Band 1B).

Three panels are shown for each scenario:

- Left: Sun-normalised radiance
- Centre: the relative error (NESR, noise equivalent spectral radiance / measured radiance) at each of the three integration times. Shown also on the plot are:
  - Dotted vertical line: nominal Band 1A /1B boundary (for the purposes of these plots, the same integration time is applied across the whole band)
  - Green dashed line: the error floor applied (1%) in profile retrieval. In the nominal retrieval case, Band 1A noise will follow the greed solid curve and Band 1B the black curve. Where errors shown by these curves drop below the green-dashed 1% line, the additional precision is not exploited by the retrieval scheme and perturbations to the noise model will not have any effect in retrieval simulations.

– Red and black dashed lines show the relative position of the 1% noise floor for the 1.5s and 0.1875s cases after individual spectra at these integration times have been co-added to 12s. The intention is to show the position of the noise floor relative to the modelled error for 12s co-added spectra. Since the errors are random, co-adding spectra will result in errors reduced by the square root of the number of spectra averaged. Rather than repeat the middle panel with red/black curves lowered by factors of $\sqrt{8}$ and $\sqrt{64}$, the dashed curves are instead raised by the appropriate factor. These lines illustrate the wavelength ranges where the read-out noise increase might have significant impact on Band 1 retrievals, e.g. Fig B2.1.1 January 5N, 0.05 albedo. A Band 1 retrieval from spectra averaged for 12s over the whole band (no 1A/1B boundary), the noise used in the retrieval would be the same above ~290 nm for all three read-out options. Between 280 nm and 290 nm, the 0.1875s (64 read-outs) case is the only one degraded from full 12s integration. Below 280 nm the 1.5s (8 read-out) case is also degraded, but by a factor less than might be expected above ~265 nm, since 12s case is below the noise floor above that wavelength.

- Right: Ratio of errors to the 12s case, when co-adding spectra to 12s or 24s (which correspond to 640 x 320 km and 640 x 640 km pixels respectively). In the purely photon noise limited case, the ratios for 12s co-adding would be 1. The curves reflect the increasing dominance of read-out noise towards low wavelength.

Figure 15-1 Noise simulations corresponding to processing options for Band 1 for July, 5N with surface albedo of 0.05 and 0.8

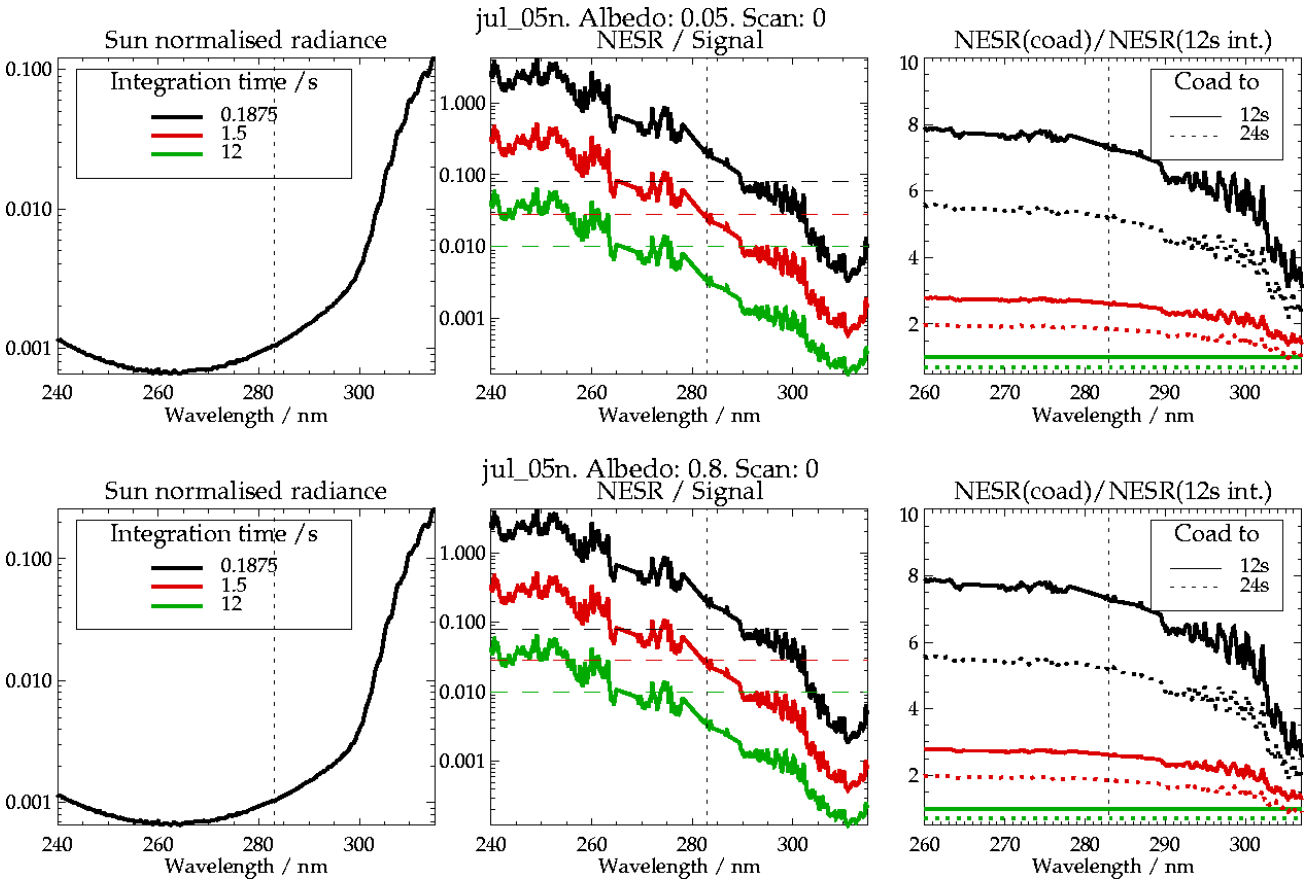

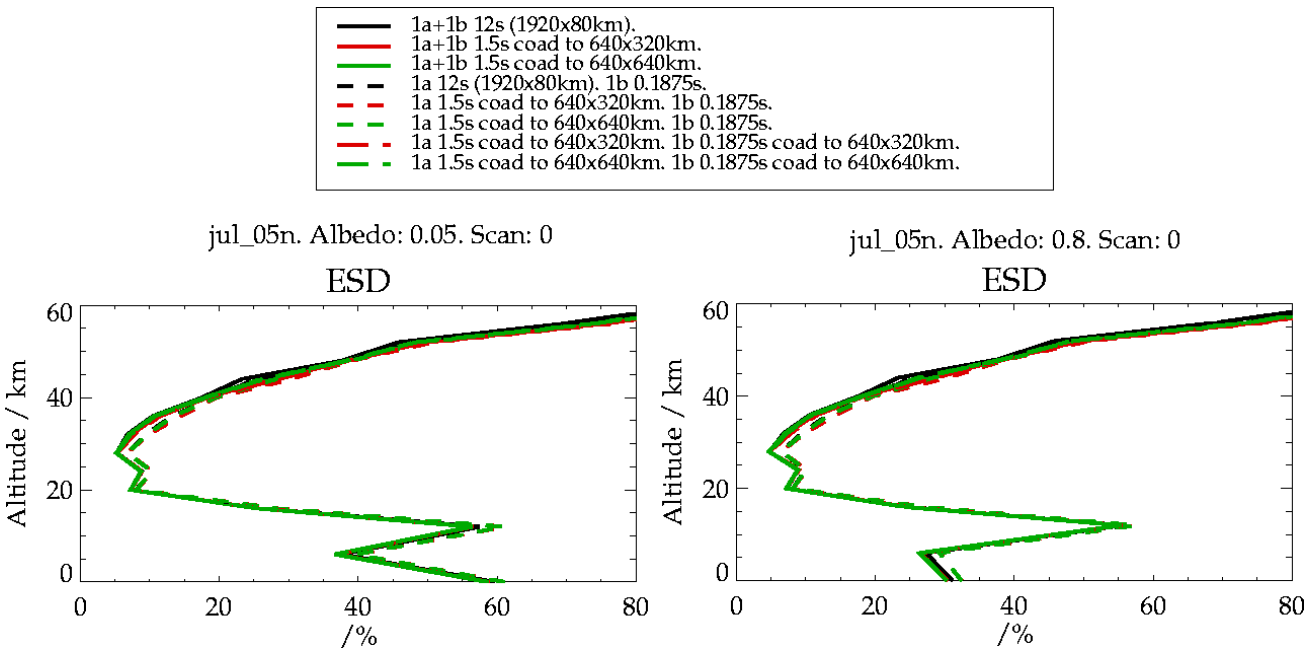

Figure 15-2: Retrieval results for Band 1 processing options for July, 5°N with a surface albedo of 0.05 and 0.8

15.4 Retrieval simulations

Figures B2.2 in Appendix B and, for the example of April 55°N,

Figure 15-2 show the impact of read-out options on basic retrieval diagnostics calculated using the results of the noise model described above. Results for the following options are presented for each geo-temporal / albedo case:

Solid curves:	Bands 1A/1B processed with the same sampling/integration time.
Black:	12s integration.
Red:	1.5s spectra co-added to 12s (640 x 320 km)
Green:	1.5s spectra co-added to 24s (640 x 640 km)
Short Dash lines:	Band 1B at 0.1875s, Band 1A times according to colours above (black curve is the nominal case)
Long Dash lines:	as above but Band 1B co-added to the same sampling as Band 1A

Based on these retrieval simulations, it can be concluded that:

- Co-adding 1.5s integrated Band 1A data to 12 or 24s produces retrieval diagnostics very close to optimum (i.e. those obtained with 12s full integration over Band 1)
- However, reading-out Band 1A at 1.5s is preferable to 12s to avoid anticipated problems (lack of scene homogeneity, radiative transfer complexity) associated with 1920 km wide pixels
- The 1.5s integration time option can therefore be recommended for GOME-2 operation

It is also noted that, co-adding Band 1B produces retrievals of similar quality to treating whole of Band 1 with Band 1A read-out rate (no significant loss through increased read-out rate above 283 nm). There is therefore no major requirement to raise Band 1A/1B boundary from the current setting.

16 WP230: Reduction in Spectral Resolution (RAL)

16.1 Scenarios simulated

Retrieval simulations have been conducted based on the following slit-function scenarios. Only the effects on Channel 2 have been considered. (The Channel 1 slit function is a 2 px FWHM Gaussian throughout).

1. Gaussian slit of varying width. Scenarios simulated are 1, 2, 2.3, 2.7, 3, 4, 8 and 20 pixels FWHM (0.119, 0.239, 0.275, 0.323, 0.358, 0.478, 0.956, 0.390 nm respectively).
2. OG measured data, based on the EQM. From this data, the following cases are simulated:
   - "Focussed" and "Defocused/vacuum" Slit functions at 311 nm and 348 nm are scanned from the corresponding figures in the defocus analysis document. The slit function at intermediate wavelengths is formed by linearly interpolating the two shapes. (The slit functions are stored on a common wavelength grid and linear interpolation performed at each tabulation point. Each interpolated shape is re-normalised after the interpolation. B2 wavelengths outside the range 311 - 348 nm are not used in the profile retrieval.)
   - "Defocused / vacuum – equivalent Gaussian". A Gaussian-slit of the same full-width-half-maximum as the interpolated OG slit function is simulated. (The width of the Focussed case changes only marginally with frequency, 2.02 - 2.03 px from 311 – 348 nm vs. 2.6 - 2.1 px in the defocused case, and is not therefore not simulated separately – the nominal, 2 px Gaussian case being an almost identical scenario.)
   - "Pixel-sampled" versions of the "Focussed" and "Defocused / vacuum" cases: Slit function is chosen to be the step function formed by averaging the interpolated OG functions into detector pixel-width bins. This case is intended as a 0^{th} order representation of the error arising characterising the slit function from a GOME-2 line-lamp spectrum, without knowledge of the sub-pixel shape. This case allows an upper-limit estimate of the errors arising from imperfect shape knowledge only, while neglecting further errors, which would arise in practise from the assumption that the slit function shape at line-lamp positions can be used to infer the shape at intermediate wavelengths.

It should be noted that the GOME-2 line lamp spectrum has a no strong peaks between 306 nm and 333 nm (see Figure 16-1). Characterisation of the variation of slit function shape across the Channel 2 wavelength range of interest for profile retrieval (315 - 334.6 nm) is therefore not possible from the lamp alone. The behaviour of the slit function shape in the Channel 1 / Channel 2 overlap is likely to be non-linear with wavelength and so the 306 nm point is unlikely to be useful as a reference for the spectral range of interest.

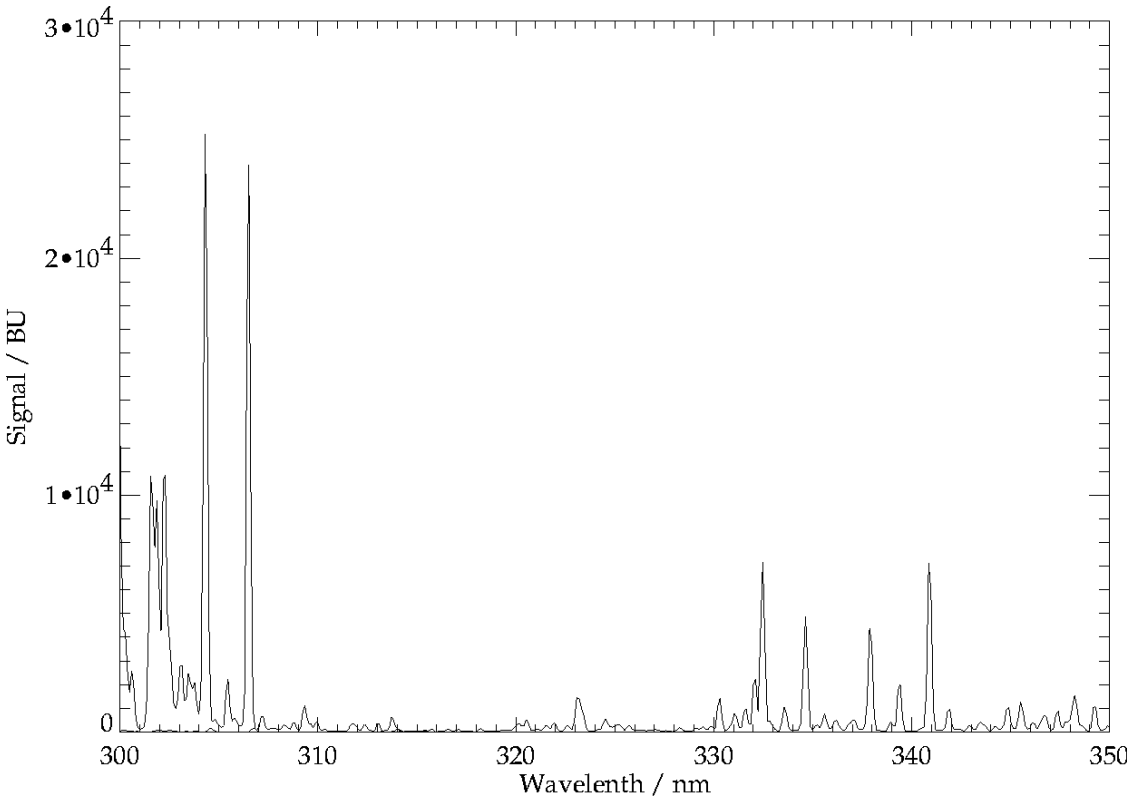

Figure 16-1: GOME-2 EQM Line-lamp spectrum in Channel 2 from Oficine Galileo

16.2 Retrieval of wavelength calibration and slit-width from solar spectra

To overcome limitations arising from the lack of appropriate lines in the lamp spectrum and inadequate pre-flight characterisation, the RAL GOME-1 scheme retrieves Band 2B wavelength calibration and slit function width (assuming Gaussian shape) by fitting measured solar spectra to a convolved, high-resolution solar reference spectrum. By using the fitted wavelength calibration and (spectrally dependent) slit function in the O_3 profile retrieval; adequate fitting precision can be achieved from 323.5 nm to 334.6 nm. Below 323.5 nm the GOME-1 B2 spectra cannot be modelled sufficiently accurately to be of use in the RAL scheme, fundamentally limiting the GOME-1 retrieval quality achieved to-date.

The implementation of a similar approach for GOME-2 has been simulated in an attempt to quantify the errors, which can be expected if the GOME-2 slit function / wavelength calibration is similarly poorly characterised a priori.

The following approach is adopted for retrieval simulations reported here:

1. A "true" slit function scenario is defined (prescribing the shape of the slit as a function of wavelength), as described in the preceding section.
2. The K. Chance solar reference spectrum is used to simulate a Channel 2 GOME-2 solar spectrum with the given "true", wavelength dependent slit.
3. A retrieval of wavelength calibration and slit width is performed using this solar spectrum as measurement. Measurement errors are as taken from the photometric budget document (MO-NT-GAL-GO-0023; SNR Approx. 5000). Fit parameters are coefficients of a 4th order wavelength shift from 311-350nm and a 6th order dependent slit broadening, relative to a 2 px baseline. The "true" scenarios are nominally simulated without wavelength shifts, however the non-symmetric nature of the OG slit functions will be accommodated by a finite wavelength shift in the

fitted Gaussian slit. The retrieval algorithm is non-linear least squares with Levenberg-Marquart iteration.

4. Linear retrieval simulations are performed using the retrieved slit-functions/ wavelength calibration to define the linearisation point. The difference between sun-normalised radiance simulated with the true and retrieved slit functions is then mapped, providing the error due to imperfect slit function knowledge in the retrieval. Note that the simulation of sun-normalised radiance in Band 2 involves modelling both radiance and irradiance at high resolution, adding Ring effect to the radiance, convolving both with slit functions and then ratioing the two (convolution pre-ratio simulates saturation effects of deep Fraunhofer lines). This approach leads (realistically) to the appearance of Fraunhofer-based structure in the sun-normalised radiance, at a level significant for the profile retrieval.

"Pixel-sampled" scenarios: Retrievals involving the Gaussian, OG and OG-equivalent Gaussian "true" slit scenarios are treated as above. The "pixel-sampled" scenarios are special cases intended only to illustrate the importance of sub-pixel resolution slit-function shape, assuming wavelength dependent effects are known. In these cases the "true" (interpolated with wavelength) OG slit function shapes are used as the linearisation point. The difference in sun-normalised radiance between the step-function ("pixel sampled") spectra and those simulated with the true slits is mapped (at each wavelength the interpolated OG slit is averaged into pixel-width bins to form the equivalent "pixel sampled" slit function at each wavelength). *No wavelength / slit retrieval is involved in these cases.*

Figures B3.2 in Appendix B show illustrate the retrieved parameters for the OG based slit function scenarios.

Figure 16-2 compares the OG, fitted Gaussian and "pixel-sampled" slit function shapes the beginning, middle and the end of the fit wavelength range. Figures B3.4 in Appendix B show the measurements simulated with the retrieved slit functions, together with B2 measurement error (note the 0.5% imposed floor) and the mapped signature (difference between sun-normalised radiance simulated with retrieved and true slit function) for the October 75S, 0.8 albedo scenario. (The mapped spectra are very similar from one scenario to the next). The residuals for the 5 cases are shown in Figure 16-3. Only results based on the EQM scenarios are illustrated, when the "true" scenario is Gaussian, the solar spectrum fit is almost perfect, resulting in very much smaller amplitude mapped spectra.

16.3 Impact of under-sampling

The information content of the sun-normalised spectrum is clearly expected to increase as resolution is improved. However, the presence of pronounced high resolution structure in the solar spectrum, coupled to (a) the different Doppler shifts of back-scattered and earth shine spectra and (b) thermally induced wavelength calibration changes between their acquisition times lead potentially to so-called "under-sampling" errors appearing when the sun-normalised radiance is formed.

One can attempt to correct for the wavelength miss-registration by interpolating from one wavelength sampling to another, however this will be imperfect if resolution is sufficiently high that structure between the sample points is not measured (even if the wavelength calibration / Doppler shift is well known). The RAL GOME-1 scheme makes use of a high-resolution solar spectrum (from K. Chance) to characterise the high-resolution structure in the solar spectrum to allow the under-sampling errors to be corrected, however the success of approach is limited by the accuracy of the solar spectrum (and its variability).

The impact of the under-sampling error has been quantified in two ways:

1. In the baseline algorithm, the solar/earth wavelength miss-registration is retrieved (a 4th order polynomial across the Band 2 spectral range to the miss-registration is fitted). This miss-registration retrieval includes modelling of high-resolution structure in the solar spectrum. Assuming the forward model is perfect with respect to under-sampling errors, then the impact is only to degrade the O_3 ESD through any correlation between

the respective weighting functions. The degradation in ESD caused by fitting the miss-registration gives a best-case estimate of the impact of under-sampling errors.

2. The miss-registration retrieval is removed from the retrieval scheme (improving the O_3 ESD to some extent), but under-sampling errors are mapped. The scenario chosen is to map the effect of a 0.01 nm miss-registration (typical value experienced in GOME-1). The error is mapped as a covariance matrix (i.e. reported error is RMS error in O_3 due to 0.01 nm RMS miss-registration). Only under-sampling errors are included in the signature mapped which is formed as follows:
   - The measurement perturbation Δy due to the 0.01 nm miss-registration is calculated including high-resolution solar structure.
   - The perturbation which could be modelled given perfect knowledge of the miss-registration but using GOME-2 measurements only (no use of an independent higher-resolution solar spectrum) $\Delta y'$, is calculation by linearly interpolating the simulated radiance measurement (at the appropriate resolution / sampling) to the shifted grid and reforming the sun-normalised radiance.
   - The difference $\Delta y - \Delta y'$ (which contains only the under-sampling effect) is then mapped.

     This approach is a worst case in the sense that it neglects the possibility of modelling the error thought the use of a high-resolution spectrum, as is done in the GOME-1 scheme. However, it is a best case in the sense that wavelength calibration of the spectra being ratioed is assumed to be perfectly known.

Note that the magnitudes of these mapped errors depend on the slit function shape. In most cases the retrieval linearisation point is a Gaussian slit (fitted to the "true" scenario). The "pixel-sampled" cases illustrate the case when the linearisation point is non-Gaussian, defined by the OG-EQM measurements.

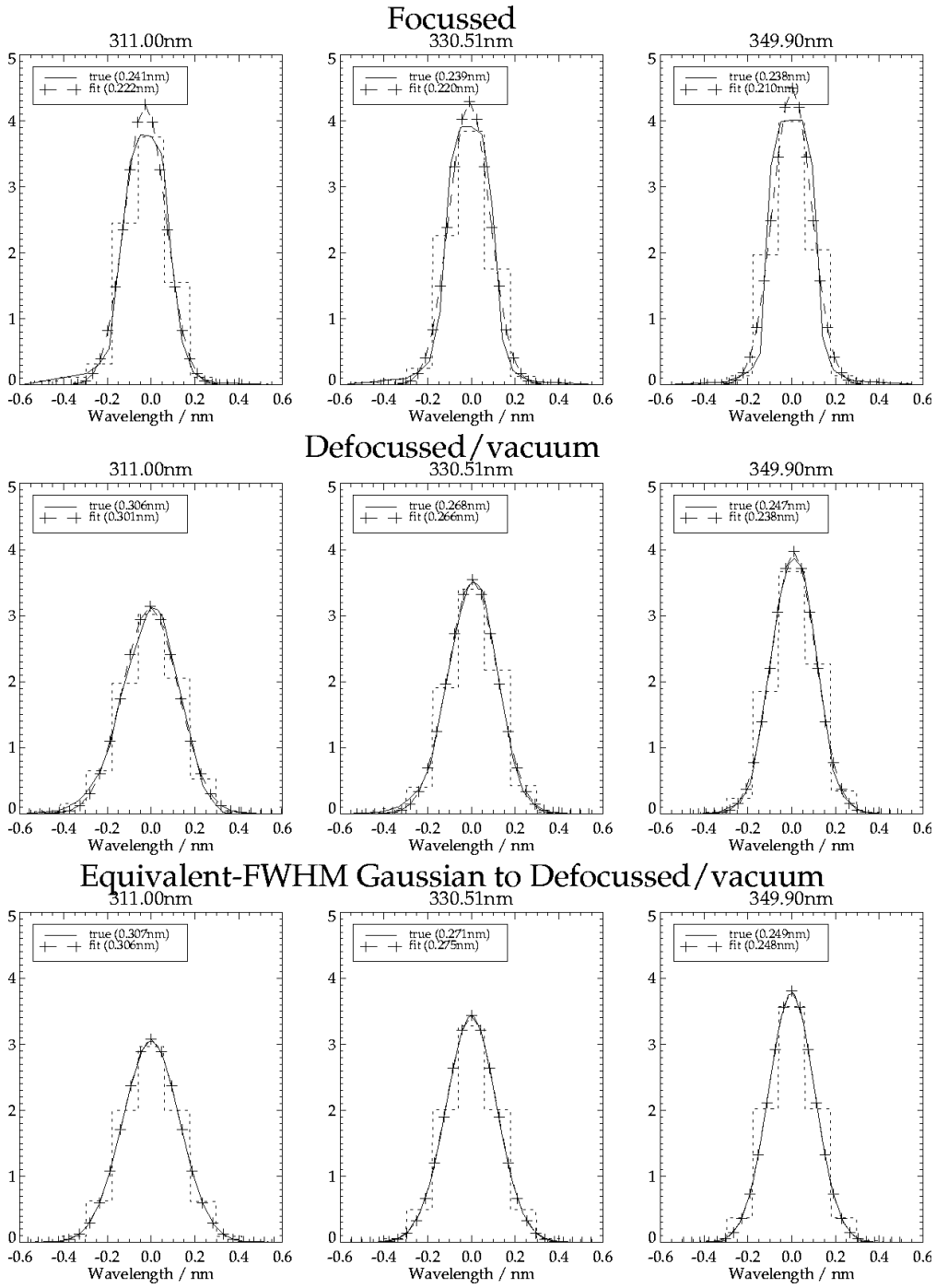

Figure 16-2: Comparison of slit functions used in retrieval simulations

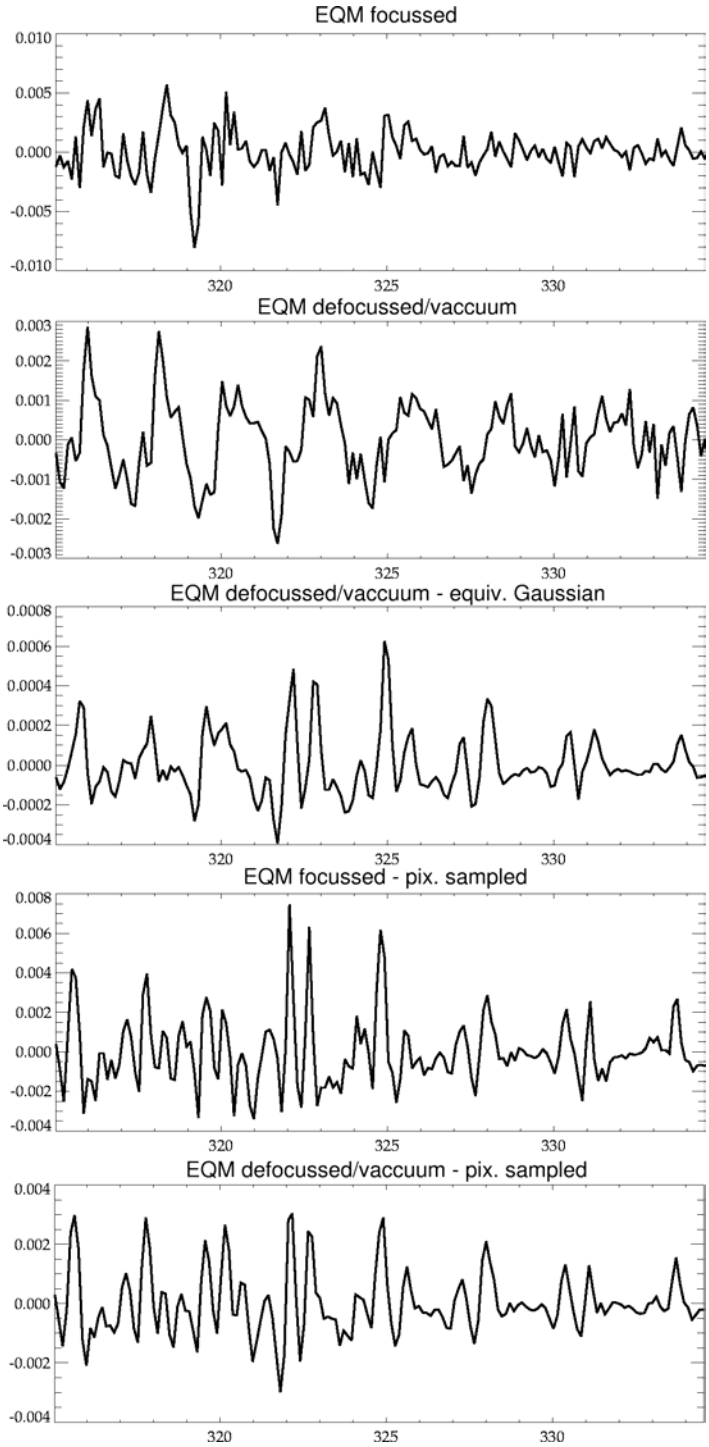

Figure 16-3: Band 2B signature mapped for indicated scenarios

Band 2B signature (differential absorption signature vs. wavelength / nm) mapped for indicated scenarios

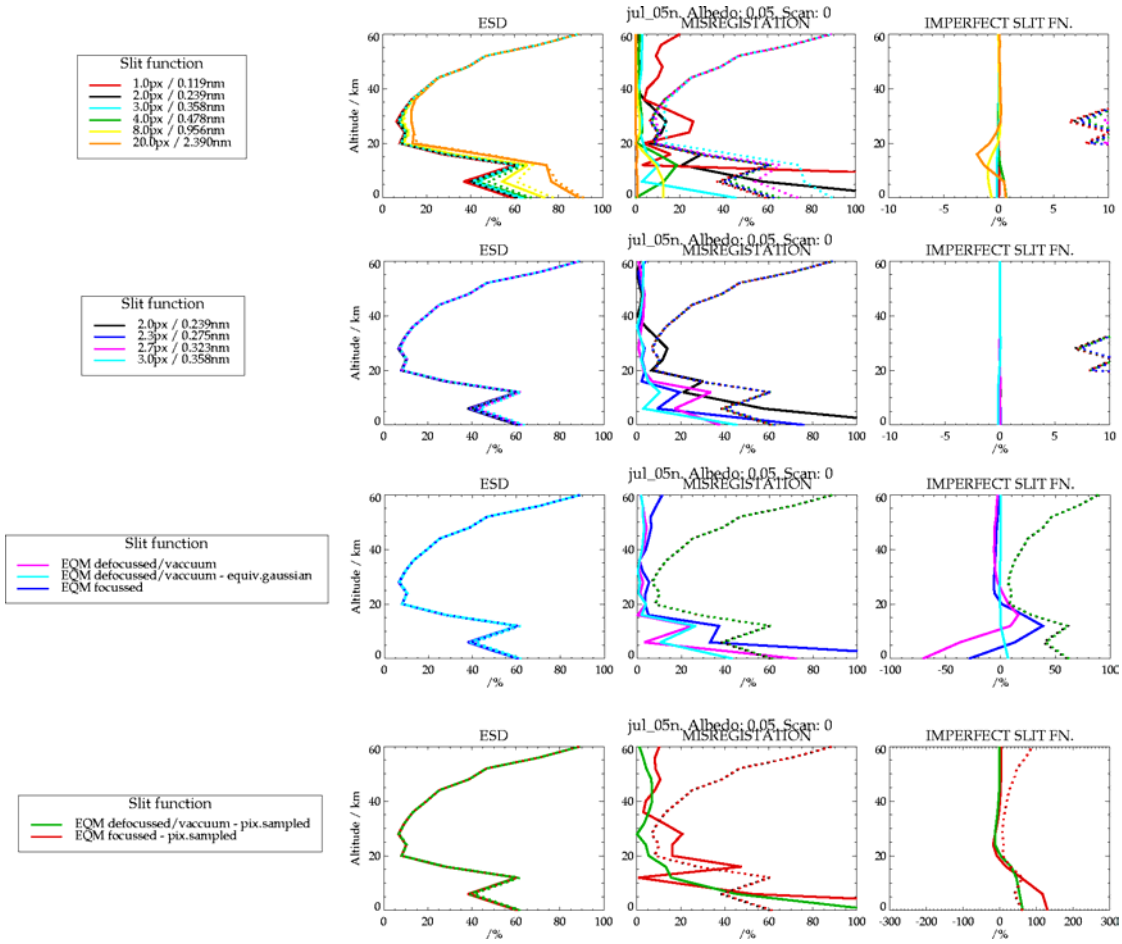

Figure 16-4: Retrieval diagnostics at modified spectra resolutions and assuming different slit function representations

16.4 Results

Retrieval results are plotted in Appendix B in Figures B3.6 (Band 1 spectral range 265-307 nm) and Figures B3.7 (265-314 nm). Results for the July 5N scenario only are shown in Figure 16-4. The three panels for each geo-temporal scenario show the following:

Panel 1: Solid lines: ESD for each resolution if miss-registration *not* included as retrieved parameter. Dotted lines: ESD if miss-registration included. In some cases there is a noticeable (though small) degradation in retrieval quality associated with the inclusion of this parameter (e.g. B3.6.9, July 5N, 0.05 albedo).

Panel 2: Effect of mapping 0.01nm RMS miss-registration and not fitting. Again dotted lines show the ESD for the retrieval in which miss-registration is not fitted.

Panel 3: Effect of mapping error arising assumed wavelength calibration / slit-function. (Retrieval includes miss-registration fit). Dotted lines are, again, the ESD for reference.

For clarity the plots are split across 4 pages in the appendix and 4 rows in the July 5N example included here, as follows:

1. Results for Gaussian slits at 1, 2, 3, 4, 10 pixel FWHM. Note that in general sensitivity to the troposphere is greatly reduced when resolution is degraded beyond 4 px. Low errors in panel 3 indicate that provided the shape of the slit is well known, the solar spectrum fitting process eliminates errors due to imperfect a priori errors in slit width.
2. Gaussian slits at 2, 2.3, 2.7, 3 pixels FWHM.
3. Scenarios based on OG EQM measurements propagated through solar wavelength calibration / slit-width retrieval. Mapping of under-sampling error (panel 2) is consistent with results for the 2-3 px Gaussian cases in plot sets 1 & 2. The "defocus-equivalent Gaussian" cases results in relatively low errors due to imperfect slit function knowledge, but the two cases mapping deviations between the EQM measured shapes and the assumed, fitted Gaussian, lead to large errors in the troposphere. Perhaps surprisingly, the defocused case appears generally worse (despite having more Gaussian shape). Although the amplitude of the mapped signature is smaller (factor 2-3) than in the focussed scenario (Figs B1.4), there is a stronger correlation with the O_3 absorption cross section leading to greater impact on the profile retrieval. The O_3 signature presumably appears in the defocused signature due to the error is the wider slit function allowing the propagation of structure at Huggins-bands spectral scales.
4. Scenarios in which OG measurements taken as linearisation point, but impact of "true" slit being the step-function "pixel-sampled" scenario is mapped. The impact of the miss-registration error is greater in these scenarios than in set 3, since here the linearisation about the non-Gaussian measured slit shape as opposed to the fitted Gaussian. As might be expected, the slit function as sampled at pixel resolution, introduces smaller errors in the defocused case (more samples across the slit).

Note that the x-axis range used in panel 3 varies depending on the plot set above.

16.5 Conclusions

With respect to the trade-off between resolution, ESD and under-sampling error the following conclusions can be drawn:

- There seems to be little to gain in ESD terms by increasing resolution beyond the nominal (red and black cases almost indistinguishable on ESD), whereas the sensitivity to the mapped under-sampling error is dramatically increased at higher resolution
- Tropospheric ESD degrades rapidly as resolution is degraded beyond 4 px
- Degrading resolution from 2 to 3 pixels greatly reduces sensitivity to under-sampling errors, but has little impact on ESD
- Consequently, the degrading from the focussed to the defocused EQM cases has little impact on ESD and reduces sensitivity to undersampling error. (Although the defocused case is *worse* with respect to slit function knowledge, as noted below.)

With respect slit function knowledge:

- The "pixel-sampled" cases indicate the great importance of characterising the shape of the slit function at sub-detector pixel resolution. In the absence of such information profile errors reach order 300% in the troposphere.
- Large errors (50-100%) are also introduced when the slit is assumed Gaussian in the solar spectrum wavelength calibration / slit width retrieval, but the true function is defined by the OG EQM measurements. The focussed case performs better than the defocused version, since uncertainties in the broad slit function seem to propagate more structure correlated with the O_3 absorption cross section into the error signature. It is interesting to note that the character of the error in the focussed case is similar to the negative ~40% bias experienced with the RAL GOME-1 retrievals. In GOME-1 the spectral resolution is found to vary between 0.26 nm and 0.16 nm in the range 323 - 335 nm, and is more comparable to the focussed than defocused case.
- i.e. the defocused GOME-2 would appear to be more sensitive to errors in assumed slit than was the case for GOME-1.
- These errors might be reduced by using a more realistic slit function shape in the solar spectrum fitting. However, no method was found to model a slit shape, which would differ realistically from the true slit function, used in the scenarios based on the OG EQM measurements. A model of the error in the shape derived from the OG measurements, together with a realistic model of the variation in shape with wavelength would be required to perform this retrieval simulation.
- Despite this caveat, the O_3 profile retrieval at low altitude is clearly highly sensitive to slit function knowledge. It is considered unlikely that the internal line-lamp could be used for adequate characterisation since (a) the slit function shape varies below 333 nm (apparently the only useful line in the wavelength range of interest) and (b) even if the wavelength dependence could be accounted for (modelled) there remains the problem of adequately characterising the sub-pixel shape.
- Characterisation of the wavelength dependent, sub-pixel resolution slit-function by means other than the internal lamp therefore appears to be essential for the retrieval of O_3 into the troposphere. Given an error budget for a measurement approach, retrieval simulations could be conducted to quantify the impact on profile retrievals (given adequate time and resources).

17 WP230: Reduction in Spectral Resolution and Column Retrieval (IUP)

17.1 Overview

For the investigation of S/N errors for cases of variable GOME-2 spectral resolutions highly resolved FTS spectra for O_3, NO_2, BrO and OClO were used. Slit-function FWHM from 0.24 nm to 0.6 nm (Channel 2, 0.12 nm steps) and from 0.48 nm to 1.20 nm (Channel 3, 0.24 nm steps) were applied using convolution with a Gaussian function. The linear mapping approach were applied for four of the study scenarios, which were January 55N, April 55N, July 5N and October 75S, albedo 5%.

This aspect of the study is split into two parts. Part 1 concentrates on the defocusing aspect maintaining the instrumental noise unchanged. In Part 2 the open slit approach is tested by applying noise spectra calculated for increased slit width. It is expected that slant column errors will be significantly reduced due to increasing SNR. On the other hand, acceptable tracegas retrieval results could be achieved by reducing the read-out time and increasing the spatial resolution. The effects for spatial aliasing are also investigated: here an error reduction is also expected.

17.2 Defocusing

The smallest considered resolutions (FWHM = 0.24 nm for Channel 2, FWHM = 0.48 nm for Channel 3) are similar to the conditions of the SNR analysis in WP150, described in Task Report 1, and therefore give consistent results. See the description of WP150: note that slight differences occur due to the fact that the defocusing aspects have been investigated using a dataset with different relative azimuth set-up.

For reduction of spectral resolution as described, for fittings in the UV, the O_3 errors rise almost linearly by factors of about 1.15 (January) to 1.2 (April) between smallest and highest resolution (see Figure 17-1). If using the visible O3 fitting window, errors do hardly change with varying spectral resolution.

For NO_2 (Figure 17-3) the increase of errors from smallest to highest resolution is also roughly linear and is stronger than for O_3 (UV) (factors of 1.4 to almost 1.6, maximum for January). The different slopes are expected as NO_2 spectral features are significantly narrower than for O_3. NO_2 is much more sensitive to spectral resolution changes.

In contrast, for BrO (Figure 17-4) the error increase is relatively small with decreasing spectral resolution due to the broad absorption features of BrO.

17.3 Open slit

Simulations of noise have been done for broadened slit width having Full Widths at Half Maximum (FWHM) of approximately 3, 4, and 5 times the nominal spectral pixel width using the same factors applied on integration time, which gives equivalent noise.

Figure 17-1 to Figure 17-4 show linear mapping errors calculated for O_3 (UV and visible), NO_2 and BrO using the achieved noise spectra. Investigations have been performed using the 5%-albedo scenarios, for which no saturation occurs when applying a saturation level of 50 kBU (ME, PM4, 16.04.02). For the cases of 80% albedo saturation occurs for some of the scenarios, especially for Channel 3, when opening the slit. An overview of these cases is given in Table 17-1.

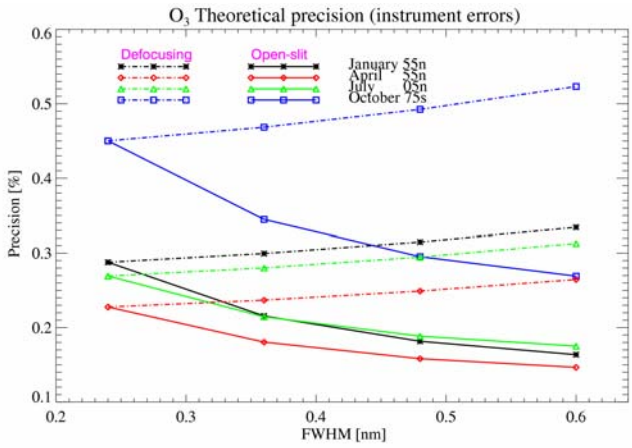

Figure 17-1: **O_3 (UV) slant column errors for various defocusing and open-slit configurations**

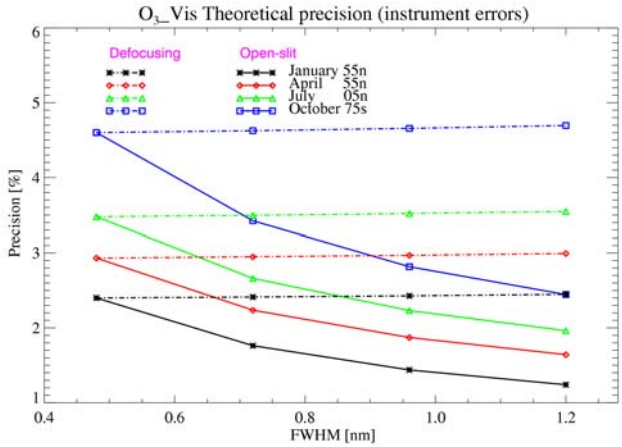

Figure 17-2: **O_3 (VIS) slant column errors for various defocusing and open-slit configurations**

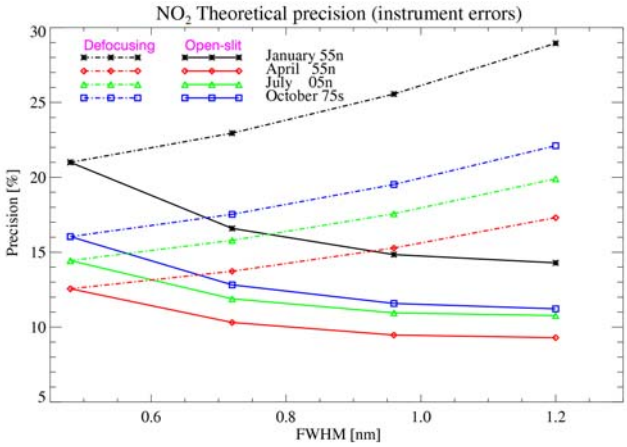

Figure 17-3: **NO_2 slant column errors for various defocusing and open-slit configurations**

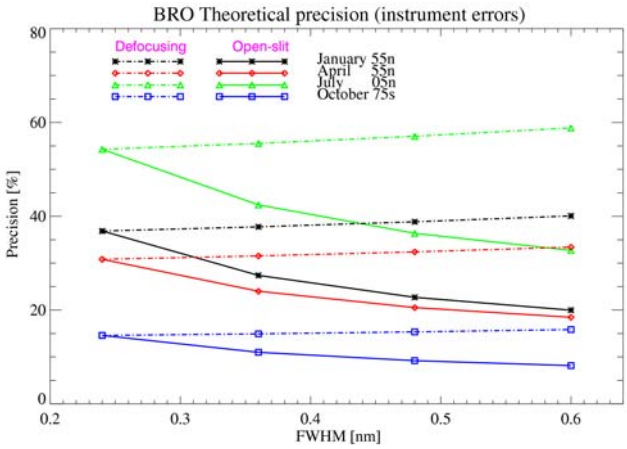

Figure 17-4: BrO slant column errors for various defocusing and open-slit configurations

Table 17-1: Saturation with increase of slit widths: ground-pixels and scenarios

GOME-2 ground pixel numbers for different instrumental slit widths (FWHM [in spectral pixels]) given if saturation occurs in case of 80% albedo.

Ground pixel 1: East Ground pixel 24: West.

For 75S and also for nominal slit width as well as for all cases of 5% albedo, no saturation occurred.

Lat	Jan	Apr	Jul	Oct	Jan	Apr	Jul	Oct	FWHM
	O_3 UV				O_3 Vis				[px]
5N					1-15	1-24	1-24	1-24	3
					1-24	1-24	1-24	1-24	4
	1-5	1-24	1-24	1-24	1-24	1-24 1-15	1-24	1-24 1-16	5
55N						1-5	1-24		3
						1-24	1-24		4
			1-24			1-24	1-24 1-6	1-7	5
75N									3
							1-24		4
						1-10	1-24		5
	BrO				NO_2				
5N									3
					1-11	1-24	1-24	1-24	4
	1	1-24	1-23	1-24	1-24	1-24	1-24	1-24	5
55N									3
						1-2	1-24		4
			1-24			1-24	1-24		5
75N									3
									4
							1-19		5

Using half of the nominal integration time combined with co-adding (on-board or on-ground) has been checked to overcome the saturation problem (except for the O_3-vis window, for April, 5N, July, 55N, and October, 5N, where for FWHM=5 px (!) the 100 kBU limit is slightly exceeded, indicated green in Table 17-1). For the case of on-ground transfer, this option additionally enables to double spatial resolution with only slight increase in SNR error compared to the nominal case. Table 17-2 gives an overview of precision percentage estimates when doubling the slit by simultaneously using half the nominal integration time (OS $^1/_2$ IT). It is the technical aspect of doubled data rate transfer which remains to be applied. For this case, loss of spectral information is largest for NO_2, which has smallest spectral features of the trace gases considered. However, all open-slit options discussed remain valid via co-adding.

	O_3UV		O_3Vis		NO_2		BrO	
	Nominal	**OS $^1/_2$ IT**	**Nominal**	**OS $^1/_2$ IT**	**Nominal**	**OS $^1/_2$ IT**	**Nominal**	**OS $^1/_2$ IT**
Jan 55N	0.29	0.31	2.40	2.43	21.0	25.6	36.4	38.3
Apr 55N	0.23	0.25	2.93	2.97	12.6	15.3	30.5	32.0
Jul 5N	0.27	0.29	3.48	3.52	14.4	17.6	53.7	56.4
Oct 75S	0.45	0.49	4.60	4.66	16.0	19.5	14.4	15.2

Table 17-2: Open-slit precisions versus nominal SNR errors

Open-slit precisions (OS˜1 IT, 1 confidence) versus nominal SNR errors. Errors are percentages relative to the perfect-fit slant column retrieval result.

17.4 Undersampling error

Since the measured solar irradiance spectra are convolved with an instrument apparatus function, the errors arising from a shift in these spectra cannot be rejected just applying a shift correction.

The remaining error can be analysed by convolving a high-resolution solar irradiance spectrum with an appropriate apparatus function first at a selected wavelength grid (λ_i) and then at a shifted grid ($\lambda_i + \delta\lambda$). The results of this convolution will be denoted as $S(\lambda_i)$ and $S(\lambda_i + \delta\lambda)$,respectively.

The error arising without any correction is then given by:

$$D_1 = S(\lambda_i + \delta\lambda) - S(\lambda_i)$$

More representative is the error obtained from the difference between the true values $S(\lambda_i)$ and shift-corrected values $S'(\lambda_i)$ obtained by interpolation of $S(\lambda_i + \delta\lambda_i)$ on the original grid:

$$D_2 = S'(\lambda_i) - S(\lambda_i)$$

The dependence of errors on solar irradiance spectrum shift and the instrument spectral resolution was investigated. The shift was selected to be between -0.008 nm and 0.008 nm.

Corresponding theoretical precisions are estimated according to optimal estimation approach as:

$$T_1 = (A^T S_{D1}^{-1} A)^{-1} \qquad T2 = (A^T S_{D2}^{-1} A)^{-1}$$

where A is the parameter matrix and S_D is the covariance matrix of spectral shift errors D containing as diagonal elements variances estimated from errors D calculated for 17 equidistant shifts between -0.008 nm and 0.008 nm.

The accuracy is investigated employing numerical simulations. This means that the error (D_1 or D_2) is added to the simulated spectra and then the retrieval is performed. The difference between obtained and true parameter values are considered as the retrieval error.

Figure 17-5 to Figure 17-10 show how estimated theoretical precisions (black) and the retrieval error when applying a shift of +0.008 nm (red), which is a good approximation of Doppler-shift to be expected for GOME-2. Statistical evaluation of all retrieval errors obtained from the applied shift ensemble show that the assumption of Gaussian statistic, underlying the above theoretical precision estimates, is not valid, as these estimates do not represent retrieval error RMS values determined. I.e. there is no simple statistical parameter to describe the obtained error ensemble. Therefore, the Doppler-shift case (red curves) should be of focus. For this case, the spectrum $S(\lambda_i + \delta\lambda)$, where $\delta\lambda$ = 0.008 nm, can be interpreted as measured solar irradiance, which before Doppler-shift correction has to be assigned to wavelength grid λ_i (Doppler-shift is -0.008 nm).

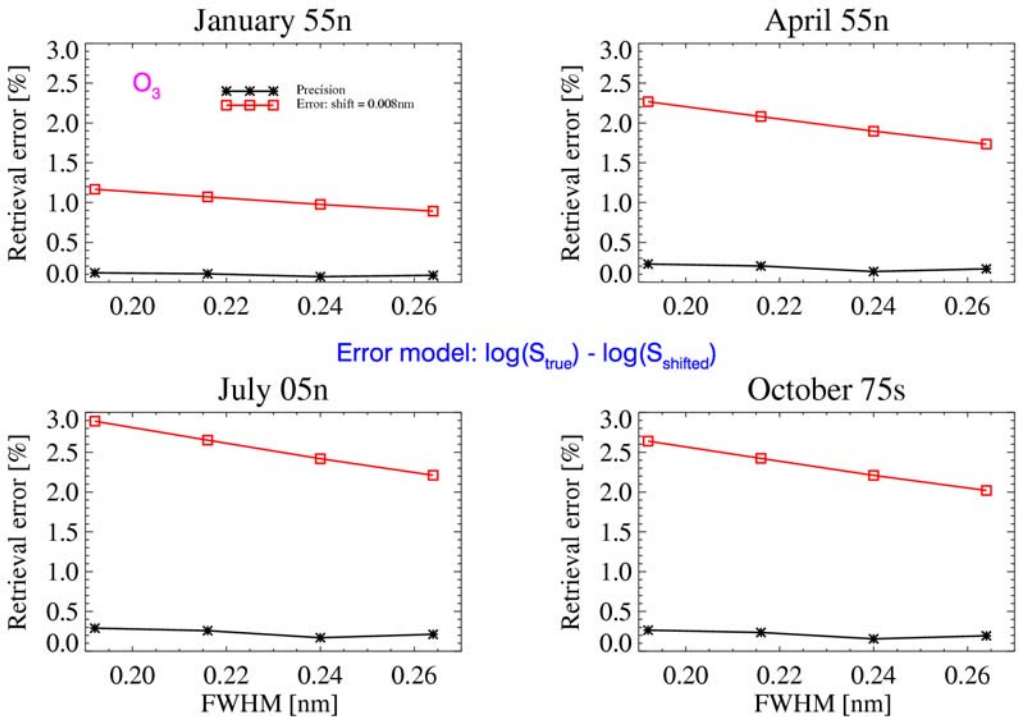

Figure 17-5: O_3 (UV) undersampling errors for FWHM 1.6, 1.8, 2.0 and 2.2 spectral pixel

- Undersampling errors for FWHM 1.6, 1.8, 2.0 and 2.2 spectral pixel width (FWHM = 0.192 nm, 0.216 nm, 0.240 nm, and 0.264 nm) and various simulated spectral shifts
- Theoretical precision estimated from error patterns of all 17 considered shifts.
- No undersampling correction applied.

Figure 17-6: O_3 as in Figure 17-5 but with undersampling correction (back-interpolation)

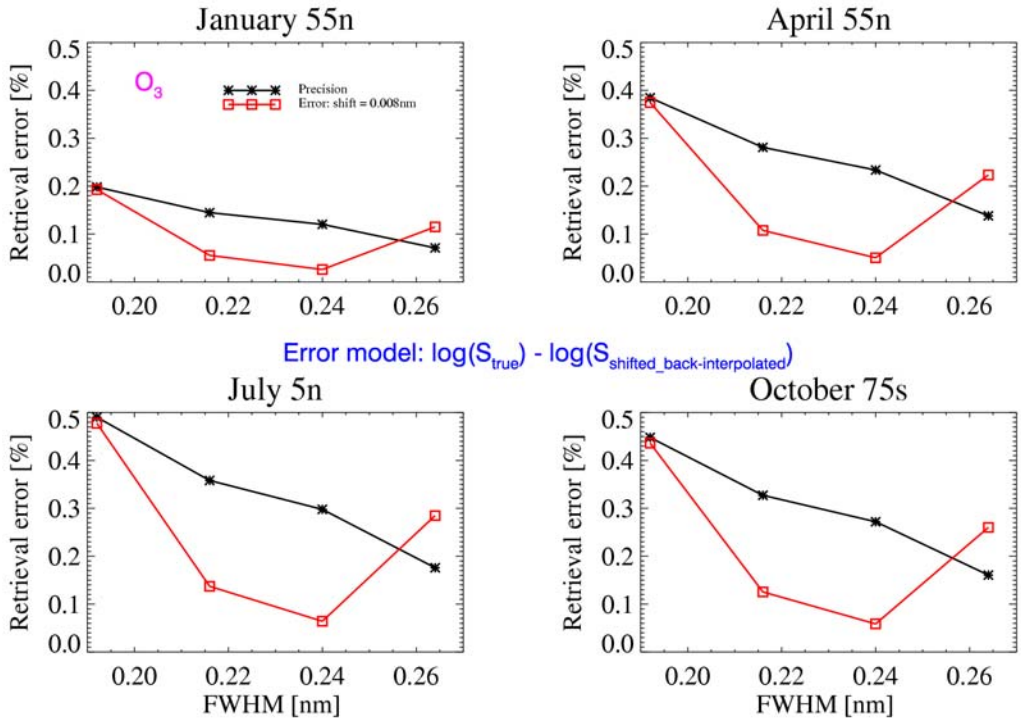

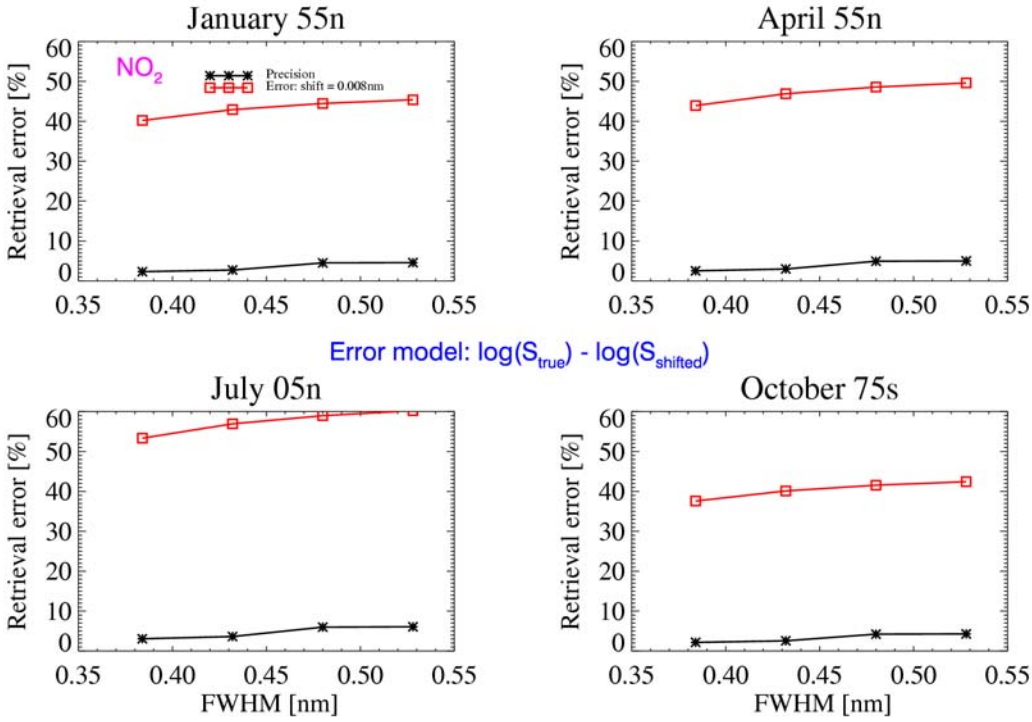

Figure 17-7: NO_2 undersampling errors for FWHM 1.6, 1.8, 2.0 and 2.2 spectral pixel

- Undersampling errors for FWHM 1.6, 1.8, 2.0 and 2.2 spectral pixel width (FWHM = 0.192 nm, 0.216 nm, 0.240 nm, and 0.264 nm) and various simulated spectral shifts
- Theoretical precision estimated from error patterns of all 17 considered shifts.
- No undersampling correction applied.

Figure 17-8: NO_2 as in Figure 17-7 but with undersampling correction (back-interpolation)

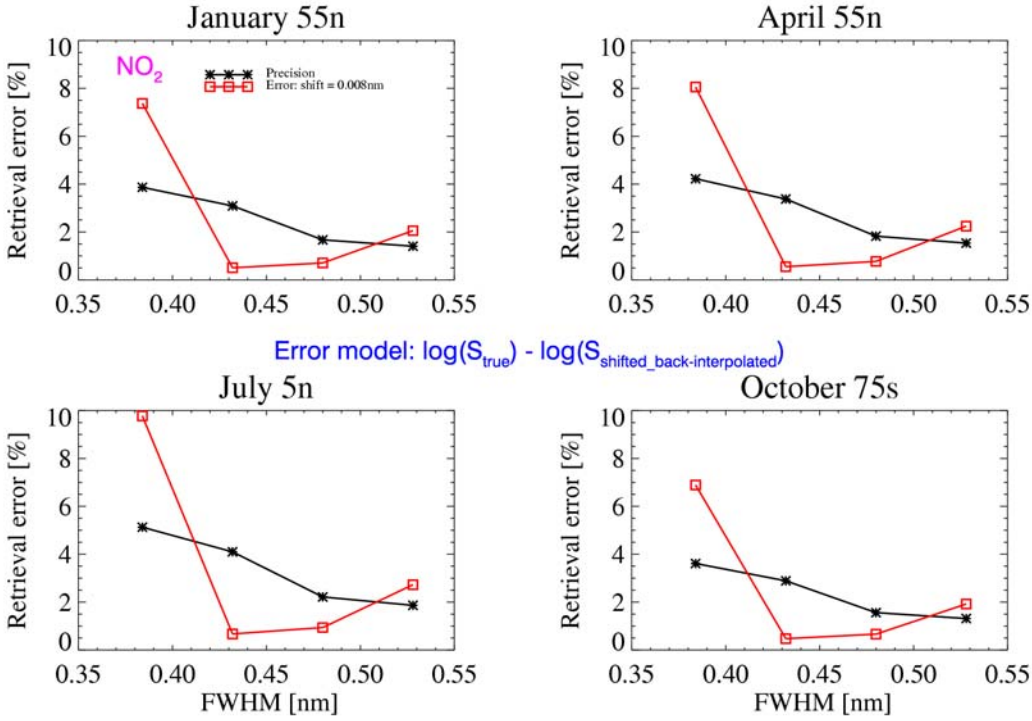

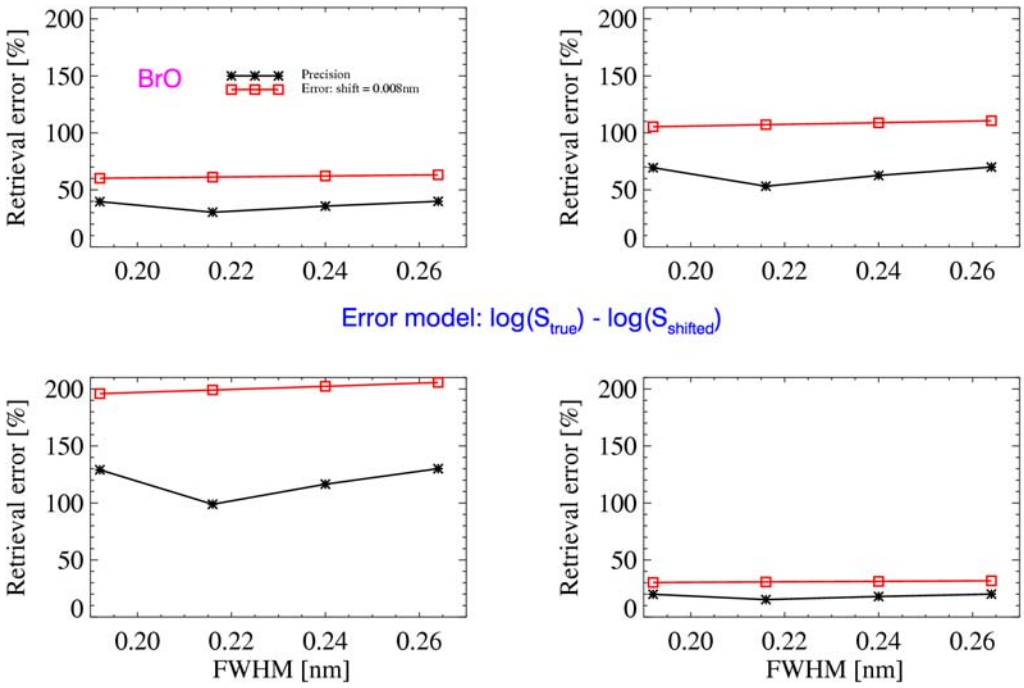

Figure 17-9: BrO undersampling errors for FWHM 1.6, 1.8, 2.0 and 2.2 spectral pixel

- Undersampling errors for FWHM 1.6, 1.8, 2.0 and 2.2 spectral pixel width (FWHM = 0.192 nm, 0.216 nm, 0.240 nm, and 0.264 nm) and various simulated spectral shifts
- Theoretical precision estimated from error patterns of all 17 considered shifts.
- No undersampling correction applied.

Figure 17-10: BrO as in Figure 17-9 but with undersampling correction (back-interpolation)

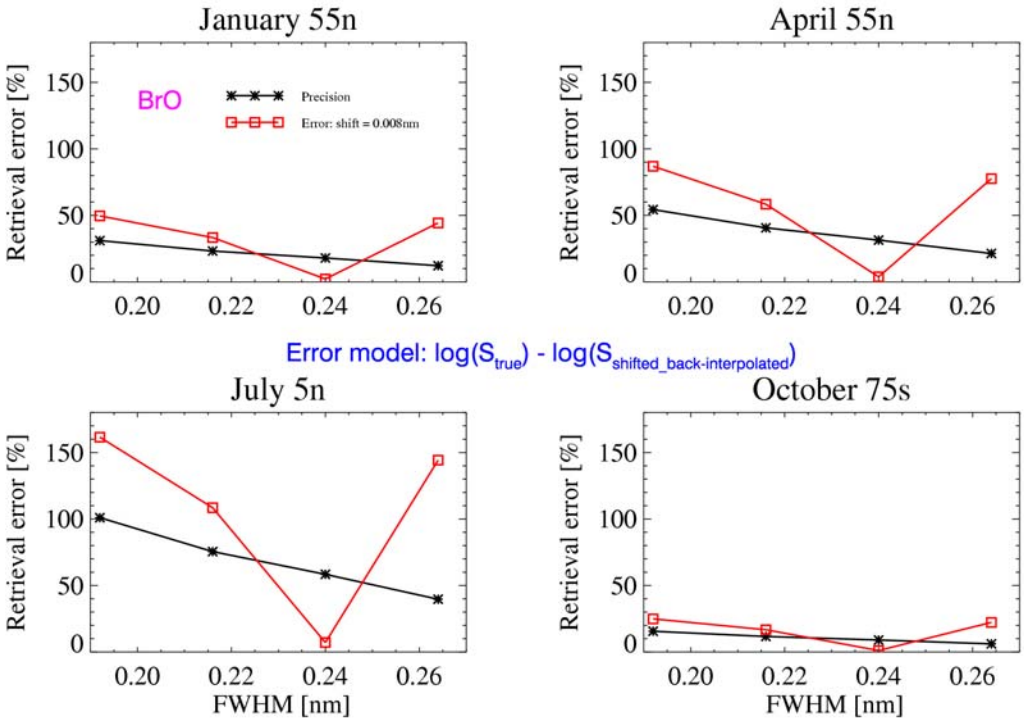

17.5 Undersampling and defocusing

For the case of FWHM = 2.2 px the defocusing/open-slit precision has been estimated in order to give a comprehensive picture of the errors to be expected due to undersampling (over-sampling) in case of Doppler-shift. For the scenarios considered, Table 17-3 gives an overview of all defocusing and open-slit precisions versus undersampling errors (Doppler-shift = 0.008 nm, ME, PM4, 16.04.2002) obtained for FWHM = 2.2 px using back-interpolation correction (see previous section).

	O_3UV			NO_2			BrO		
	US (0.008nm)	Def (1Φ)	OS (1Φ)	US (0.008nm)	Def (1Φ)	OS (1Φ)	US (0.008nm)	Def (1Φ)	OS (1Φ)
Jan 55N	0.11	0.29	0.27	2	21.5	20	45	37	35
Apr 55N	0.22	0.23	0.22	2.2	13	12	80	32	30
Jul 5N	0.29	0.27	0.26	2.7	15	14	>100	55	52
Oct 75S	0.36	0.46	0.43	2	16.5	15.5	22	15	14

Table 17-3: Defocusing and open-slit precisions versus Doppler-shift undersampling errors

Defocusing (Def) and open-slit (OS) precisions (1□) versus Doppler-shift undersampling errors (US, 0.008nm, back-interpolation correction)

Errors are percentages relative to the perfect-fit slant column retrieval result

Values given in Table 17-3 have to be interpreted differently, either if they are specific retrieval errors having systematic character (undersampling error in case of Doppler-shift) or precisions, which have statistical meaning (1-Φ confidence). A direct combination of both errors is valid only under the assumption, that both error sources are independent. A more detailed investigation, including, e.g. correlations and interpolation errors, is beyond the scope of this study. However, aspects of end-to-end errors concluded from the results obtained are discussed in Section 25 (Task 3).

17.6 Summary and conclusions

For the defocusing approach, slant column errors rise almost linearly by factors of 1.1 (BrO), 1.2 (O_3-UV) and 1.4 (NO_2) from the nominal 2 to 5 spectral pixels per FWHM. For O_3-vis, changes in error are negligible.

In contrast, for all cases considered, errors are significantly reduced by opening the slit (modelling includes slit function convolution as for defocusing and modification of SNR). This option additionally enables a reduction of integration time and enhancement of spatial resolution on the ground.

Species	2 px	3 px	4 px
O_3-UV	0.46%	0.35%	0.3%
O_3-vis	4.6%	3.5%	2.9%
NO_2	21%	17%	15%
BrO	54%	43%	36%

Errors are maxima of considered cases for the specific FWHM.

Table 17-4: Error budget for Opening the Slit

Using the applied 17 spectral shifts, precision estimates made basing on Gaussian statistics are unsuitable to represent the obtained ensemble of undersampling errors. Therefore, only the specific case of Doppler-shift is considered, which has been approximated to be 0.008 nm.

If undersampling correction (e.g. by back interpolation to the original wavelength grid) is applied, Doppler-shift undersampling errors for O_3-UV are up to 0.5% for slitfunction FWHM of 1.6 spectral pixel and below 0.1% for FWHM of 2 spectral pixel (about the nominal case). Errors rise again to 0.3% in case of over-sampling (2.2 spectral pixel).

With undersampling correction, NO_2 undersampling errors are equal or below 2%, except for 1.6 pixel per FWHM, and are therefore negligible.

With undersampling correction applied for nominal slit width (2 pixel per FWHM), BrO undersampling errors are below 10%. However, for the cases of under-/over-sampling they can be up to more than 100% depending on the scenario. Undersampling is thus a significant error source for BrO.

18 WP240: Atmospheric Profile Related Effects (RAL)

18.1 Cloud effects

There are two different effects on sub-pixel cloud properties of moving to the wide swath. Firstly, in broken cloud fields the vertical extent of the cloud contributes to the cloud fraction seen, Figure 18-1. Secondly, the longer path length through the atmosphere results in an increase in the apparent optical thickness of transparent clouds, Figure 18-2. The along-track viewing geometry of ATSR is similar to the extreme across-track geometry of GOME-2 (ATSR 55° off-nadir vs. GOME-2 46.5°). A comparison cloud statistics derived from ATSR nadir and along track views therefore allows an examination of these effects, as they will apply to GOME-2.

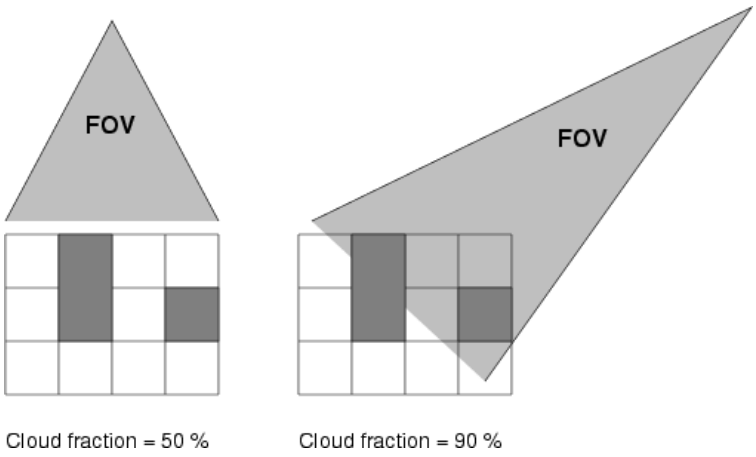

Figure 18-1: Field of view (FOV) effect on viewed cloud fraction

Field of view (FOV) effect on viewed cloud fraction - in the nadir viewing case, the horizontal extent of the cloud is dominant. For off nadir viewing, the vertical extent of the cloud also becomes important.

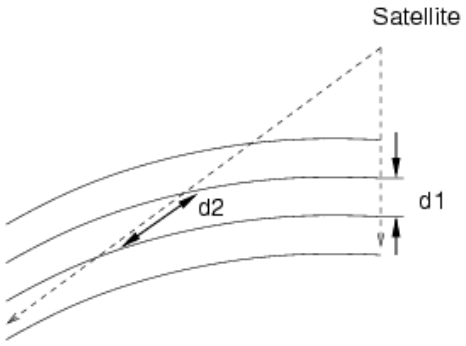

Figure 18-2: Geometric enhancement of the path length

Geometric enhancement of the path length - effective optical depth of a layer will increase as the path length through the layer increases.

18.2 ATSR cloud-flagging

A cloud-flagging algorithm for ATSR images has been developed by A. Stevens at RAL. This scheme has been modified to also work on forward view data and appears to work well, but it must be noted that it was designed to work with nadir images. The scheme has been checked as far as possible within the limits of this project.

The scheme works by considering a number of ratios of visible images (in a similar way to NDVI calculations). From examining a large number of scenes, the ratios have then been classified into various types including: ice, water, thick cloud, thin cloud over water, very thin cloud over water, thin cloud over vegetation, very thin cloud over vegetation, desert, sparse vegetation. Sun-glint often causes ocean scenes to be classified as containing various levels of cloud. A spatial coherence test is used in combination with a consideration of the solar viewing geometry to help ascertain the correct classification. An example of the cloud flagging is shown in Figure 18-3.

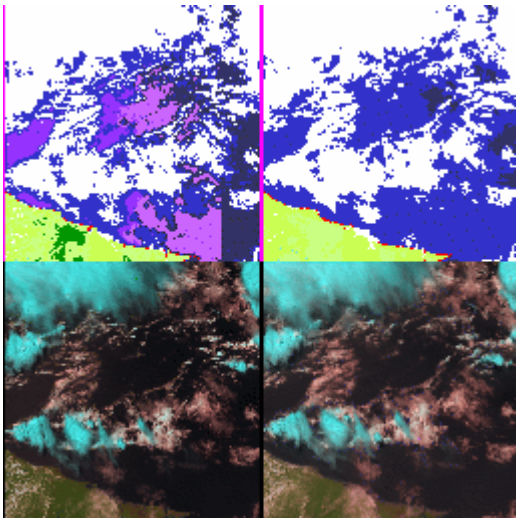

Figure 18-3: ATSR nadir and forward view: classified and pseudo-colour images.

ATSR scenes (512 km x 512 km): classified images (top) pseudo-colour images (bottom)
nadir view images (left) forward view images (right)

Top images: White = cloud Blue = water Mauve = various sun glint contamination
Green = vegetation, some cloud present Pink vertical stripe = invalid data.

Bottom images: Pseudo colour composite of 0.55, 0.67 and 1.6 micron channels.
Black = water Green =vegetation Red = low altitude clouds (warm)

18.3 Cloud statistics

517 orbits of available ATSR-2 GBROWSE (1 in 4 pixel sub-sampled version of full 1 km resolution images) have been classified spanning 1 year, sampled 1 day in 10. The data mainly consists of narrow swath mode images, although some wide swath data was also available. The processed data has then been sampled for the amount of cloud contamination in each view using a sample size corresponding to 80 x 40 km GOME-2 pixel. The sample pixel is stepped every half pixel both across and along track. For a sample to be considered at all, a minimum of 80% valid data within the sample pixel, in both forward and nadir view, was required. Only pixels within the sample, which are valid in both nadir and forward views, are then included in the statistics calculated for the sample. (The forward view data contains much more invalid data than the nadir. This is mainly due to missing or error flagged data in the GBROWSE images, not from the scheme failing on the forward view.)

Figure 18-4 shows the distribution of cloud contamination from the entire data set in 10% bins, both for *thick* cloud and *any* cloud contamination (i.e. thick + thin/very thin over water or vegetation). As expected there is a decrease in number of low cloud fraction scenes and an increase in the number with high cloud fraction, although the intermediate contamination distribution remains almost unchanged.

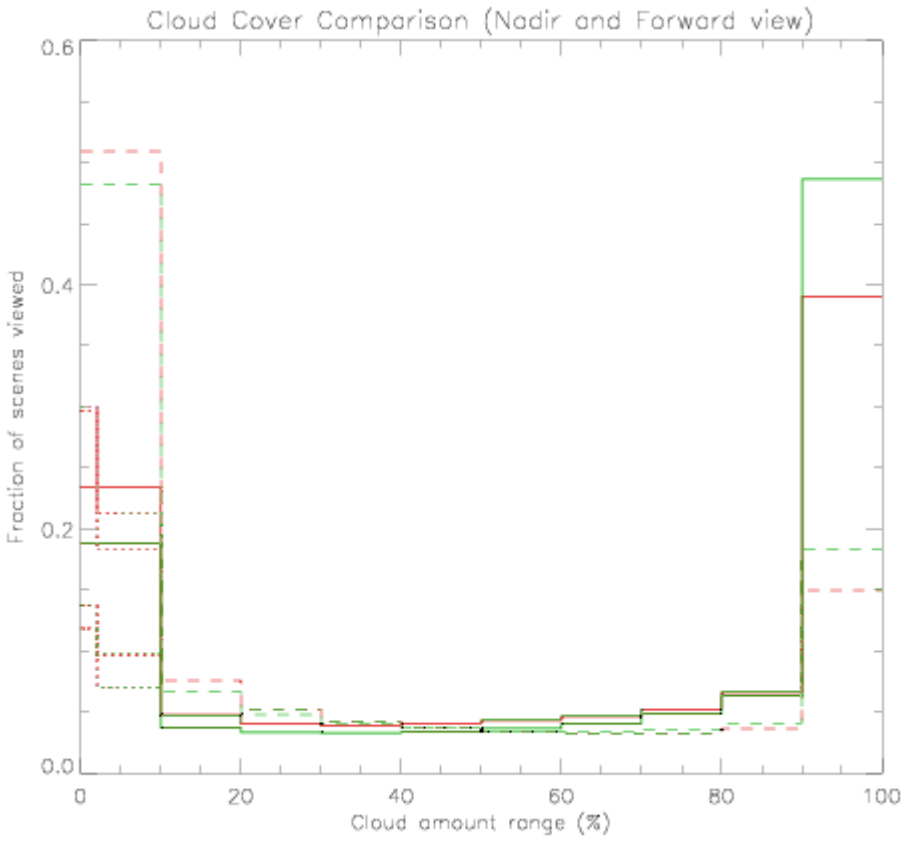

Figure 18-4: Distribution of cloud contamination for nadir and forward views

Cloud contamination distribution: Solid line: any cloud Dashed: only thick cloud
Red: nadir view Green: forward view

The distribution is shown as fraction of all sampled scenes containing a given cloud amount, 0-10% cloud, 10-20% cloud etc. Also shown (dotted) in the 0-10% region is the amount of totally cloud free (0-2 on x-axis) compared with less than 10% (2-10 on x-axis)

18.4 Impact of temperature gradients

Temperature gradients and associated air-density fluctuations lead to gradients in the refractive index of air. If these gradients are large enough to significantly impact the radiative transfer, then the retrieval problem will be significantly complicated since even current state-of-the-art scattering RTMs assumes spherical symmetry in computing refracted ray-paths. The effect will be largest at the extreme viewing angle of GOME-2, i.e. 46.54° off-nadir angle at satellite (elevation approx. 35° at the ground).

This effect has been investigated for as follows:

- ECMWF temperature fields associated with the ATSR-2 fields analysed above were used to determine a maximum possible temperature gradient. The figure arrived at was 0.14 K/km. Note that the horizontal resolution of the ECMWF data available is 100 km (1.12°), whereas the surface distance travelled by the extreme swath LOS ray

is approximately 30 km (considering the ray path from 20 km down to the surface – refraction being negligible above 20 km). I.e. the ECMWF data does not capture the structures giving rise to this effect. Note also that although temperature / refractive index gradients over the scale of the extreme ground pixel across-track dimension (80 km or 640 km for the proposed B1 integration scheme) will also have an effect, this would be handled by computing sub-pixel spherically-symmetric pencil beam radiances (in any case required in retrievals due to changing view geometry effects). Hence structure on scales larger than the pencil-beam horizontal extent within the refractive lower atmosphere is not relevant here.

- Refraction for GOME-2 geometry under the 0.14K/ km gradient was simulated using the 2-D ray-tracing scheme developed at RAL for the purposes of studying limb refractive geometry [Reburn W.J., et al]. The gradient in temperature was applied at all levels from 0 - 40 km. Note that the pressure/altitude profiles were kept fixed in the horizontal and not hydrostatically constrained by the temperature gradient.
- To ensure this unrealistic lack of hydrostatic constraint did not (unexpectedly) lead to an underestimation of the effect in question two more realistic cases were selected from the temperature fields from 15UT on 4 April 1998. Surface fields from the ECMWF data are shown in Figure 18-5. From this fields regions of high temperature gradient were selected, excluding mountainous regions (apparently high temperature gradients on model levels are not necessarily high gradients on altitude or pressure surfaces). Two cases were selected along longitude 22.5°E, near 54° and 74°N. The meridional cross section is shown in Figure 18-6.

Figure 18-7 and Figure 18-8 show the results of the simulations. The panels show the following:

- Top: LOS path length in 1 km layers from 0-20 km for off-nadir angle 46.5° (satellite altitude 825 km, Earth radius 6370 km). Solid line shows path length when refraction is neglected. Dashed line shows refracted path, assuming a horizontally symmetric mid-latitude temperature profile.
- Middle: The ratio of the refracted to non-refracted path lengths are plotted as percentage change in path length.
- Bottom: The percentage change in refracted path length of the 0.14K/km gradient vs. the symmetric case. (The temperature gradient is simulated as positive away from the LOS; hence negative density and refractive index gradient in that direction).

In the case of the realistic scenarios, panels are added showing the temperature field as function of surface distance and altitude in the LOS plane.

It can be concluded that the effect of even horizontally symmetric refraction on LOS path lengths is small (<0.1%), and that the impact of gradients at the level simulated is completely negligible (<0.001%). Note that perturbations in path length can be expected to map to errors of comparable magnitude in retrieved constituent sub-columns (the effect on radiances being equivalent to a trace-gas slant column perturbation). Given the negligible perturbation is the LOS path lengths associated with the simulated gradient, the planned mapping of LOS perturbations though retrieval algorithms (column and profile) is no longer deemed necessary.

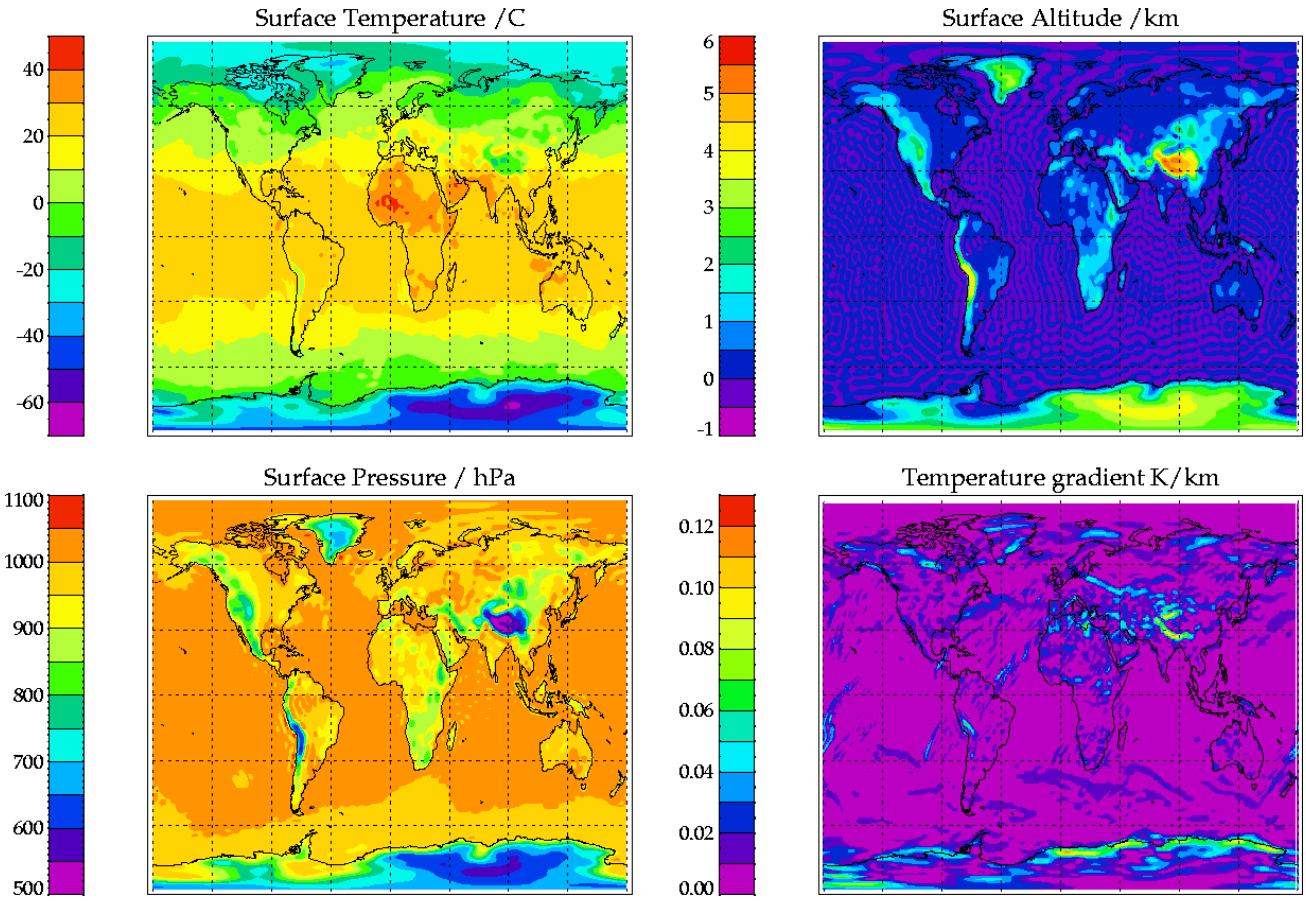

Figure 18-5: Surface fields from the ECMWF analysis for 03:00 UT on 4th April 1998

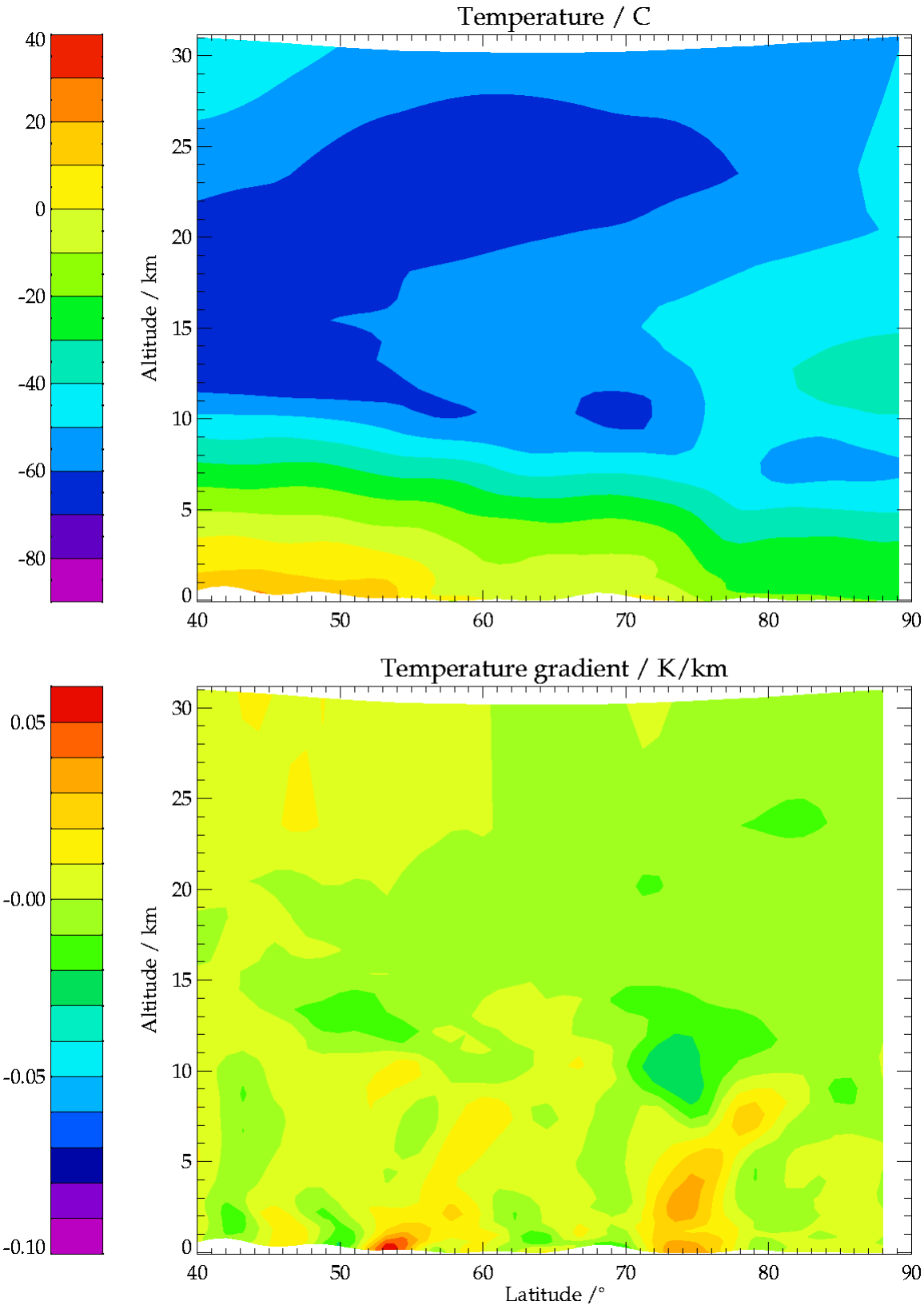

Figure 18-6: Cross-section through ECMWF temperature fields from 40 to 90°N along 22.5°E

Cross-section through ECMWF temperature fields for 03:00 UT on 4th April 1998 from 40°N to 90°N along 22.5°E

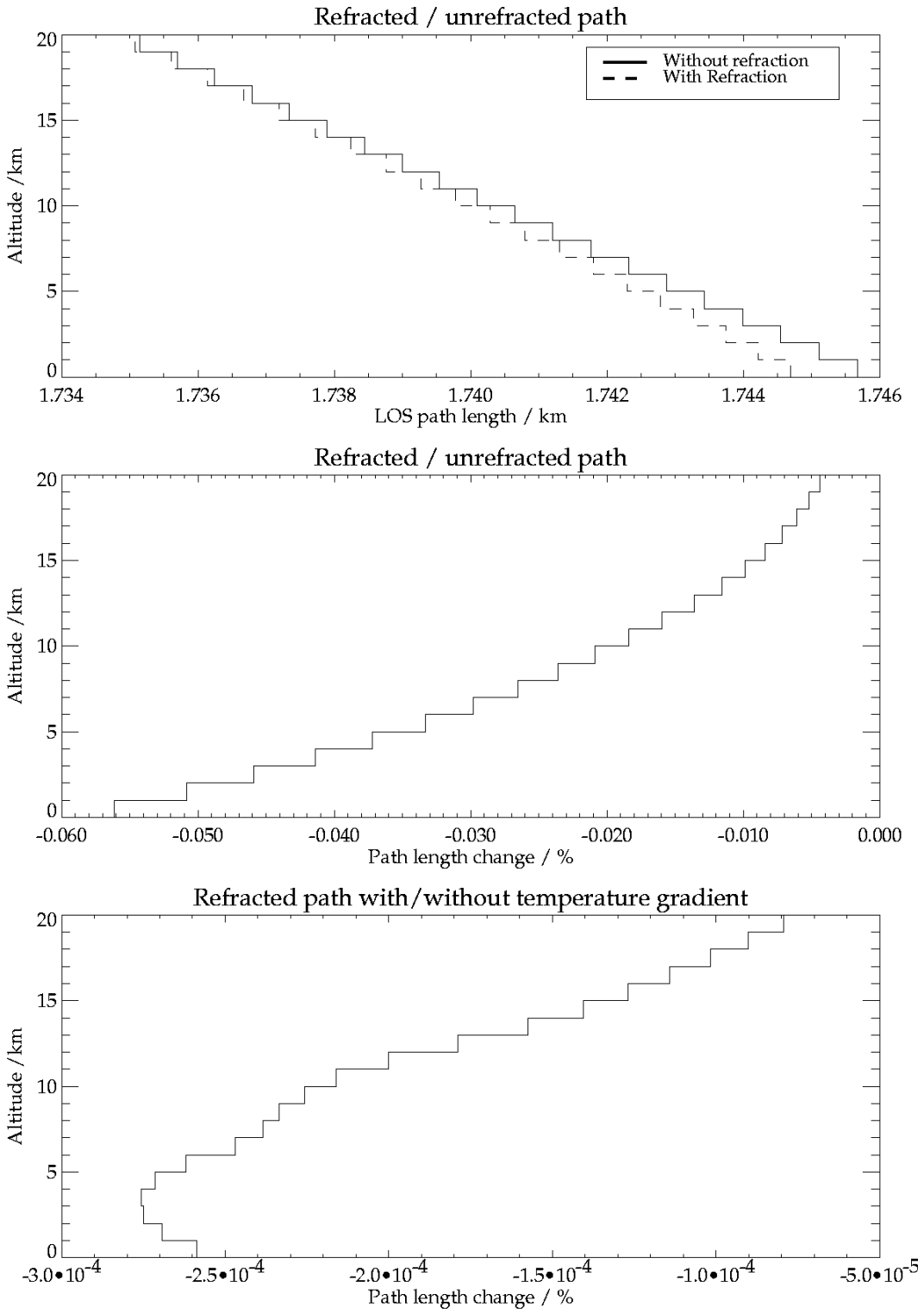

Figure 18-7: Line-of-sight layer path lengths for high uniform temperature gradient case

Top panel: Compares refracted and unrefracted path lengths
Middle panel: Relative difference of refracted – unrefracted path lengths
Bottom panel: Relative difference between path lengths computed with and without the assumption of horizontal symmetry

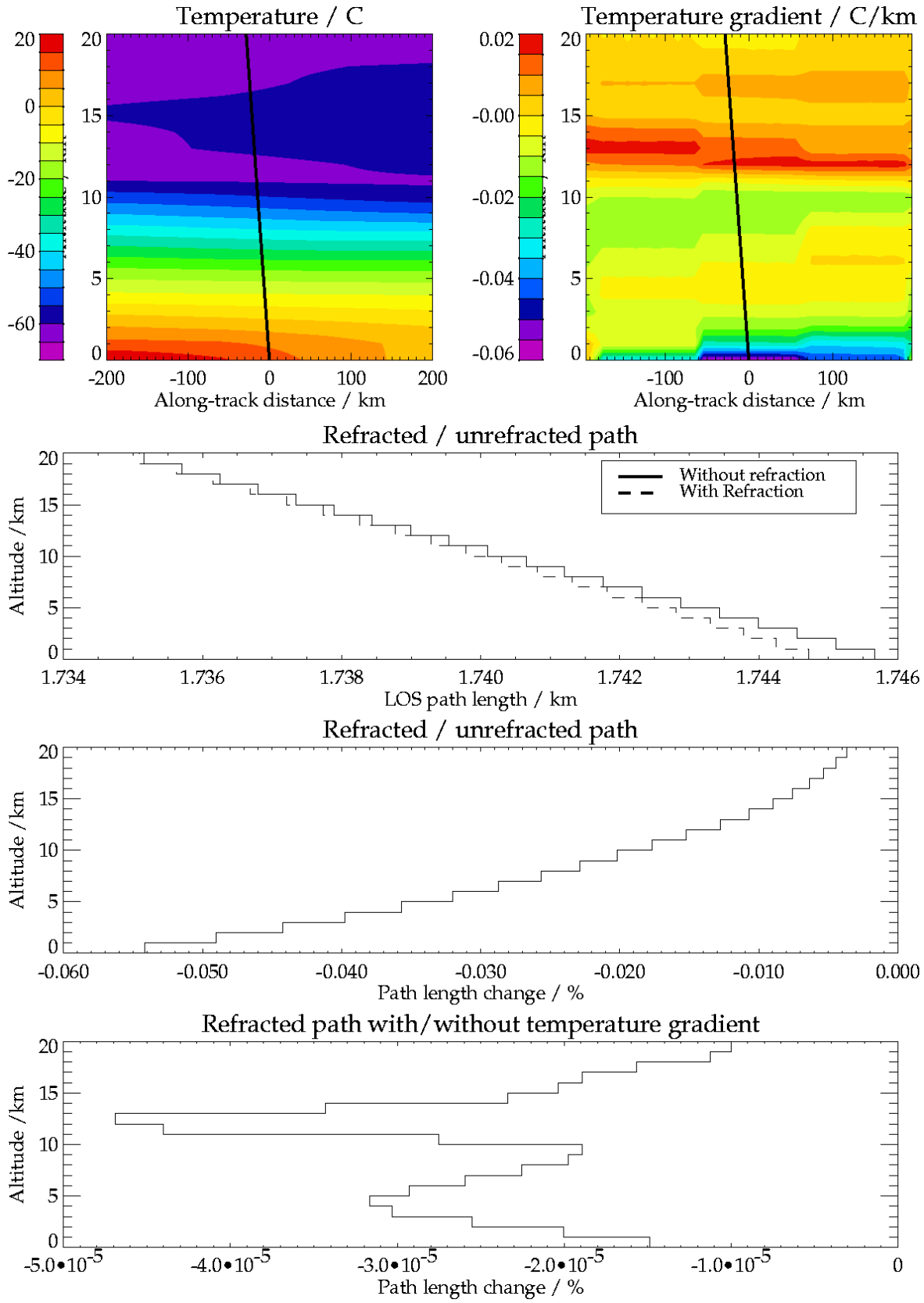

Figure 18-8: LOS layer path lengths of temperature gradient selected from ECMWF field

Line-of-sight layer path lengths of realistic temperature gradient selected from ECMWF field (53.8°N, 22.5°E)

19 WP250: Earth Curvature and RTM Assumptions *(RAL)*

19.1 Pseudo-spherical approximation

Reflectance spectra have been calculated with CDI using both full spherical geometry (no refraction) and the pseudo-spherical approximations for all study scenarios. Two sets of geometrical parameters have been used for the pseudo-spherical mode, ground level and top-of-atmosphere (TOA), both calculated from geometrical parameters at satellite altitude (default input for CDI full-spherical mode).

Figure 19-1 and Figure 19-2 shows, for April 55N, the spectral variation across the swath introduced by the pseudo-spherical approximation for both the ground and top of atmosphere defined solar view geometries (for all scenarios see Figures B5.1 and B5.2 in Appendix B). Positive angles indicate westward (right hand side of scan) measurements, negative being eastward. The dashed lines on the left hand plots indicate the edges of the 960 km and 1920 km swath options (approximately 29° and 45° respectively). The spectral difference can be seen to grow most rapidly beyond the 960 km swath edge. The plots on the right show the actual radiances at the selected view angles and the corresponding differences.

The spectral difference introduced in each case due to the pseudo-spherical approximation has been linearly mapped. The CDI spherical mode weighting functions were used in the mapping with all spectral differences being calculated from CDI spherical and pseudo-spherical calculated spectra. (In Band 2B, DOAS values are used in the mapping, i.e. after subtraction of polynomial from the logarithm of the reflectance, rather than the absolute differences shown in the figures).

These spectral differences are then mapped for the nadir and the edges of both the 960 km and 1920 km swath, as shown in Figure 19-3 and Figure 19-4 for the two Band 1 wavelength coverage options (Figures B5.3 and B5.4 in Appendix B show the options for all scenarios). Each set shows the errors associated with both ground and top of atmosphere specified solar geometry angles. The errors associated with a given view can be seen to be insensitive to surface albedo in the upper atmosphere, as would be expected. The errors are generally smaller for the 960 km swath, than for the 1920 km option, again as would be expected.

19.2 Conclusion

The pseudo spherical approximation can be seen to introduce significant errors into the calculated radiance, particularly towards the edges of the 1920 km swath. On mapping these errors, in both swath options, the errors are generally within the ESD at all altitudes, although significant oscillations can be seen in many cases, most noticeably in the 1920 km swath edges. It is possible these errors would be somewhat reduced in a full non-linear retrieval, which is beyond the scope of this investigation.

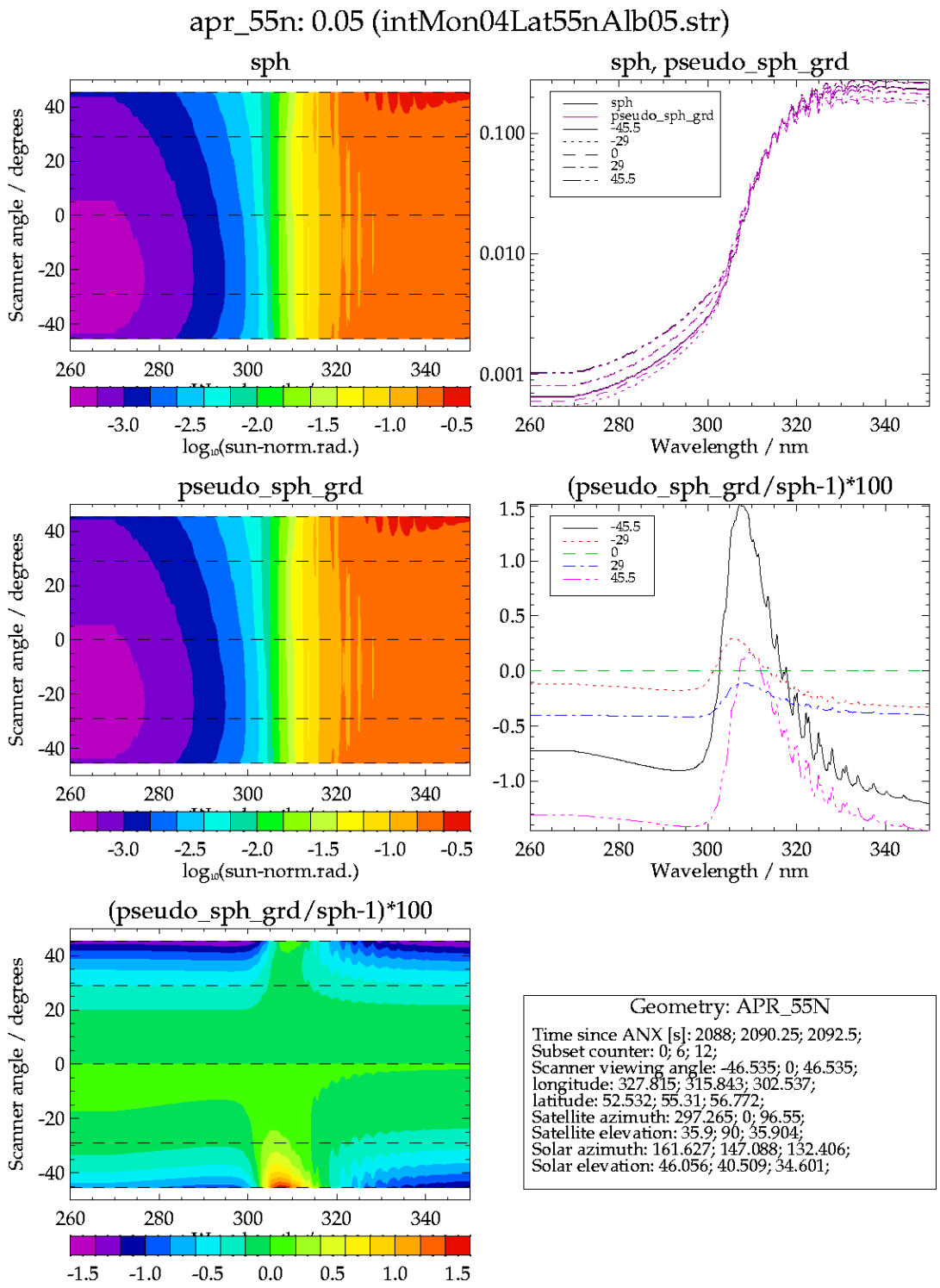

Figure 19-1: Psuedo-spherical approximation spectral difference as function of across track view angle using GROUND solar geometry

Band coverage:	260-350 nm	Albedo:	0.05
Top left:	full spherical calculations	Top right:	spectra for selected angles
Centre right:	spectral difference for selected angles		
Centre left:	pseudo-spherical using **ground** solar geometry angles,		
Bottom left:	pseudo-spherical approximation difference		

The dashed lines indicate nadir and approximate swath edges: 960 km = ±29°, 1920 km = ±45.5°.

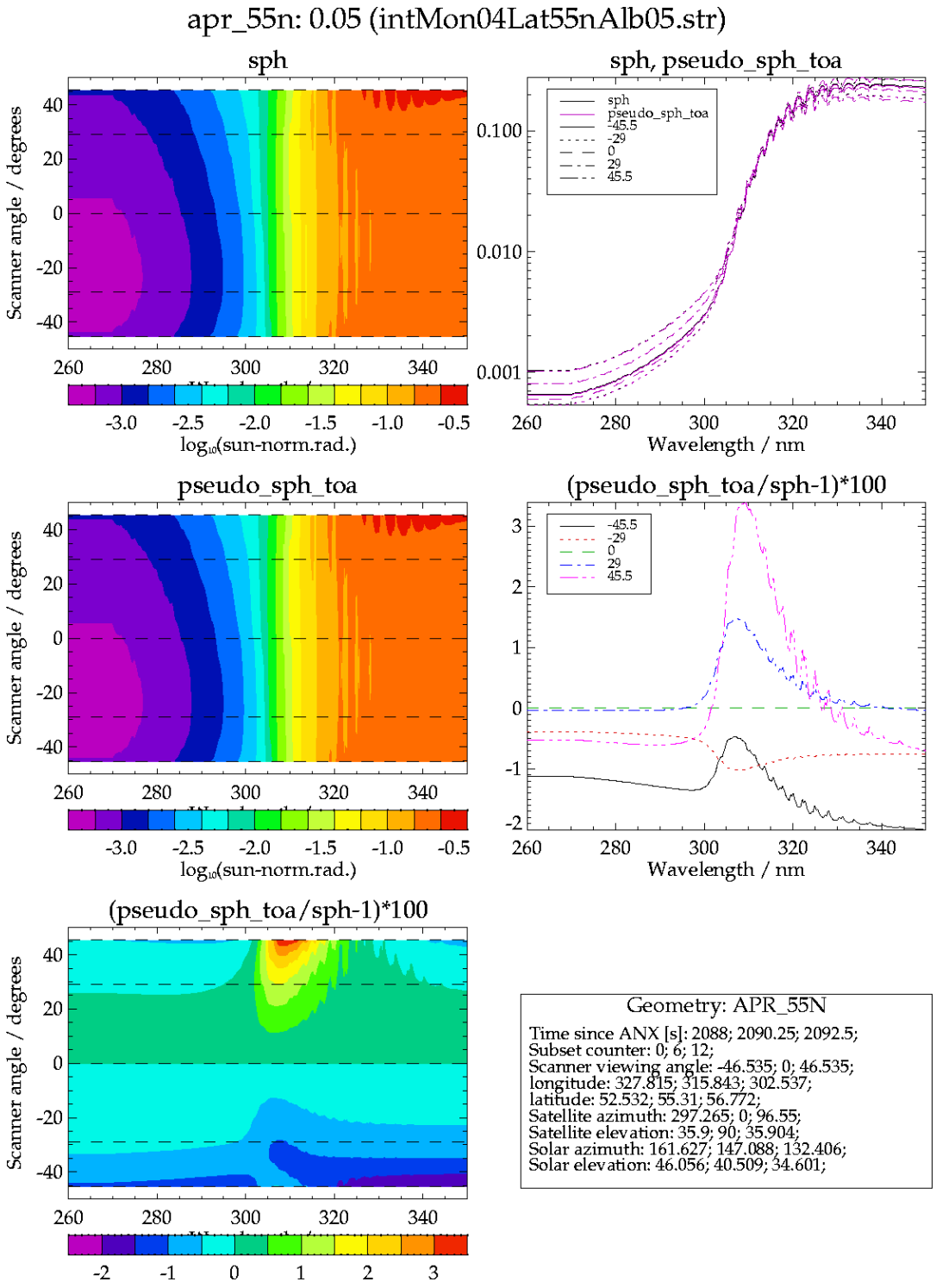

Figure 19-2: Pseudo-spherical approximation spectral difference as function of across track view angle using TOA solar geometry

Band coverage:	260-350 nm	Albedo:	0.05
Top left:	full spherical calculations	Top right:	spectra for selected angles
Centre right:	spectral difference for selected angles		
Centre left:	pseudo-spherical using **top of atmosphere** solar geometry angles,		
Bottom left:	pseudo-spherical approximation difference		

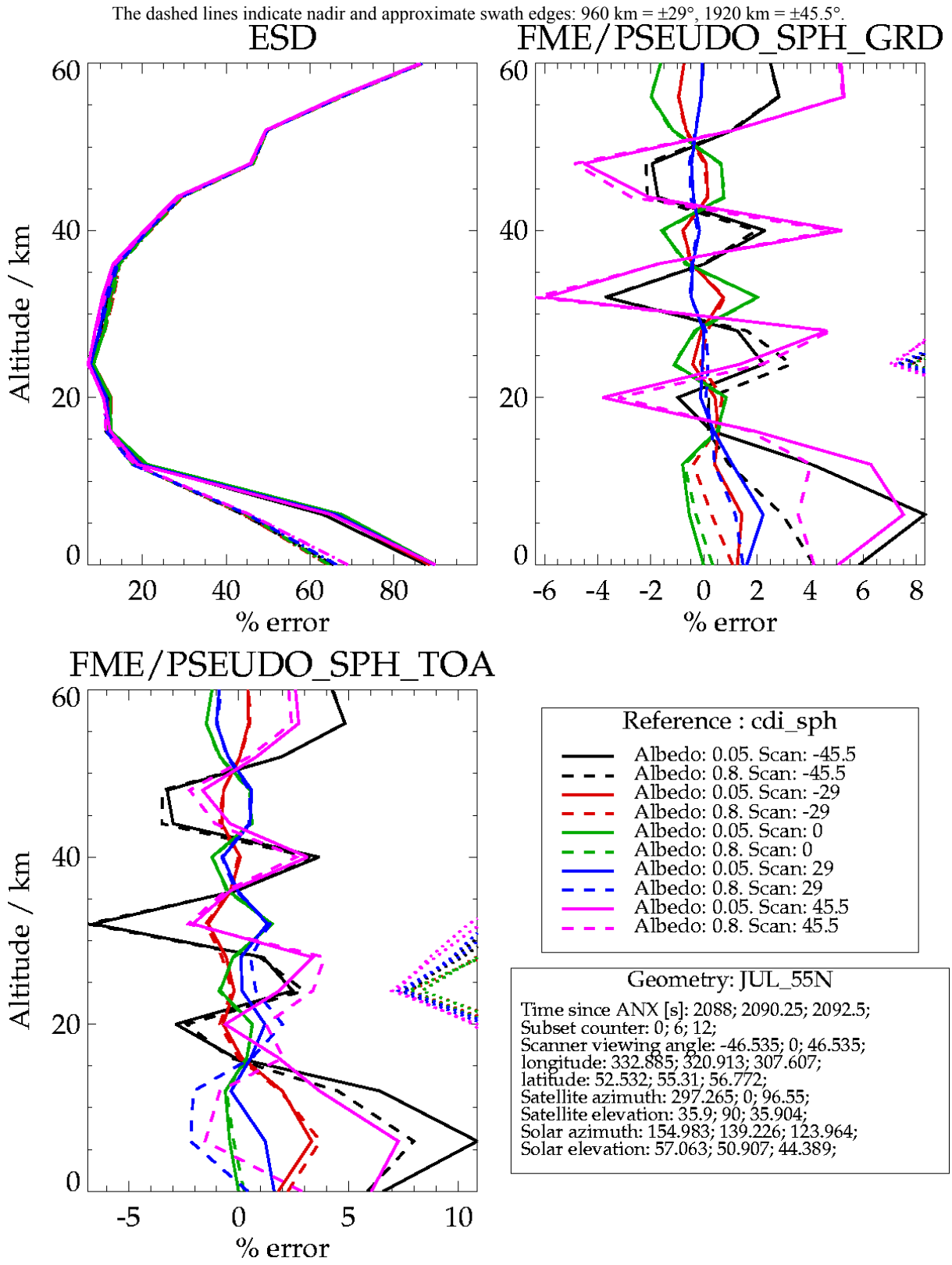

Figure 19-3: Pseudo-spherical approximation error using CDI weighting - Band 1 265-307 nm

Pseudo-spherical approximation error for July 55N, using CDI weighting functions
Band 1 coverage: 265-307 nm.
Dotted line in RSS panel shows associated ESDs

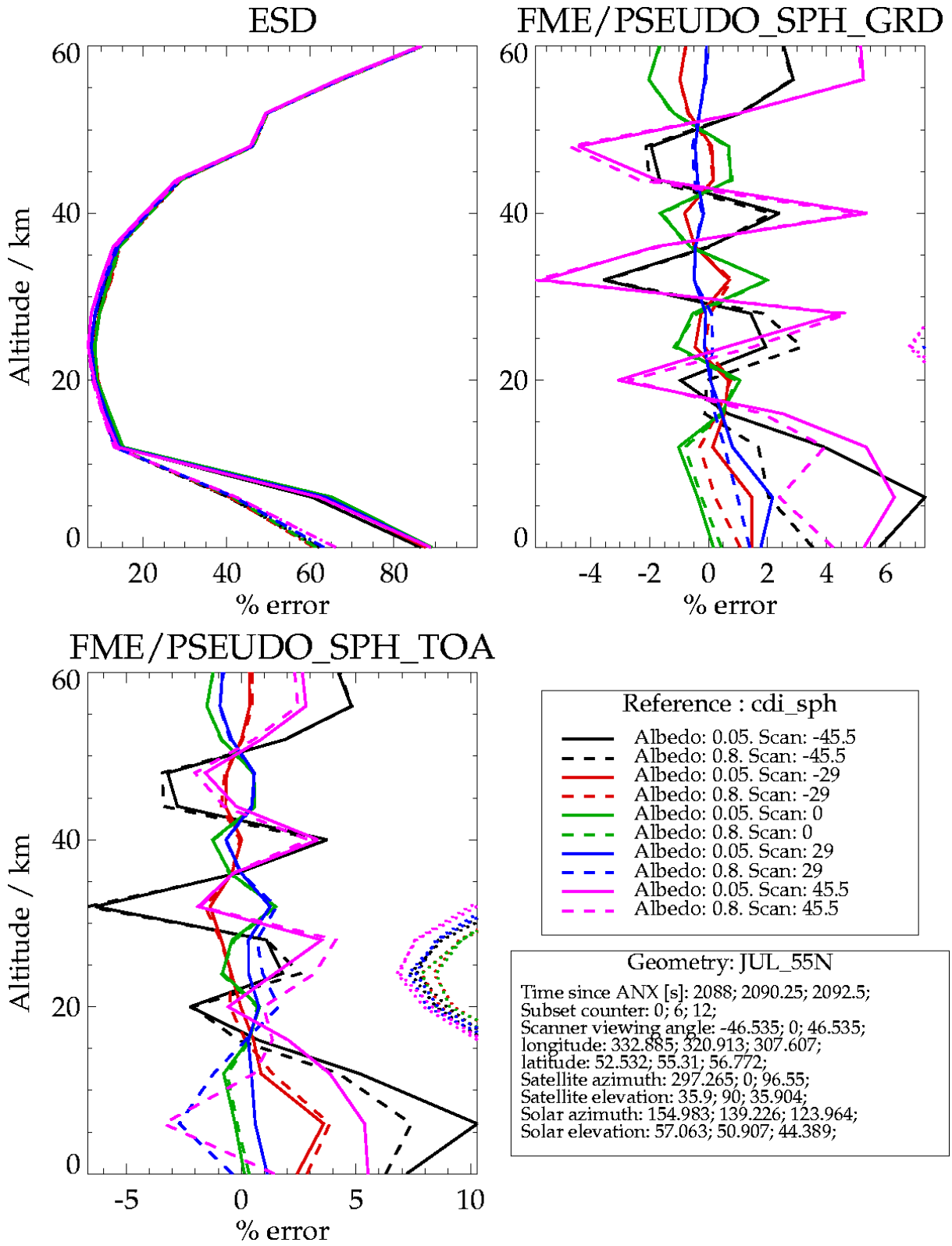

Figure 19-4: Pseudo-spherical approximation error using CDI weighting - Band 1 265-314 nm

Pseudo-spherical approximation error for July 55N, using CDI weighting functions
Band 1 coverage: 265-307 nm.
Dotted line in RSS panel shows associated ESDs

20 WP250: Earth Curvature and RTM Assumptions (IUP)

20.1 Introduction

Slant column errors related to refraction have been investigated using full-spherical modelling including refraction to simulate spectra for the reference fittings. Two aspects have been illuminated: first, fittings of full-spherical model spectra calculated by neglecting refraction, and second, when fitting pseudo-spherical spectra including refraction, which appeared to be of specific interest in this study.

20.2 Refraction

20.2.1 Results

Figure 20-1 and Figure 20-2 show the relative differences. Dashed lines indicate errors due to pseudo-spherical approximation, which are between –1% and 1% for the high solar zenith angle cases considered here. Neglecting refraction leads to errors of less then 0.3% for all considered gases and are therefore negligible. As a consequence, the question which spherical approximation to use for refraction modelling is answered as for GOME-2 geometries it is obsolete anyway. Consequently, the differences between pseudo-spherical and full-spherical simulations when including refraction (dotted lines) mainly reflect the differences when not accounting for reflection at all (see Section 19.2).

20.2.2 Conclusion

Even at large solar zenith angles and therefore long slant paths refraction effects on the direct transmission, i.e. slant column errors, are negligible.

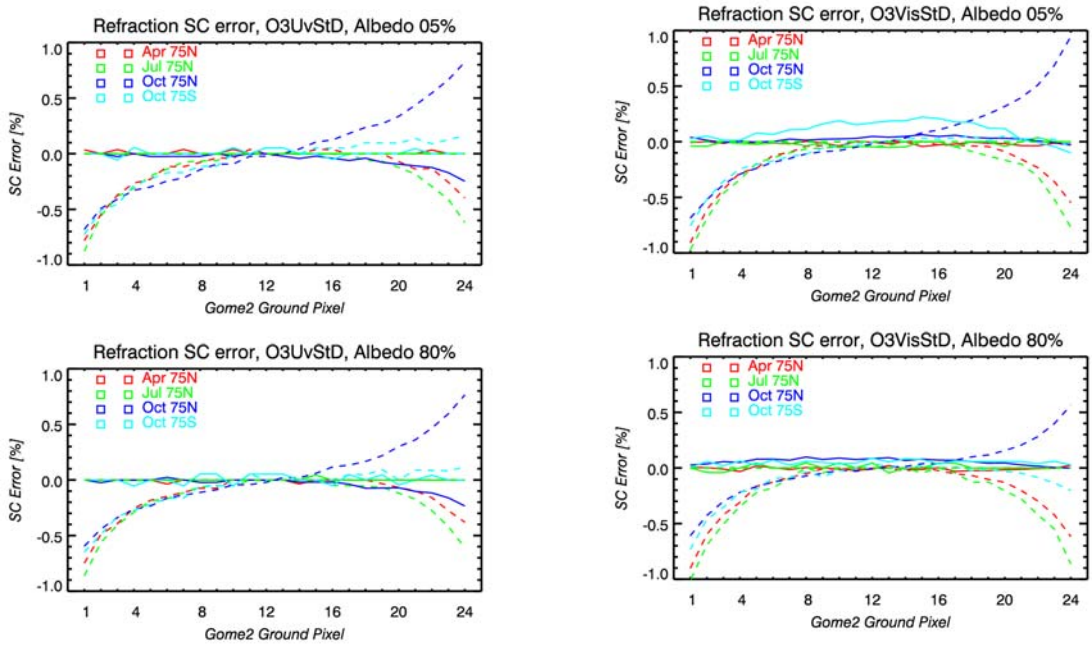

Figure 20-1: O_3 relative slant column errors referenced to fittings of full-spherical simulations including refraction for high SZA scenarios.

Solid: Full spherical w/o refraction.
Dashed: Pseudo-spherical including refraction.

Figure 20-2: NO_2 and BrO relative slant column errors referenced to fittings of full-spherical simulations including refraction for high SZA scenarios

Solid: Full-spherical w/o refraction (BrO errors rise up to more than 40%)
Dashed: Pseudo-spherical including refraction.

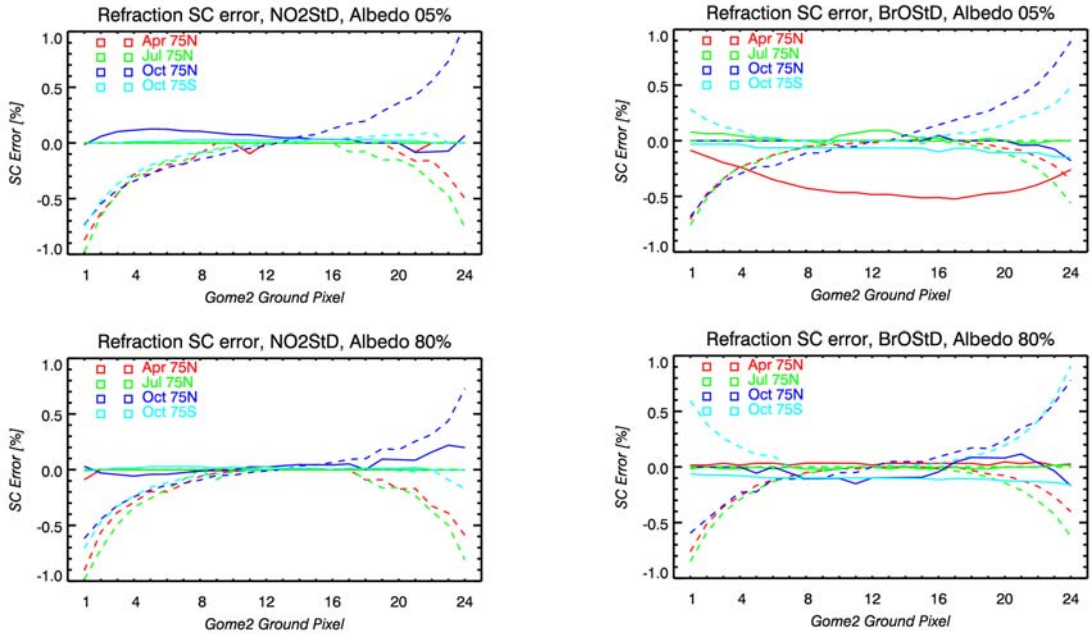

20.3 Pseudo-spherical approximation

20.3.1 Method and results

Pseudo-spherical approximations have been performed using CDI for all study scenarios. Two sets of geometrical parameters have been used for the pseudo-spherical mode, ground level and top-of-atmosphere (TOA), both calculated from geometrical parameters at satellite altitude (default input for CDI full-spherical mode). An example of simulations for Oct 75S, is given in Figure 20-3. Broadband and also differential ozone absorption structures can be clearly seen in the difference plot (bottom).

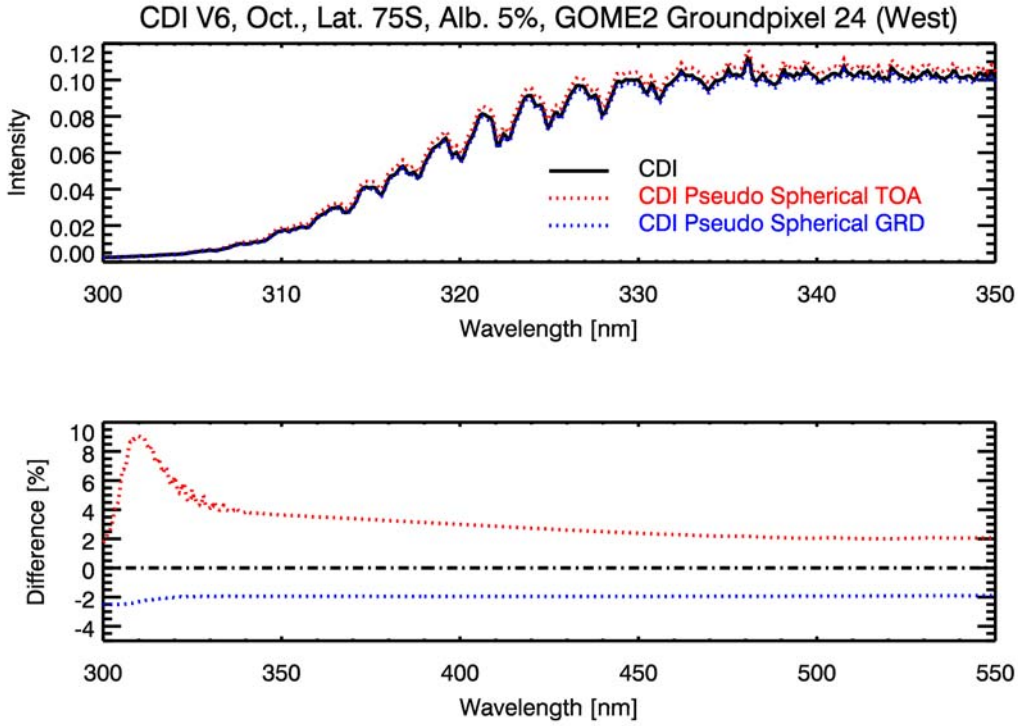

Figure 20-3: CDI intensities calculated using pseudo-spherical and full spherical mode.

Top: Intensities calculated using an identical scenario for TOA (red): top-of-atmosphere geometrical parameters, and GRD (blue): ground level geometrical parameters used in pseudo-spherical mode
Bottom: Percentage differences.

The consequences of these differences for DOAS trace gas retrieval are illustrated in Figure 20-4 to Figure 20-9 for O_3, NO_2 and BrO. Slant column retrievals from full-spherical simulations have been taken as references for percentage error estimates.

Errors are below 1% for all cases when using ground-level geometrical parameters. From ground pixel number 6 to 19 (+/- 23° LOS) errors are below about 0.2%. From ground pixel number 4 to 21 (+/- 31° LOS, GOME range) errors are below 0.4%. For TOA angles, errors can rise up to more than 4 to 7% and can be several percent even within the GOME range. This can be explained by multiple scattering contributions, which are most effective in the lower layers.

Table 20-1 gives an overview of maximum errors observed for both small (960 km) and large GOME-2 swath width (1920 km).

20.3.2 Conclusion

Using geometrical parameters calculated for ground level in pseudo-spherical simulations, leads to negligible slant column errors for O_3, NO_2, and BrO.

Season	Geom. for PS	Maximum Slant Column Error w.r.t fitting full-spherical spectra					
		O_3-UV %		NO_2 %		BrO %	
		960 km	1920 km	960 km	1920 km	960 km	1920 km
Jan	TOA	2.5	5.0	3.5	8.0	3.0	5.0
	GRD	0.3	1.0	0.3	1.0	0.3	1.0
Apr	TOA	1.0	2.0	1.5	2.7	1.0	2.0
	GRD	0.3	1.0	0.3	1.0	0.3	1.0
Jul	TOA	1.0	1.7	1.0	2.0	0.8	1.7
	GRD	0.3	1.0	0.3	1.0	0.3	1.0
Oct	TOA	2.0	3.5	4.5	10.0	2.5	3.5
	GRD	0.3	1.0	0.3	1.0	0.3	1.0

Table 20-1: Max Slant Column error w.r.t. fitting full-spherical spectra

Maximum slant column errors w.r.t. fitting full-spherical spectra
The error is due to the pseudo-spherical approximation

TOA and GRD geometry parameters used within:

(a) Small GOME-1 swath (960 km) (b) Large swath (1960 km).

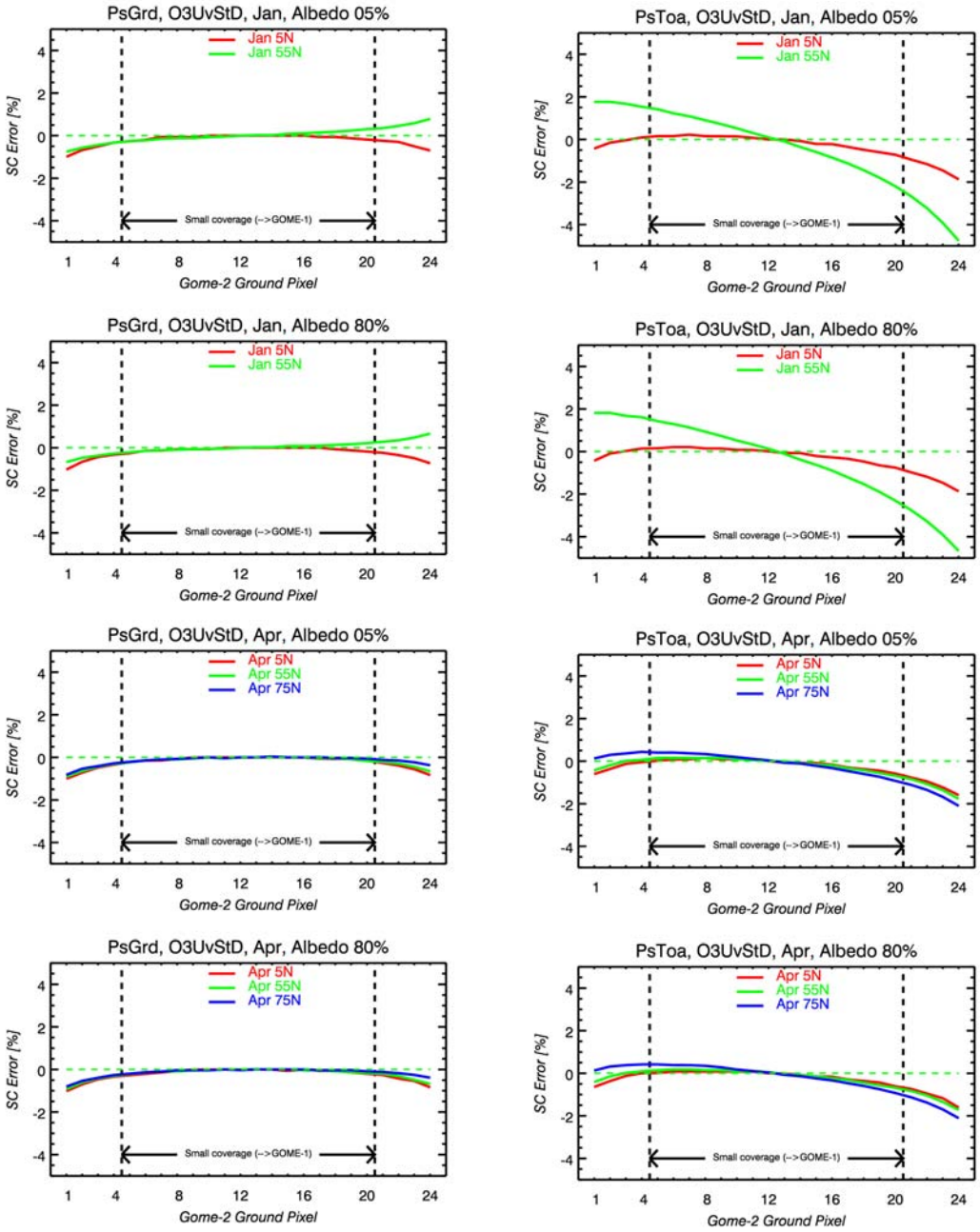

Figure 20-4: O_3 slant column errors due to pseudo-spherical approximation - Jan and Apr

Left: Ground level angles Right: TOA angles

Used for CDI pseudo spherical simulations (scales are different!)

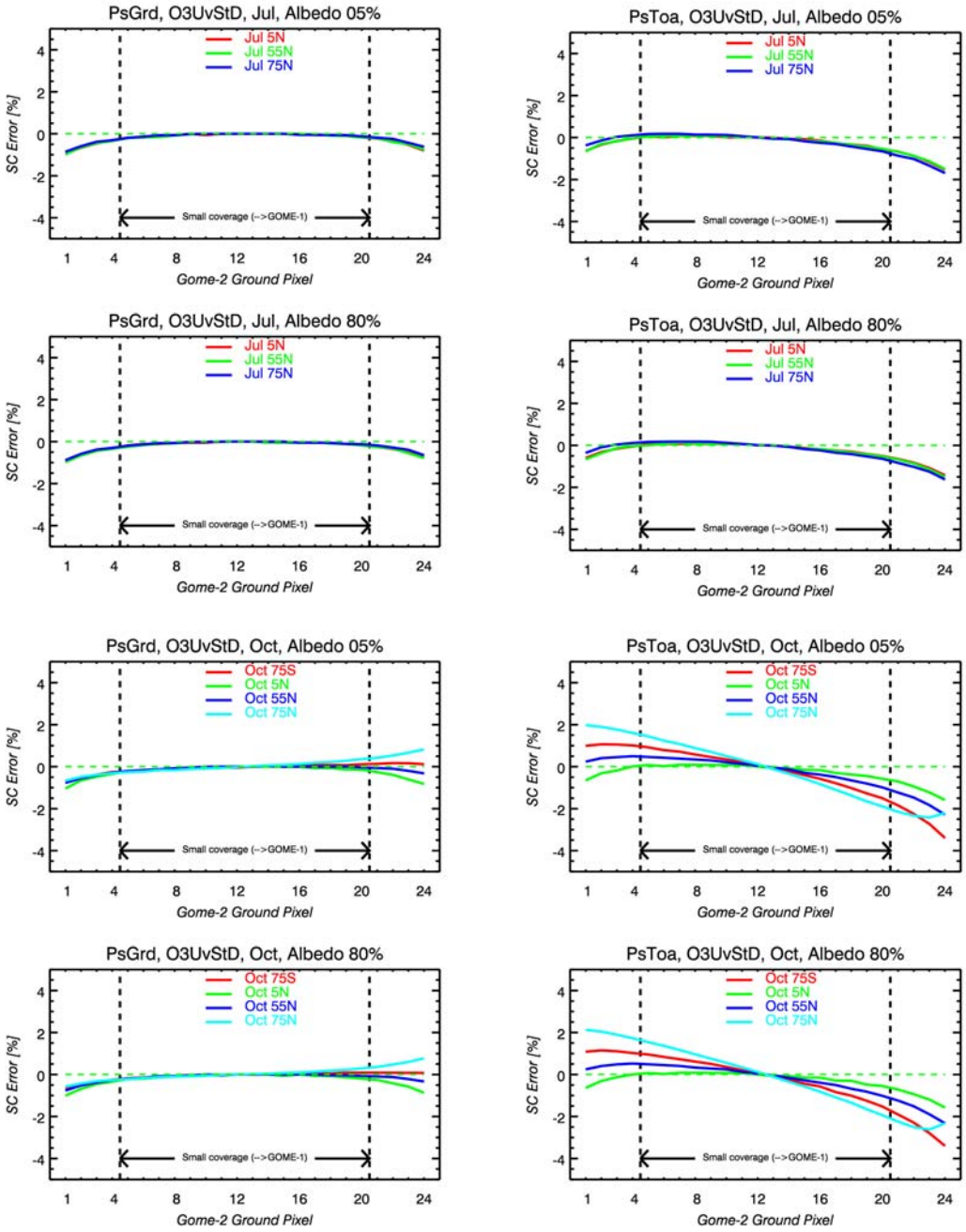

Figure 20-5: O_3 slant column errors due to pseudo-spherical approximation - Jul and Oct

Left: Ground level angles Right: TOA angles

Used for CDI pseudo spherical simulations (scales are different!)

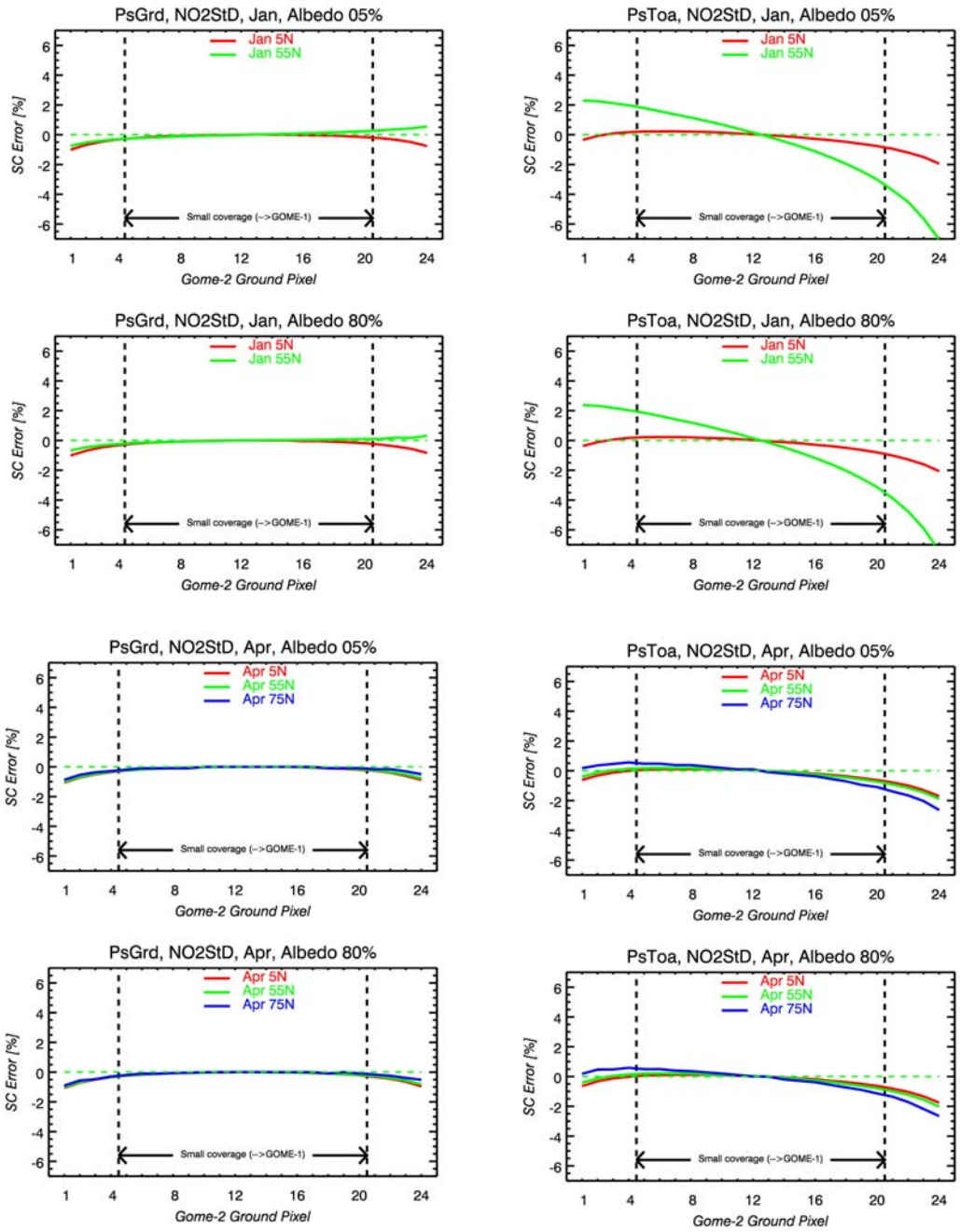

Figure 20-6: NO_2 slant column errors due to pseudo-spherical approximation - Jan and Apr

Left: Ground level angles Right: TOA angles

Used for CDI pseudo spherical simulations (scales are different!)

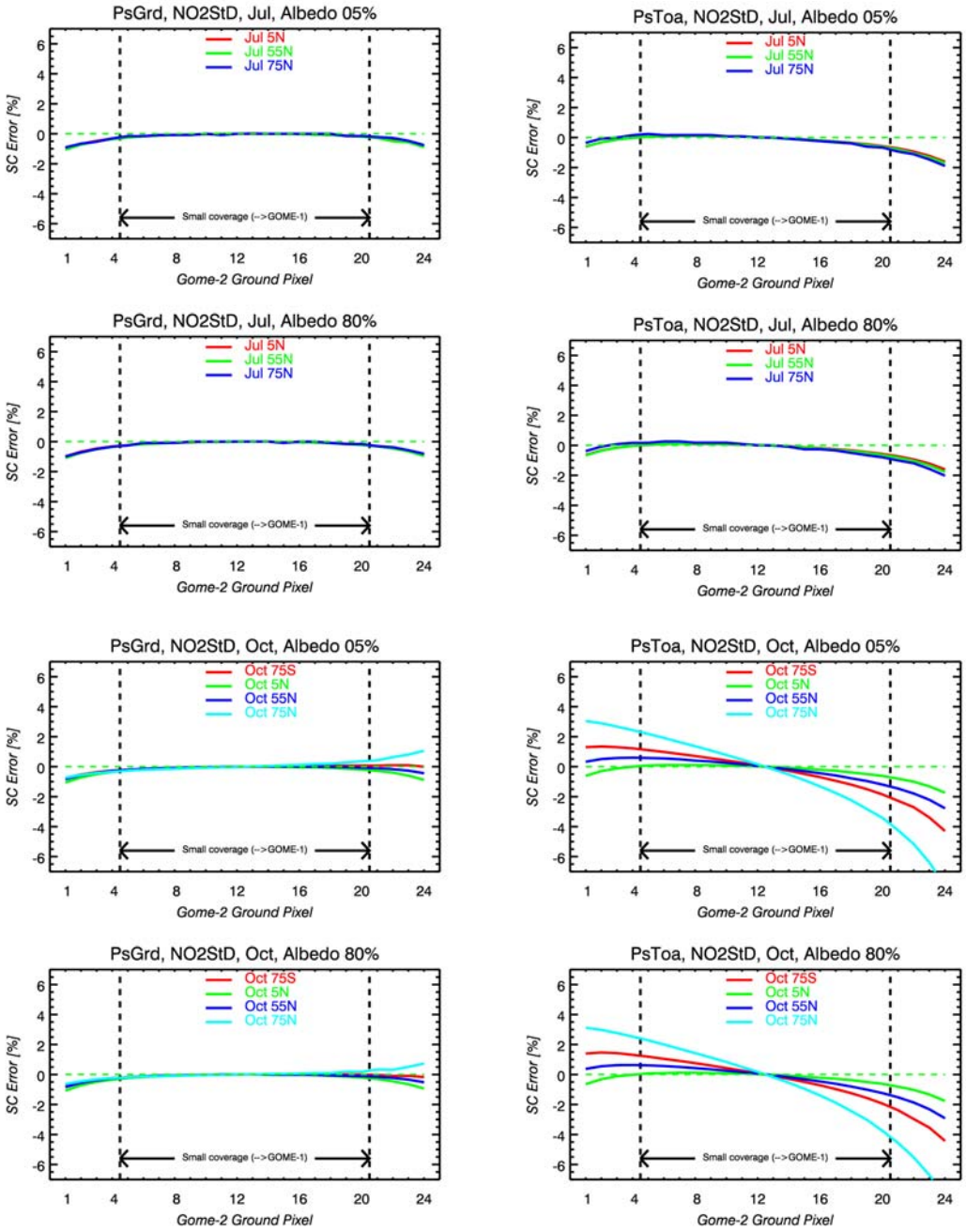

Figure 20-7: NO_2 slant column errors due to pseudo-spherical approximation - Jul and Oct

Left: Ground level angles Right: TOA angles

Used for CDI pseudo spherical simulations (scales are different!)

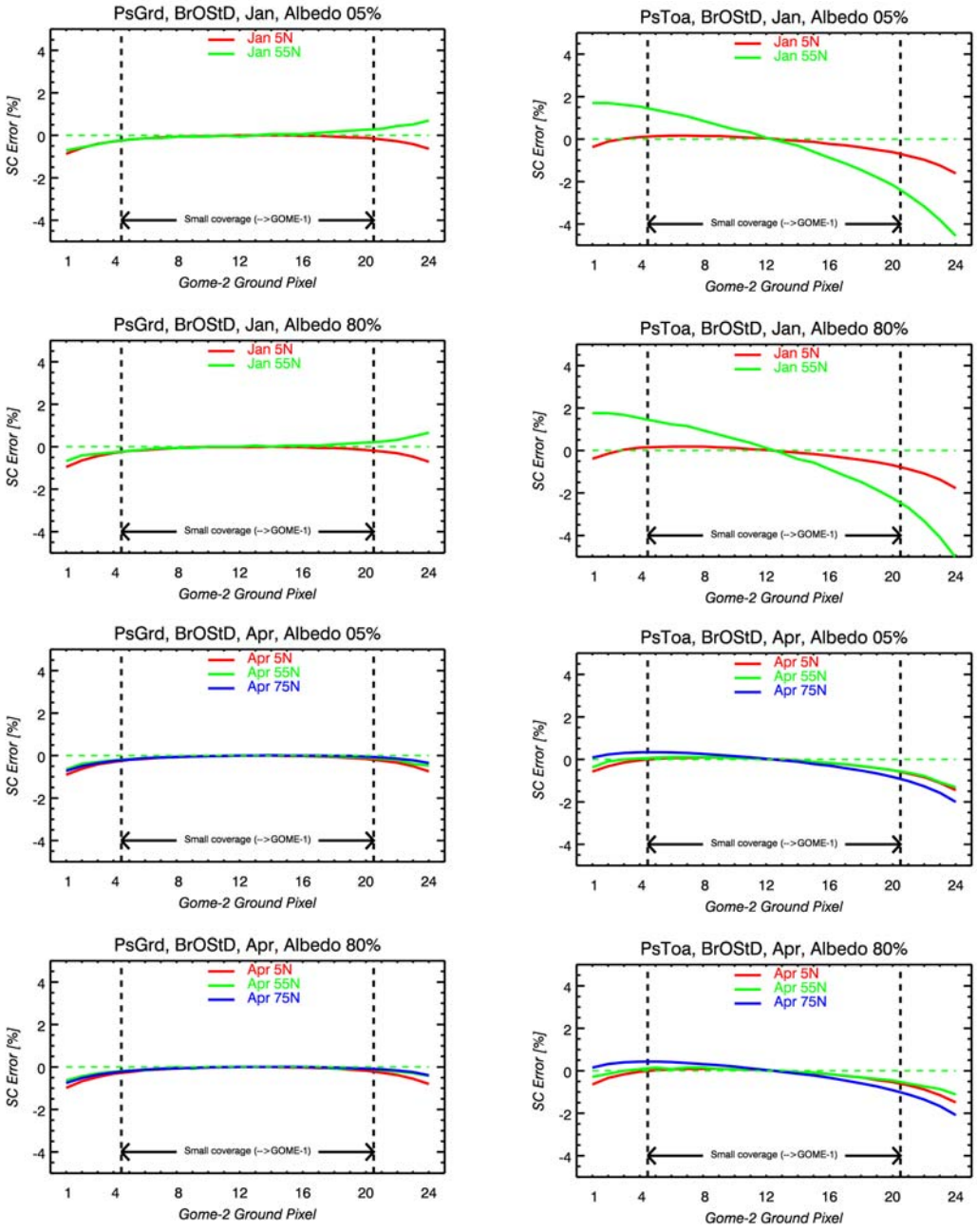

Figure 20-8: BrO slant column errors due to pseudo-spherical approximation - Jan and Apr

Left: Ground level angles Right: TOA angles

Used for CDI pseudo spherical simulations (scales are different!)

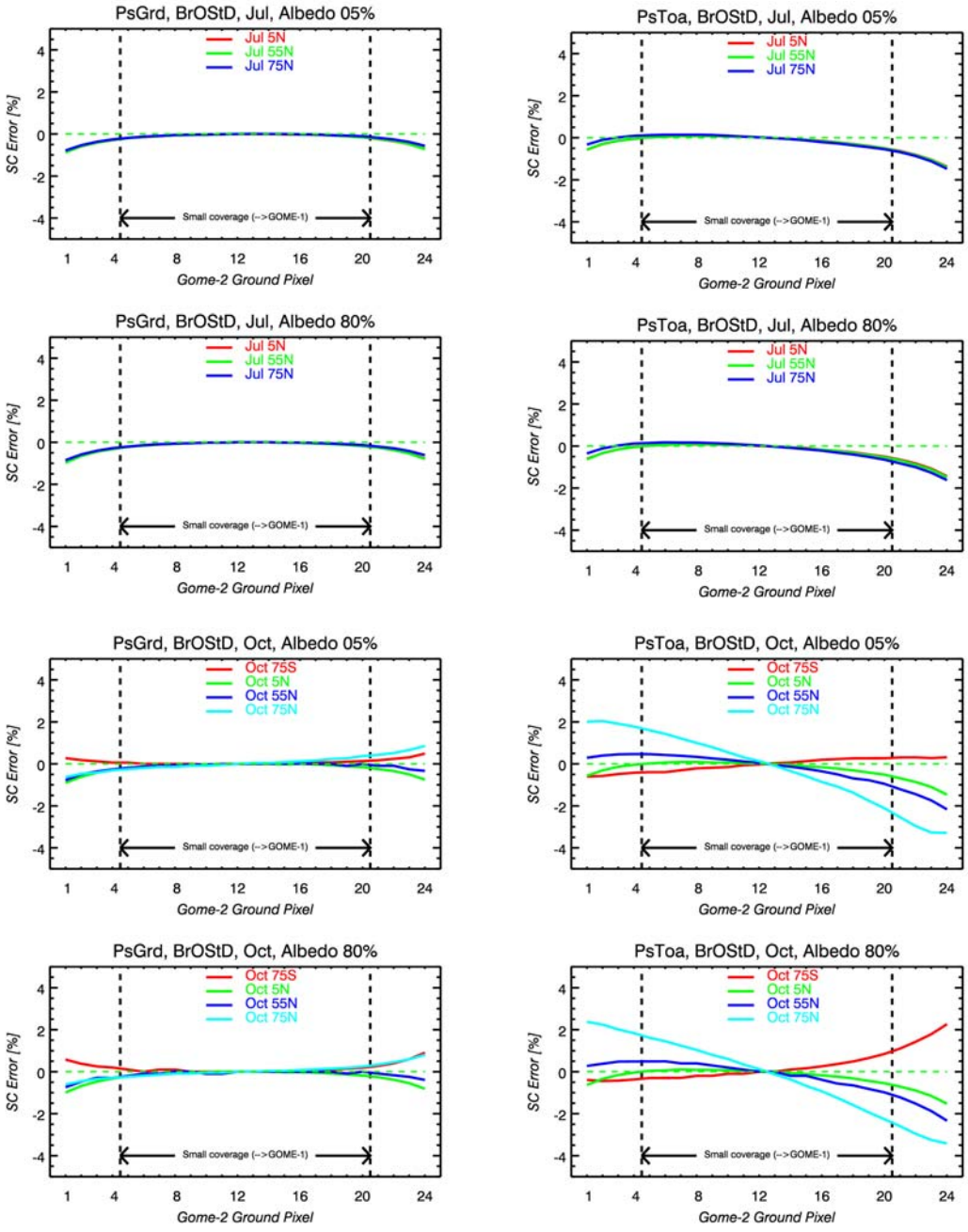

Figure 20-9: BrO slant column errors due to pseudo-spherical approximation - Jul and Oct

Left: Ground level angles Right: TOA angles

Used for CDI pseudo spherical simulations (scales are different!).

21 WP260: Non-Lambertian Surface Reflectance and BRDF (IUP)

21.1 Method and results

The influence of the surface reflection was investigated comparing the outgoing radiation simulated considering a bi-directional surface reflection and assuming a Lambertian surface reflection. The bi-directional reflectance distribution function for surface types "bright" and "dark" was simulated according to RPV model. For "snow" surface type a modified RPV model was used. The ocean reflectance was modelled as described by Cox and Munk (1954). The corresponding Lambertian albedo was calculated as follows (Popp, 1995):

$$A = \frac{\int\int\int\int \rho(\mu,\varphi,\mu',\varphi')\,\mu\mu'\,d\mu,\,d\varphi,\,d\mu',\,d\varphi'}{\int\int\int\int \mu\mu'\,d\mu,\,d\varphi,\,d\mu',\,d\varphi'}$$

All calculations were performed for April 55N. A solar zenith angle of 49.5° was selected. Figure 21-1 to Figure 21-4 show the comparison results for "bright", "dark", "snow", and "ocean" surface types respectively. The upper and middle plots are polar plots showing the outgoing radiation at the top of the atmosphere simulated assuming bi-directional and Lambertian surface reflectance, respectively. Here, the radial coordinate corresponds to the zenith angle and the angular coordinate to the azimuth angle. The calculations were performed at 550 nm. The lower plots show the outgoing radiation at the satellite position as function of viewing geometry and wavelength. The zenith and azimuth angles were selected according to realistic scan geometry appropriate to the selected scenario.

A special ocean glint BRDF effect on intensities is shown in Figure 21-5. In this case the April 5N scenario was selected and the relative azimuth was selected to be 0° and 180°, which means that the GOME-2 scan goes through the hot spot. Intensity errors can reach up to 50% as compared to the Lambertian equivalent albedo case.

In order to investigate the sensitivity of NO_2 air mass factors to the surface reflectance, the "ocean" surface type was selected which leads to the largest errors in the intensity of the outgoing radiance apart from the ocean glint case. As clearly seen in Figure 21-6, the difference between the air mass factors for the bi-directional and Lambertian surface reflectance is always below 0.4%.

Figure 21-7 shows the absolute difference between differential spectra of the logarithms of the outgoing radiation as used in DOAS retrieval calculated for the bi-directional and Lambertian surface reflectance.

Finally, Figure 21-8 shows slant column errors for all considered surface types and trace gases. Retrievals from BRDF simulations have been taken as reference. Errors are below 0.7% except for OClO. Ocean glint can lead to errors of up to 3%.

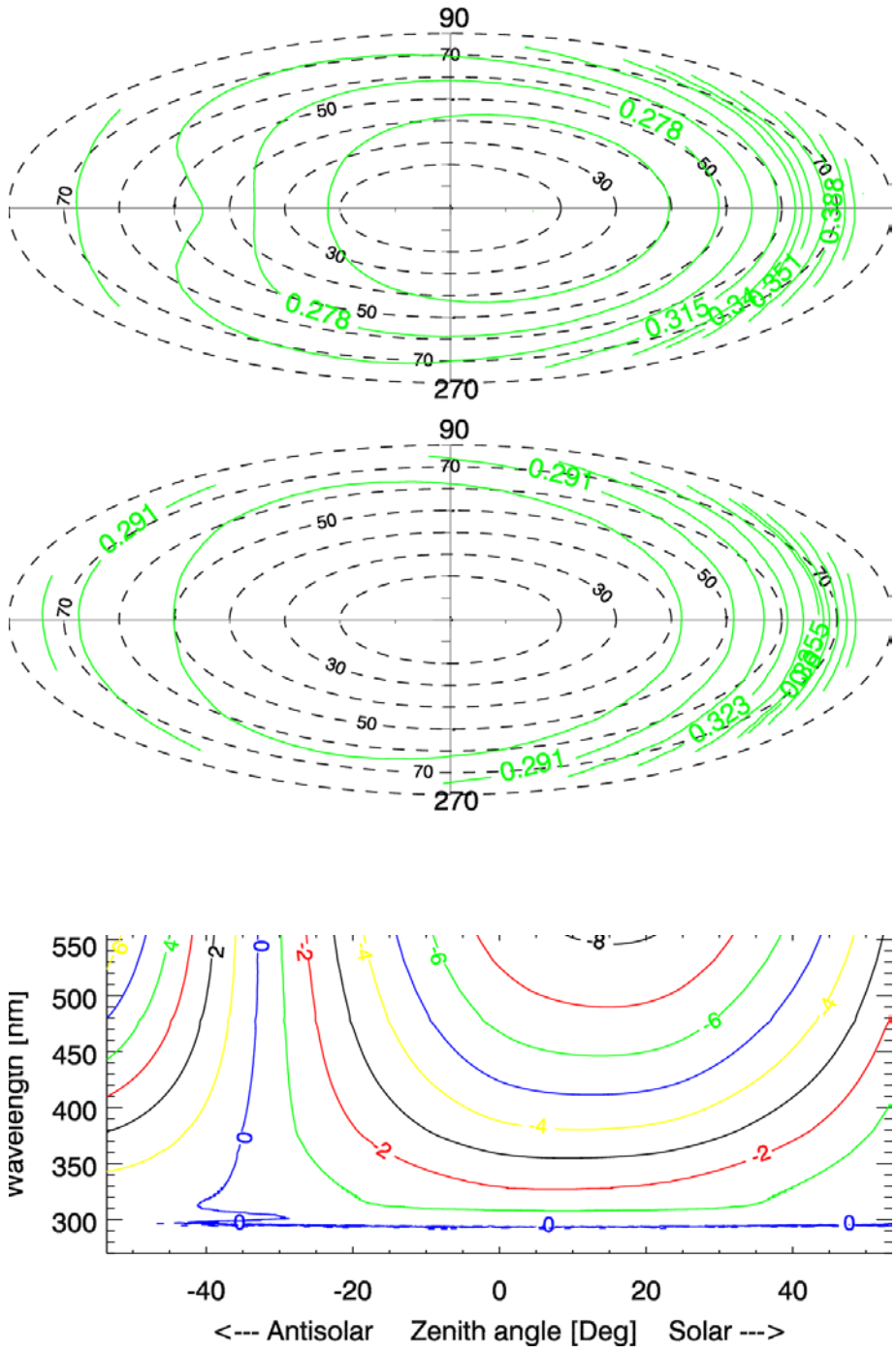

Figure 21-1: BRDF Surface type – "bright"

Top and middle (polar plots): Outgoing radiation at TOA as function of zenith angle and azimuth angle at 550 nm calculated using bi-directional and Lambertian surface reflectance, respectively

Lower plot: Relative percentage difference ([Lambertian/BRDF - 1] x 100) as function of viewing geometry and wavelength

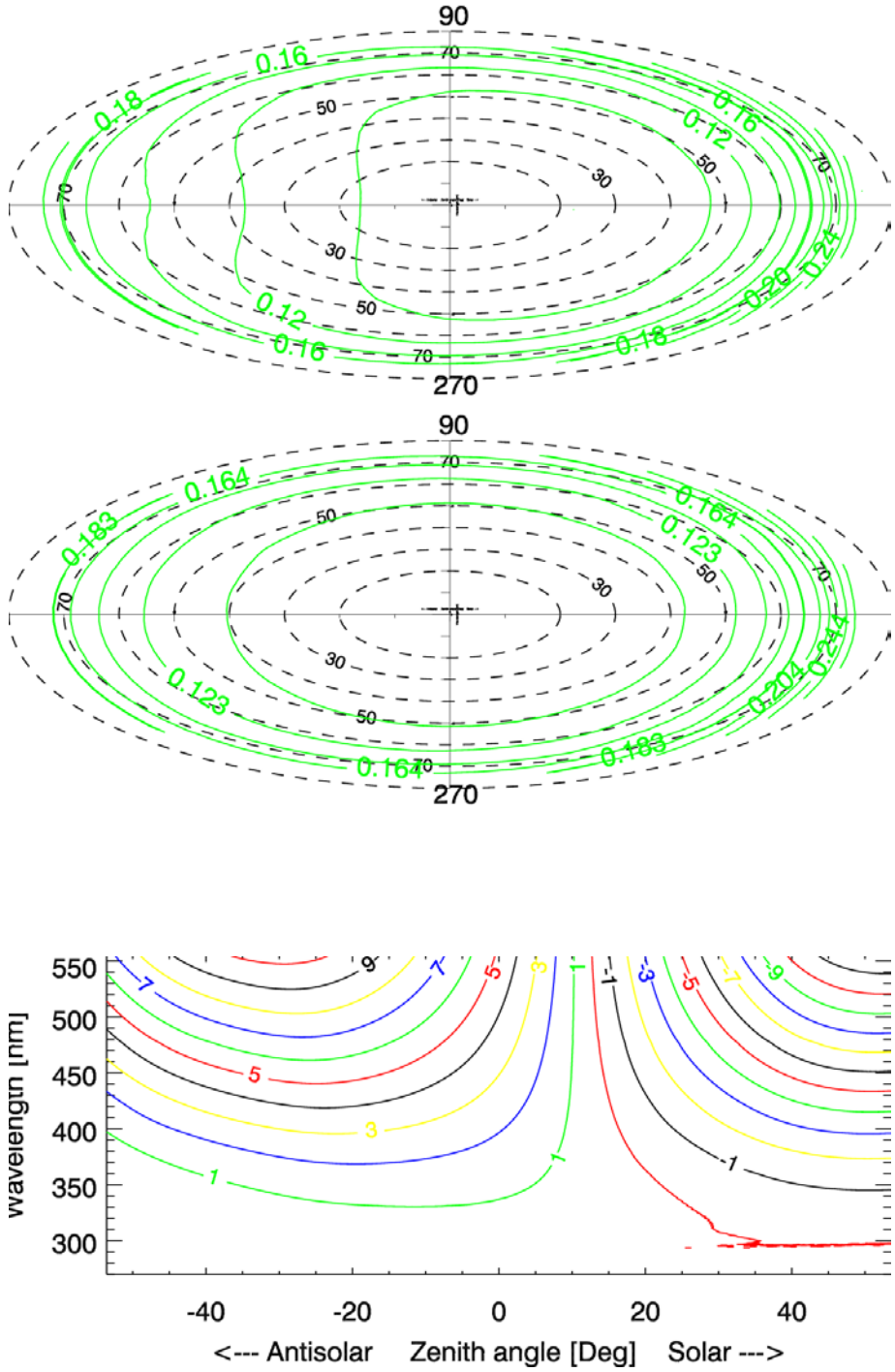

Figure 21-2: BRDF Surface type – "dark"

Top and middle (polar plots): Outgoing radiation at TOA as function of zenith angle and azimuth angle at 550 nm calculated using bi-directional and Lambertian surface reflectance, respectively

Lower plot: Relative percentage difference ([Lambertian/BRDF - 1] x 100) as function of viewing geometry and wavelength

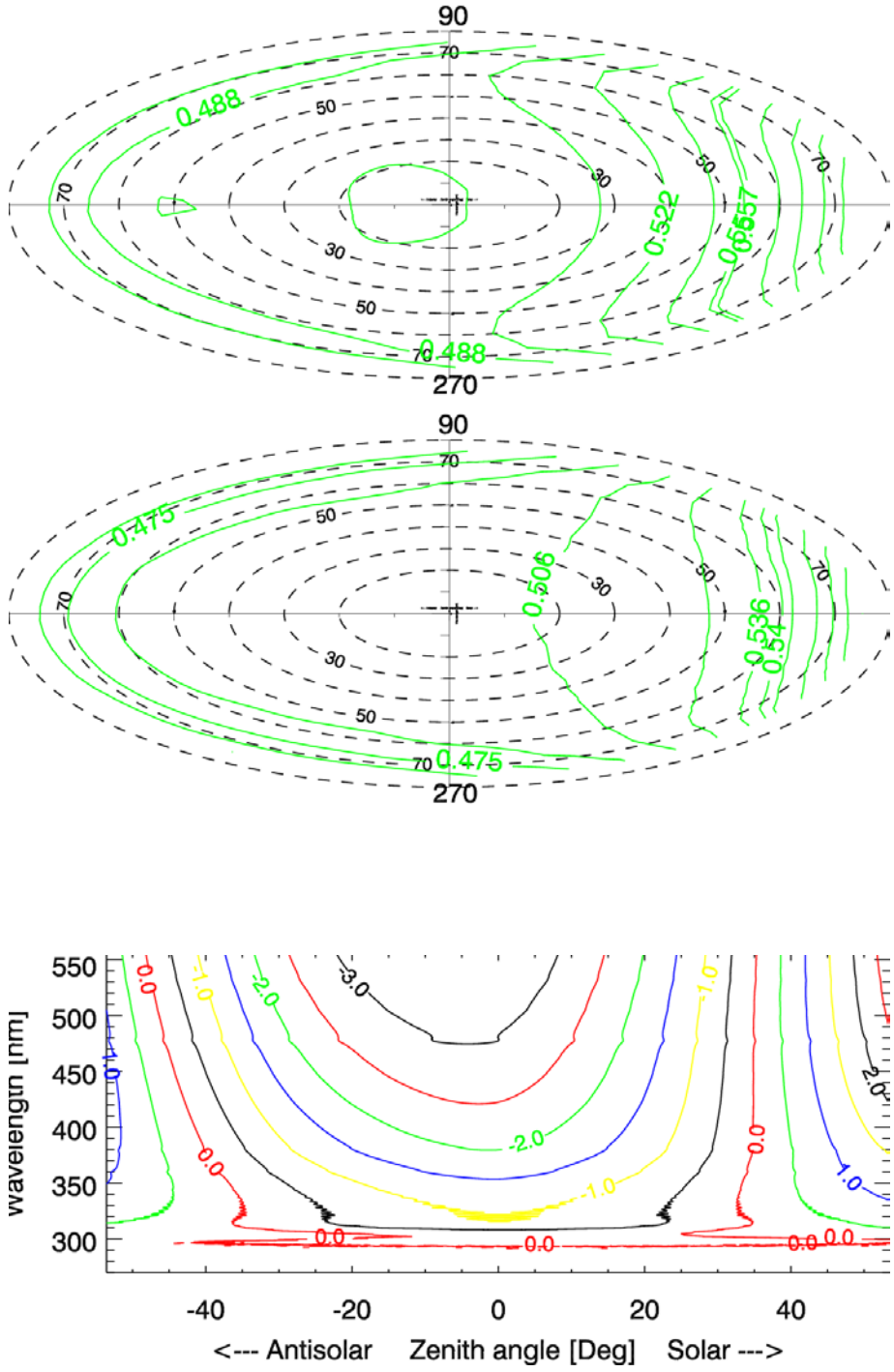

Figure 21-3: BRDF Surface type – "snow"

Top and middle (polar plots): Outgoing radiation at TOA as function of zenith angle and azimuth angle at 550 nm calculated using bi-directional and Lambertian surface reflectance, respectively

Lower plot: Relative percentage difference ([Lambertian/BRDF - 1] x 100) as function of viewing geometry and wavelength

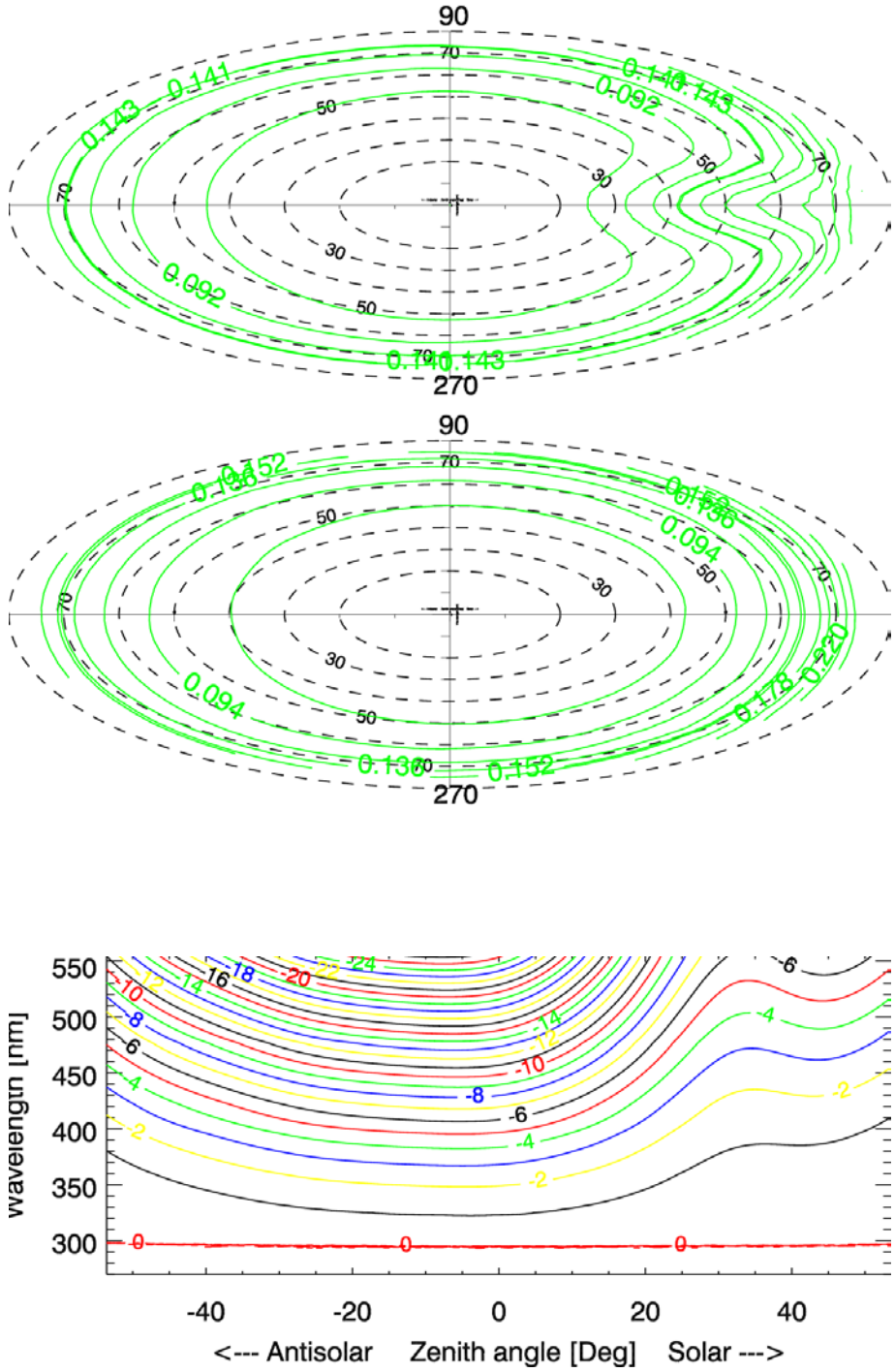

Figure 21-4: BRDF Surface type – "ocean"

Top and middle (polar plots): Outgoing radiation at TOA as function of zenith angle and azimuth angle at 550 nm calculated using bi-directional and Lambertian surface reflectance, respectively

Lower plot: Relative percentage difference ([Lambertian/BRDF - 1] x 100) as function of viewing geometry and wavelength

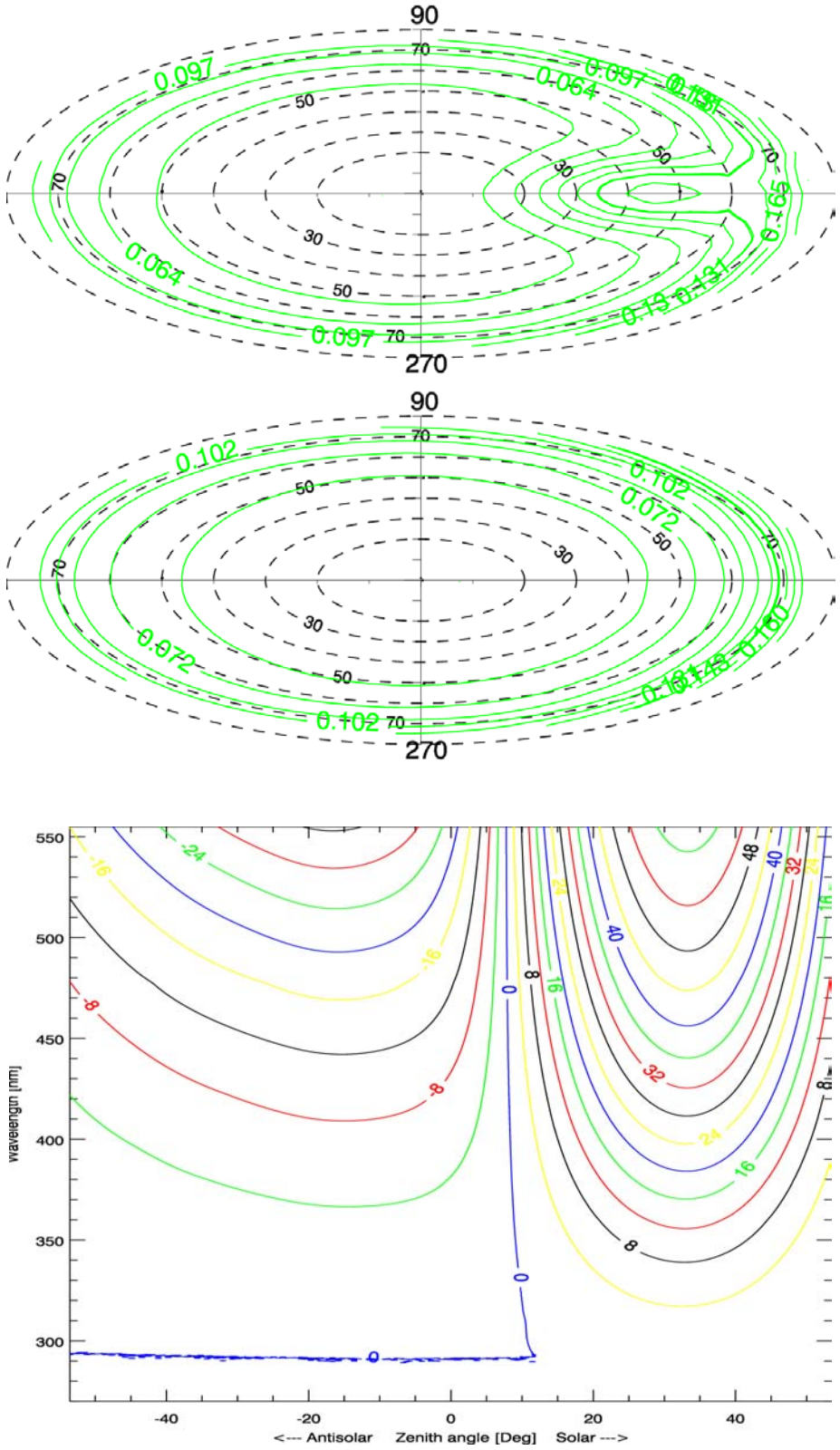

Figure 21-5: BRDF Surface type – "ocean-glint"

Top and middle (polar plots): Outgoing radiation at TOA as function of zenith angle and azimuth angle at 550 nm calculated for April 5N using bi-directional and Lambertian surface reflectance, respectively

Lower plot: Relative percentage difference ([Lambertian/BRDF - 1] x 100) as function of viewing geometry and wavelength

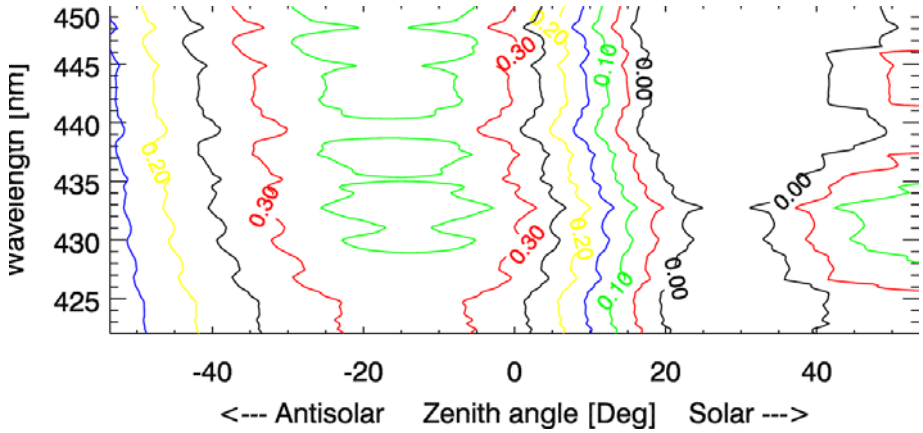

Figure 21-6: AMF differences for NO_2

Relative percentage difference between NO_2 air mass factors calculated for the bi-directional and Lambertian surface reflectance ([Lambertian/BRDF - 1]*100) as function of viewing geometry and wavelength

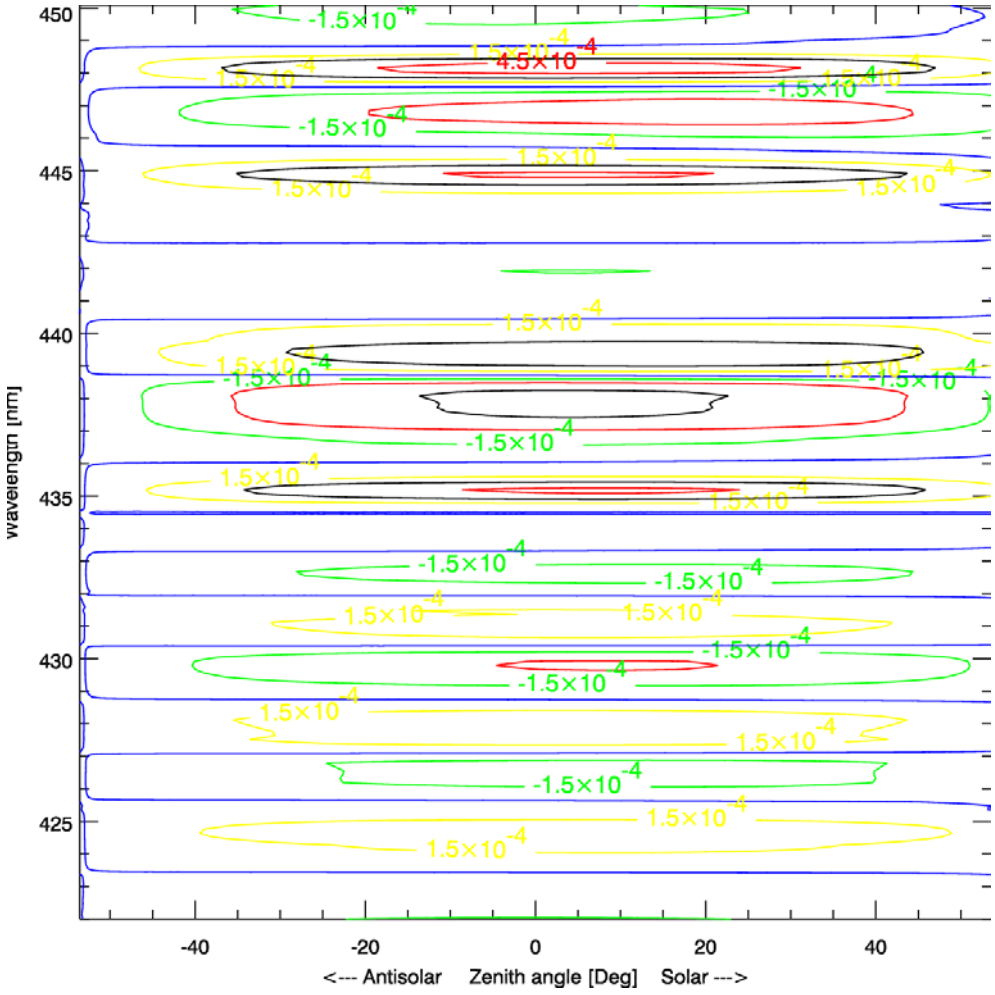

Figure 21-7: AMF differences for NO_2

Absolute difference between differential spectra simulated for the bi-directional and Lambertian surface reflectance as function of viewing geometry and wavelength

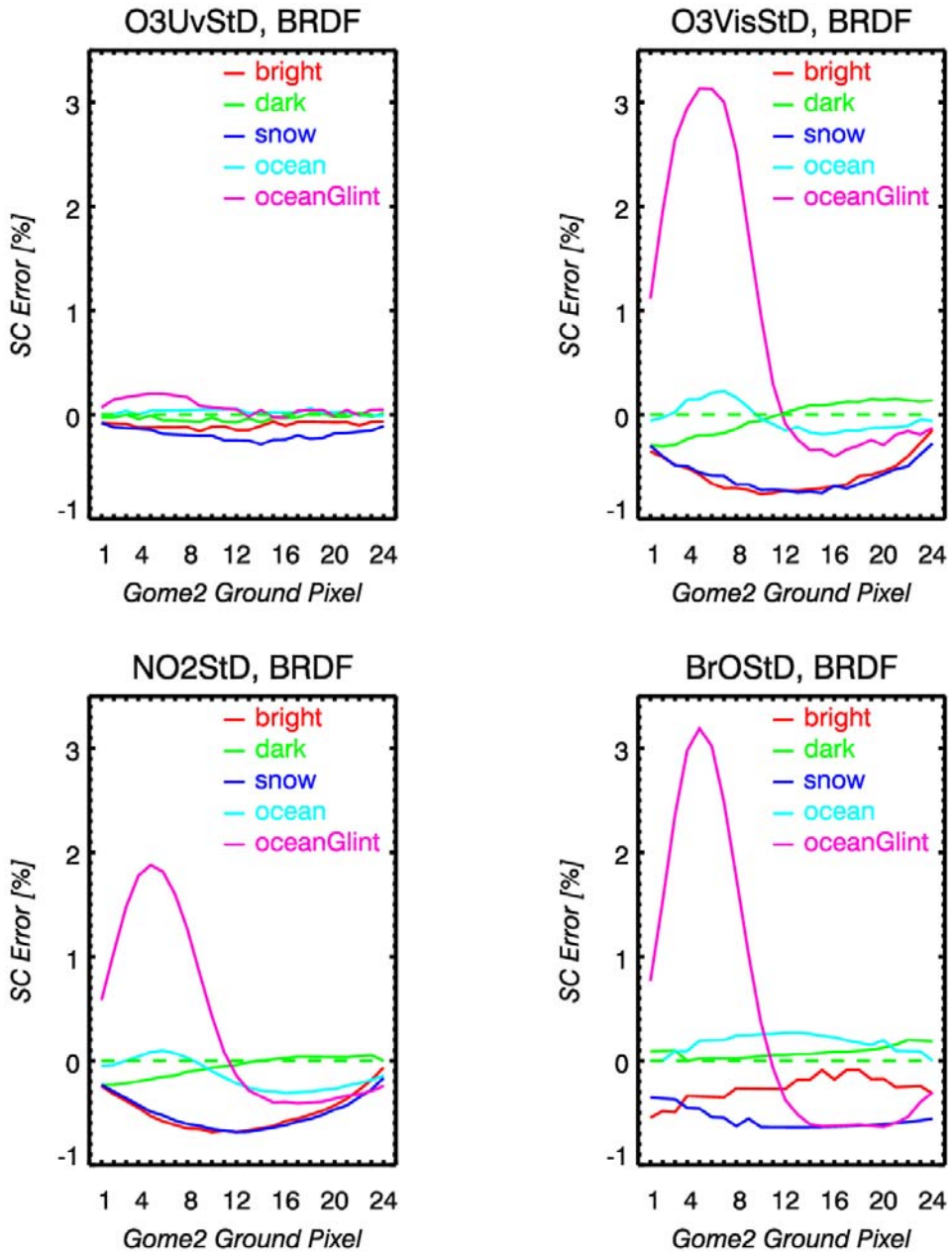

Figure 21-8: Slant column errors for all trace gases considered due to Lambert-equivalent reflection relative to BRDF simulations.

Relative slant column difference between fittings of differential spectra simulated for the Lambertian and bi-directional surface reflectance.

Spectra have been simulated for April 55N and April 5N (ocean glint, $0^o/180^o$ relative azimuth).

21.2 Conclusions

For the mid-latitude scenario (Apr. 55N), the error due to negligence of the BDRF is below 0.5%. Largest errors are generally observed for the snow-covered scenes. For the tropical scenario (Apr. 5N, ocean-glint) errors for NO_2, BrO, and O_3-vis are more significant (2%, 3%, and >3%, respectively). Potential improvement can be achieved by using appropriate AMF calculated using effective Lambertian albedos derived from the spectra directly, e.g. averaging reflectivity over the individual ground pixel. One should again keep in mind here that the errors are not in the slant column retrieval but will be caused by assumptions in the albedo to be applied in the RTM to calculate the AMF.

21.3 References

[21-1] Cox, C., and W. Munk, "Measurement of the Roughness of the Sea Surface from Photographs of the Sun's Glitter", J. Opt. Soc. Am., 44, 838-851, 1954

[21-2] Popp, T., "Correcting atmospheric masking to retrieve the spherical albedo of land surfaces from satellite measurements", Int. J. Remote Sensing, 16, 3483-3508, 1995

22 WP260: Non-Lambertian Surface Reflectance and BRDF - Impact on Ozone Profile Retrievals (RAL)

22.1 Retrieval formulation

The quantification of impact of the Lambertian surface assumption in the O_3 profile retrieval is not obviously amenable to the standard linear approach adopted for other errors sources since the main impact of the BRDF is to change the apparent surface albedo seen at the specific solar/viewing geometry of a given measurement. It can be anticipated that, to a large degree, this surface albedo perturbation would be accommodated by the profile retrieval scheme (which fits albedo in a non-linear manner). This "apparent" albedo is not straightforward to define since it depends on the specific viewing geometry. Hence it is also not obvious what to use as the appropriate linearisation point about which to estimate the mapped effect of more subtle differences introduced "true" BRDF (on layer photon path lengths).

To avoid the problem of defining the linearisation point, a quasi-non-linear retrieval (as per WP210) is adopted:

1. CDI spectra for the five cases described above (bright land, dark land, ocean, snow, ocean with sun-glint) define the measurements. Note due to the computational expense of these calculations, spectra are only available for one geo-temporal scenario (April 5N for the sun-glint case and April 55N for all others).
2. CDI calculated spectra for a range of Lambertian surface albedos (sampling at intervals of 0.1 from 0.1 to 0.9, plus the Lambert-equivalent albedos for each surface type), are taken to define a look-up-table (LUT) of sun-normalised radiance vs. albedo.
3. A similar LUT of weighting functions for all retrieved parameters for the 3-step retrieval is constructed using GOMETRAN++, linearised at the same set of albedos.
4. A quasi-nonlinear ozone profile retrieval is performed (as in WP210). In this minimization, the forward model spectra are formed by linearly interpolating the CDI LUT to the iteratively fitted surface albedo. Measurement perturbations due to the other fitter parameters in the 3-step retrieval are formed using the interpolated GOMETRAN++ weighting function LUT. I.e. the retrieval is linear in all parameters other than surface albedo.
5. After convergence of the 3-step retrieval, the difference between the fitted O_3 and the true profile is taken as the error introduced by the Lambertian surface approximation in retrieval model FM.

Ideally CDI (Lambertian) weighting function would, of course, be used in this analysis: any inconsistencies between the GOMETRAN++ weighting functions and the CDI intensities might potentially lead to convergence problems, however the minimum of the cost function (if found) should be insensitive to the weighting functions used and depend only on the "measured" and modelled intensity spectra (which both come from CDI and are only different, as intended, in their treatment of the surface reflectance). In practice no problems were found with convergence, so the estimated errors, based on can be considered as robust.

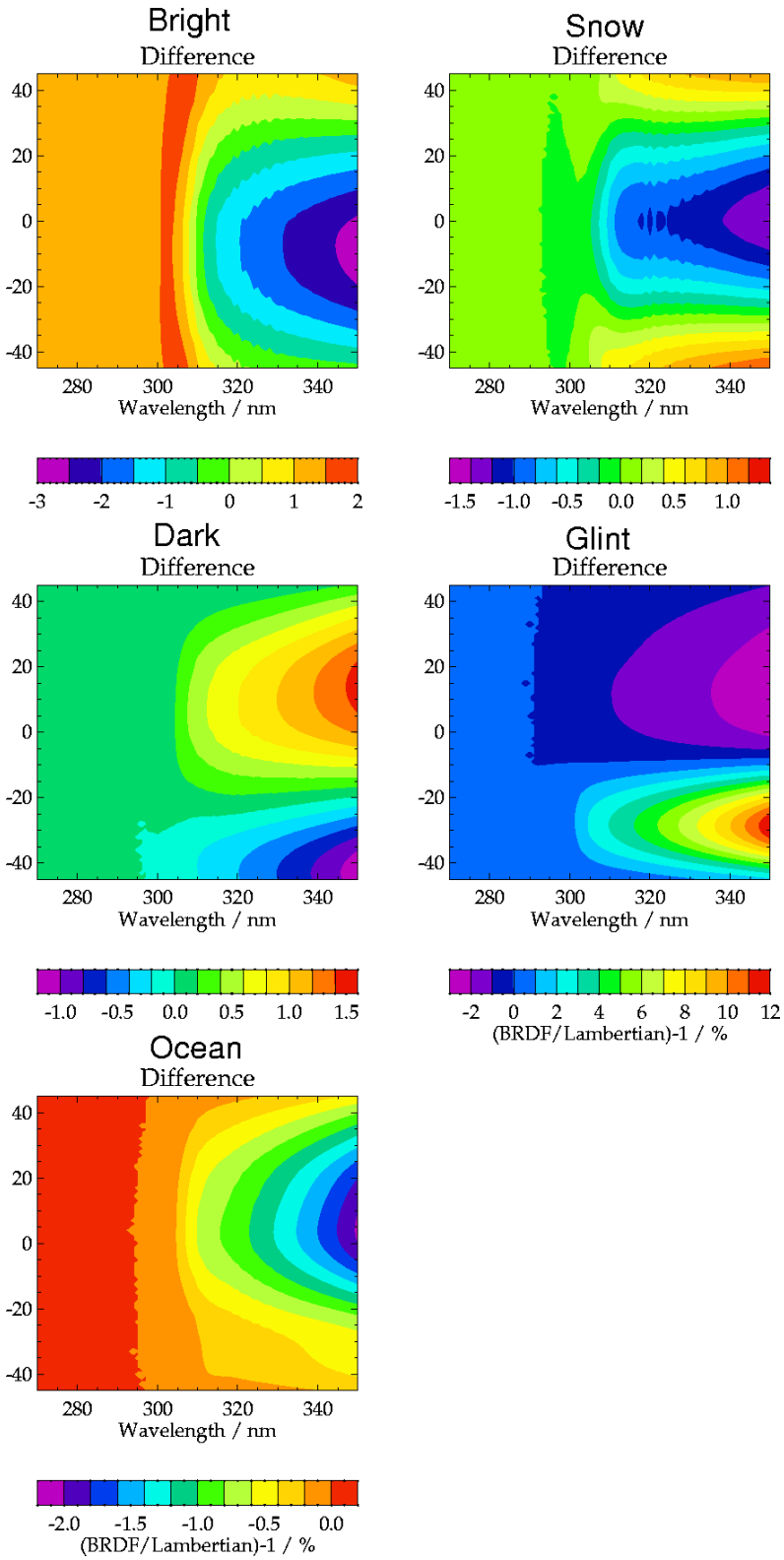

Figure 22-1: CDI simulated BRDF/Lambertian spectral differences as function of x-track scan angle

Plots of CDI simulated BRDF/Lambertian spectral differences as a function of across track scan angle for the "bright", "snow", "dark", "glint" and "ocean" surface cases

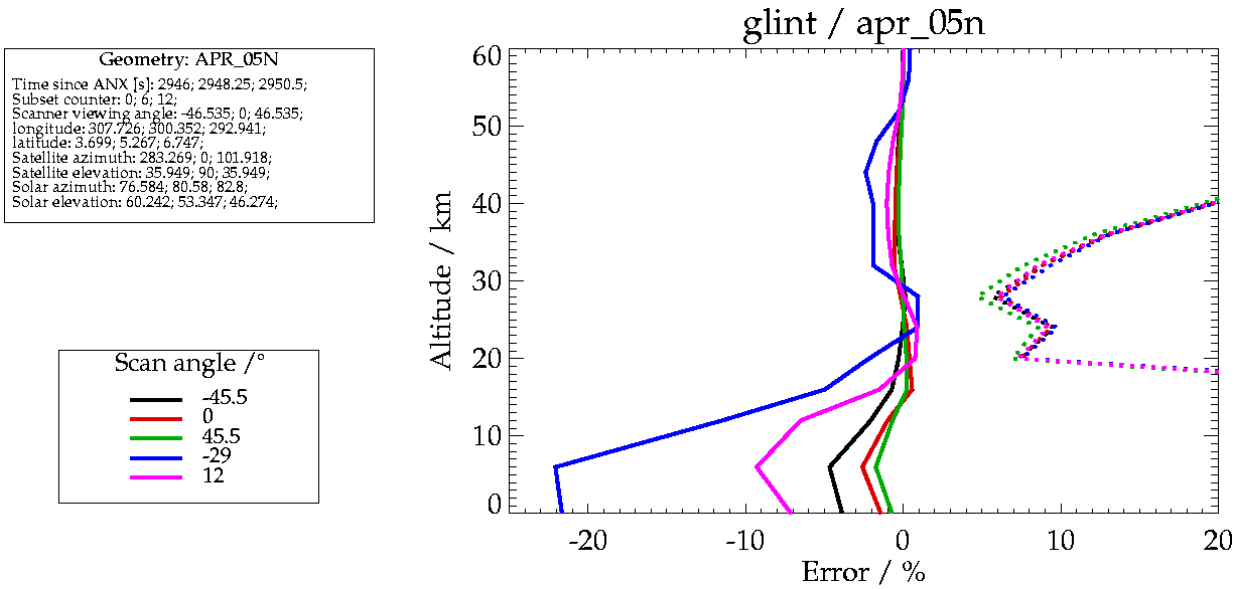

Figure 22-2: Retrieval simulations showing impact of Lambertian BRDF

Retrieval simulation results showing impact of Lambertian BRDF assumption for April 5N "glint" scenario for Band 1 wavelength range 265-307 nm. Solid lines indicate quasi-nonlinear mapped errors for 5 scan angles (nadir, extreme of 1920 km swath, plus two case-specific angles corresponding to the maximum and minimum spectra difference in the mapped signature at 340 nm). Dotted lines indicate the corresponding ESDs.

22.2 Results

Figure 22-1 shows the spectral differences between CDI simulations with and without the Lambertian albedo assumption for the 5 scenarios. (Figures B6.1.1 and B6.1.4 in Appendix B show sun-normalised radiance simulated with CDI and those simulated at the case-specific Lambert-equivalent albedo, together with the relative difference). Since the difference (and by implication magnitude of the associated errors) does not always peak at the edge of the 1920 km swath (+/-45.5° scanner angle), it is not adequate in this case only to simulate profile retrieval errors at nadir and extreme swath angles. So, in each case, two additional angles have been selected corresponding to the angles at which the maximum and minimum in the relative difference at 350 nm is reached.

Corresponding errors in the ozone profile retrieval are shown in Appendix B in Figures B6.1.2 and B6.1.5 (Band 1 - 265-307nm) and Figures B6.1.3 and B6.1.6 (Band 1 - 265-314nm).

Errors are less that 7% in all cases excepting the glint scenario, where errors exceed 20% in the troposphere. The glint scenario is shown in Figure 22-2,.

22.3 Sun-glint distribtion for GOME-1 and GOME-2

Given the relatively large magnitude of the mapped error due to sun-glint, and that the single scenario simulated may not necessarily represent the worst case encountered by GOME-2, the ocean reflectivity model used to construct the glint BRDF [21-1], was applied to calculate reflectivity for the direct sun-surface-observer geometry along four GOME-2 orbits, corresponding to 15 January, April, July and October (provided by ESTEC, based upon the GOME-2 orbit propagator). The quantity calculated is the Lambertian reflectance, which would result in the same observed radiance (neglecting the atmosphere) as the true BRDF for the specific line of sight and solar geometry. The same calculation is performed for the ERS-2/GOME-1 orbit geometry (1 hour later local time). Even in this case, data for a hypothetical 1920 km swath is plotted. The nadir point and extent of the 960km swath are indicated.

Figure 22-3 shows results for three wind speeds (1, 5 and 10ms^{-1}), assuming the April solar geometry and Figure 22-4 shows the seasonal variation for the 5ms^{-1} case. (Figures B6.2.1-B6.2.4 in Appendix B show results the 3 wind-speeds for all 4 months). Also shown in the figures are across-track cross-sections through the point of maximum reflectance, to illustrate the shape of the reflectance function more clearly, and to compare the maximal cases for each month to the tropical April scenario, simulated in the CDI calculations and through retrieval. Note that although the nominal latitude of the simulated scenario does not coincide with the April glint maximum, the relative azimuth was modified (to be 180/0 depending on scan direction relative to nadir) to ensure a maximal glint effect.

Figure B6.2.5 shows a colour composite image from the GOME-1 PMDs for 11 January 1996, showing sun-glint as predicted by the model for approx. 5ms^{-1} wind speed.

It can be seen that:

1. Depending on wind-speed the sun-glint is observed over large geographical areas. The larger the wind-speed, the lower the peak reflectivity but the greater the geographical area affected.
2. The magnitude of the glint reflectivity increases with the solar/LOS zenith angle at which it occurs. Hence higher glint reflectivities are observed by GOME-2 than GOME-1.
3. In GOME-1 the glint effect peaked well within the 960km swath. For GOME-2 the peak is close to the edge of the 960 km swath.
4. The scenario simulated in CDI/retrievals is close to the maximum glint encountered by the GOME-2 for the 5 ms^{-1} wind speed considered. Higher glint reflectivities and hence presumably larger errors can be expected for lower wind-speeds, although these will be associated with a reduced affected geographical area.

22.4 Conclusions

Of the scenarios simulated, only the sun-glint case introduces errors, which might be considered significant for O_3 profile retrieval. These errors will be likely to increase at low wind-speed although the geographical area affected will be relatively small. Reduction of the swath from 1920 km to 960km would approximately halve the number of pixels affected by sun-glint, but not avoid the peak reflectivity.

It must be noted other geo-temporal scenarios may show more significant errors than the single scenario simulated here.

22.5 References

[22-1] Watts, P., M.R. Allen, C.T. Mutlow, Aerosol Properties derived from Meteosat Second Generation Observations. RAL/TN/EUM/004, 2000

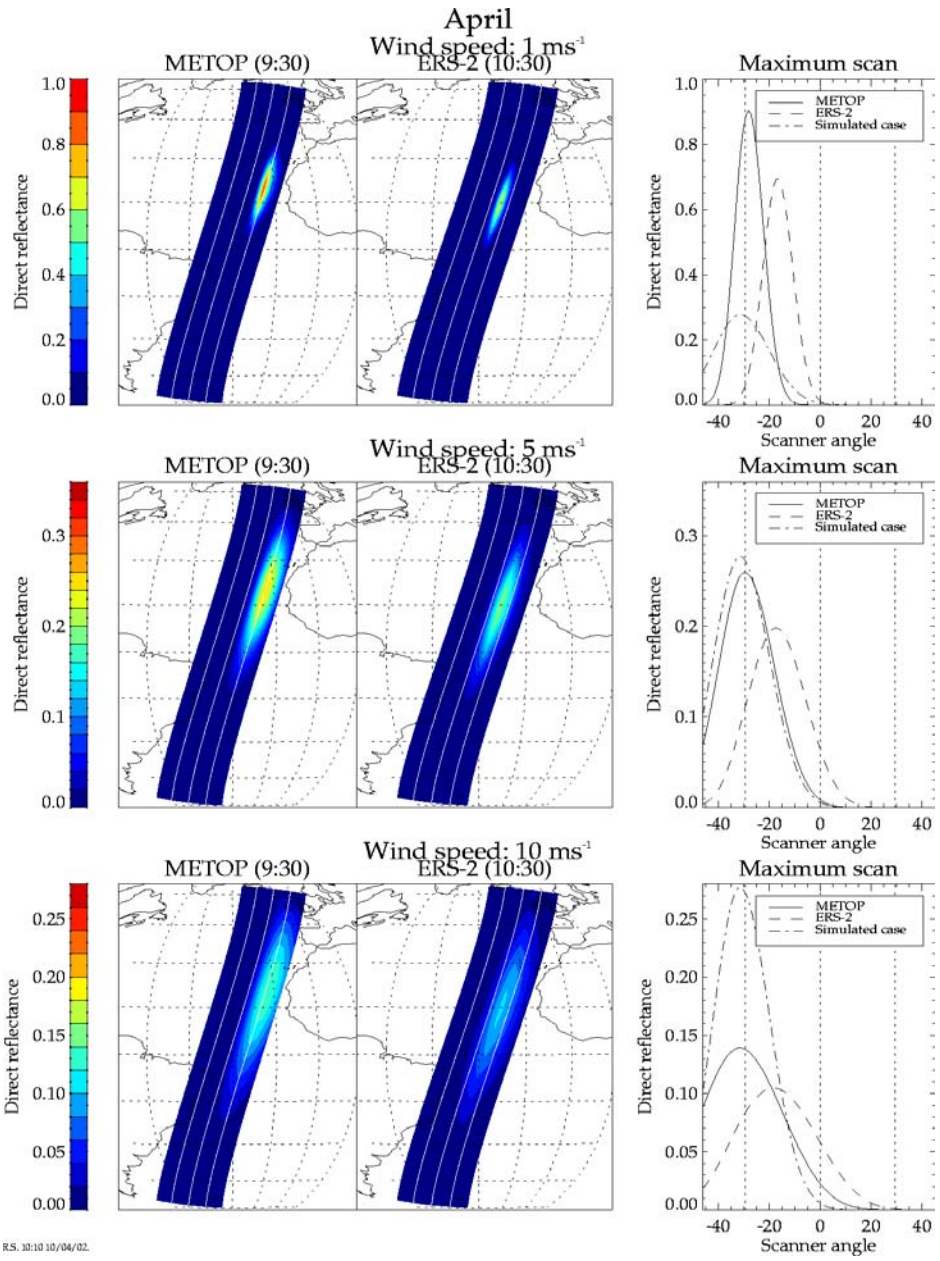

Figure 22-3: Illustration of sun-glint distribution for METOP / ERS-2 for April and various wind speeds

The three rows compare results for different wind-speeds.

Left hand panels: Distributions across the 1920 km swath of the reflectance for the sun-surface-satellite ray.

The two sub-panels compare conditions for the GOME-2/METOP orbit (9:30am local time equator crossing time of descending node) and the GOME-1/ERS-2 orbit (1 hour later).

Right hand panels: Across-track cross-sections of the same data, through the point of maximum reflectance, for both observing geometries. The case implemented in the retrieval simulations is also illustrated on this panel (nominally the April case, 5ms^{-1} wind speed, with relative azimuth set to 0 to maximise the glint reflectance).

The 960 km swath extent and nadir-point are indicated by the white and vertical, dotted lines of the left and right-hand panels, respectively.

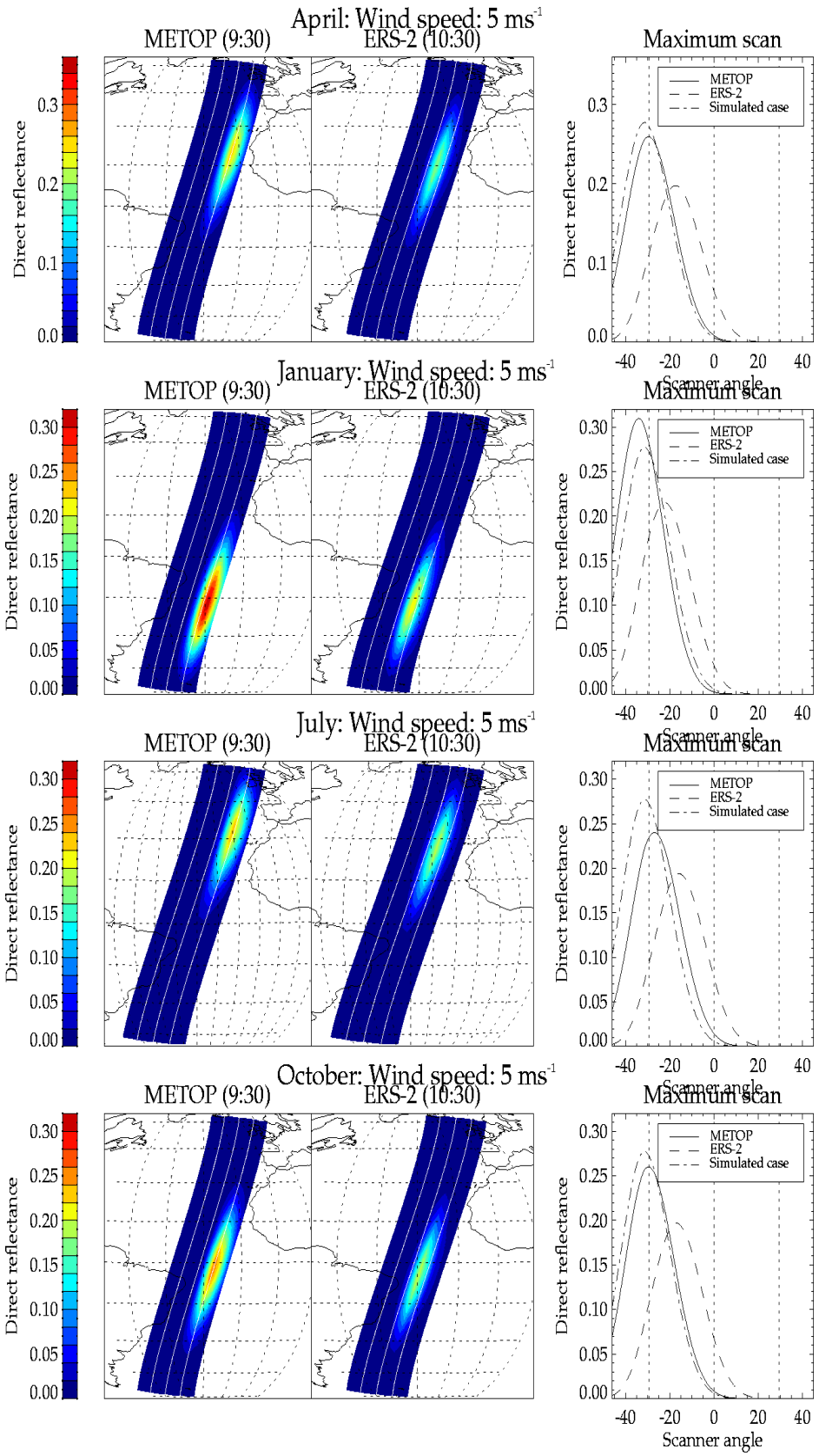

Figure 22-4: Illustration of sun-glint distribution for METOP/ERS-2 for various months and wind speed of 5 ms^{-1}

As Figure 22-3, but for various months with a wind speed of 5 ms^{-1}

23 WP270: Pointing and Geolocation (RAL)

23.1 Geolocation error budget

Realistic pointing accuracies for GOME-2 have been obtained from the EPS Design Justification Document Geolocation and Co-registration Budget (EUM.EPS.SYS.TEM.990014). These are summarised in Table 23-1 and are specified as uncertainties in ground pixel position. They have been converted to angular errors in GOME-2 pointing, in both the along- and across-track directions. These derived angular errors are slightly larger at the edges of the swath than at the nadir, although by a smaller factor than the errors tabulated in horizontal distance co-ordinates. Linear mapping simulations have adopted a fixed angular error, using the edge-of-swath value for the 1920 km swath, rather than the 960 km swath. So the results can be considered to represent an "upper limit" on this error, except for the fact that the *as built* estimates after bias removal have been used.

Table 23-1: Summary of geolocation errors

	As built				Specs			
	Nadir		Edge of swath		Nadir		Edge of swath	
	Along	Across	Along	Across	Along	Across	Along	Across
Inc. Bias (km)	1.6197	1.2445	3.2048	3.8673	3.5941	3.5935	6.9617	11.3083
Bias removed (km)	1.5616	1.1558	3.1339	3.5918	2.5411	2.5411	4.9617	11.3083

23.2 Scenarios simulated

Linear mapping has been performed separately for the along- and across-track errors. For the *across-track* errors, the reflectance is actually calculated for a 0.1° offset to the true view angle. The result is then scaled to an angular error of 0.089° (equivalent to 3.5918 km at edge of swath). The *along-track* error is calculated by using the solar illumination geometry for the next along- track location, i.e. 40 km displacement, to calculate the reflectance. The result is then scaled down to the required error (3.1339 km).

23.3 Results

The resulting WP270 geolocation and pointing error plots are given in Figures B7.1 in Appendix B. Results for a typical case of April 55N are shown in Figure 23-1.

In all the scenarios considered, there was very little difference between results for the two Band 1 wavelength range options. The magnitude of the error is related to the solar elevation angle, with simulations at smaller elevation angles producing larger errors. This is likely due to the change in path-length caused by the pointing error. The mapped errors are much larger for the errors across-track than for those along-track, due to the viewing geometry causing larger path length modifications.

23.4 Conclusion

Errors in the geometry used for radiative transfer modelling caused by across-track pointing errors of the magnitudes stated in the EPS Design Justification Document Appendix B1-2: *Geolocation and Co-registration Budgets* (EUM.EPS.SYS.TEM.990014) would yield errors in GOME-2 ozone profile retrieval of low importance by comparison to other sources. Pointing errors of the specified magnitudes in the along-track direction would have a negligible impact.

GOME-2 pointing errors could also potentially have indirect impacts on O_3 profile retrieval via co-registration errors with respect to AVHRR3 images and/or databases of surface topography and/or scene-type.

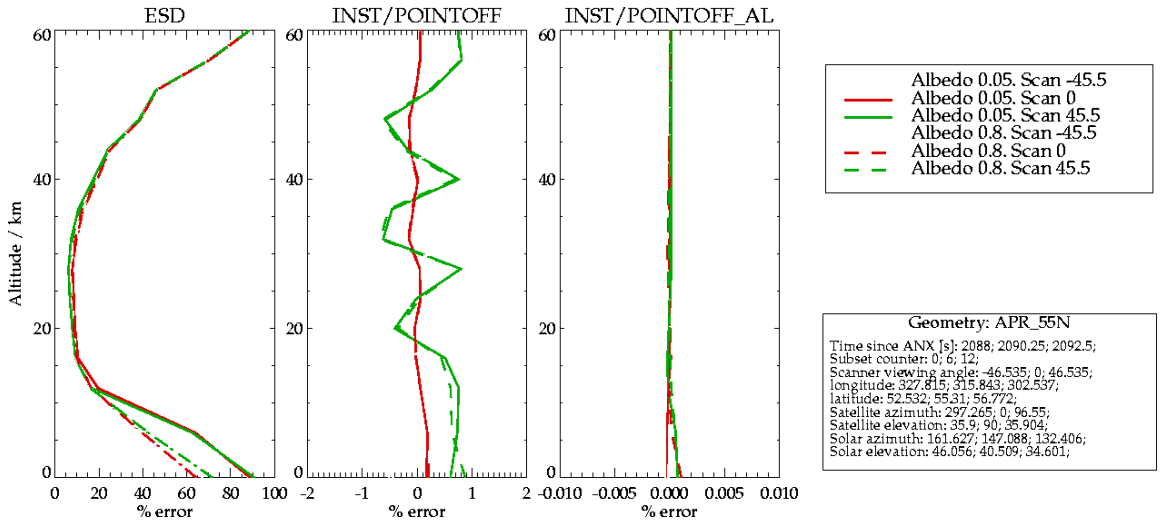

Figure 23-1: ESDs and mapped pointing errors for nadir & extreme scan angles, & both albedos for April 55N

ESDs and mapped pointing errors for nadir and extreme 1920 km scan angles and both albedos for April 55N, assuming band 1 wavelength range 265-314 nm.

Left hand panel shows ESDs, middle and right panel show effect of across track and along-track pointing errors, respectively

24 WP270: Pointing and Geolocation (IUP)

24.1 Method and results

Pointing and geolocation errors have been simulated using the CDI database of intensity spectra calculated for 240 equidistant LOS separated by about 0.39°. GOME-2 ground pixel equivalent intensities assuming IT=0.1875 sec were approximated by integrating 10 LOS for each ground pixel. A shift of one LOS grid point from east to west direction has been applied except for the most westerly pixel where the shift direction was reversed.

A maximum pointing inaccuracy of 0.25° (3.5 km on the ground in nadir direction) or better was specified for GOME-2 (see Table 11-1). Therefore the applied shift represents a worst case for all ground pixels.

Figure 24-1 shows differences between nominal simulations and intensities for shifted LOS. Differential structures on these differences can lead to errors in DOAS retrievals. Such structures are shown on the right side of Figure 24-1. Larger spectral features occur for the west pixels (ground pixel 24), which can be explained by larger atmospheric slant paths as shown in Figure 24-2. However, similar errors can also occur on the east side.

Figure 24-3 shows the maximum spectral differences (log-ratios) and the according maximum differential structures for all ground pixel simulations. Differences are below 1-2%, differential structures are about 0.1% deep at the maximum except for January, 55N, and October, 75N (0.2%).

For all scenarios, slant column errors from DOAS fittings due to the pointing inaccuracies are shown for O_3, NO_2 and BrO in Figure 24-4 to Figure 24-6 A change of sign in the error for ground pixel 24 is caused by the negative LOS shift as opposed to positive shifts applied for all other ground pixels..

24.2 Conclusions

Errors are generally below 0.5% except for NO_2 in January 55N, and October 75N (up to 1%). Shapes of the error function looks similar for all cases except for those just mentioned and for BrO in October 75S, where the sign is opposite.

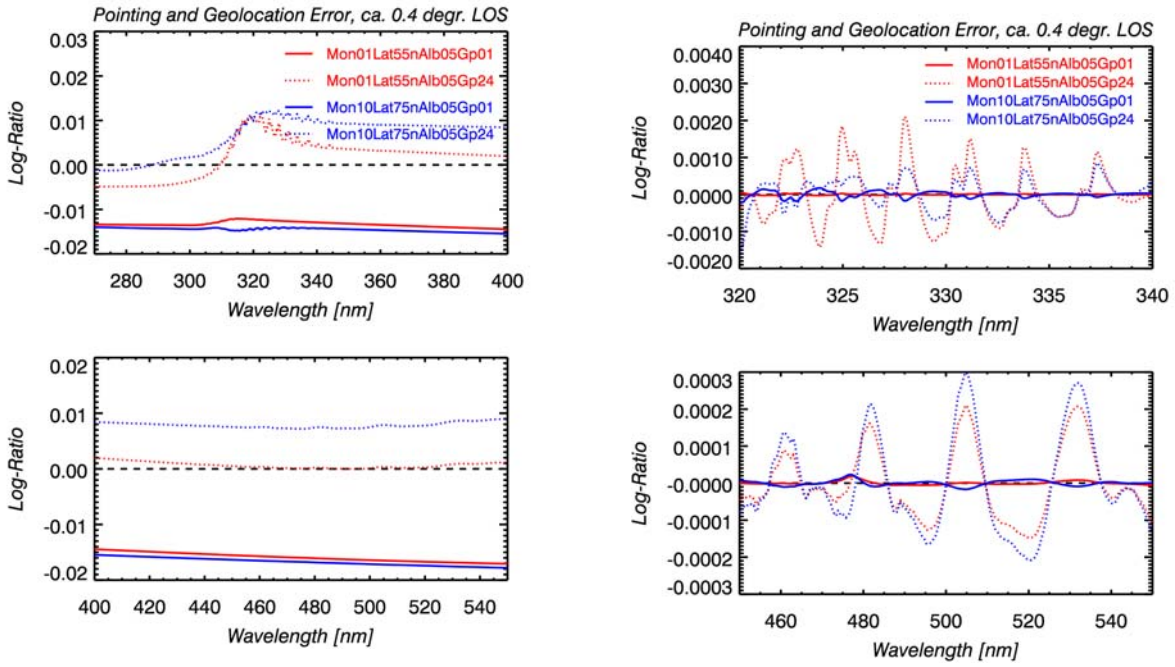

Figure 24-1: Differences (log-ratios) of GOME-2 ground pixel-equivalent spectra and introducing a LOS shift of about 0.3°

Left: Difference Right: Differential structure

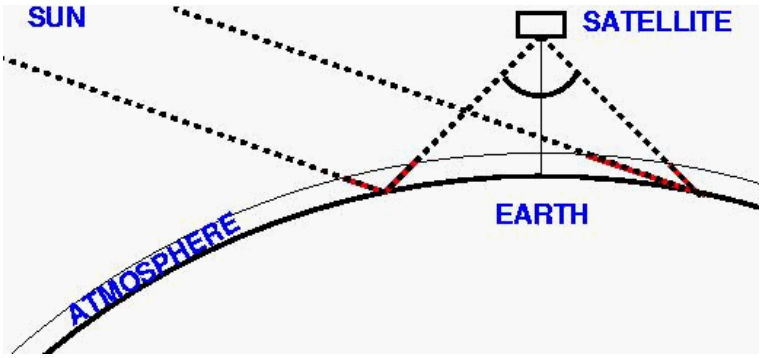

Figure 24-2: **Illustration of atmospheric slant paths (red) for +-46° line-of-site**

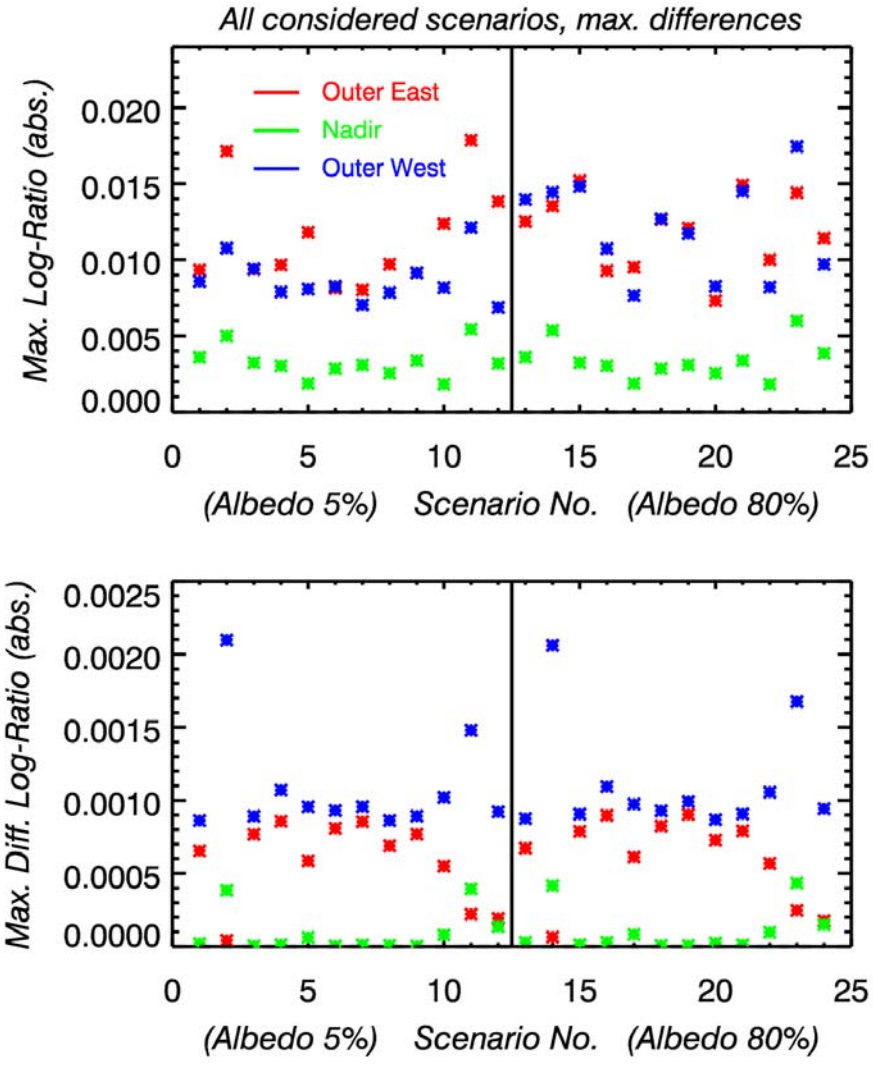

Figure 24-3: **Maximum spectral differences (top) and maximum differential structures (bottom) calculated from simulated pointing inaccuracies**

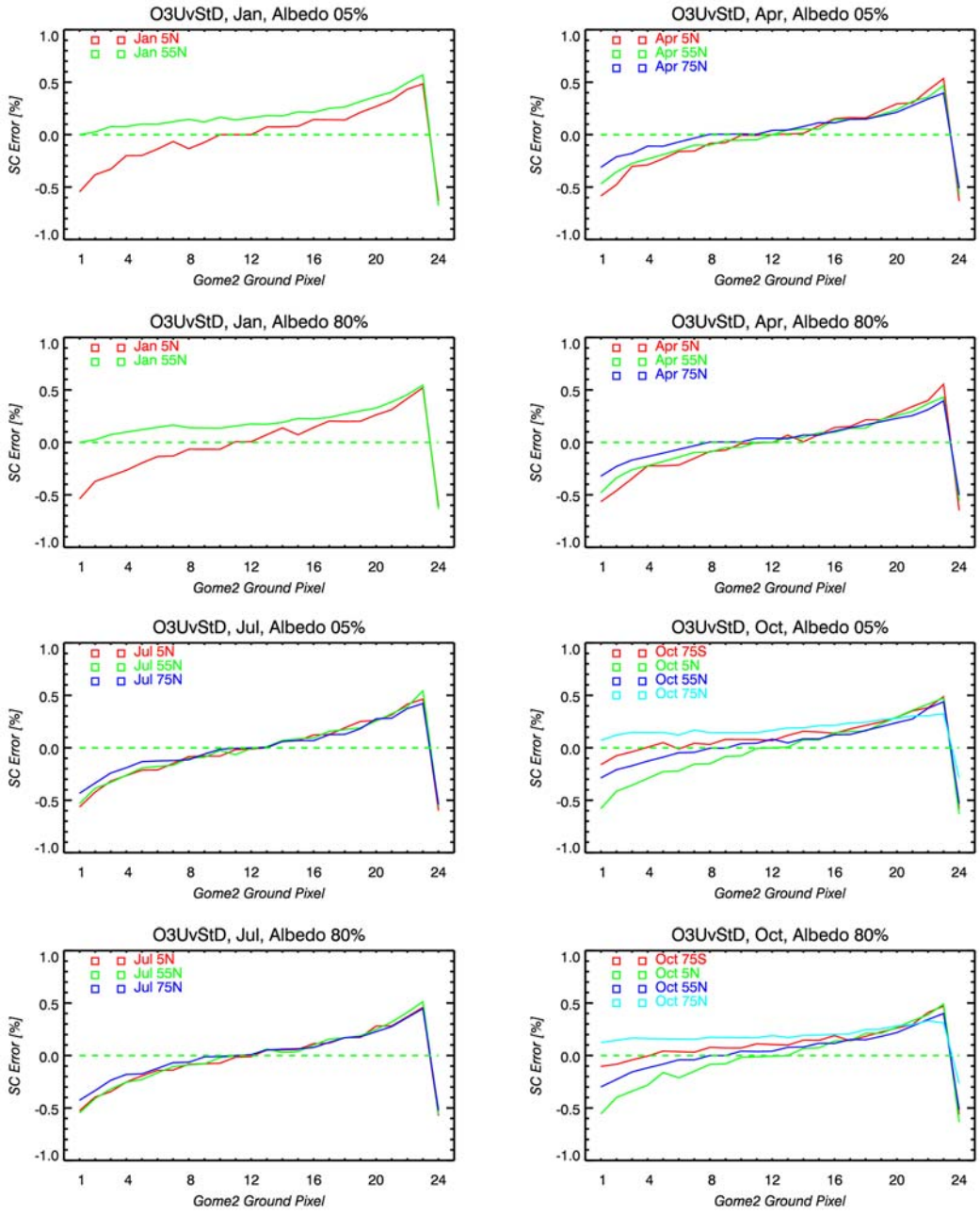

Figure 24-4: O_3 slant column errors from simulated pointing inaccuracies

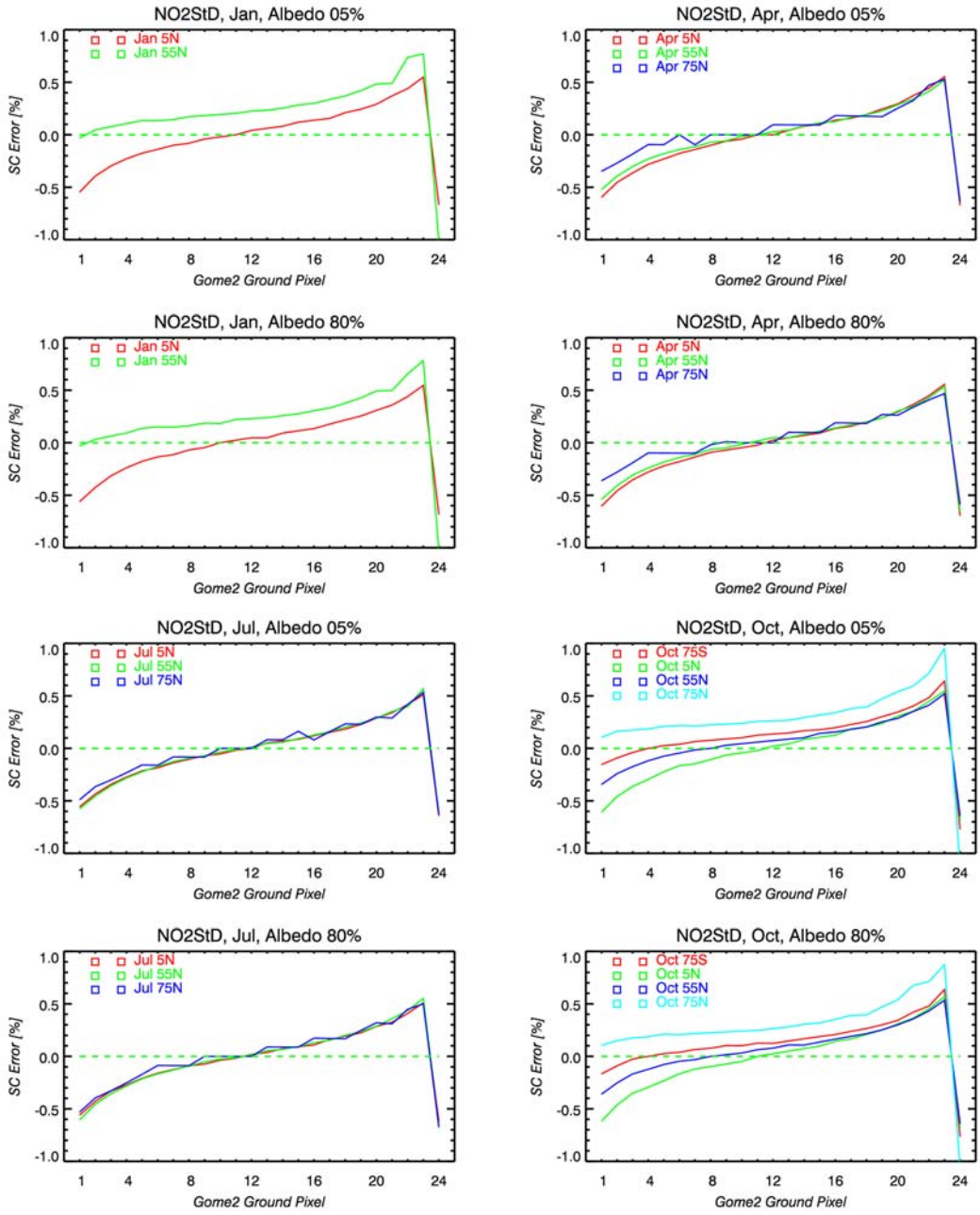

Figure 24-5: NO_2 slant column errors from simulated pointing inaccuracies

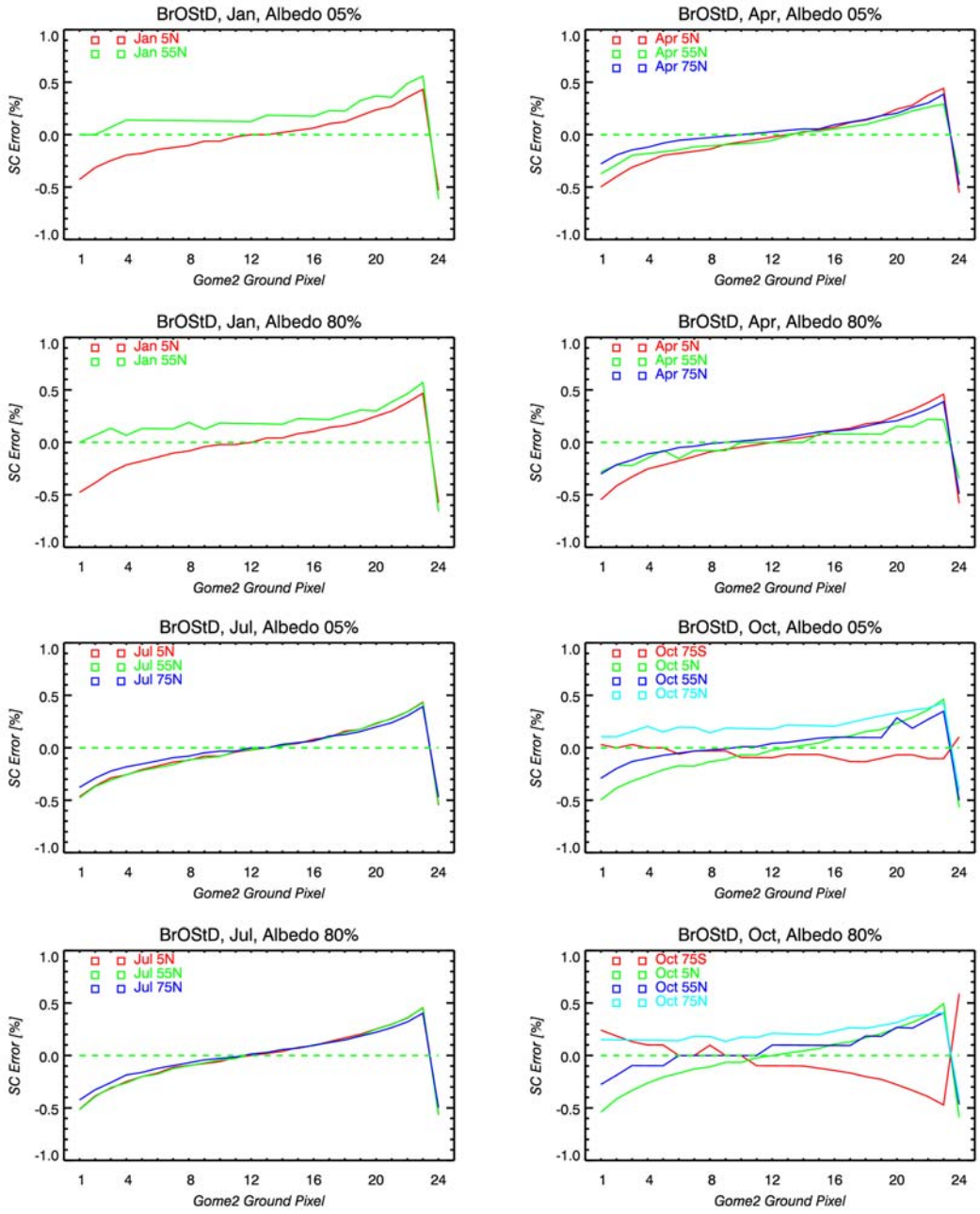

Figure 24-6: BrO slant column errors from simulated pointing inaccuracies

TASK 3: OPTIMAL OPERATIONAL SETTINGS AND ERROR MITIGATION

25 WP300: Recommendations for Optimal Operational Settings and Error Mitigation

25.1 Baseline Error Budgets

25.1.1 General

In order to gauge the importance of error sources specifically identified for attention in Task 2, errors known to have affected GOME-1 retrievals were reviewed and *baseline error* budgets compiled in Task 1. The components of the *baseline error* budgets for ozone profiles and trace gas columns are briefly outlined again below.[1]

25.1.2 Ozone profiles

The baseline *precision* of GOME-2 was defined as the *estimated standard deviation (ESD)* at each retrieval level, evaluated from the diagonal elements of the solution error covariance matrix (S_x) for the retrieval. The ESDs were based solely on linear propagation of *measurement noise* through the optimal estimation retrieval equations, adopting an *a priori* uncertainty of 100% on ozone at each level (with vertical Gaussian correlation lengths as described in the final report). Measurement noise is estimated from a GOME-2 noise model, which combines *photon noise* with *read-out* noise. Based on GOME-1 experience, measurement precision from this model is better than can realistically be achieved in fitting simulated to measured spectra (due to forward model errors and/or unaccounted for instrumental errors). "*Noise-floors*" corresponding to 1% and 0.05% of sun-normalised radiance were therefore imposed in Bands 1 and 2, respectively. Other errors were handled by *linear mapping*.

For retrieval levels at 20 km and above, the ESD is markedly lower than the *a priori* uncertainty. For retrieval levels below 20 km (i.e. at 0, 6, 12 and 16 km), however, the ESDs are often >50% of the *a priori* uncertainties, so the a priori constraint is quite significant. It should be borne in mind that the error estimates obtained by linear mapping will also have been influenced by this *a priori* constraint[2].

The sources and magnitudes of errors included in the *baseline error* budget by linear mapping are as specified in Table **Error! No text of specified style in document.**-1

Table Error! No text of specified style in document.**-1** **Components of baseline error budget for O_3 profiles**

Error Source	Magnitude
Radiometry	2% of sun-normalised radiance
Wavelength-dependent degradation of scan-mirror UV reflectance.	Equivalent to uncorrected GOME-1 degradation after 3 years (excl. from RSS)
Residual error from polarisation correction	SRON prescription for GOME-2
Surface pressure uncertainty	10hPa
Temperature profile uncertainty	Error covariance matrix from IASI retrieval
Aerosol profile uncertainty	LOWTRAN "high" - "background" cases

[1] It should be noted that the baseline error budgets did not include clouds, spectroscopic or instrumental errors other than those described.

Linearly mapped *baseline errors* were combined in a root-sum-squared (RSS) way for comparison with the ESDs and with the specific errors addressed in this study.

It should be noted that, although a realistic *wavelength-independent* error in sun-normalised radiance was included in the RSS (in accordance with the error budget for pre-flight radiometric calibration), *wavelength-dependent* error in sun-normalised UV radiance arising from degradation in the UV reflectivity of the scan mirror was quantified (for a case equivalent to GOME-1 after three-years operation) but was not incorporated into the RSS. The reason for this is two-fold: firstly, it is very difficult to predict the character (e.g. wavelength and time dependencies) that such degradation will exhibit for GOME-2 and, secondly, if similar to GOME-1 Band 1, this would dominate over all other errors after several years of operation, unless corrected for.

Aerosol is highly variable in the troposphere, especially in the boundary layer, and also in the lower stratosphere following volcanic eruption. In this study, the aerosol profile was fixed in the GOME-2 FM to be the LOWTRAN "*background*" profile (as it is in the RAL GOME-1 ozone profile retrieval scheme) and enhancements to aerosol loading were treated as a potential source of error. As discussed in the final report, this error has been estimated by linear mapping of the spectral difference between LOWTRAN "*background*" and "*high*" cases. Aerosol loading in the LOWTRAN "*high*" case makes this a conservative estimate in many circumstances. However, it was beyond the scope of this study to investigate and account for errors in the FM due to neglect of cloud, and the nature of such errors is somewhat similar to that of a large tropospheric aerosol excursion. RSS *baseline errors* were therefore calculated both with and without inclusion of the mapped aerosol error. The latter can be considered to be a lower limit, applicable to a cloud-free, background aerosol situation[3]. The former can be considered to be representative of an extreme aerosol event and also indicative of pervasive, thin cloud.

In considering the specified errors and their importance in relation to the baseline GOME-2 error budget, it is useful to distinguish between those, which vary in a quasi-random way with time and location, and those, which vary in a non-random way. The former affect precision but can be reduced by averaging, whereas the latter give rise to systematic biases, which cannot be reduced by averaging but can in certain conditions be amenable to *a posteriori* correction. The more relevant comparisons for the quasi-random and non-random errors are therefore with the ESD and RSS, respectively. In the following sections, quasi-random errors are deemed to be significant if comparable to the ESD and non-random errors are deemed significant if comparable to the RSS. The RSS is typically <5% at 20 km and above and ~10-20% at 16 km and below.

25.1.3 Trace gas columns

The standard DOAS approach, as investigated in this study and used in operational GOME-1 retrieval, consists of a two-step procedure. Firstly, a slant column density is retrieved from spectral fitting. Secondly, airmass factors are calculated using a multiple scattering radiative transfer model (RTM), assuming *a-priori* knowledge of the profile shape. Division of the slant column density by the airmass factor results in the vertical column density (total column). Both steps involve errors, which can be combined into an overall error budget. In the application to real data, the error sources from both steps can be distinguished. In this study, however, perfect *a-priori* knowledge has been assumed, so a distinction between AMF and slant column errors for a given error source is not always clear-cut.[4].

Attribution of the error sources to AMF and/or slant column has important implications for strategies of error mitigation. Slant column errors tend to be instrument related and improvable only by operational

[2] In the limit in which there is no reduction in the *a priori* uncertainty at a given altitude, due to absence of information in the measurements, the retrieved ozone mixing ratio at that altitude will not deviate from the *a priori* value, and linearly mapped errors will be identically zero.

[3] This lower limit would also apply if accurate independent information on aerosol/cloud scattering properties within the GOME-2 pixel could be derived either from other GOME-2 measurements (e.g. O_2 A-band and/or PMDs) or from co-located AVHRR3 images.

[4] An extensive study of possible AMF errors due to assumptions made in RTM and imperfect *a-priori* knowledge was beyond the scope of this study.

settings or hardware changes. On the other hand, errors assigned to AMF can be reduced by algorithm improvements.

For trace gas columns, photon noise and read-out noise were combined using the GOME-2 measurement noise model and ESDs were calculated by fitting the Ring cross-section in addition to trace gas columns. Residual errors following the application of the polarisation correction were linearly mapped but found to be negligible. Errors potentially arising from spectral structures in the diffuser plate BRDF were imported directly from a study on GOME-1 (see annex to Final Report), where they had been shown to be dominant for trace gases other than ozone.

In the following sections, the specified error sources analysed as part of this study are referenced to the basic ESDs for an integration time of 0.1875 sec. This corresponds to a 40 x 80 km^2 ground pixel area at nominal swath width of 1920 km across-track. In general, error sources are considered significant if they are of same order of magnitude or higher than the baseline ESD.

25.2 Analysis of Instrument Parameters and Comparison of Task 2 Errors with Baseline Errors

25.2.1 Sampling Options for Band 1

The baseline integration times for GOME-2 going into the study were: 12s for Band 1A and 0.1875s for Band 1B, with the 1A/1B boundary being set at 283 nm. For Band 1A, a 12s integration time would give rise to a ground pixel of 1920 km x 80 km, for the 1920 km swath option. However, there are known to be several disadvantages to such a large ground pixel, e.g.:

- Non-linear dependence of radiative transfer on view angle over the range ± 45^o
- Errors (e.g. pseudo-spherical approximation) in modelling radiative transfer at large view angles
- Horizontal variability of the stratospheric O_3 profile

For GOME-2, the flexibility exists to read out Band 1A at 1.5s (640 km x 40 km) and co-add spectra to recover signal to noise, and this co-addition could be performed in the along-track direction as well as the across-track direction, thereby alleviating the above-mentioned problems. However, more frequent read-out of detector arrays would result in increased read-out noise. This was quantified for ozone profile retrieval in the frame of a 1% noise floor.

Co-addition of 1.5s Band 1A pixels to 12s (640 km x 320 km) or 24s (640 km x 640 km) was found to yield similar ESDs to those for a single 12s Band 1A pixel. Additional read-out noise associated with more frequent read-out was also found to be insignificant for co-addition of 0.1875s Band 1B pixels to 1.5s.

It was therefore concluded that there would be no impediment to reading out Band 1A at 1.5s and Band 1B at 0.1875s.

25.2.2 Spatial Aliassing and Static Scene Inhomogeneities

Because spectral pixels in the GOME-2 detector array are read-out sequentially and this takes a finite time, the scene over which each spectral pixel integrates is slightly different. The possibility therefore exists for spatial variability in the scene to be aliased into the measured spectrum. The most extreme difference in scene is between spectral pixels at the ends of the arrays, and spectral discontinuities at Band boundaries had provided clear evidence of spatial aliasing in GOME-1 flight data. The ratio of integration time to read-out time is smaller for GOME-2 than for GOME-1, so GOME-2 is more susceptible to this phenomenon. An

important component of the study was therefore to quantify spatial aliasing as realistically as possible for GOME-2 and to determine its impact on trace gas columns and ozone profiles.

Several Landsat ETM+ images were acquired (~180 km x 180 km at 1 m resolution) for this purpose. From these, an ensemble of >350 spatially-aliased signatures were calculated (in terms of dependent surface albedos) for each of the 12 geo-temporal scenarios. Spatially-aliased signatures were then linearly-mapped and the ensemble error extremes, mean (bias) and RMS were examined.

An important finding from this work, which had not previously been appreciated, was that the GOME-2 IFOV (0.29° ~4 km on ground) will effectively filter out high-frequency structure (i.e. spatially-aliased noise)[5].

Ozone profiles

For O_3 profile retrieval, the impact of spatial-aliasing was determined separately for the Band 1 and 2 steps. Band 1 can see down to the surface and can therefore detect low-frequency spectral structure from spatial aliasing only at the longest wavelengths. Spatially aliased errors were found to be less than ESDs when the Band 1 wavelength range was restricted to 265-307 nm but to exceed ESDs in extreme cases when the range was extended to 265-314 nm. By shortening the read-out time sufficiently, spatially-aliassed errors could be reduced below the ESD levels, even for these extreme cases.

From the point of view of O_3 profile retrieval, it was therefore concluded that a reduction in the Band 1B detector read-out time would be desirable.

It was found from simulations in which detector read-out time was reduced to a negligible value by comparison to integration time that errors still arise if surface albedo varies spatially within a scene between high and low values (e.g. cloud/sea, land/sea). Such errors were ~10-20% in the troposphere, and could therefore exceed the RSS and sometimes approach the ESD. Such (static) errors are inherent to *scene inhomogeneity* and are due to the non-linear dependence of radiative transfer on surface albedo. Because their occurrence is related to geography and meteorology, it will not be random. Such errors are therefore significant even though they fall below the ESD.

Because only a small spectral interval (~100 of 1024 detector pixels) of Band 2 is used and a 2nd order polynomial is fitted to log(sun-normalised radiance), the Band 2 retrieval step is insensitive to *low-frequency* structure from spatial aliasing. However, alternative algorithms which attempt to use (a) sun-normalised Band 2 radiances directly and/or (b) extensive intervals of Bands 1 and 2 simultaneously would be more vulnerable.

Trace gas columns

Windows used in spectral fitting of trace gas columns are very narrow in comparison to the widths of the GOME-2 bands (n.b. Bands 2 and 3). Trace gas column retrievals were therefore found to be insensitive to low-frequency structure in the spatially-aliased signatures. The maximum errors from spatial aliasing were: 0.02% O_3, 2% NO_2, 1% BrO, 10% OClO), all of which were below the ESDs

From the point of view of trace gas column retrieval, it was therefore concluded that no further reduction in detector read-out time would be necessary.

25.2.3 Spectral Resolution and Slit-Function Shape

The ability to resolve absorption signatures of target gases in sun-normalised spectra is fundamental to the GOME-class of measurement. As resolution is degraded, the ability to retrieve information on trace gases tends to decrease. However, spectral resolution had been deliberately decreased in the optical design of GOME-2 in comparison to GOME-1, in order to reduce the degree to which fine structure in the solar spectrum is undersampled. This undersampling had resulted in artificial spectral structure in sun-

[5] This means that images with much coarser resolution than Landsat ETM (e.g. ATSR-2, 1 km x 1 km) would suffice for a future, more comprehensive study of spatial-aliasing.

normalised GOME-1 spectra, due to minute changes in the wavelength registration of detector pixels between the measurements of direct-sun and backscattered spectra. An issue for the GOME-2 study was to assess the extent to which a further decrease in spectral resolution might be beneficial.

At the initiative of the study-team, this topic was broadened to also consider the impact of errors in knowledge of slit-function shape and how these would vary with spectral resolution (i.e. slit-function FWHM).

Ozone profiles

a) Slit-function FWHM

Although undersampling errors are controlled to a satisfactory level by the RAL algorithm, accounting for them in the retrieval is a source of non-linearity which limits computational efficiency and which it might be possible to avoid if the slit width was increased. The trade-off between *increasing ESD* and *decreasing undersampling error* was examined in simulations of defocusing, in which the slit function FWHM was increased, redistributing but conserving the total photon flux on the detector array. In a *worst case* estimate, in which no attempt was made to retrieve wavelength misregistration between direct-sun and backscattered spectrum using the high-resolution solar reference spectrum, the undersampling error was found to be comparable to and sometimes exceed the ESD for the nominal slit width, but to be substantially reduced when the slit width was increased from 2 to 3 px. The corresponding increase in ESD from defocusing from 2 to 3 px was found to be very modest. So, for ozone profile retrieval with the RAL algorithm, the net *direct* impact of such an increase in slit width would be positive. It can be anticipated that such an increase would also facilitate alternative algorithms, which do not attempt to retrieve wavelength misregistration parameters using a high-resolution solar reference spectrum. However, consideration of the *indirect* impact of an increase in slit width (see below) complicates this picture.

b) Slit-function shape

In the ozone profile retrieval scheme, the slit-function shape is assumed to be Gaussian. However, analysis by Officine Galileo of the GOME-2 EQM had indicated: (i) the true shape to be non-Gaussian and asymmetric and (ii) to be broader and more strongly wavelength-dependent (though more Gaussian) in the *defocused* case than in the *focused case*.

Errors from assuming the slit-function shape to be Gaussian were simulated explicitly and found frequently to exceed not only the baseline RSS but also the ESD, making this the dominant error simulated for ozone profile retrieval (exceeding 100% in the troposphere). Although such errors in retrieved ozone will not be random and have a characteristic height-dependence, they will adversely affect *precision* as well as *bias*.

It was found that, if the true shape of the slit function is that appropriate to defocusing (by a factor of ~1.3 to ~1.5, depending on wavelength, as in the Officine Galileo analysis), then sensitivity to the error of assuming a Gaussian shape in the retrieval scheme increases dramatically, despite the fact that the true shape then more closely resembles a Gaussian[6].

Because undersampling errors are controlled quite well by explicitly retrieving misregistration parameters, errors in knowledge of slit-function shape are of paramount importance for the RAL ozone profile algorithm. It is also very likely that errors in knowledge of shape would be crucial for alternative algorithms. To meet user requirements on the accuracy of ozone profile retrievals from GOME-2, it is clear from this study that great attention will have to be paid to characterising slit-function shape in the relevant wavelength interval of Band 2 (<340 nm). It is also clear that the only opportunity to measure the slit-function shape adequately will be during pre-flight characterisation of the FM. Moreover, the increase in sensitivity to shape errors from increasing the width of the slit-function is a strong argument against defocusing (or physically opening the slit) unless pre-flight characterisation of slit-function shape will be undertaken.

[6] This is because, although its amplitude is smaller, the spectral signature of the error in the defocused case is actually closer in structure to the O_3 Huggins bands than that in the focussed case.

Trace Gas Columns

For trace gas columns, simulations were performed of an increase in slit-function FWHM due to defocusing from 2px to 5 px (0.24-0.6 nm Band 2 and 0.5-1.25 nm Band 3). The ESDs for O_3 (<1%) and BrO (<60%) were found to increase by only a factor ~1.1, whereas that for NO_2 (<20% at 2 px) was found to increase by a factor ~1.24 by 3 px. Undersampling errors were found to be small for O_3 (<0.5%) and NO_2 (<2%), but substantial for BrO (≤100%). The variation of undersampling error with FHWM was found to be complicated and to differ greatly from one trace gas to another, i.e. it did not simply decrease monotonically with increasing FWHM.

At the initiative of the study team, an initial assessment was also made of *slit opening*. This potentially offers an alternative means to reduce undersampling errors, and the increased photon flux could also permit: (a) reduction in integration time, hence ground pixel size, or (b) increased S/N (by 30% for NO_2 from doubling the slit width). Small ground pixel sizes are particularly beneficial to tropospheric column retrieval due to the enhanced probability of cloud-free scene occurrences It is, however, recognised that the fixed GOME-2 data rate and detector saturation would provide practical constraints on (a) and (b), respectively, and that the other consequences and implications of slit opening also need to be evaluated.

25.2.4 Pseudo-Spherical Approximation and Earth's Curvature

Radiative transfer models (RTMs), in current usage for GOME-1 data processing, employ the pseudo-spherical approximation and also neglect the curvature of Earth's surface. More sophisticated models are now becoming available which dispense with the pseudo-spherical approximation and account for Earth's curvature. However, because the CPU power required for a fully-spherical calculation would be prohibitive for GOME-2 data processing on contemporary computers and might still be too expensive in 2006, when GOME-2 will first deliver data, the accuracy of these approximations was examined.

Calculations by the fully-spherical model, CDIPI, demonstrated the less-rigorous model, CDI, to be sufficiently accurate for the viewing geometry of GOME-2. By differencing calculations by the CDI model, with and without the pseudo-spherical approximation, the spectral signature of this approximation was derived for all geo-temporal scenarios and these were then linearly mapped.

Ozone Profiles

For the 960km swath-width (i.e. view angles ±29º), errors from the pseudo-spherical approximation (as implemented in CDI) were found always to be <10%, and therefore only rarely to exceed the RSS, and never to exceed the ESD. For the 1920km swath-width western extreme (+46º) pixel, however, errors were found always to exceed the RSS and to exceed the ESD for the three geo-temporal scenarios in which solar zenith angle was largest (Jan 55ºN, Oct 75ºN and Oct 75ºS). It would therefore be necessary to avoid the pseudo-spherical approximation if the accuracy of ozone profile retrieval is not to be compromised at high solar zenith angles near the western edge of the 1920 km swath.

Trace Gas Columns

Errors on O_3, NO_2 and BrO slant-columns were found to be negligible (<1%), provided that solar geometry for the ground rather than the top-of-atmosphere was used by the pseudo-spherical calculation.

25.2.5 Non-Lambertian Surface BRDF

Another approximation of radiative transfer models in contemporary use for GOME-1 is to neglect the angular dependence of surface BRDF, i.e. to assume that surfaces are all lambertian. The error due to this approximation was quantified in the study for comparison to those arising from other sources. The CDI model was used to calculate spectra as a function of view-angle for a variety of surface-types (dark land, bright land, ocean and snow (April 55ºN) and sunglint (April 5ºN), employing angle-dependent BRDFs and their Lambertian equivalents.

Ozone profiles

For ozone profiles, a quasi non-linear simulation was employed in which gross deviations between the angle-dependent and Lambertian equivalent BRDFs were accommodated through retrieval of a (Lambertian) surface albedo. Errors from the Lambertian assumption were found to be <5%, except for sunglint where they were sometimes as high as 30%.

The extent to which sunglint will affect a given GOME-2 spectrum will depend upon the fraction of cloud obscuring the ocean, which is quasi-random, but in the absence of cloud the impact of sunglint is predictable. Such errors are therefore more usefully compared with the RSS than with the ESD. Errors of >10% (comparable to the RSS) were found for sunglint in the troposphere at tropical and mid-latitudes. For GOME-2 on METOP, sunglint will occur in eastward views, peaking near the 960 km swath edge. It will affect a substantial fraction of data in tropics south of the equator. The peak intensity and affected geographical area were shown to depend on surface wind-speed.

Because its occurrence is predictable, it would be feasible to adapt the ozone profile retrieval algorithm to utilise an angularly-dependent BRDF at sunglint locations, with surface wind-speed being either taken from met service analysis or retrieved from the GOME-2 measurements themselves. It can be anticipated that this should reduce errors on ozone profiles caused by sunglint to levels below the RSS.

Trace gas columns

Errors on O_3, NO_2 and BrO slant-columns were found to be <1%, except for sunglint, where they were up to 3% for all gases. It was noted that these errors would arise via airmass factors, and could be reduced via retrieval of (Lambertian equivalent) surface albedo directly from the spectra.

25.2.6 Cloud Obscuration and Horizontal RI Gradients at Edge of Swath

The extent to which cloud obscuration and/or horizontal gradients in refractive index at the swath edge were likely to be more for important for a 1920 km swath than for a 960 km swath was another issue addressed by the study.

Cloud obscuration

The ATSR-2 forward view (~46° from nadir) is a good surrogate for the GOME-2 extreme across-track views in the 1920 km swath (±46° from nadir). The statistics of cloud occurrence for a ground pixel size of 80 km x 40 km (appropriate to the 1920 km GOME-2 swath) were analysed for the forward and nadir-views of ATSR-2 for one year. Forward/nadir differences were found not to be significant, even for the occurrence of totally cloud-free scenes: 12% vs. 14%. Ground pixel *size* is a separate issue though.

Horizontal gradient in RI

Line-of-sight path-lengths were calculated with a ray-tracing model for a non-refracting atmosphere and for a refracting atmosphere with and without a horizontal temperature gradient of 0.14K/km (at all altitudes from 0-40 km). Differences were found to be negligible, even for the extreme view angles of the 1920 km swath.

25.2.7 Pointing and Geolocation

Errors were specified according to the EPS Geolocation and Co-registration Budget

- Nadir: 1.6 km along-track, 1.2 km across-track
- 1920 km swath edge: 3.1 km along-track, 3.6 km across-track

Spectra were calculated with and without these errors and the resulting spectral signatures were linearly mapped.

Ozone profiles

Across-track errors were found to be generally <2% (even at 1920 km swath edge) and along-track errors were found to be <<1%. The direct impact of pointing errors at the levels specified is therefore negligible by comparison to other sources of error[7].

Trace gas columns

Errors were found to be always <1% and generally <0.5%

25.2.8 Error Budget Summaries

Ozone Profiles

The significance of individual errors in relation to the baseline ESDs and RSS errors was described in preceding sections and illustrated in an extensive series of plots in an annex to the Final Report. The four most salient points to be recalled here are that:

- Error from assuming an incorrect (Gaussian) slit-function shape is pervasive, and dominates over other the RSS and ESD.
- Error from the pseudo-spherical approximation in extreme westerly views of the 1920km swath exceeds the ESD at large solar zenith angles and always exceeds the RSS.
- Error from sunglint exceeds the RSS in easterly views at tropical and mid-latitudes.
- Error from static scene inhomogeneity is often significant in comparison to the RSS.

Trace gas columns

Table **Error! No text of specified style in document.**-2 summarizes the various error sources discussed in this study. Error estimates in most cases are precision estimates for 1σ. Errors cited for undersampling (interpolation) and RTM assumptions are systematic errors and introduce biases in the retrieval results. Numbers given in that table present average numbers from all scenarios and may be higher for specific atmospheric conditions. Maximum errors are indicated by the "< smaller" sign. In light yellow those errors are indicated which are on the same order of magnitude as the basic ESD, while orange marks errors which exceed the ESD. It is difficult to assess the combined effect of all errors. In cases of precision estimates, one can assume that the overall errors are obtained by the square root of summed squares. Before detailing the individual error sources and trace gases two general remarks can be made here:

- The various errors for UV total ozone are generally quite small, but they are in many cases significant because of the small baseline error due to SNR.
- For all trace gases other than ozone, by far the most dominant error comes from the differential spectral structure caused by the diffuser plate.

The impact of the diffuser plate spectral characteristics on the NO_2 and BrO column retrieval was taken directly from the technical note for GOME-1 by Richter and Wagner, given in Appendix D of the Final Report.

[7] The direct impact is the error in view-angle adopted in radiative transfer modelling. Indirect impacts associated with errors in geolocation (data bases on coastline, land surface type and topography) and co-location with AVHRR images (cloud fields) could also result, but were outside the scope of this study.

GOME2 trace gas column error budget

		O3	O3 VIS	NO2	BrO	OClO O3 hole, alb=0.8
Basic SNR (IT=0.1875s)		**<0.5% (~0.3%)**	**<5% (~3%)**	**<30% (~15%)**	**<60% (~30%)**	**>100% (~100%)**
polarisation error diffuser plate		<0.4% ~0.3%	? (larger than UV)	50%	70%	?
Spatial aliassing WP210		0.2%		<2%	<1%	<15%
Spectral Resolution WP 230	Defocusing (1/2)* Open slit (1/2)* usampl./defoc(2.2px. FWHM)*	0.3% 0.2% 0.2%±0.3%	3% 2%	18% 11% 2%±15%	35% 25% 80%±30%	
basic SNR included						
RTM assumption WP250	PS vs Spherical w/ refraction Spherical w/o refraction Spherical vs. PS GRD Spherical vs PS TOA	<1% <0.3% <1% <4%	<1% <0.2%	<1% <0.5% <1% <6%	<1% <1% <1% <5%	
BRDF WP260		<0.3%	<3%	<2%	<3%	
Pointing accuracy WP270		<0.5%		<1%	<0.5%	

Table Error! No text of specified style in document.**-2: Trace gas column error budgets for GOME-2**

For a fixed wavelength shift between measurements of backscattered and direct-sun spectra (i.e. for a fixed Doppler shift), undersampling gives rise to a systematic error. Combining the basic ESD and undersampling error is not possible, thus the bias can only be added to the ESD (i.e. bias±1σ shown in Table **Error! No text of specified style in document.**-2). Here the undersampling error is given as an error resulting from correcting a 0.008 nm shift (characteristic Doppler shift for GOME-1) by back interpolation. For the particular case of a 0.008nm shift, the undersampling error was found to vary in a highly non-linear way (even in terms of sign) with slit-function FWHM and in a different way for different trace gases. Although a suitable undersampling correction may suffice for most trace gases, systematic errors due to undersampling were observed to be important for BrO. In the following, each trace gas is discussed individually.

Total ozone

In the UV (Band 2), ozone absorption is strong and this results in a very small baseline ESD for the nominal integration time of 0.1875s. Spatial aliasing[8] and geolocation/ pointing errors have negligible impact on total ozone. All other error sources are non-negligible, though still fairly small[9].

Interference from other trace gases, notably water vapour, and the angular dependence of sunglint BRDF have more severe impacts on the VIS retrieval[10]. Slant column errors in the visible are higher than in the UV, however, the advantage lies in the negligible wavelength dependence of the AMF in this spectral region. The influence of the diffuser plate on the retrieved total ozone column is still unknown, but may be on the order of few tenths of a percent (higher in the visible) and may be non-negligible.

Nitrogen dioxide

In case of nitrogen dioxide, the error is clearly dominated by diffuser plate signatures (50%) and photon noise (30%). ESDs can be improved by co-adding. This leads, however, to larger ground pixel areas, which is unfavourable for tropospheric retrieval. The latter is hampered by reduction of the clear-sky occurrences with

[8] Spatial aliasing was investigated with a few representative Landsat images. Further investigations may be needed to confirm this result.

[9] One should note that violation of the weak absorber approximation is not accounted for in this error budget. It may be more appropriate to use either modified or weighting function DOAS in the UV window. Operational GOME-1 retrieval is still based on the standard DOAS approach. The standard two-step DOAS retrieval is more appropriate in the visible (450-497 nm) where absorption is weak.

[10] Because of dichroic features in Channel 3 of GOME-1, the visible window has been only occasionally used for ozone retrieval.

larger pixel areas. Opening the slit leads to a net reduction in ESD. (The increase in photon flux outweighs the information loss from reduced spectral resolution). Defocusing, by contrast, leads to an increased ESD. (There is no increase in photon flux to compensate the decreased spectral resolution.) For some scenarios, saturation of detectors would occur if the slit was opened. This could be overcome by halving the integration time to 93.75 ms and: (1) co-adding to 0.1875 sec; (2) reading-out every second 93.75ms ground pixel or (3) reading-out every pixel and doubling the data rate. In the second and third cases, ground pixel size would be decreased to 40X40km2 (1920 km swath width) benefiting tropospheric retrieval. The second option leads to gaps in the ground coverage in the across-track scan but keeps the data rate unchanged in comparison to the 0.1875 sec ground pixel observations, as does the first option. It is appreciated by the study team that the increase in GOME-2 data rate associated with the third option would be difficult to accommodate in practice. All other error sources are insignificant against the baseline and diffuser plate error.

Bromine oxide

Similar conclusions to NO_2 can be drawn for bromine oxide retrieval. Largest error sources are diffuser plate spectral interference (70%) and photon noise (<70%). A systematic bias of up to 80% is also estimated due to interpolation error at 2.2 pixels FWHM spectral resolution in combination with defocusing option. One has to keep in mind that BrO is photochemically active, and is near the detection limit at low solar zenith angles (tropics). Opening the slit could, in principle, improve ESDs significantly for BrO, as for NO_2. However, the reduction in sensitivity to undersampling from this or defocusing appears very sensitive to the precise choice of FWHM, fitting window and jointly retrieved parameters.

Chlorine dioxide

Chlorine dioxide is a photochemically active species and can only be retrieved under twilight condition and under ozone hole condition. The error is dominated by photon noise (~100%). Some co-adding may be required to improve retrieval, however, one should keep in mind that OClO column amounts have a strong solar zenith angle dependence.

25.3 Recommendations for Operational Settings and Error Mitigation and for Further Studies

25.3.1 Background to the Recommendations

The recommendations made below are based principally, though not exclusively, on quantitative error estimates from GOME-2 retrieval simulations performed in this study. The schemes employed in simulations for ozone profiles and trace gas columns are based very closely on those applied to real GOME-1 measurements by RAL and IUP, respectively. Both these schemes are the result of nearly a decade of development work, so are now mature and have been demonstrated to be among the most reliable of their kind. Although the magnitudes of simulated errors are specific to the detailed formulations of these two particular algorithms, the recommendations made below are expected to prove quite robust and to be applicable also to other schemes, which might be adopted for operational processing of GOME-2 data.

Most simulations in this study have been performed for a set of realistic and representative, geo-temporal scenarios (24 in total), which span a diverse range of observing conditions. The recommendations below are therefore expected to be applicable to GOME-2 observing conditions generally (though not universally).

Although an extensive set of instrumental and geophysical parameters and error sources have been addressed, it should be noted that errors in the high-resolution solar reference spectrum, trace gas absorption cross-sections and atmospheric scattering parameters have not been considered. These are considered likely to contribute significant additional non-random errors.

Recommendations labelled "A" concern instrument operational settings, ground processor settings and instrument pre-flight characterisation. Those labelled "B" concern the instrument itself. Those labelled "C" concern further studies to define instrument settings and mitigate errors.

25.3.2 Band 1 sampling

Long-wave limit

The sensitivity of ozone profile retrieval to the longwave limit adopted in Band 1B was assessed, in terms of ESD and the other components of the baseline error budget. Although it would be worthwhile in terms of ESD to extend to 314 nm, this would not be desirable in terms of the magnitudes of other simulated errors and their RSS. More decisively, the sensitivity to static and dynamic (spatial aliasing) scene inhomogeneity is substantially greater, when it is extended to 314 nm.

Recommendation A1

For ozone profile retrieval, the recommended longwave limit in Band 1B is 307 nm.

Spatial/temporal

For simulations with the RAL algorithm in which a "noise floor" of 1%[11] is imposed on sun-normalised Band 1 radiances, the additional read-out noise associated with reading-out Band 1A spectra at 1.5s intervals and reading out Band 1B spectra at the nominal 0.1875s instead of the nominal for B1A of 12s has a negligible impact on ESDs. Reading-out Band 1A at a higher frequency reduces the range of (across-track) viewing angles in a given ground-pixel. This would be very desirable in order to alleviate forward modelling errors associated with the strongly non-linear view-angle dependencies of (a) atmospheric radiative transfer and (b)

[11] The noise floor of 1% is based on typical RMS fitting residuals in Band 1attained in processing of GOME-1 flight data. This noise floor comes into play at long wavelengths in Band 1 (typically 290 nm at Band 1B integration time) where the predictions from a noise model which combines only photon and read-out noise falls below this value. The noise floor therefore represents the combined effects of other noise sources, which are in practice significant at these wavelengths, e.g. errors in the high-resolution solar reference spectrum, slit-function shape and modelling of the Ring effect.

GOME-2 instrumental properties (n.b. wavelength-dependent polarisation properties of the scan-mirror). Co-adding 1.5s Band 1A spectra along-track could then yield comparable radiometric precision to a single 12s integration but more easily modelled spectra.

Reading out Band 1B at the same frequency as Band 2 allows correspondence between their views of the troposphere (n.b. cloud). Retrievals from individual Band 1B ground pixels should therefore provide more consistent a priori estimates in the troposphere for the corresponding Band 2 pixels.

Recommendation A2

For ozone profile retrieval, it is recommended that the integration times for Band 1A and Band 1B be 1.5s and 0.1875s, respectively.

25.3.3 Diffuser

The impact of spectral structures in the BRDF of the diffuser plate on trace gas column retrieval was reviewed. For GOME-1, such spectral structures had been found to limit the accuracy (and in some cases detectability) of trace gases other than ozone. For GOME-2, it was confirmed that a diffuser plate with much improved spectral characteristics would be needed to measure trace gases other than ozone.

Recommendation B1

For retrieval of trace gases other than ozone, it is strongly recommended to switch to a diffuser plate with peak-to-peak spectral signatures of less than 10^{-4}.

25.3.4 Pre-flight characterisation of slit-function shape

It has been demonstrated unequivocally in simulations for GOME-2 in this study that characterisation of the slit-function shape in the relevant wavelength interval of Band 2 is of critical importance to ozone profile retrieval. Use of the onboard line-lamp alone to characterise slit-function shape will not suffice because:

a. Absence of suitable lamp lines in the wavelength interval between 307 and 333nm

b. Lamp-lines at fixed, discrete wavelengths outside this interval do not permit the slit-function shape to be adequately resolved.

Retrieval of absolute wavelength registration and slit-function width from direct-sun spectra is part of the standard RAL scheme for processing GOME-1 data. However, retrieval of additional parameters to characterise slit-function shape would be a difficult to formulate and ill-posed problem.

Pre-flight measurements of slit-function shape at sub-pixel resolution in the relevant wavelength interval of Band 2 will therefore be necessary to meet user requirements on the accuracy of GOME-2 ozone profile retrieval. Such measurements would also offer a major advance on GOME-1, for which errors in knowledge of slit-function shape can now be identified to be a limiting factor on accuracy.

Recommendation A3

For ozone profile retrieval, it is strongly recommended that the slit-function shape in Band 2 below 340nm be accurately determined before flight at sub-pixel resolution.

Recommendation C1

Specify requirements for laboratory measurements of slit-function shape and quantify the benefits for the Band 2 step of O_3 profile retrieval.

The impact on trace gas columns of error in knowledge of slit-function shape was not addressed within this study. However, total column processing options to (a) use absorption cross-sections measured at higher resolution than GOME-2 and (b) correct for wavelength misregistration between direct-sun and backscattered spectra using a high-resolution solar reference spectrum would depend on this[12].

Recommendation C2

Quantify errors in knowledge of slit-function shape for: (a) the Band 1 step of O_3 profile retrieval; (b) trace gas column retrieval and (c) aerosol and cloud retrieval using O_2 A-band.

25.3.5 Slit-function width

Defocusing

For ozone profile retrieval, simulations in which the slit width was increased while overall photon flux on the detector arrays was held fixed showed that defocusing from 2-3px (0.24 –0.36nm) in Band 2 would not significantly degrade ESDs but would substantially reduce sensitivity to undersampling errors. This could potentially allow a much simpler correction scheme to be applied for wavelength misregistration between backscattered and direct-sun spectra[13], which in turn could substantially improve computational efficiency. Defocusing could therefore offer a potential net gain for ozone profile retrieval.

For trace gas column retrieval, the variation of ESD with FWHM was found to be trace gas specific and the variation of undersampling error with FWHM was found to be highly non-linear and trace gas specific. It was therefore not possible on the basis of results from this study to reach a clear-cut conclusion in regard to defocusing.

Slit opening

For trace gas column retrieval, the changes to ESD associated with slit opening have been quantified and compared to those of defocusing and are again trace gas specific. For NO_2, a significant reduction (from 15% to 11%) in basic ESD could be obtained by opening the slit from 0.5nm to 1 nm in Band 3, via the increased photon flux. It is noted that the photon flux in Band 3 could also be increased, in principle, by opening the aperture stop in Band 3/4. Although it is recognised that detector saturation would provide practical constraints and that the other consequences and implications of opening the slit or aperture stop would need to be evaluated.

For ozone profile retrieval, the effects on the ESDs of opening the slit can be qualitatively inferred from those of defocusing to the same slit-function width: ESDs would either increase less than for defocusing or would actually decrease. Sensitivity to undersampling errors would not decrease as much for slit opening as for defocusing to the same slit-function width though, because the opened slit would retain its focused, non-

[12] The alternatives are to use absorption cross-sections measured by the GOME-2 FM itself and to reduce undersampling errors to an insignificant level.
[13] This misregistration is the source of the so-called undersampling error.

Gaussian shape. Since no ozone profile retrieval simulations were conducted to quantify slit opening[14], it is not possible to conclude what the net gain would be by comparison to defocusing.

Recommendation B2:

For retrieval of trace gas columns other than ozone, it is recommended to open the slit in preference to the defocusing option.

Recommendation C3:

More studies are needed to investigate the impacts of: (a) defocusing, (b) opening the slit and (c) opening the Band 3/4 aperture stop, in particular with respect to hardware implications.

25.3.6 Detector read-out time

To eliminate susceptibility of ozone profile retrieval to extreme errors from spatial aliasing, it would be desirable to reduce detector read-out time in Band 1B. *(However, the proportion of extreme cases is considered too small to warrant a fully-fledged recommendation).*

Recommendation A4:

It is recommended that the impacts of spatial aliasing be quantified thoroughly:

(a) Impact on ozone profiles and trace-gas columns via use of PMD measurements to correct polarisation response of detector arrays

(b) Global statistical analysis of ozone profiles and trace gas columns using ATSR-2 images

(c) Assess impact on geophysical products retrieved from PMD measurements

(d) Assess impact on multi-wavelength aerosol retrieval

along with possible use of PMD measurements at higher spatial resolution to mitigate these impacts.

25.3.7 Selection of swath width and ground-pixel size

A number of the issues addressed in this study have a bearing on selection of swath-width and/or ground-pixel size for GOME-2. Several factors identified from GOME-1 data analysis, though not addressed explicitly in the study, also need to be considered.

(a) Non-linear Dependencies of Radiative Transfer and GOME-2 Polarisation Response on View-Angle

- To increase the computational efficiency of the Band 1A retrieval step and to reduce errors associated with non-linear view-angle dependencies, especially in the outer pixels, it would be desirable to limit the pixel size across-track by limiting swath width, as well as the Band 1A integration time.

[14] Opening the slit would also impact on PMD measurements, and hence indirectly on ozone profile retrieval via the polarisation correction. However, the impact on PMDs was not assessed either.

(b) Horizontal gradients in RI

- Temperature-induced horizontal gradients in RI do not affect decisions on swath-width or ground pixel size.

(c) Pseudo-spherical approximation

- Selection of the 1920 km swath width would increase the complexity of either the GOME-2 operational timeline or the radiative transfer model used in Level-2 processing for the outer pixels.

(d) Sunglint occurrence

- The need to account for sunglint does not significantly influence the decision between 960 km and 1920 km swath widths.

(e) Dependence of cloud obscuration on view-angle

- The dependence of cloud obscuration on view-angle is not a significant factor for the choice between 960 km (±29°) and 1920km (±46°) swaths.

(f) Dependence of cloud-free pixel occurrence on pixel size

In work undertaken outside the scope of this study using ATSR-2 data, the frequency of occurrence of ground pixels containing a given fraction of cloud was determined as a function of ground pixel size. The occurrence of cloud-free pixels was found to be a strong function of ground pixel size:

~7% for 80 km x 40 km (nominal for GOME-2 1920 km swath)
~10% for 40 km x 40 km. (nominal for GOME-2 960 km swath)
~23% for 12 km circular (IASI)

- The rationale for GOME-2 to employ a small ground pixel size is strong, in order to maximize the fraction of cloud-free scenes and facilitate sounding of tropospheric composition.

(g) Dependence of scene-inhomogeneity on pixel size

- The rationale for GOME-2 to employ a small ground pixel size is further strengthened by the reduction in ozone profile retrieval errors caused by scene inhomogeneities which this would allow, especially in the troposphere

(h) Conclusions on swath width and ground pixel size

It can be concluded from the above considerations that:

1) The accuracy of individual ozone profile retrievals and
2) The fraction and total number of observations of the cloud-free lower troposphere

would both benefit substantially from adopting for GOME-2:

1) A ground pixel size smaller than 40 km x 40 km
2) A swath-width narrower than 960 km

However, two additional factors, which affect these decisions, are:

1) Spatio-temporal sampling of the (4-D) fields of ozone and other trace gases
2) Potential use of sub-pixel information on cloud/surface properties from AVHRR3

Although ground-pixel size is intimately linked to swath width for an across-track scanner such as GOME-2, the detector integration time is programmable. So the possibility exists to employ an integration time <0.1875s (ie 0.09375s) in Bands 1B, 2, 3 and 4. Even if the overall data-rate (and hence number of across-track pixels) could not be increased from its nominal value, it would therefore still be feasible to combine a pixel of across-track dimension <40 km with a 960 km swath or one of <80 km with a 1920 km swath. If integration time was reduced from 0.1875s to 0.09375s, it would be desirable to also reduce read-out time by a corresponding factor of two, to avoid increasing susceptibility to spatial aliasing.

To decide on the ground-pixel size and swath width to be used operationally, an objective comparison of different options must therefore be made in terms of the fidelity with which structure in the 4-D fields of ozone and other trace gases would be determined. Such an objective comparison could best be performed in the frame of a data assimilation model through an observation system simulation experiment (OSSE) in which the observational errors[15] and the sampling of the lower troposphere took into account cloud and other factors in a realistic way.

Recommendation A5

It is recommended that an OSSE be undertaken for GOME-2 to decide on optimum ground-pixel size and swath width.

[15] Observational errors would need to take into consideration static and *dynamic* (i.e. spatial aliasing) errors from scene inhomogeneity, as well as photon noise and read-out noise.

25.3.8 Summary of Recommendations

A number of specific recommendations were identified in the previous sections. These are summarised in the tables below. Table 3A concerns instrument operational settings, ground processor settings and instrument pre-flight characterisation.

Table Error! No text of specified style in document.**-3A: Recommendations for instrument operational settings, ground processor settings and instrument pre-flight characterisation**

A1	For O_3 profile retrieval, it is recommended to not use Band 1B wavelengths above 307nm.
A2	For O_3 profile retrieval, it is recommended that the integration times for Bands 1A and 1B be 1.5s and 0.1875s, respectively.
A3	For O_3 profile retrieval, it is strongly recommended that the slit-function shape in Band 2 below 340nm be accurately determined before flight at sub-pixel resolution.
A4	It is recommended that the impact of spatial aliasing be assessed more thoroughly: (a) Impact on O_3 profiles and trace gas columns via use of PMD measurements to correct polarisation response of detector arrays (b) Global statistical analysis of O_3 profiles and trace gas columns using ATSR-2 images (c) Impact on geophysical products retrieved from PMD measurements (d) Impact on multi-wavelength aerosol retrieval along with possible use of PMD measurements at higher spatial resolution to mitigate these impacts
A5	It is recommended that an OSSE be undertaken for GOME-2 to decide optimum ground-pixel size and swath width

Two recommendations identified in previous sections, flowing from the trace gas column analyses performed by the University of Bremen in this and other studies, concern the specification of the instrument itself. Eumetsat is therefore invited, in addition, to evaluate possibilities to implement modifications to the GOME-2 instrument in order to mitigate errors, which would otherwise limit the quality of trace gas column retrievals (Table 3B).

Table 3B: Recommendations from trace gas column analysis for error mitigation through instrument modifications

B1	For retrieval of trace gas columns other than ozone, it is strongly recommended to switch to a diffuser plate with peak-to-peak spectral signatures of less than 10^{-4}.
B2	For retrieval of trace gas columns other than ozone, it is recommended to open the slit in preference to the defocusing option.

The following further studies are recommended to define GOME-2 instrument settings and to mitigate errors (Table 3C).

Table 3C: Recommendations for further studies to define instrument settings and to mitigate errors

C1	Specify requirements for laboratory measurements of slit-function shape and quantify the benefits for the Band 2 step of O_3 profile retrieval.
C2	Quantify errors in knowledge of slit-function shape for: (a) the Band 1 step of O_3 profile retrieval; (b) trace gas column retrieval and (c) aerosol and cloud retrieval using O_2 A-band.
C3	More studies are needed to investigate the impacts of: (a) defocusing, (b) opening the slit and (c) opening the Band 3/4 aperture stop, in particular with respect to hardware implications.
C4	Investigate and quantify the benefits of algorithm improvements for ozone profile retrieval to mitigate errors from wavelength-dependent degradation in the uv.
C5	Assess possible use of onboard white light source to monitor wavelength-dependent degradation in the uv
C6	Implement and quantify the benefits to ozone profile and trace gas column retrievals of algorithm improvements to mitigate errors due to sunglint.
C7	Quantify errors arising from non-linear radiative transfer in conjunction with static scene inhomogeneities in cloud and surface reflectance.
C8	Assess errors on ozone profiles from the assumed vertical distribution of aerosol more thoroughly, in order to better gauge instrumental errors
C9	Assess the impact on ozone profile and ozone column error budgets of adding visible wavelengths
C10	Assess errors from uncertainties in absorption cross-sections of ozone and other trace gases, the high-resolution solar reference spectrum and polarised atmospheric radiative transfer, in order to better gauge instrumental errors

To achieve the stringent accuracy in GOME-2 Level-2 processing required for long-term monitoring of ozone, as part of EUMETSAT's remit for climate monitoring, retrieval schemes will need to be more sophisticated than those in contemporary use. Potential advances include the addition of polarization measurements, for ozone profile retrieval, and better (height-resolved) climatologies of trace gases and temperature for AMF data-bases, improved handling of the Ring effect and novel alternatives to the standard DOAS scheme, for trace gas column retrieval. In addition to their relevance to GOME-2 on METOP, studies to improve retrieval schemes could also be relevant to future re-processing of GOME-1 data, and therefore to production of a homogeneous data-set from GOME-1 and GOME-2[16]. Further analysis of the degradation to GOME-1 (UV) measurements (principally manifest through changes to scan-mirror reflectivity, and possibly also through changes to diffuser BRDF) will be necessary for this purpose, particularly to utilise height-resolved O_3 data.

High spatial sampling and high accuracy were both confirmed in this study to be important to tropospheric sounding. It would therefore be worthwhile now for ESA to look beyond GOME-2 and identify the *spatial sampling* and *accuracy* requirements of a future mission and begin to evaluate technology developments[17], which might be needed to meet these.

[16] Other UV nadir sounders of a similar class, e.g. SCIAMACHY on Envisat and OMI on Eos Aura, are also expected to contribute to this long-term data set.

[17] For example, to compare the relative merits of (2-D) CCD detectors and conventional diode array detectors.

GOME-2 Error Assessment

Appendix A

Task 1

Tool Adaptation and Definition of Data

(RAL figures)

APPENDIX A: TOOL ADAPTATION AND DEFINITION OF DATA (RAL figures)

CONTENTS LIST of CD-ROM File: GOME-2_FR_App_A.pdf

List of Figures

GOME-2 Error Assessment

Appendix B

Task 2

Analysis of Error Sources

(RAL figures)

APPENDIX B: ANALYSIS OF ERROR SOURCES (RAL figures)

CONTENTS LIST of CD-ROM File: GOME-2_FR_App_B.pdf

WP210: Spatial Aliasing

WP220: Processing Options for Band 1A

WP230: Reduction of Spectral Resolution

B3.1 Line-lamp spectrum

B3.2 Slit function retrieval from solar spectrum

B3.3 Comparison of slit functions

B3.4 Mapped spectral signatures of imperfect slit

B3.5 Ozone-profile retrieval simulation results

B3.6 B1 wavelength range: 265-307 nm

B3.7 B1 wavelength range: 265-314 nm

WP240: Atmospheric Profile Related Effects

B4.1 Impact of Temperature Gradients on

WP250: Radiative Transfer Model Assumptions and Earth Curvature

B5.1 Spectral difference - Solar geometry specified at : ground

B5.2 Spectral difference - Solar geometry specified at : top of atmosphere

B5.3 Profile errors : Band 1 wavelength range: 265-307 nm

B5.4 Profile errors : Band 1 wavelength range: 265-314 nm

WP260: Non-Lambertian Surface Reflectance

B6.1 Impact of lambertian BRDF approximation

NOTE:

The complete set of additional figures relating to Task 1 is held on the accompanying CD-ROM, in file "GOME-2_FR_App_A.pdf". The CDROM contains an electronic version (in pdf format) of the complete GOME-2 Error Assessment Study Final Report.

List of Figures

GOME-2 Error Assessment

Appendix C

Task 3

Optimal Operational Settings

and

Error Mitigation

(RAL figures)

APPENDIX C: OPTIMAL OPERATIONAL SETTINGS AND ERROR MITIGATION (RAL figures)

CONTENTS LIST of CD-ROM File: GOME-2_FR_App_C.pdf

WP310: Summary plots of Task 1 and Task 2 errors

NOTE:

The complete set of additional figures relating to Task 1 is held on the accompanying CD-ROM, in file "GOME-2_FR_App_A.pdf". The CDROM contains an electronic version (in pdf format) of the complete GOME-2 Error Assessment Study Final Report.

GOME-2 Error Assessment

Appendix D

Diffuser Plate Spectral Structures and their Influence on GOME Slant Columns

serco

APPENDIX

D Diffuser Plate Spectral Structures

GOME-2 Error Assessment CD-ROM File:
GOME-2_FR__Appendices.pdf

Diffuser plate spectral structures and their influence on GOME slant columns

A. Richter[1] and T. Wagner[2]
[1] Insitute of Environmental Physics, University of Bremen
[2] Insitute of Environmental Physics, University of Heidelberg

Technical note, January 2001

D.1 The problem

As soon as GOME spectra were available for analysis, several groups started to apply their own DOAS algorithms to derive slant columns of O_3 and NO_2, and later also BrO, OClO, SO_2, HCHO, H_2O and O_4. It soon became obvious, that the residuals obtained from the DOAS fit were not as good as expected from the SNR of the instrument, and that the residuals were not of random nature but systematic and rather stable over longer time periods. It turned out that using an earth-shine instead of the solar irradiance as a background improves the residual significantly, but this introduces the problem of an unknown amount of absorption in the background measurement. Several factors have been identified that contribute to the larger than expected residuals:

- The undersampling of the spectra in conjunction with the Doppler shift of the solar irradiance spectrum
- Small errors in the Ring spectrum
- Small variations in the effective slit function for not uniformly illuminated ground pixels

However, even with these effects considered, the quality of the residuals is poorer than expected.

A second but related problem became apparent when longer time series of NO_2 became available and could be compared with ground based measurements. While the general agreement between GOME and ground-based zenith-sky measurements is good, the **satellite data show much more variability** even at clean air sites (see Fig. 1), and **this variability is repeated in amplitude and phase almost identically from year for yea**r (see Fig. 3). Comparison between the operational product and scientific products from the University of Bremen and Heidelberg showed, that the effect is not restricted to the lv2-product but is reproduced by independent algorithms. Further analysis proved that the same problem exists for all other absorbers derived from GOME spectra, but with a specific pattern for each absorber and fitting window.

D.2 Why do we think that the diffuser plate is responsible for the problem?

In order to identify the source of the problem, several tests have been performed on GOME data as described below.

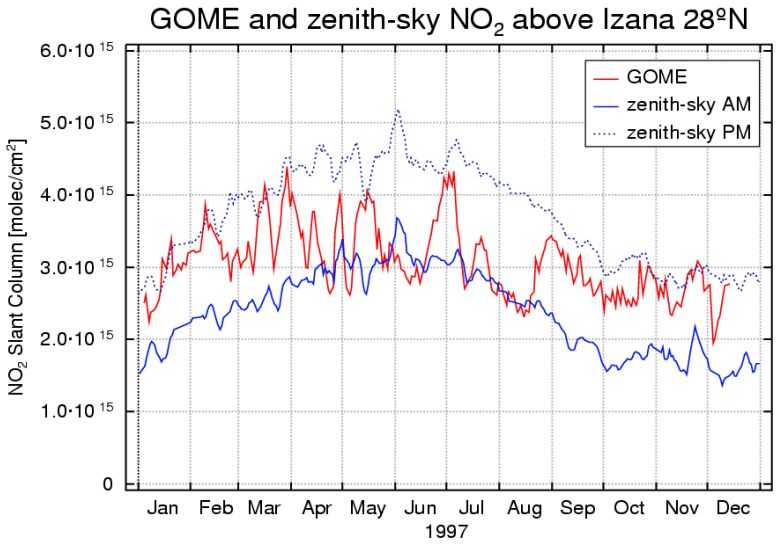

Figure D 1: GOME operational NO_2 vertical columns above Izana as compared to ground based zenith-sky measurements (data courtesy of M. Gil and M. Yela). While the general values agree well, GOME columns show much more variability than expected, in particular in summer.

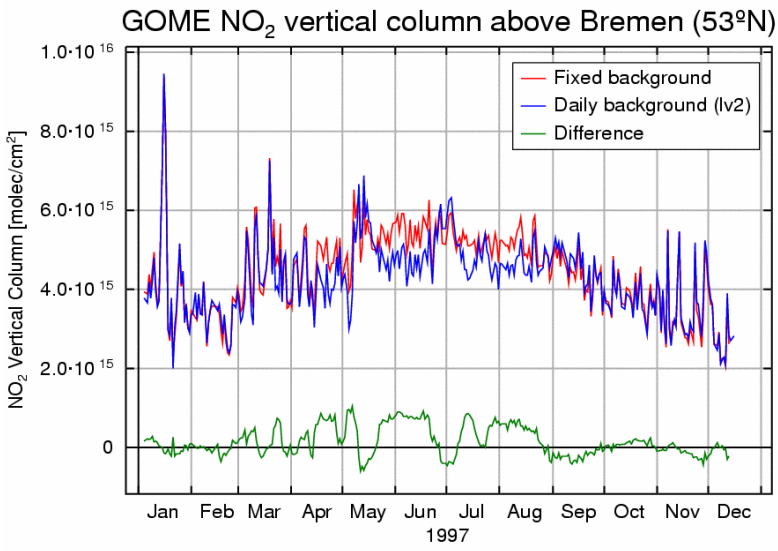

Figure 2: GOME NO_2 vertical columns above Bremen as derived with a daily irradiance spectrum (lv2 product) and a fixed background spectrum. The difference between the two evaluations is the structure introduced by the diffuser plate, but divided by the airmass factor applied to the slant columns.

First of all, a larger set of GOME data has been analysed using a single solar irradiance spectrum instead of the daily one. The resulting time series is much smoother and compares favourable to the ground-based measurements (Fig 2). However, the error cancelling achieved by using the daily irradiance spectrum is no longer in effect, and instrumental changes introduce drifts into the derived NO_2 time series. Also, the problem of what background spectrum to choose and thereby which offset to introduce to the slant columns remains unsolved. The fact, that the large variability seen in the lv2 data is not present in this special analysis shows, that **the problem lies with the solar spectra**, not with the earth-shine measurements.

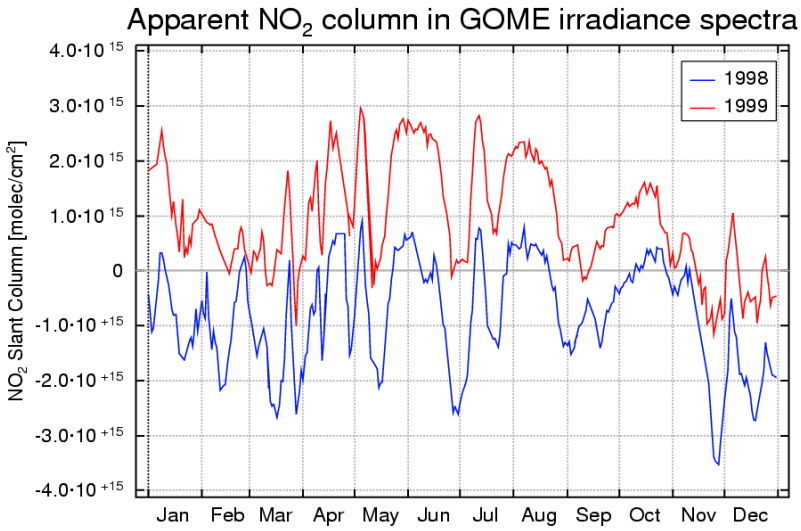

Figure 3: Apparent NO_2 slant column when applying the standard NO_2 fit to all GOME irradiance spectra, using one arbitrarily chosen solar spectrum as background. Small and random columns are expected, but large and systematic variations are found. The similarity between the structures found in this test and in Figures 1 and 2 are obvious.

In a second test, a large set of GOME irradiance measurements has been analysed for NO_2 absorptions using the same settings as in the standard NO_2 fit and an arbitrarily selected solar spectrum as background. The resulting NO_2 column should be very close to 0 and should not show any systematic structures. However, the fit retrieved large NO_2 columns (up to 3 10^{15} molec/cm^2) and a seasonal variation that matches the artifacts observed in the difference between GOME NO_2 and ground-based measurement (see Figure 3). From this result we conclude, that **the observed variation is introduced by variations in the solar irradiance measurement**.

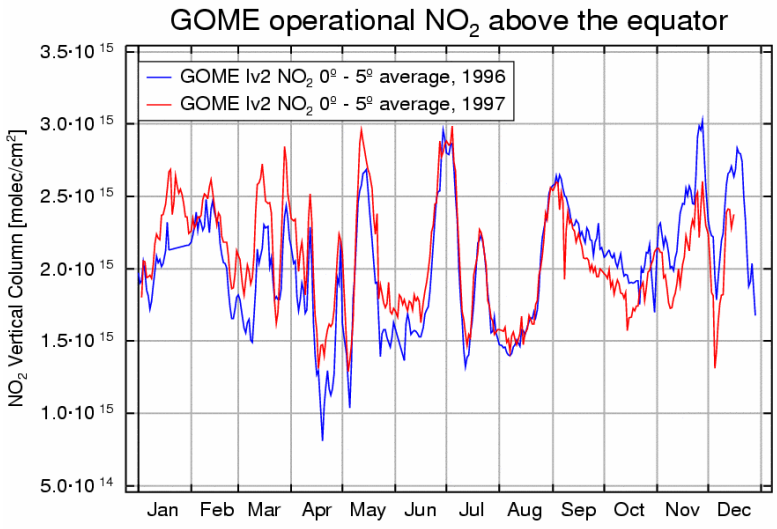

Figure 4: GOME operational NO_2 vertical columns above the equator for 1996 and 1997. Again, the structures seen in Figures 1-3 appear.

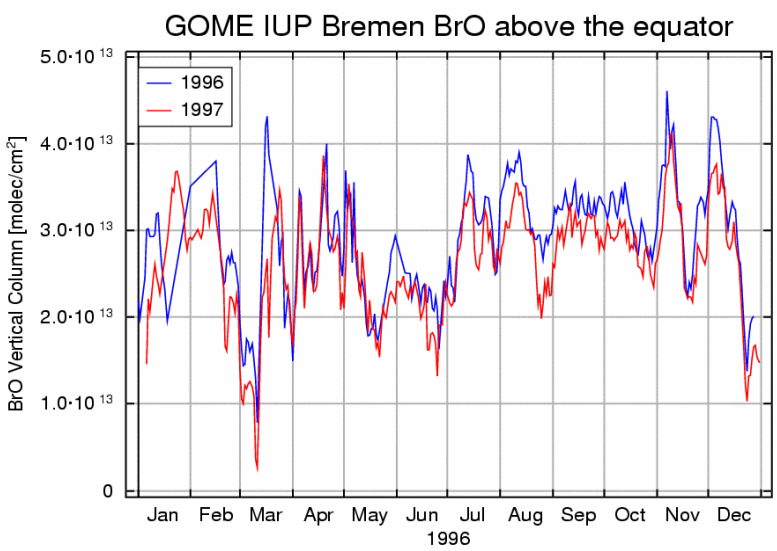

Figure 5: GOME BrO vertical columns above the equator for 1996 and 1997 as derived by the IUP Bremen. Again, similar structures seen in Figures 1 - 4 appear, however with a different amplitude and not at the same time of the year.

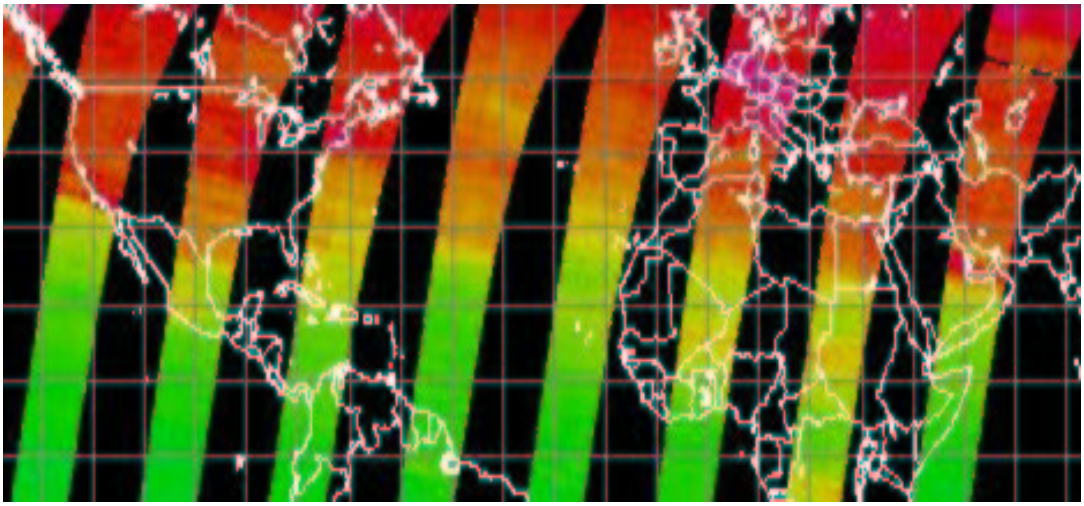

NO_2 VCD, 01.07.1997, daily solar spectrum

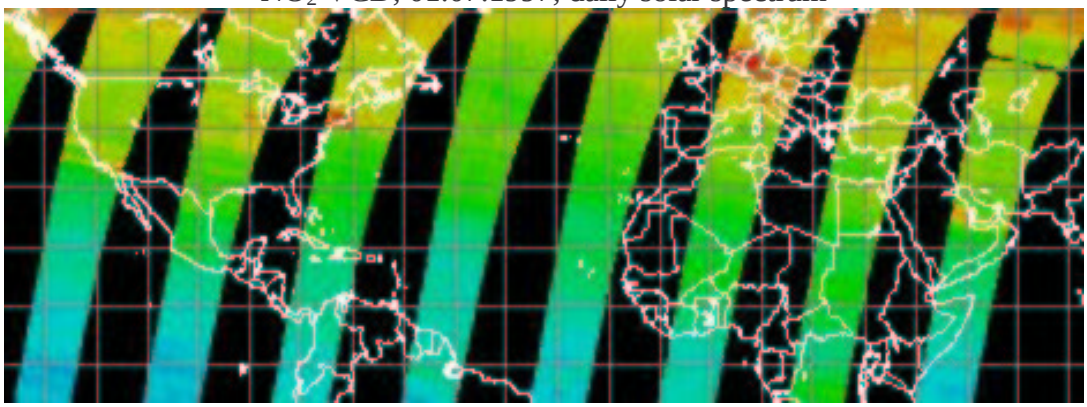

NO_2 VCD, 01.07.1997, fixed reference, solar spectrum from 01.01.1997

Figure 6: Examples GOME NO_2 maps for a day (01.07.1997) with a large uncertainty introduced by the spectral structures caused by the diffuser plate. Especially in the Tropics the difference between the evaluation with fixed or daily reference spectrum can be large (up to about 100%).

D.3 How large is the error introduced to the products?

The error introduced by the diffuser is a constant offset for slant columns derived using a specific irradiance spectrum and independent of location and solar zenith angle. The absolute error therefore depends on the airmass factor and the relative error on the vertical column to be expected. In general, the problem is most severe in equatorial regions and for small absorptions. In Figure 4, the slant columns integrated along the equator between 0° and 5°N latitude are plotted for two years for NO_2 (lv2-product), in Figure 5 the same exercise is shown for BrO. In this area, the relative **errors are up to 100% for NO_2** (see also Figure 6) and **70 – 100 % for BrO**, depending on what one assumes to be the true column. At higher latitudes, the relative errors are much smaller, but still significant as illustrated in Figure 2 for NO_2 above Bremen, where in summer errors of more than 20% are introduced . In general, the errors can only be neglected at high latitudes in winter or for scenarios with large absorptions such as OClO in the activated polar vortex, tropospheric BrO events in the polar regions or biomass burning scenarios.

D.4 What are possible solutions?

Three possible work-around solutions have been examined that could in principle eliminate the effect:

1. **Use of a single irradiance measurement as a background spectrum** for a longer time series. With this approach, the variations no longer are existent. However, instrumental changes introduce large drifts in the time series and also increase the fitting residuals with time. The method therefore gives acceptable results for NO_2 at mid- and high latitudes, but not for NO_2 at low latitudes and not for any one of the smaller absorbers (BrO, OClO, SO_2, HCHO). One general shortcoming of this method is that it remains open which solar spectrum yields the true absolute values.
2. **Use of selected earth-shine measurements as background spectrum**. With this approach, the unknown amount of absorption in the background spectrum has to be guessed and added to the derived columns. This is acceptable for OClO, where high sun scenarios with negligible OClO can be found in every orbit, but not for other absorbers where no such a priori knowledge is available.
3. For some absorbers the assumption can be made, that **concentrations in equatorial regions are constant and well known from models**, but this is difficult to justify and introduces noise and considerable uncertainty into the results. In addition, it by definition makes GOME measurements meaningless in tropical regions, one of the scientifically most interesting parts of the world.

All three methods have successfully been applied to certain questions but have large drawbacks and therefore should be avoided if possible.

D.4 Summary and conclusions

1. GOME irradiance measurements suffer from spectral artefacts, that correlate strongly with the differential absorption structures used for the retrieval of trace gases with the DOAS technique.
2. The variations introduced in the slant columns are independent of solar zenith angle and location, and are repeated from year to year.
3. The most probable explanation for the structures is a small angle dependence of the spectral reflectivity of the diffuser plate and the variation in the incident of solar radiation on the diffuser during one year.
4. The absolute error introduced by this effect depends on the molecule and the spectral region used for the retrieval and affects all absorbers. For equatorial regions it is of the order of 50% for NO_2, 75% for BrO and even more for weaker absorbers such as HCHO. With the exception of O_3, it is an important, if not the most important error source for all GOME columns at low and middle latitudes.
5. It also has to be pointed out, that with the diffuser structures, an uncertainty exists in what the *absolute* values are for all GOME products, as any choice of a specific solar irradiance spectrum will introduce its own slant column offset in the analysis.
6. There currently exists no satisfying algorithm or work around to compensate the effect for GOME data. All corrections applied to the fits or to the slant columns introduce other serious problems for the interpretation of the data.

We therefore conclude, that everything should be done to eliminate the source of the effect in the SCIAMACHY and GOME-2 instruments by introducing a diffuser with as little spectral characteristics as possible.

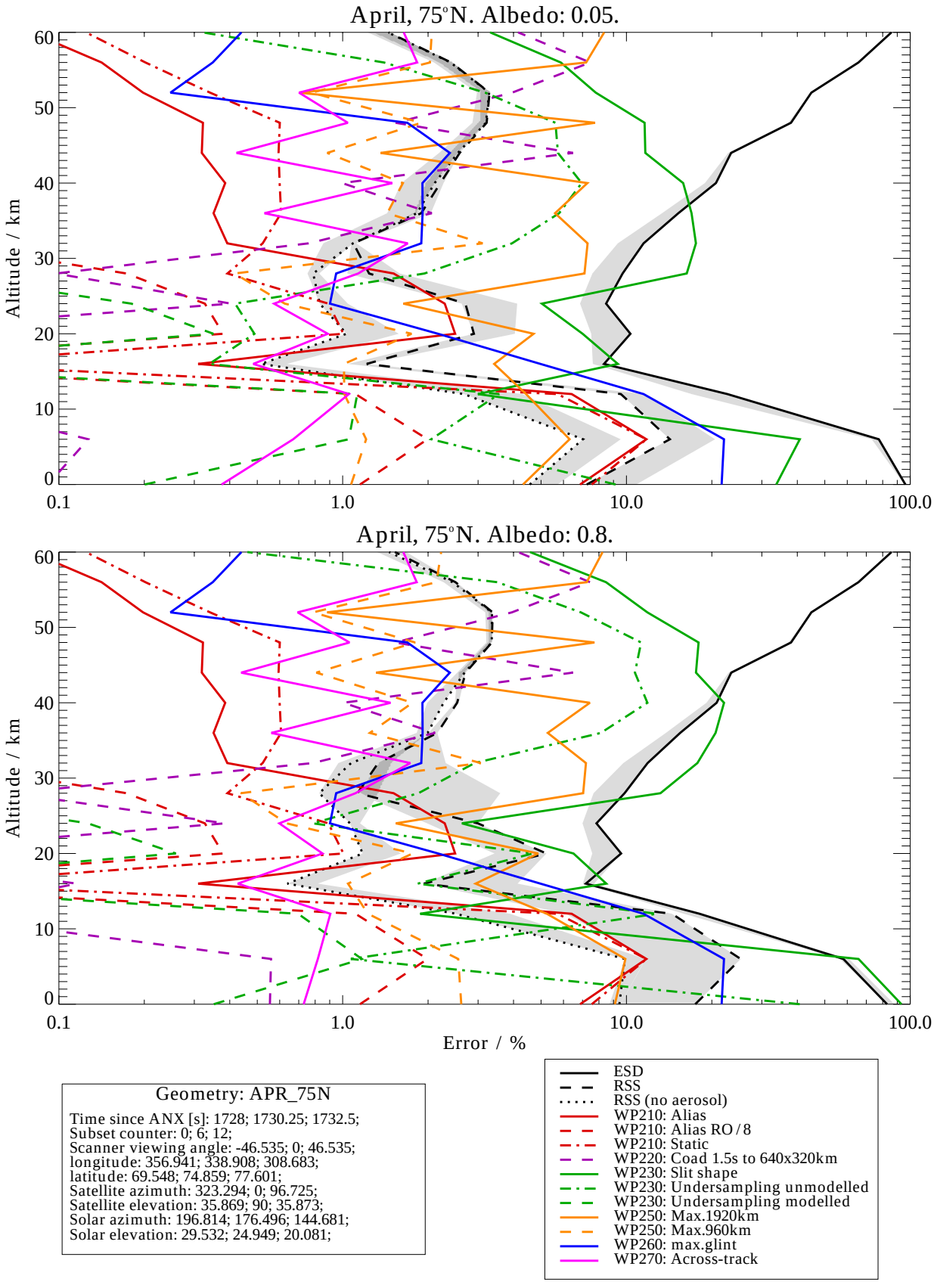

Figure C1.1.5: ESDs, RSS baseline errors and T2 summarised errors for scenario April, 75°N, assuming band 1 wavelength range 265-307nm.

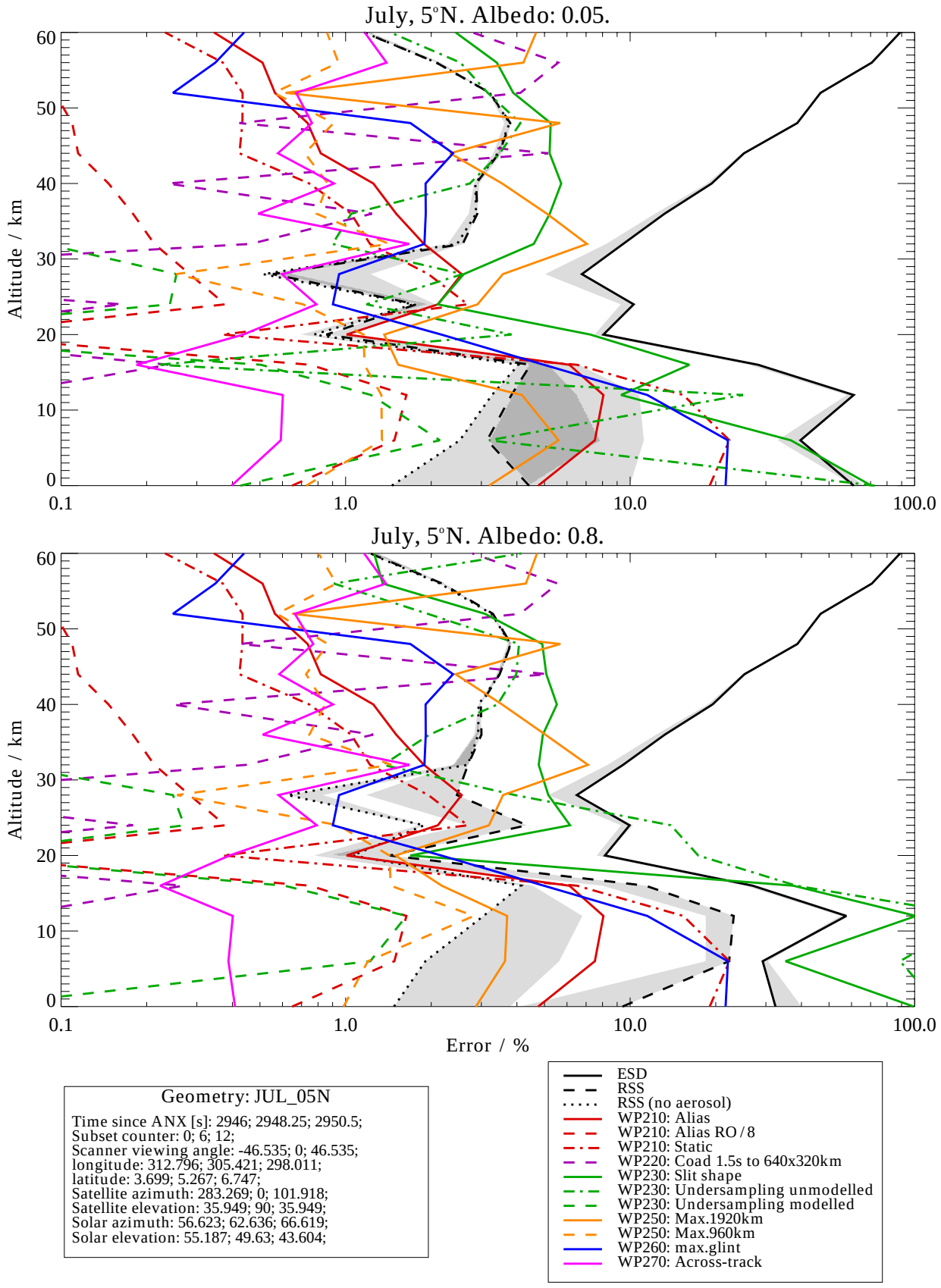

Figure C1.1.6: ESDs, RSS baseline errors and T2 summarised errors for scenario July, 5°N, assuming band 1 wavelength range 265-307nm.

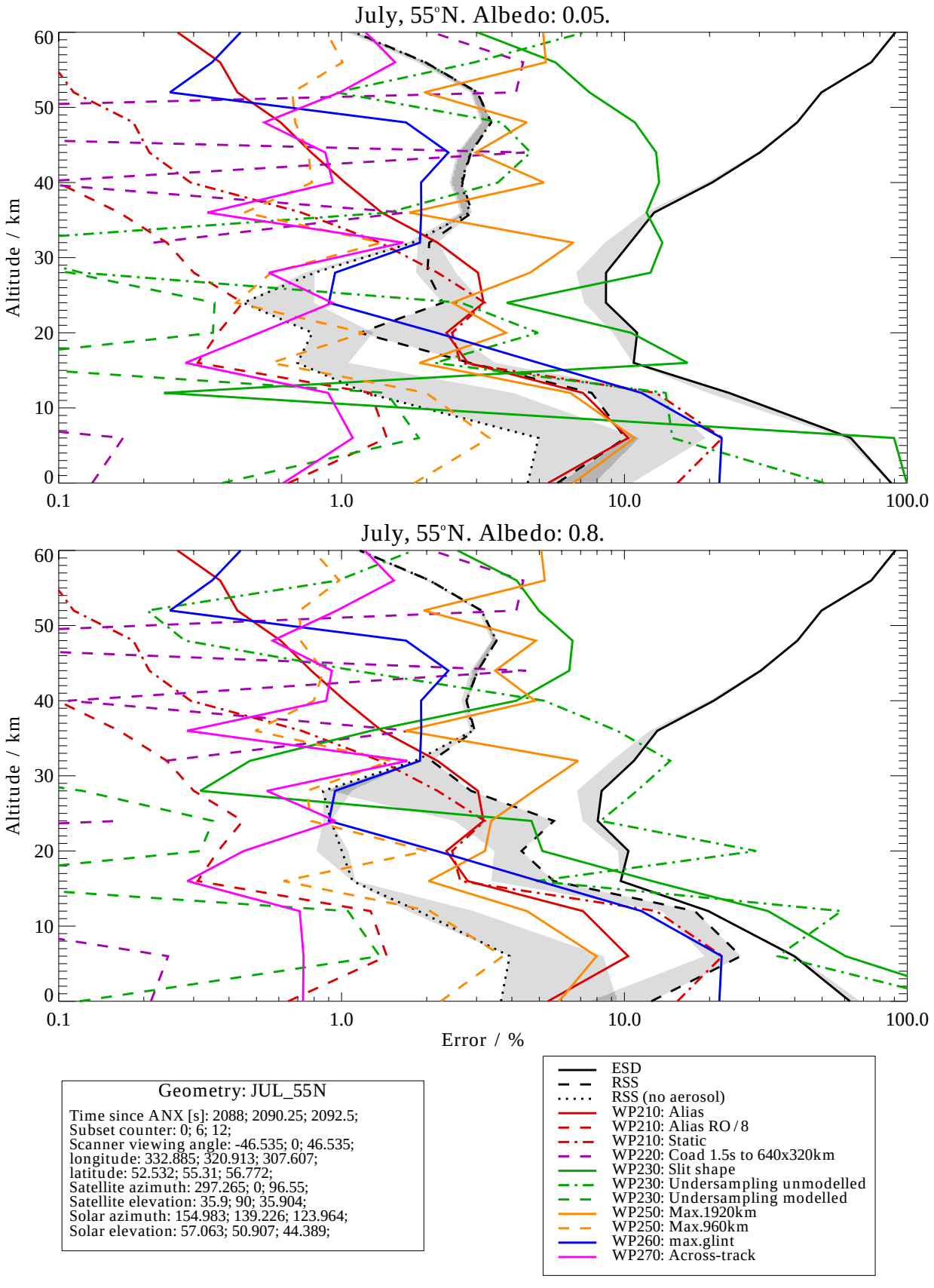

Figure C1.1.7: ESDs, RSS baseline errors and T2 summarised errors for scenario July, 55°N, assuming band 1 wavelength range 265-307nm.

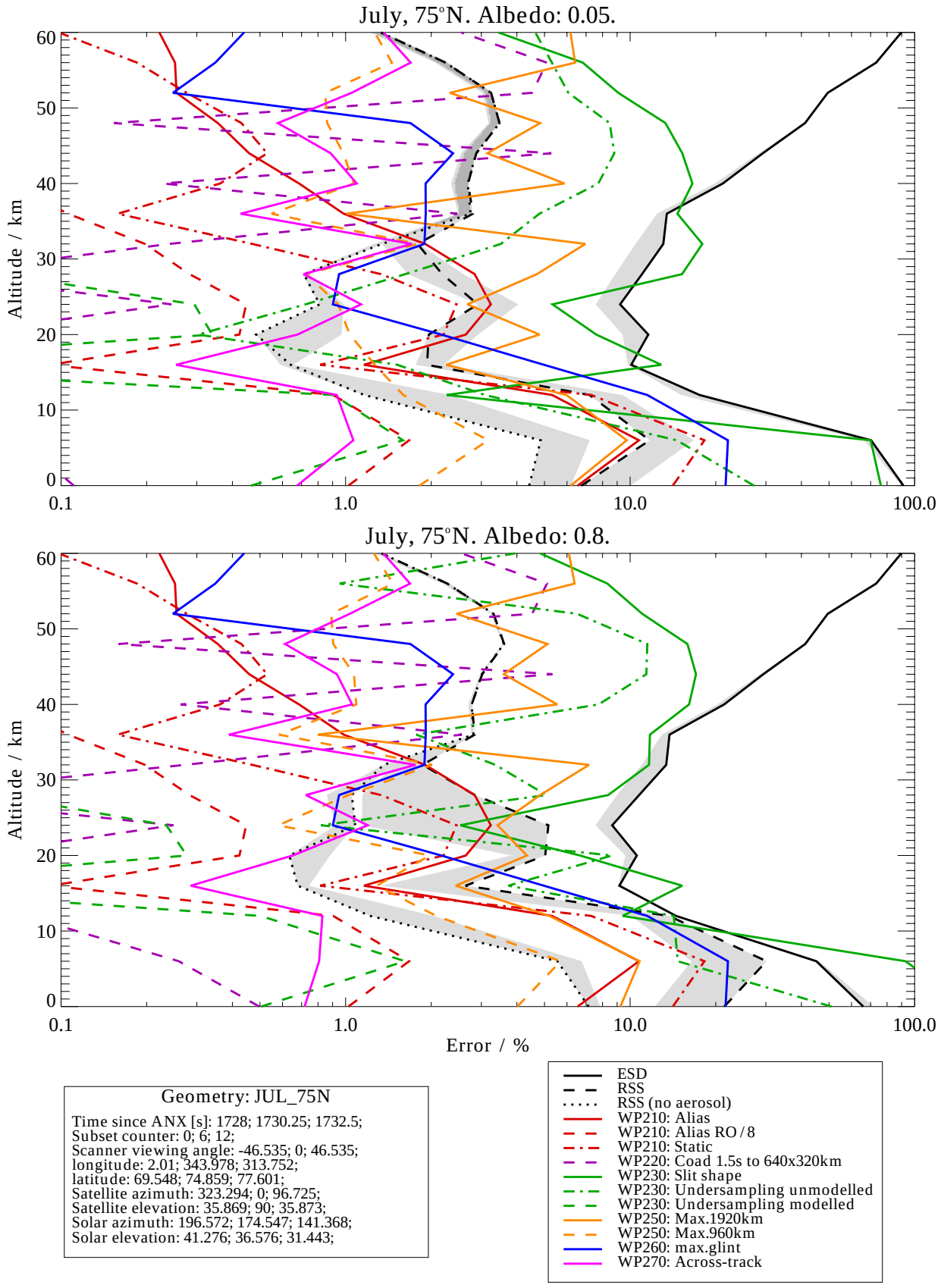

Figure C1.1.8: ESDs, RSS baseline errors and T2 summarised errors for scenario July, 75°N, assuming band 1 wavelength range 265-307nm.

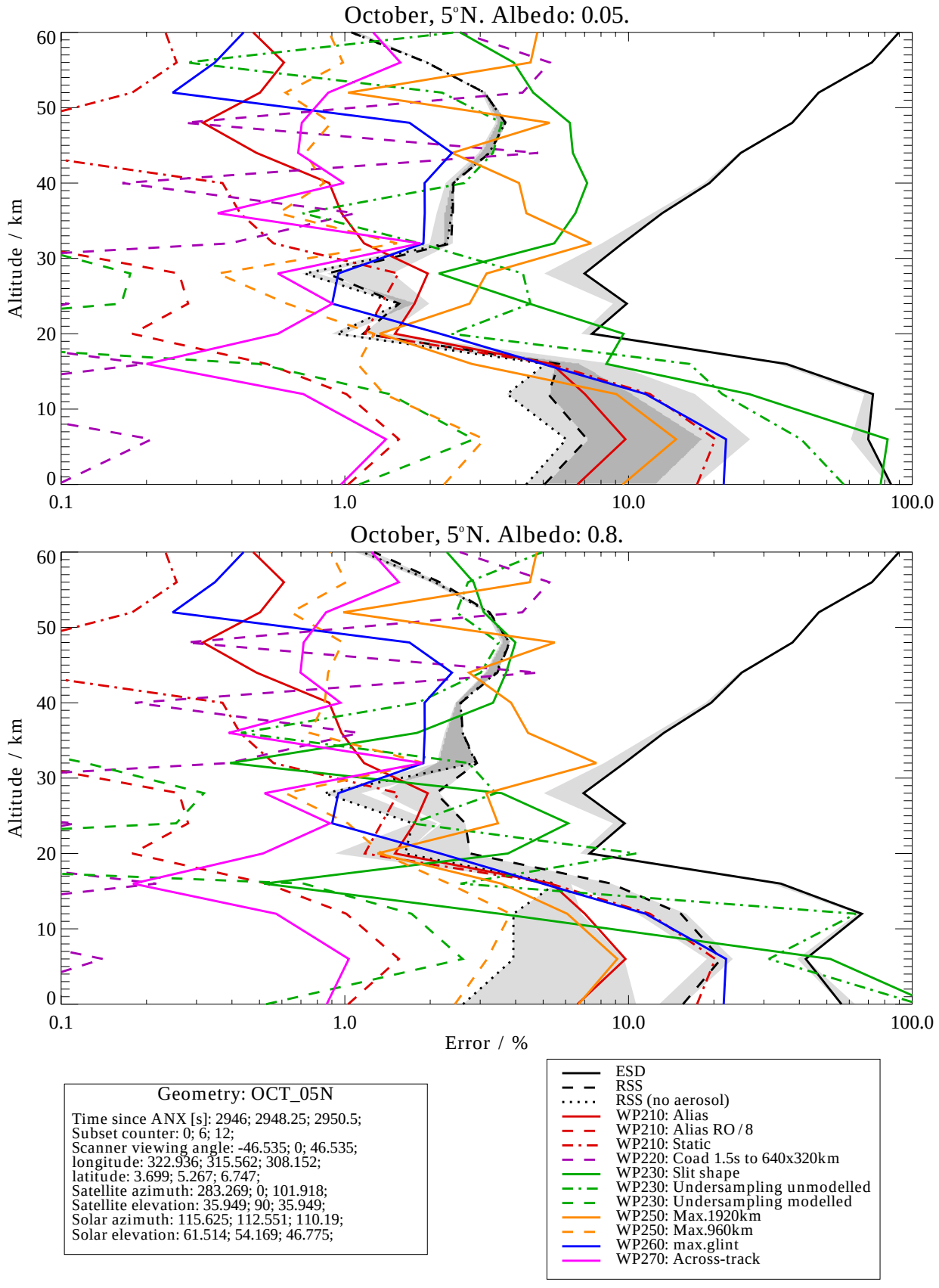

Figure C1.1.9: ESDs, RSS baseline errors and T2 summarised errors for scenario October, 5°N, assuming band 1 wavelength range 265-307nm.

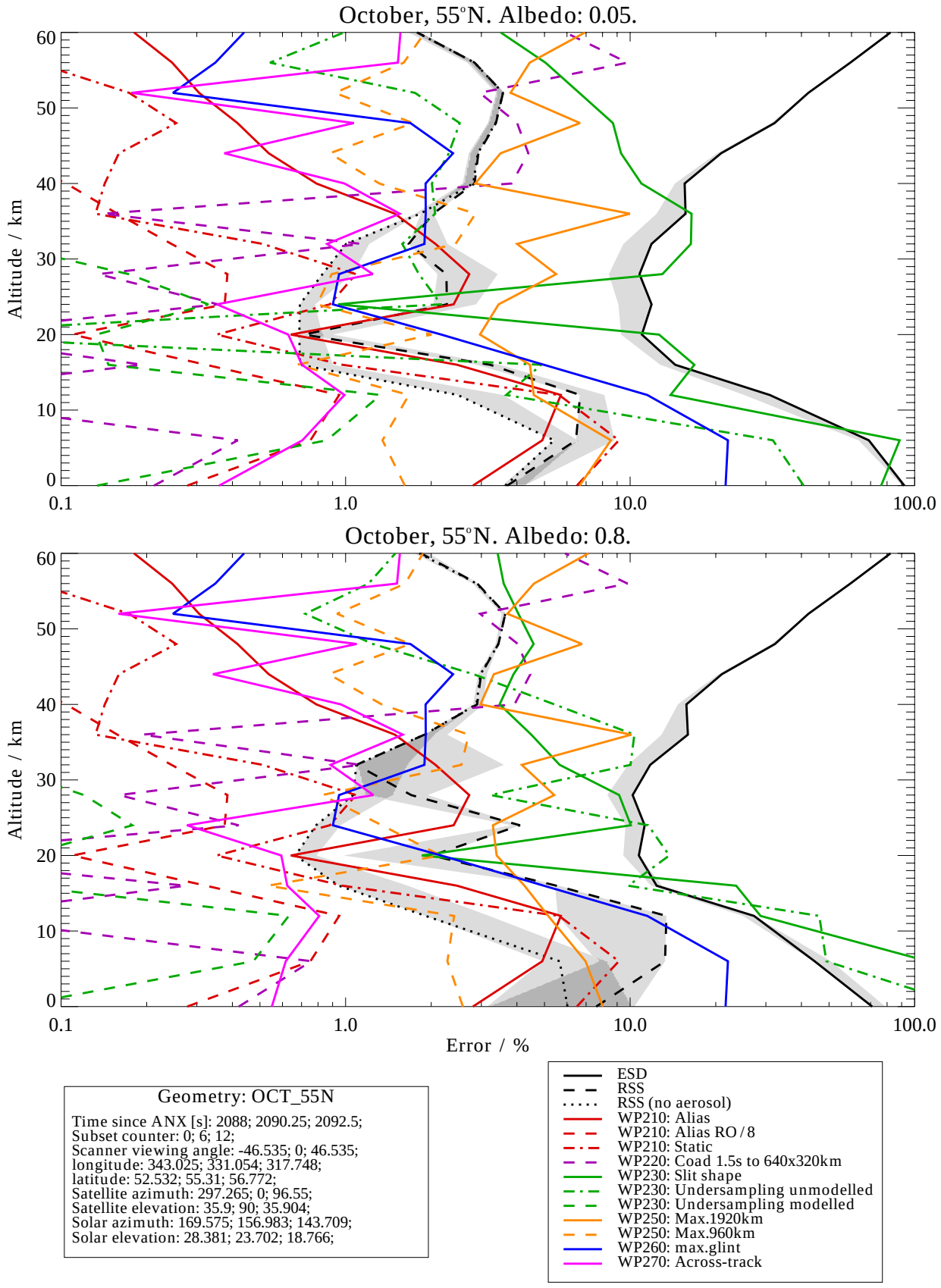

Figure C1.1.10: ESDs, RSS baseline errors and T2 summarised errors for scenario October, 55°N, assuming band 1 wavelength range 265-307nm.

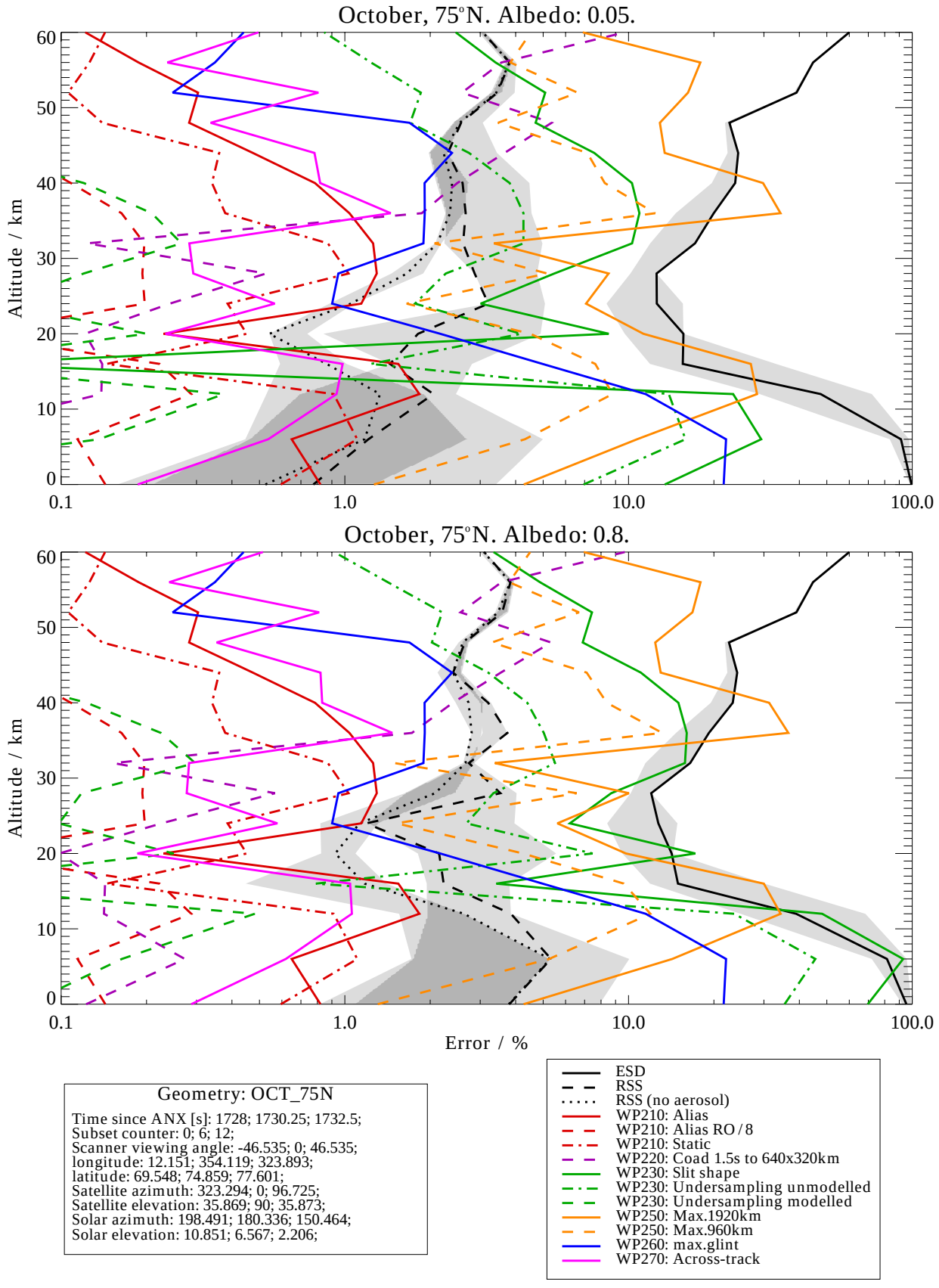

Figure C1.1.11: ESDs, RSS baseline errors and T2 summarised errors for scenario October, 75°N, assuming band 1 wavelength range 265-307nm.

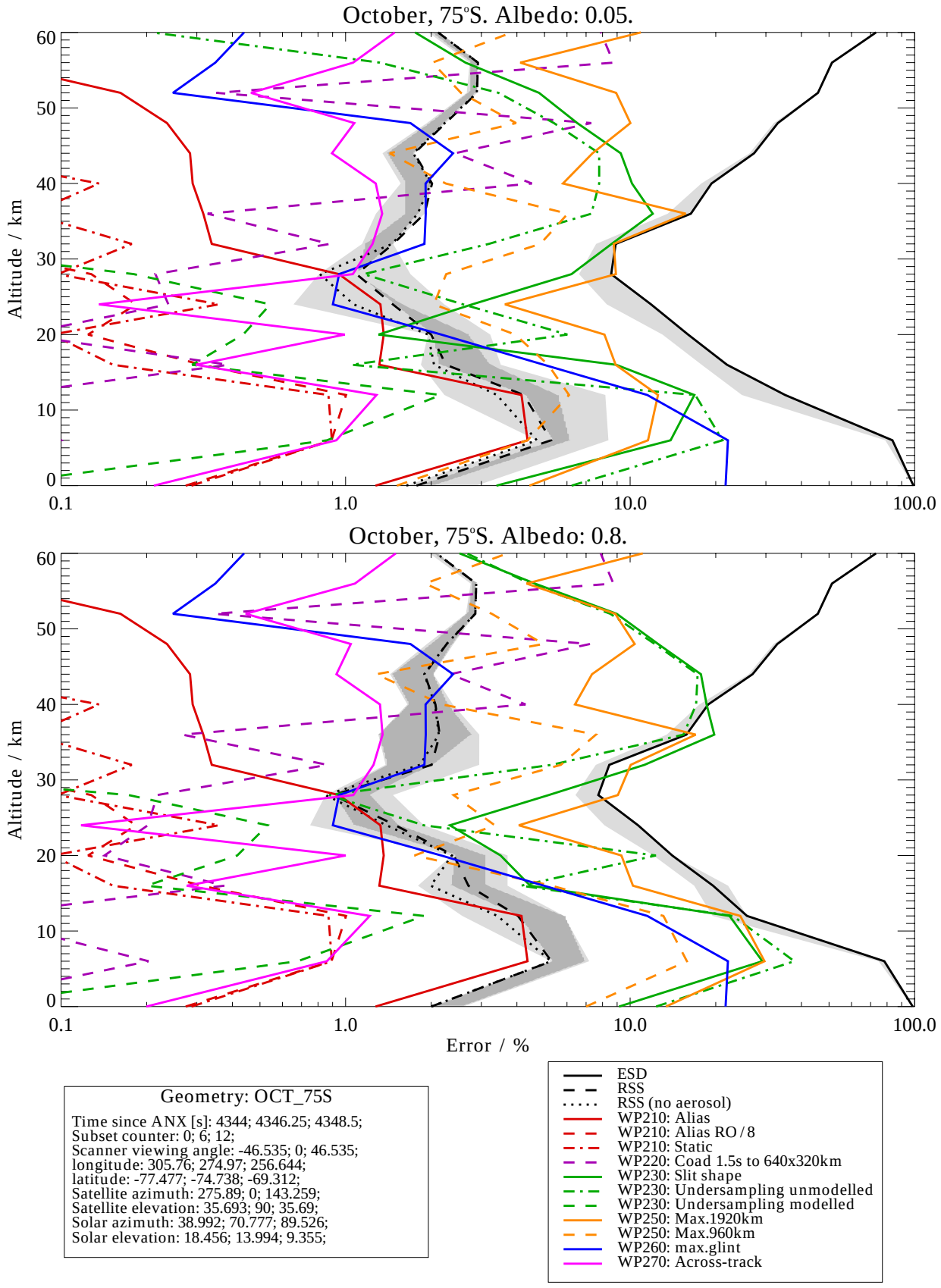

Figure C1.1.12: ESDs, RSS baseline errors and T2 summarised errors for scenario October, 75°S, assuming band 1 wavelength range 265-307nm.

C1.2 ESDs, base-line mapped errors and summary of Task 2 errors for Band 1 wavelength range 265-314nm.

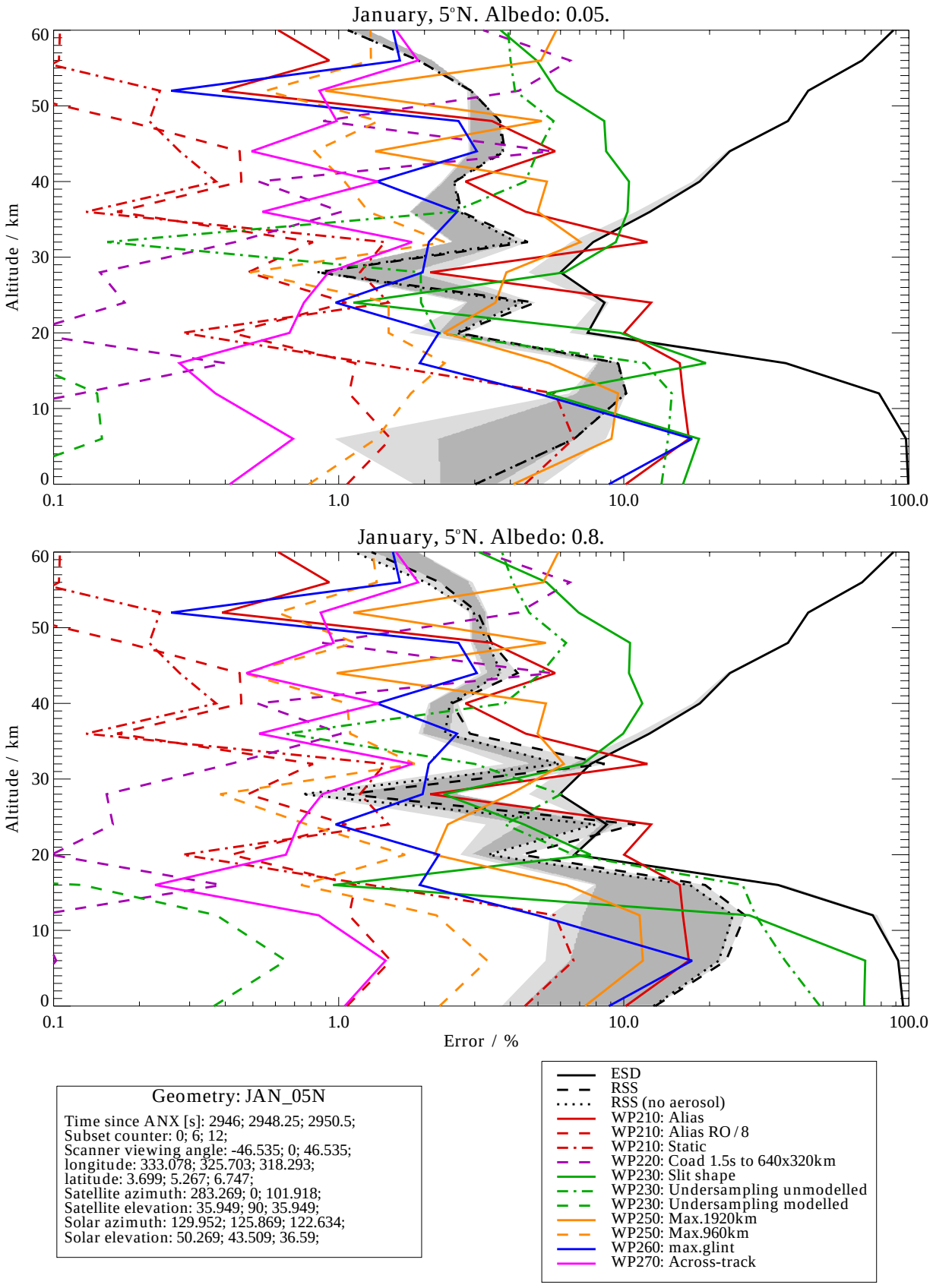

Figure C1.2.1: ESDs, RSS baseline errors and T2 summarised errors for scenario January, 5°N, assuming band 1 wavelength range 265-314nm.

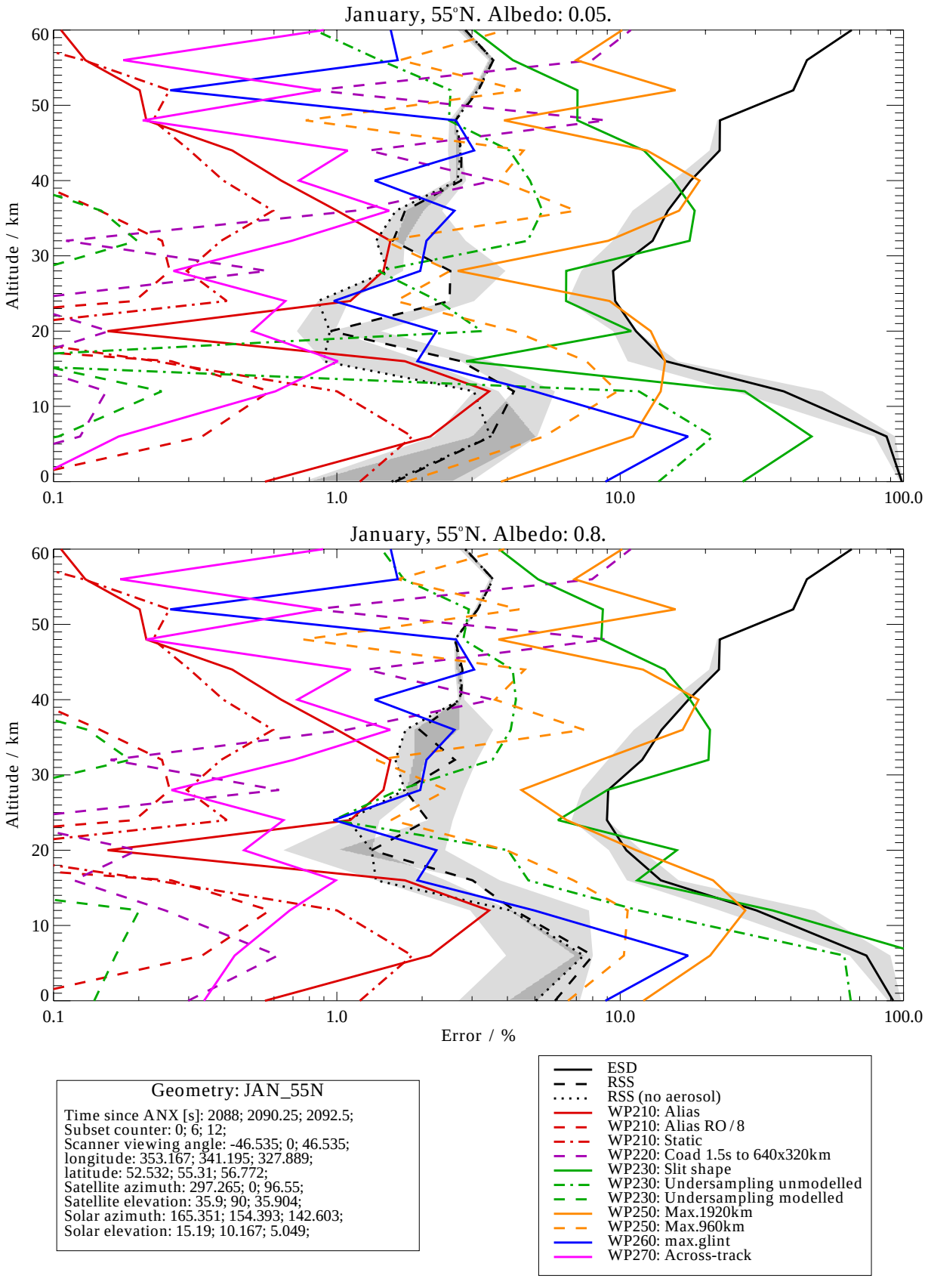

Figure C1.2.2: ESDs, RSS baseline errors and T2 summarised errors for scenario January, 55°N, assuming band 1 wavelength range 265-314nm.

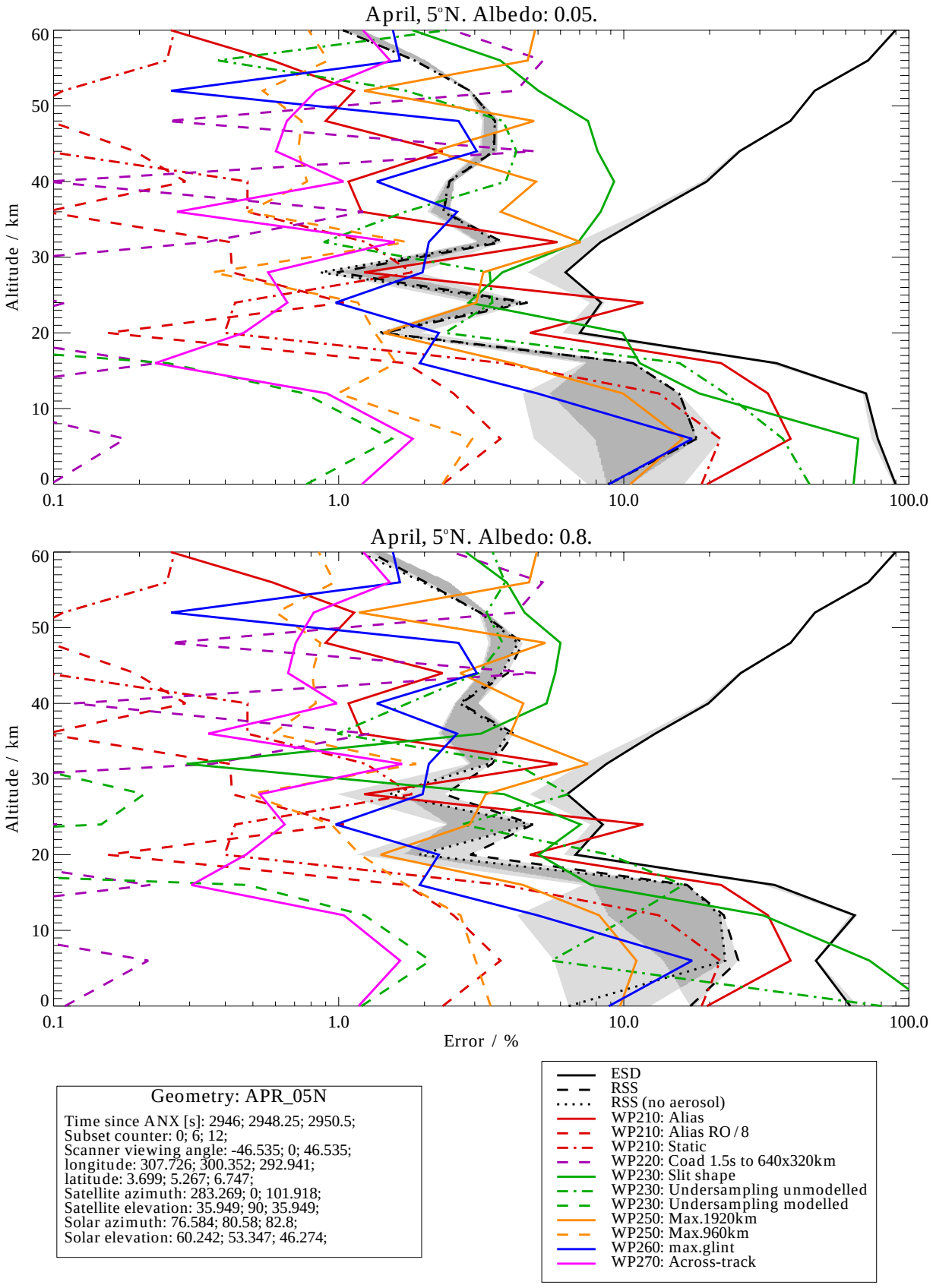

Figure C1.2.3: ESDs, RSS baseline errors and T2 summarised errors for scenario April, 5°N, assuming band 1 wavelength range 265-314nm.

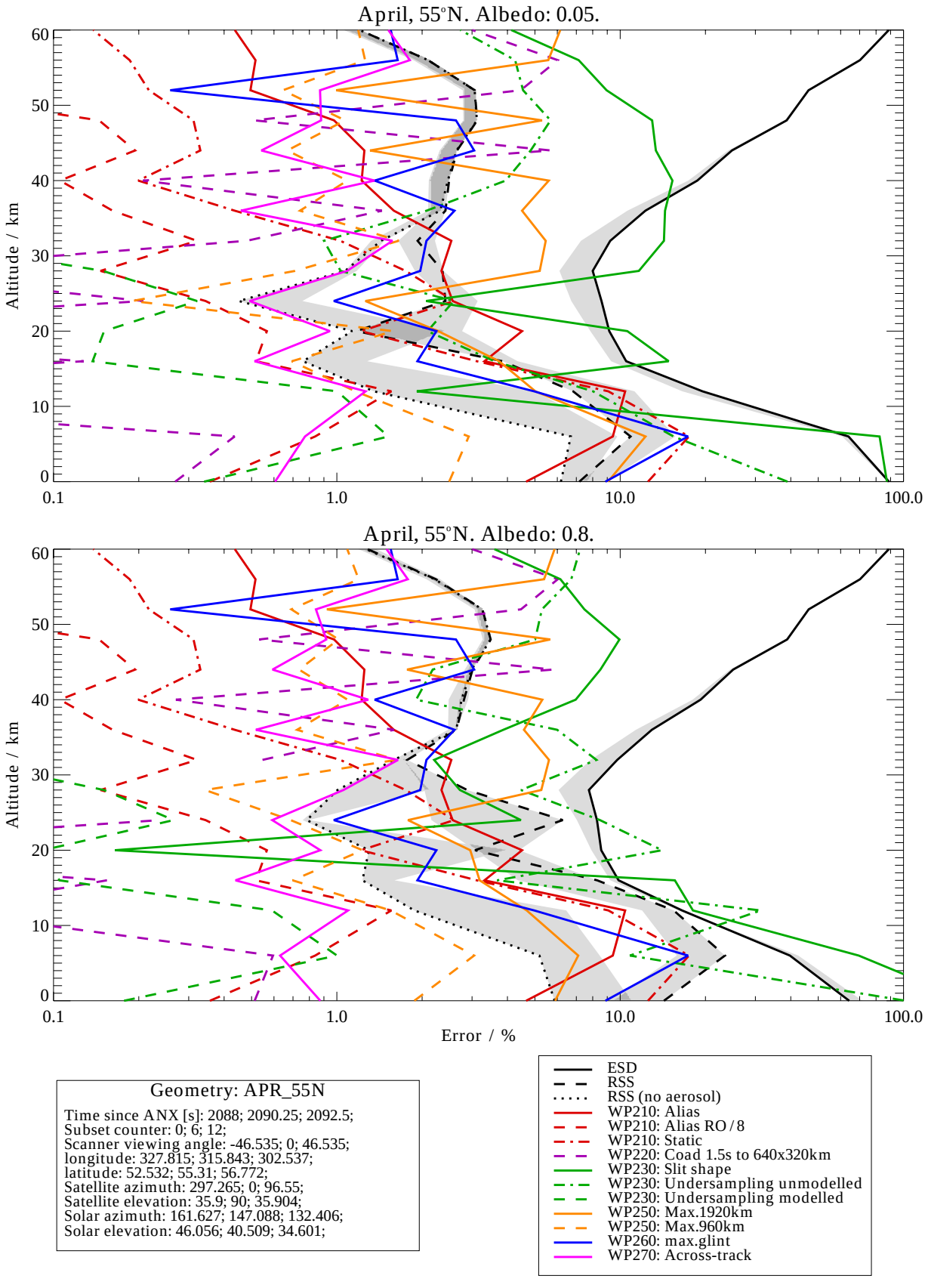

Figure C1.2.4: ESDs, RSS baseline errors and T2 summarised errors for scenario April, 55°N, assuming band 1 wavelength range 265-314nm.

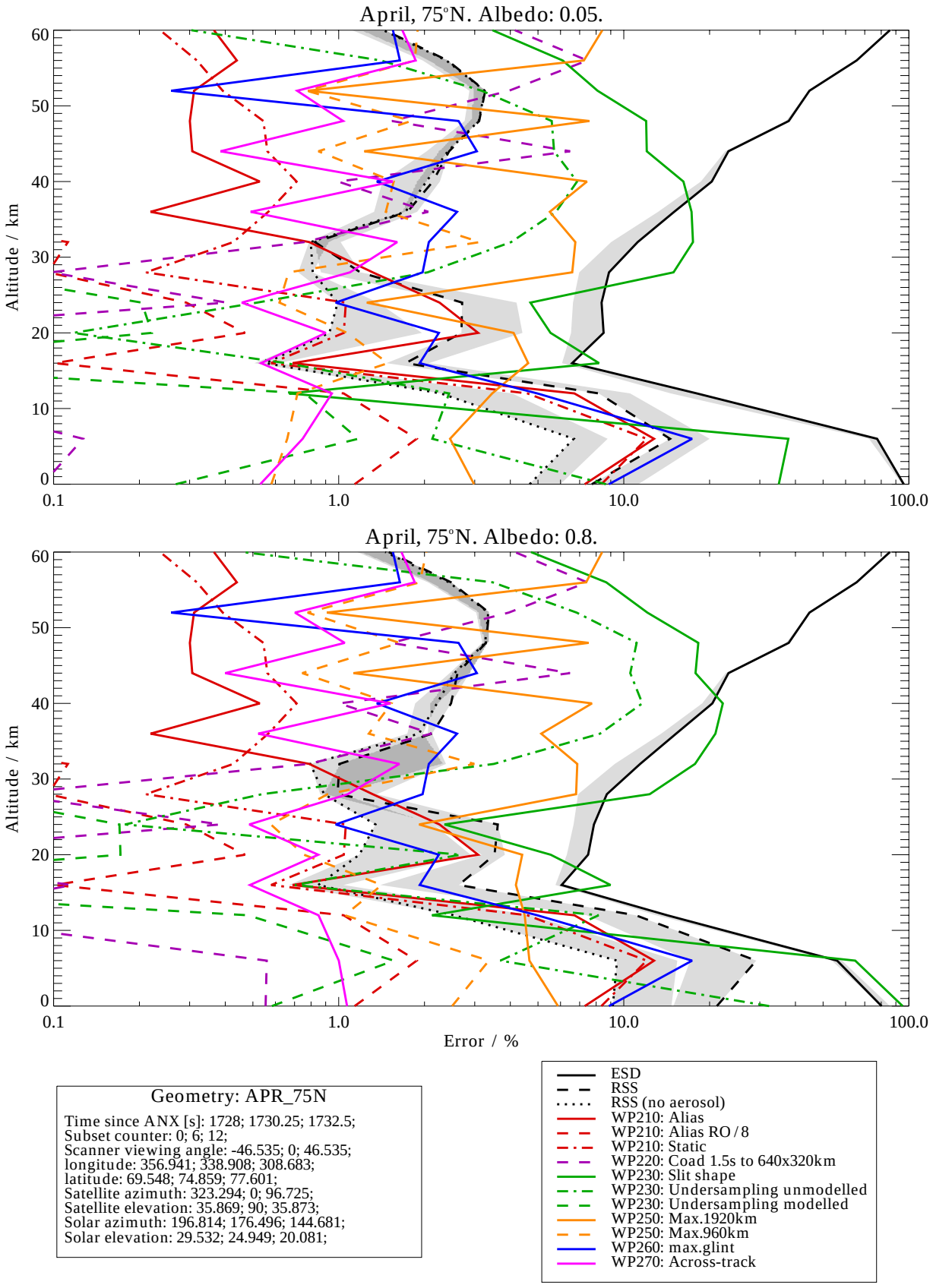

Figure C1.2.5: ESDs, RSS baseline errors and T2 summarised errors for scenario April, 75°N, assuming band 1 wavelength range 265-314nm.

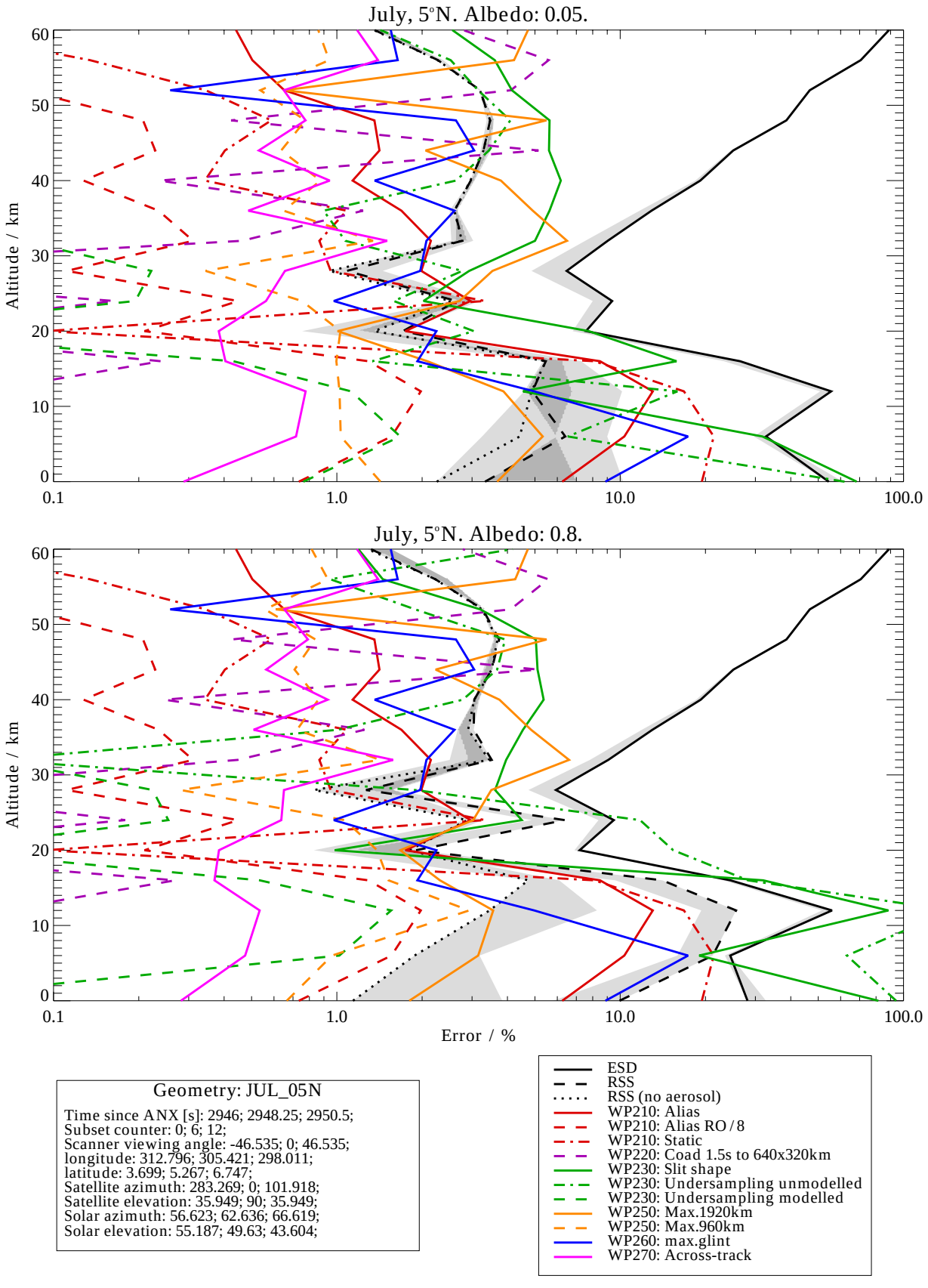

Figure C1.2.6: ESDs, RSS baseline errors and T2 summarised errors for scenario July, 5°N, assuming band 1 wavelength range 265-314nm.

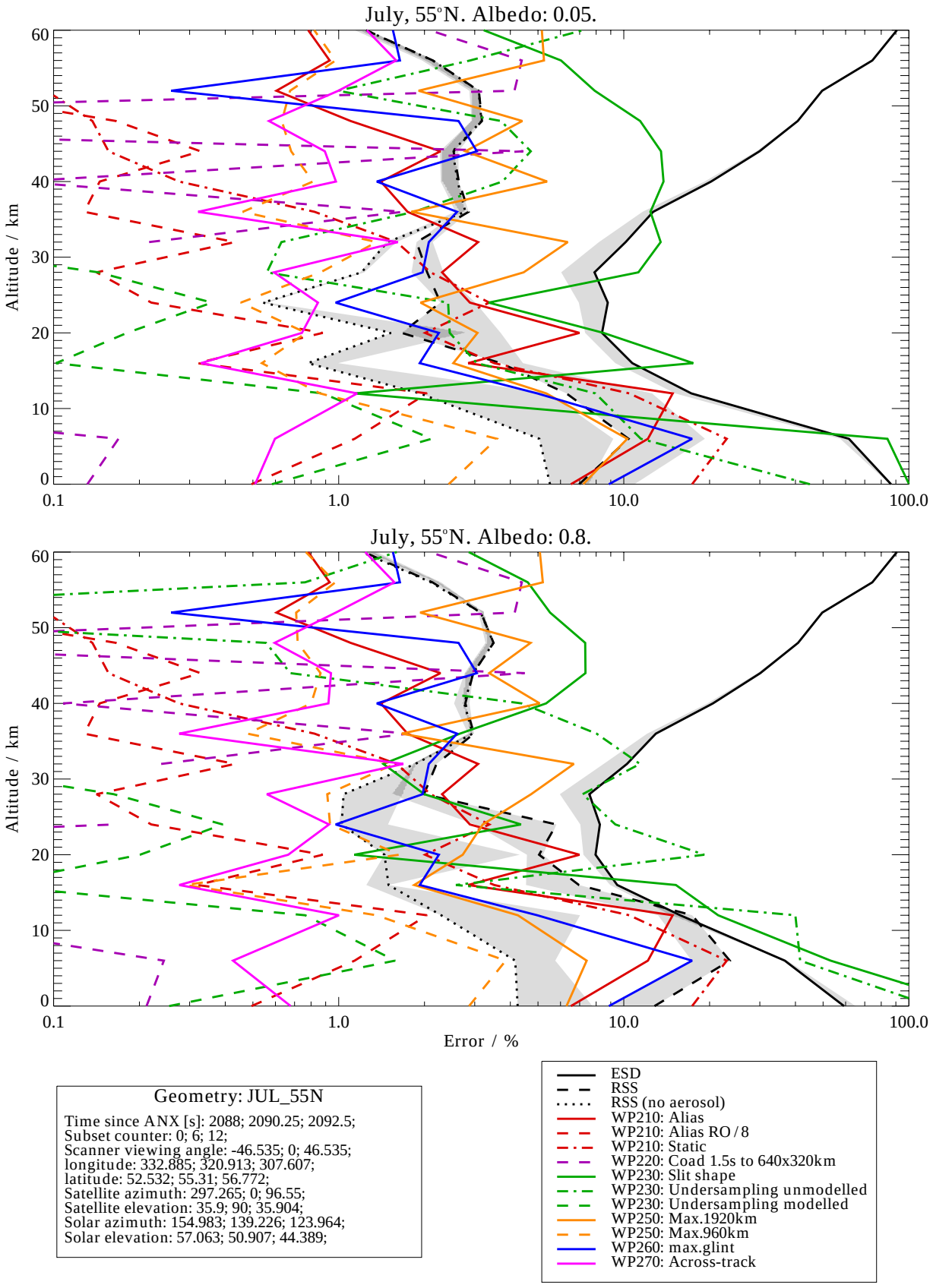

Figure C1.2.7: ESDs, RSS baseline errors and T2 summarised errors for scenario July, 55°N, assuming band 1 wavelength range 265-314nm.

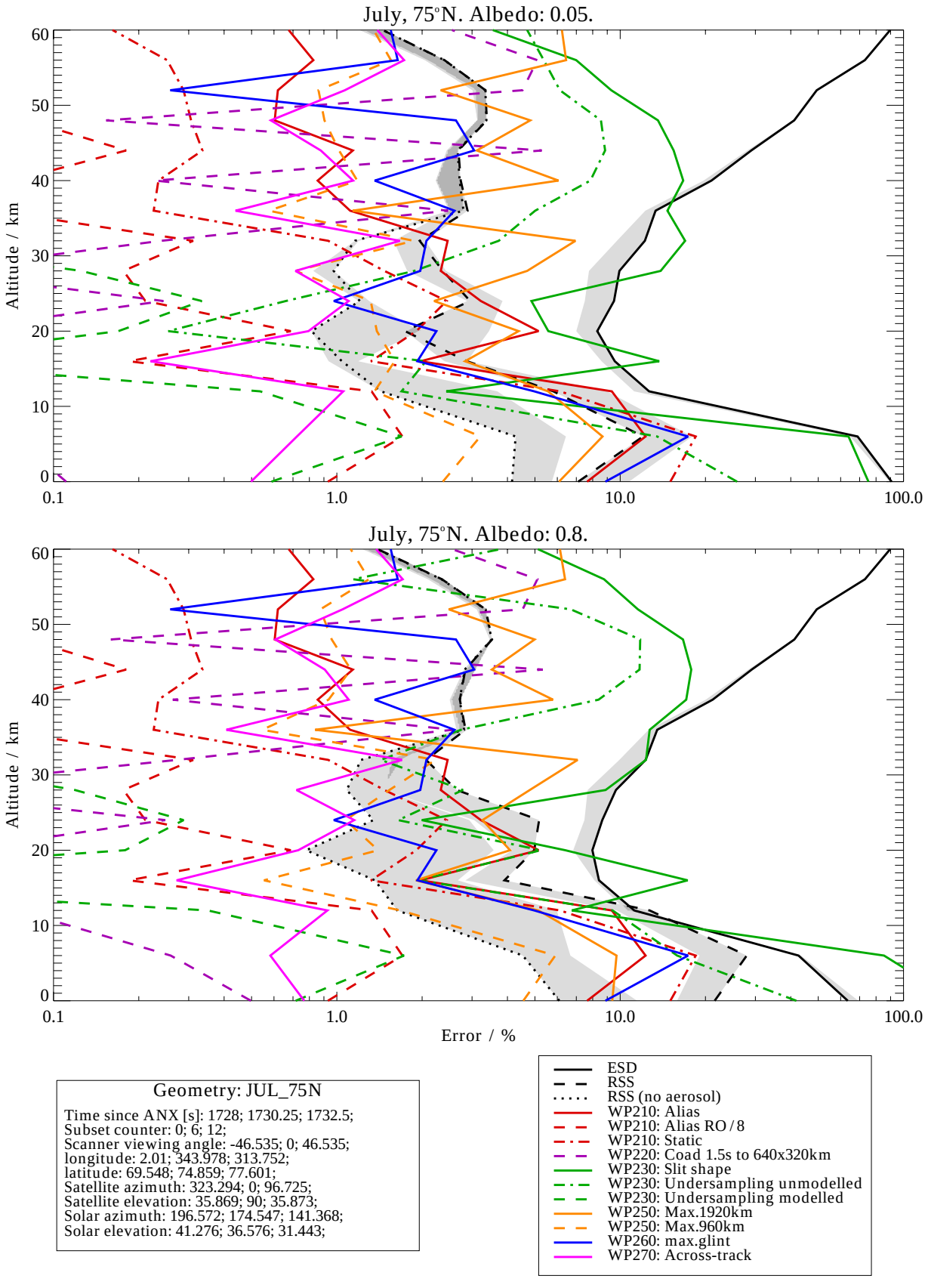

Figure C1.2.8: ESDs, RSS baseline errors and T2 summarised errors for scenario July, 75°N, assuming band 1 wavelength range 265-314nm.

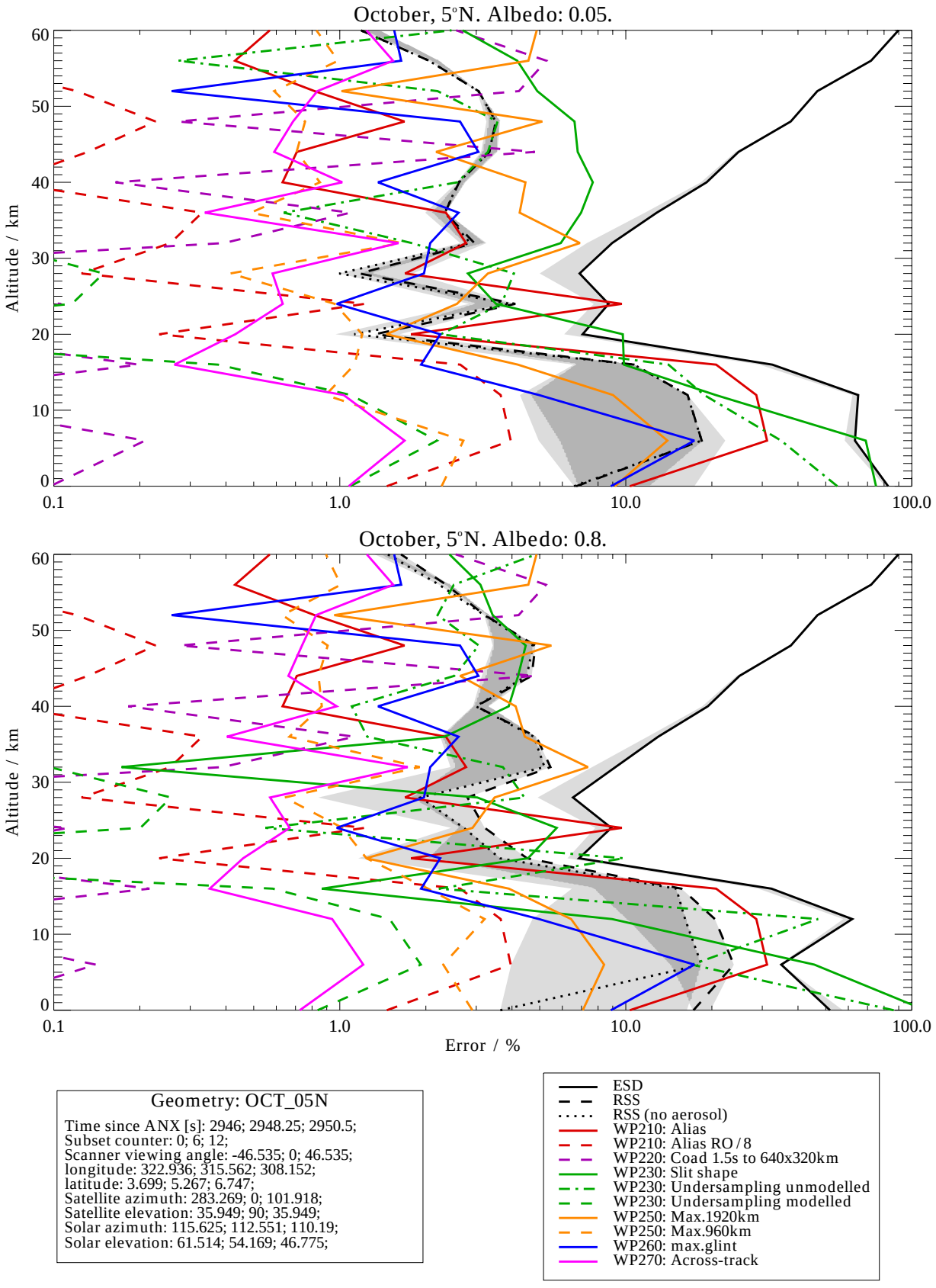

Figure C1.2.9: ESDs, RSS baseline errors and T2 summarised errors for scenario October, 5°N, assuming band 1 wavelength range 265-314nm.

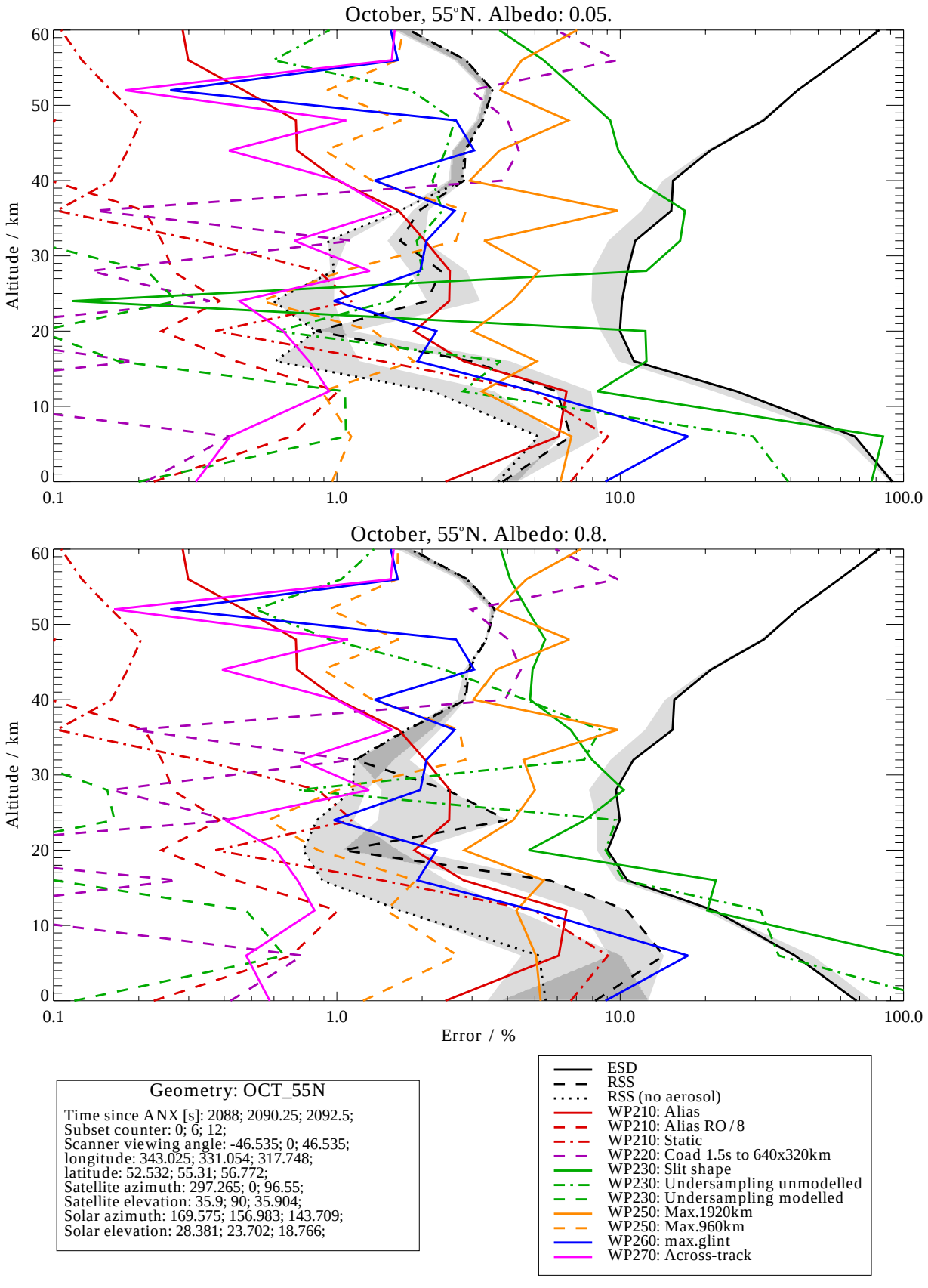

Figure C1.2.10: ESDs, RSS baseline errors and T2 summarised errors for scenario October, 55°N, assuming band 1 wavelength range 265-314nm.

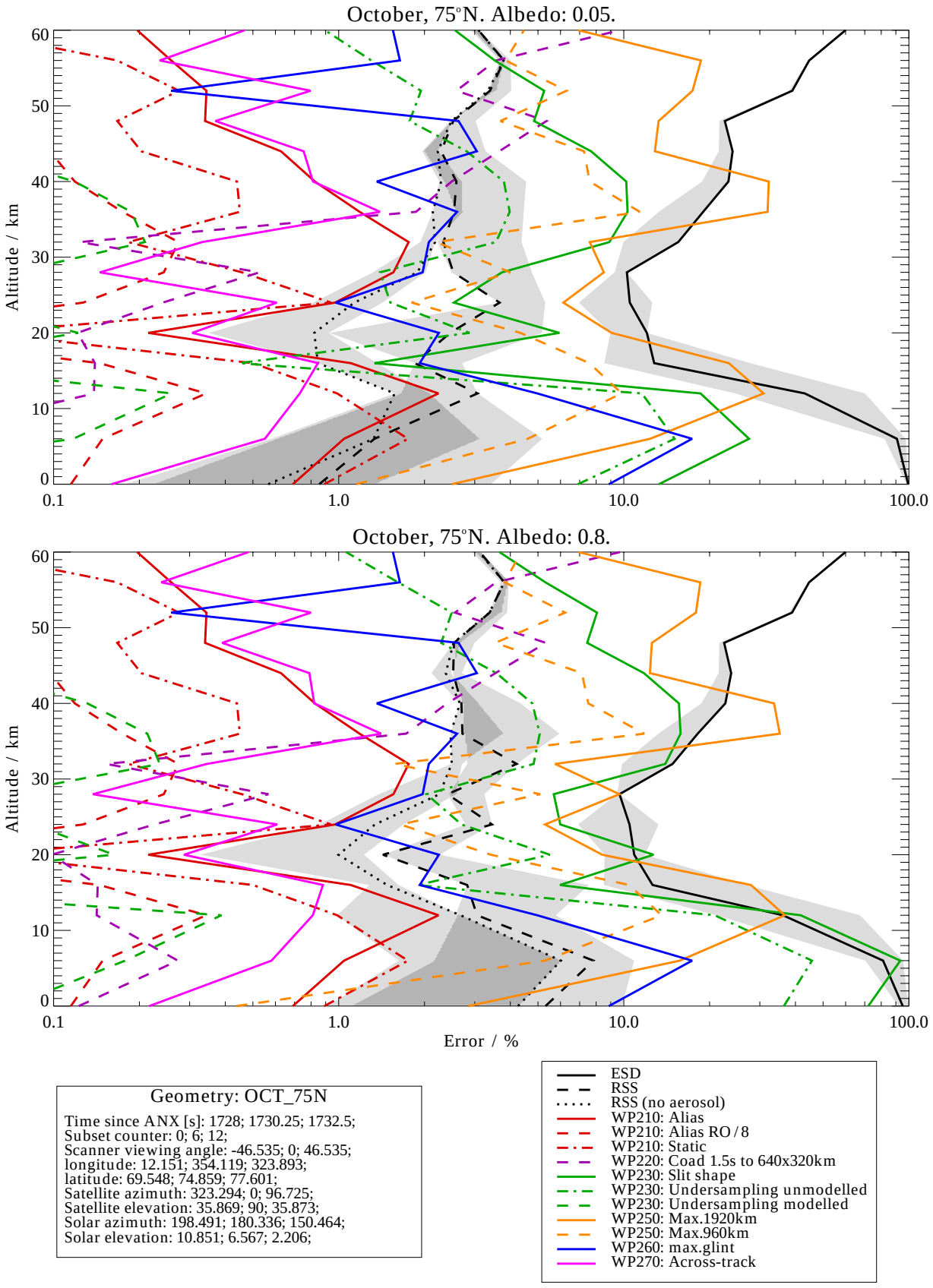

Figure C1.2.11: ESDs, RSS baseline errors and T2 summarised errors for scenario October, 75°N, assuming band 1 wavelength range 265-314nm.

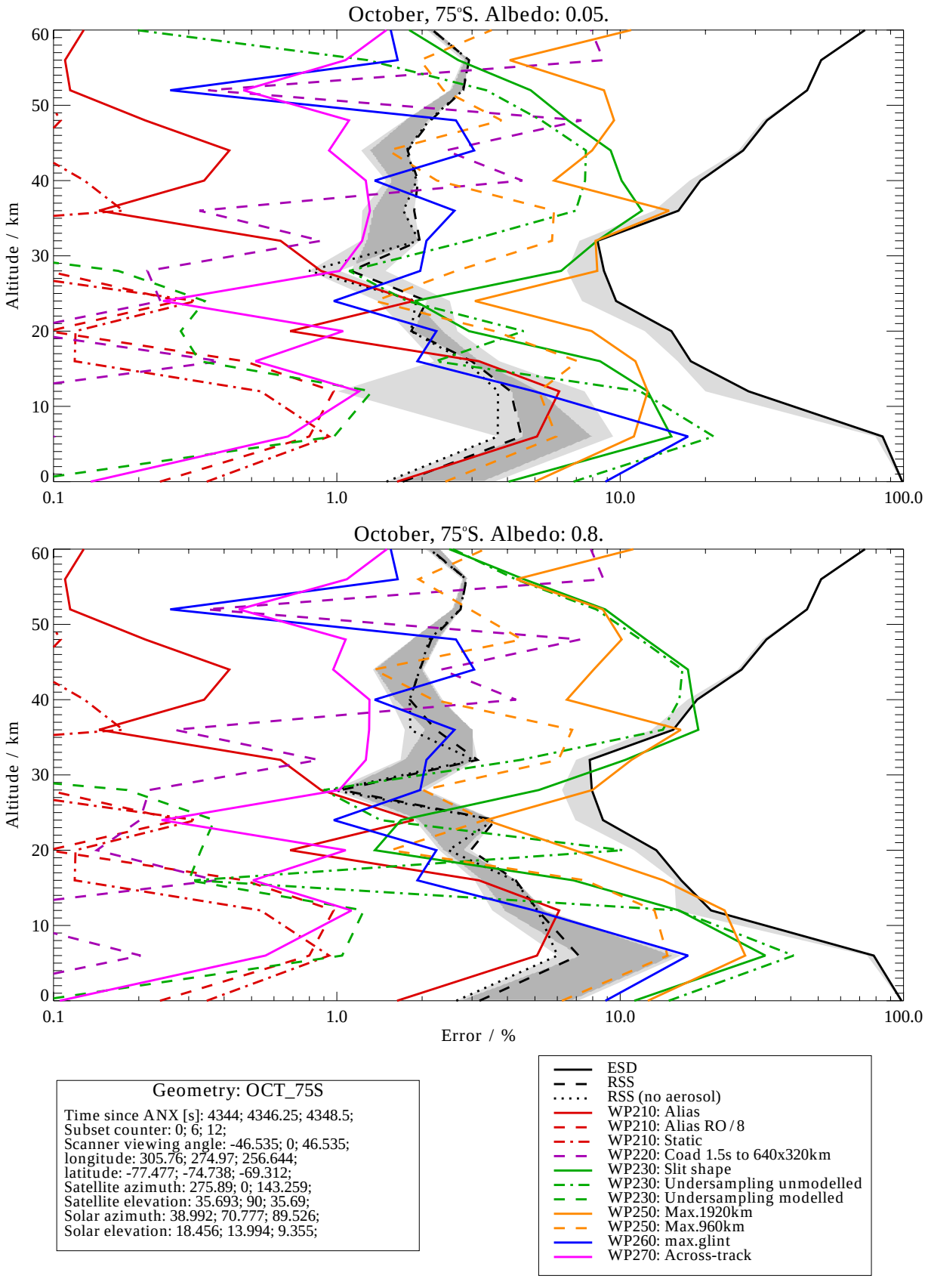

Figure C1.2.12: ESDs, RSS baseline errors and T2 summarised errors for scenario October, 75°S, assuming band 1 wavelength range 265-314nm.

C1.3 Comparison of ESDs, base-line mapped errors and WP210 summarised errors over geo-temporal scenarios

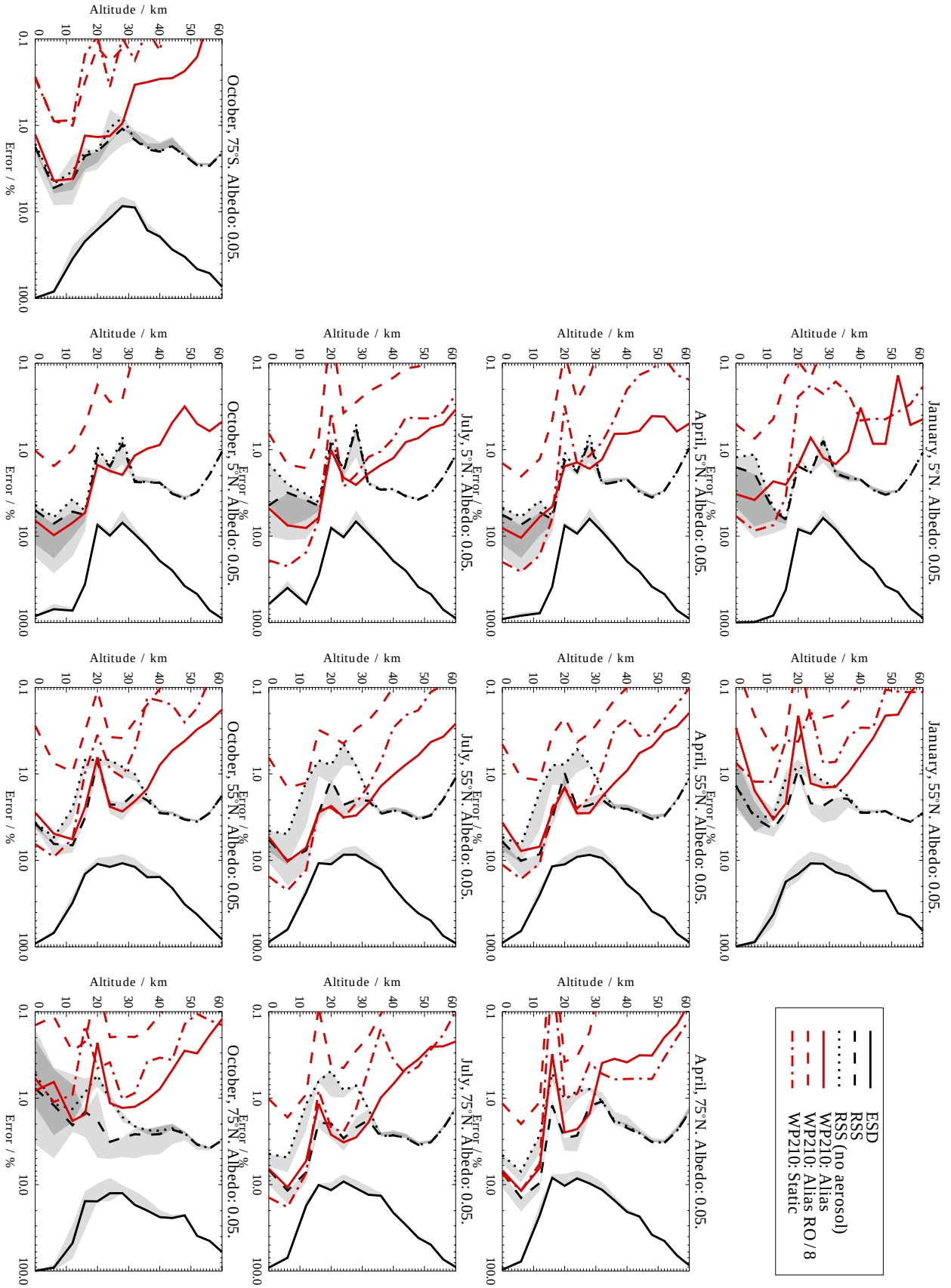

Figure C1.3.1: ESDs, RSS baseline errors and T2 summarised errors for all geotemporal scenarios, for Work Package 210 (Spatial aliasing). Band 1 wavelength range: 265-307nm. Surface albedo: 0.05. Scenarios arranged by latitude (left to right) and season (top to bottom).

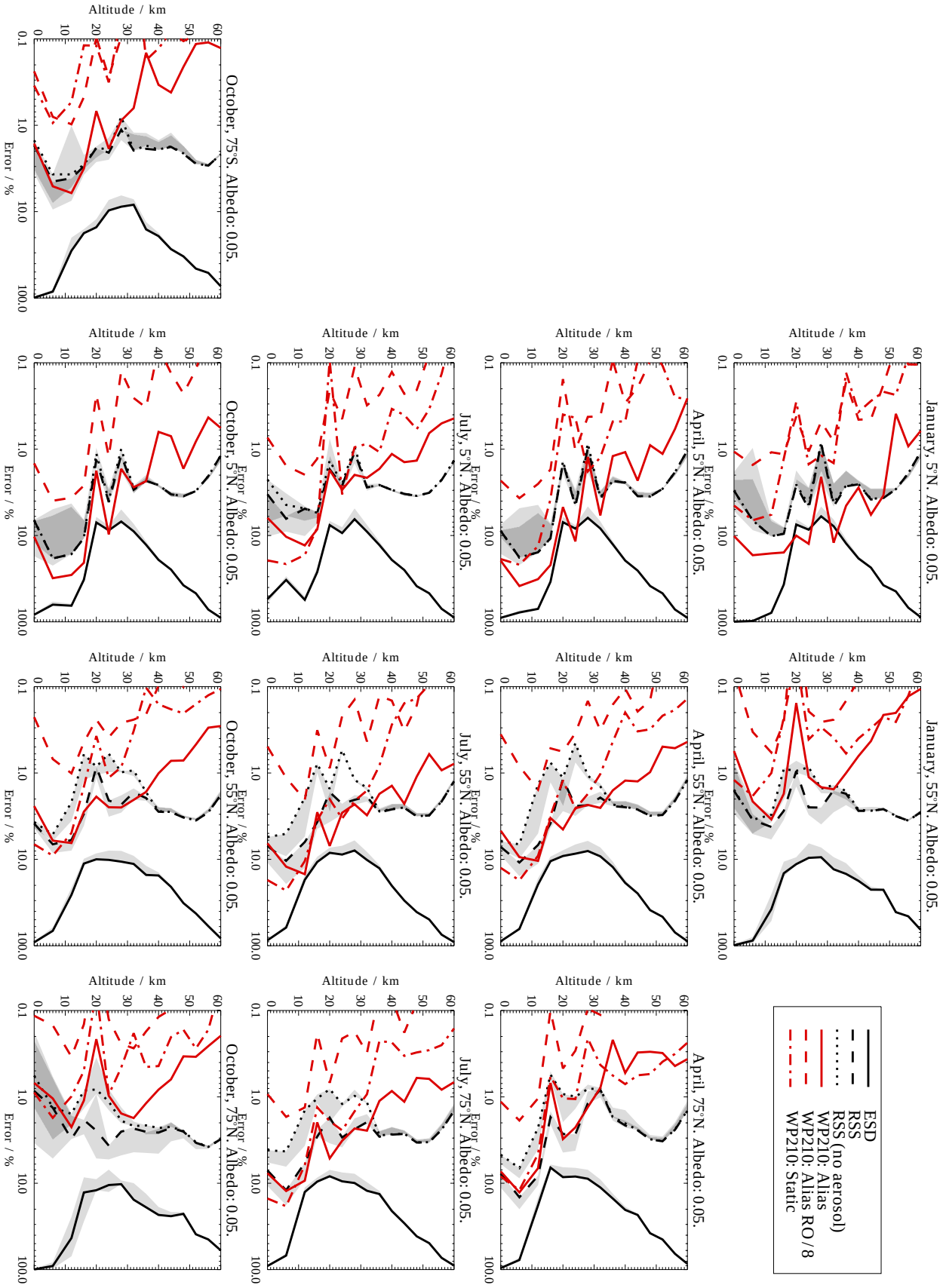

Figure C1.3.2: ESDs, RSS baseline errors and T2 summarised errors for all geotemporal scenarios, for Work Package 210 (Spatial aliasing). Band 1 wavelength range: 265-314nm. Surface albedo: 0.05. Scenarios arranged by latitude (left to right) and season (top to bottom).

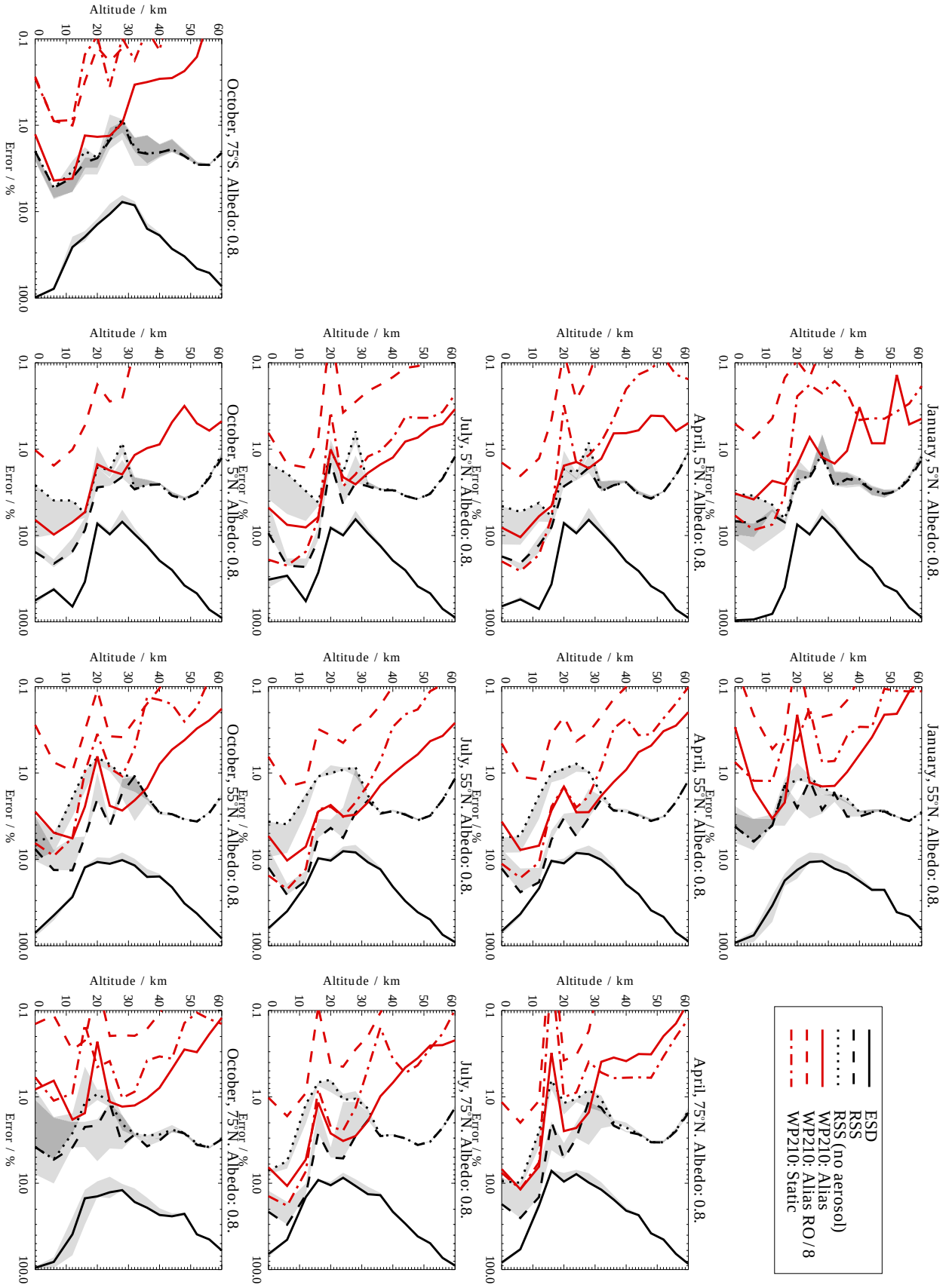

Figure C1.3.3: ESDs, RSS baseline errors and T2 summarised errors for all geotemporal scenarios, for Work Package 210 (Spatial aliasing). Band 1 wavelength range: 265-307nm. Surface albedo: 0.8. Scenarios arranged by latitude (left to right) and season (top to bottom).

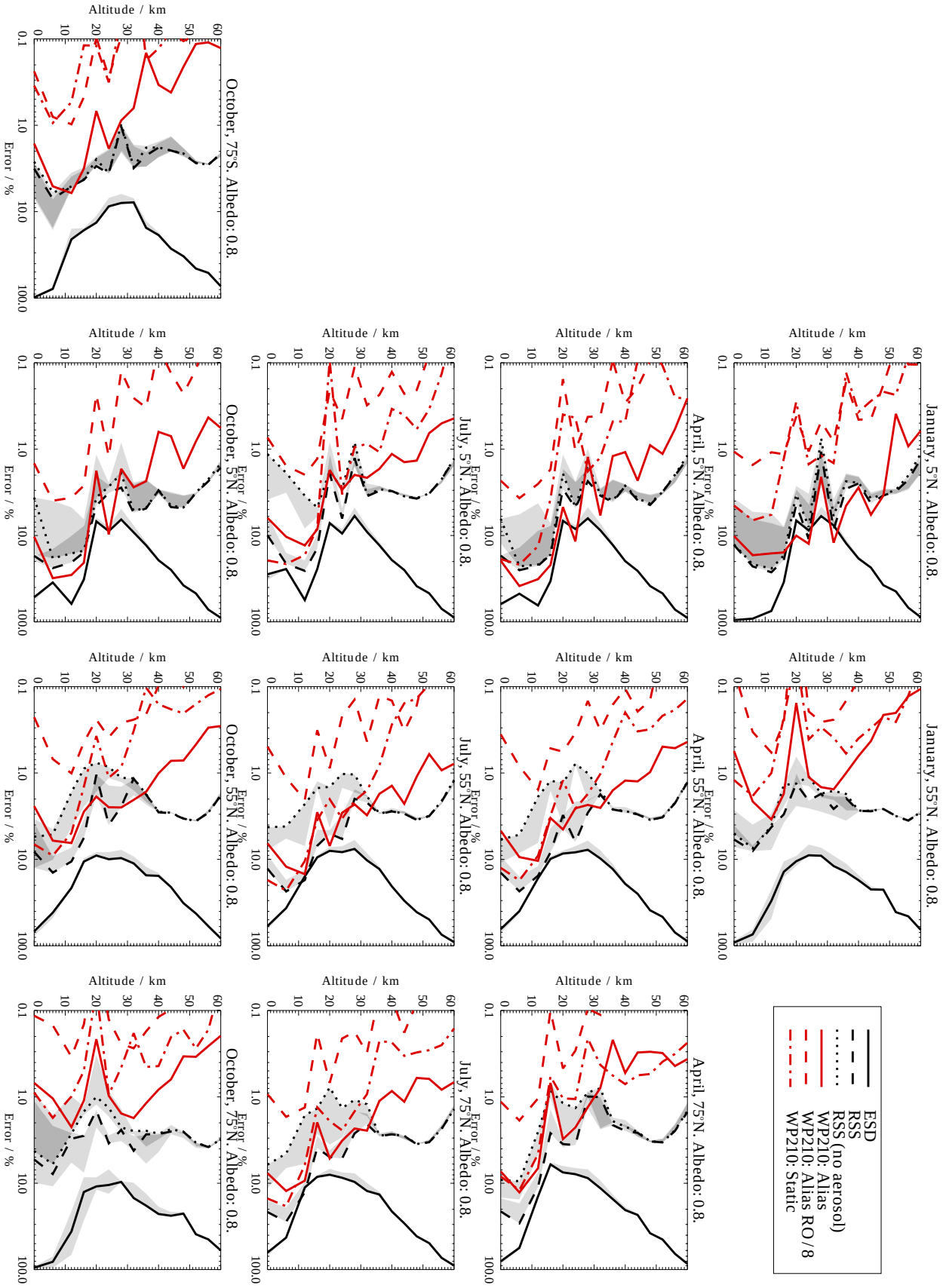

Figure C1.3.4: ESDs, RSS baseline errors and T2 summarised errors for all geotemporal scenarios, for Work Package 210 (Spatial aliasing). Band 1 wavelength range: 265-314nm. Surface albedo: 0.8. Scenarios arranged by latitude (left to right) and season (top to bottom).

C1.4 Comparison of ESDs, base-line mapped errors and WP220 summarised errors over geo-temporal scenarios

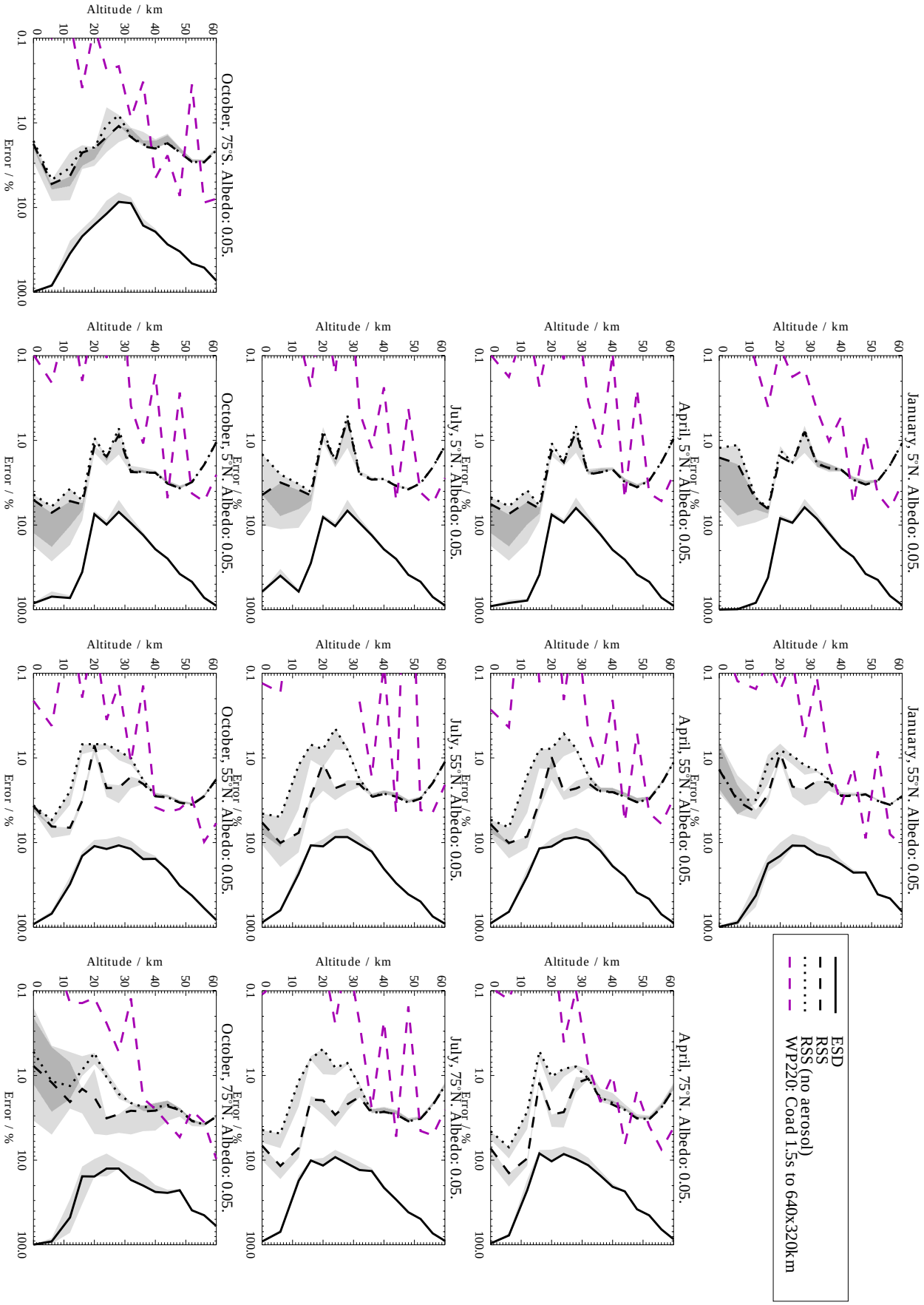

Figure C1.4.1: ESDs, RSS baseline errors and T2 summarised errors for all geotemporal scenarios, for Work Package 220 (Processing options for band 1A). Band 1 wavelength range: 265-307nm. Surface albedo: 0.05. Scenarios arranged by latitude (left to right) and season (top to bottom).

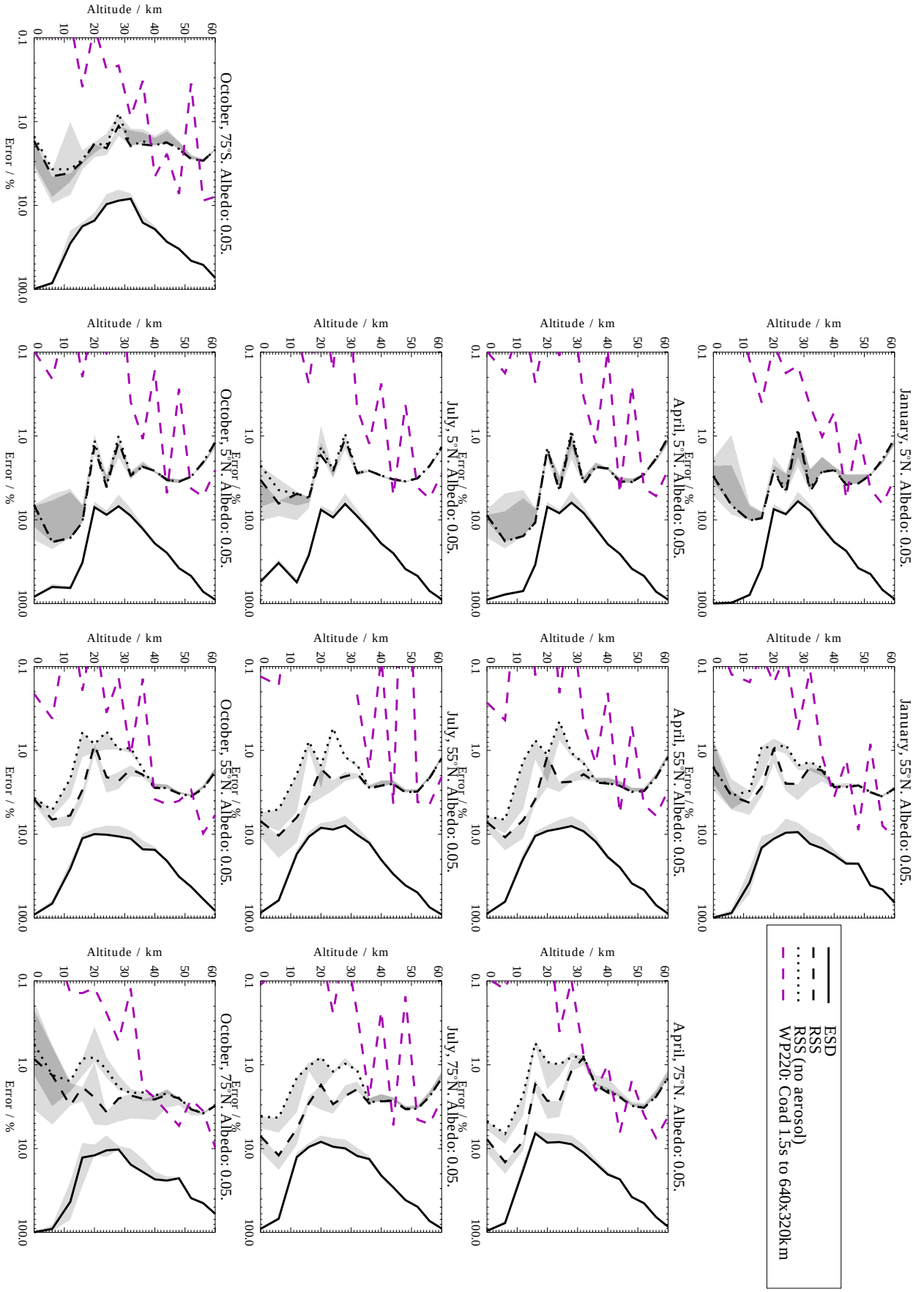

Figure C1.4.2: ESDs, RSS baseline errors and T2 summarised errors for all geotemporal scenarios, for Work Package 220 (Processing options for band 1A). Band 1 wavelength range: 265-314nm. Surface albedo: 0.05. Scenarios arranged by latitude (left to right) and season (top to bottom).

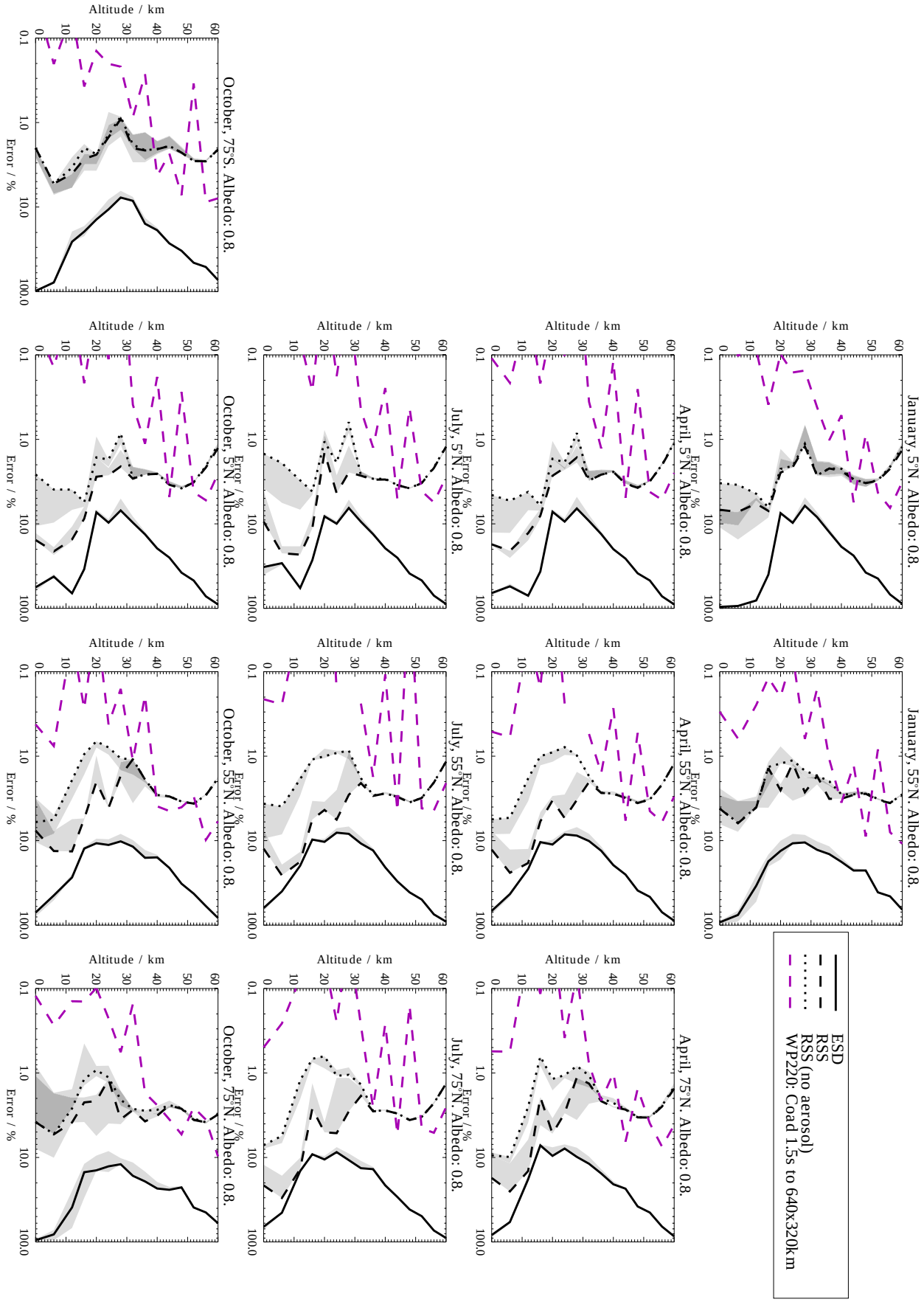

Figure C1.4.3: ESDs, RSS baseline errors and T2 summarised errors for all geotemporal scenarios, for Work Package 220 (Processing options for band 1A). Band 1 wavelength range: 265-307nm. Surface albedo: 0.8. Scenarios arranged by latitude (left to right) and season (top to bottom).

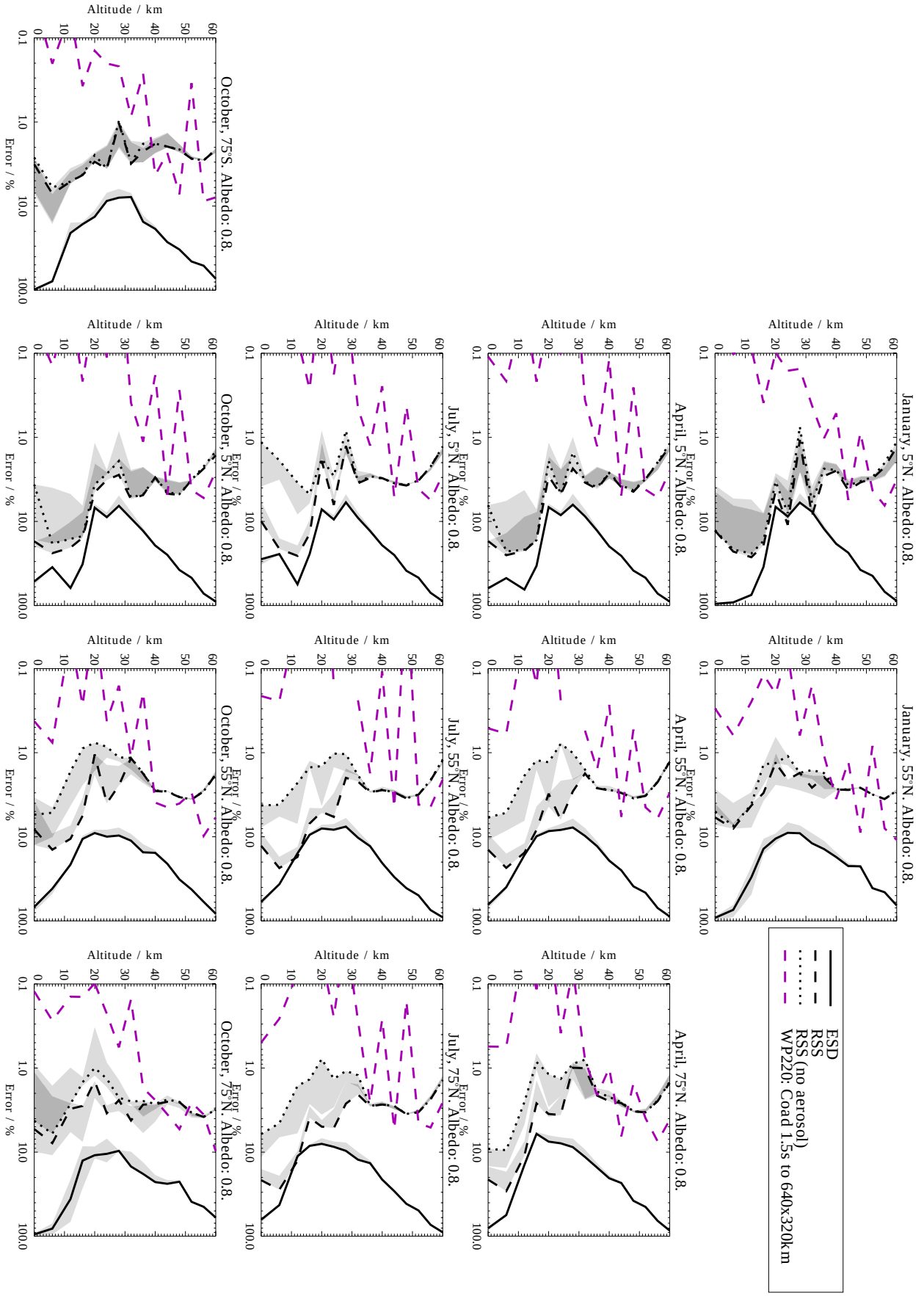

Figure C1.4.4: ESDs, RSS baseline errors and T2 summarised errors for all geotemporal scenarios, for Work Package 220 (Processing options for band 1A). Band 1 wavelength range: 265-314nm. Surface albedo: 0.8. Scenarios arranged by latitude (left to right) and season (top to bottom).

C1.5 Comparison of ESDs, base-line mapped errors and WP230 summarised errors over geo-temporal scenarios

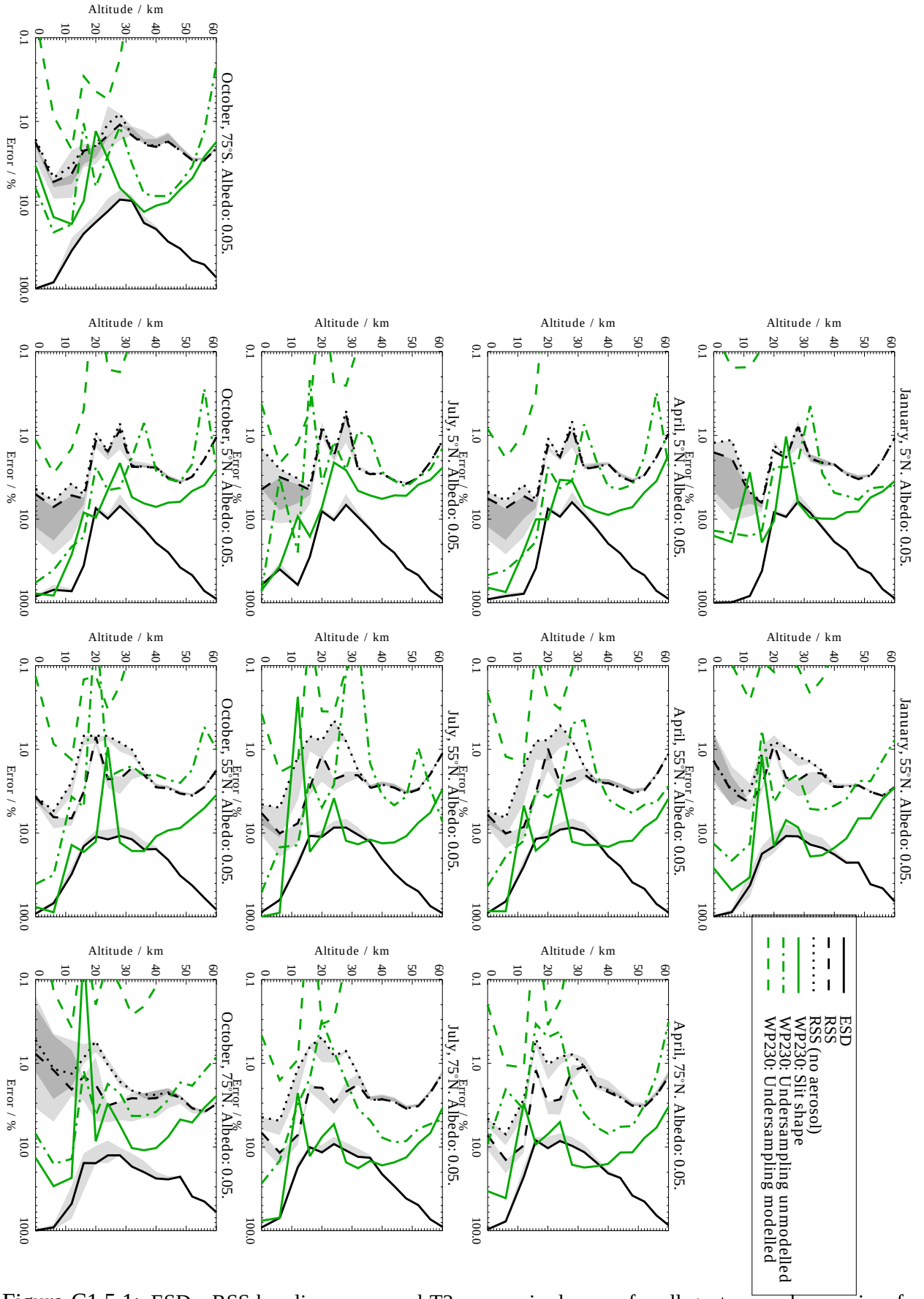

Figure C1.5.1: ESDs, RSS baseline errors and T2 summarised errors for all geotemporal scenarios, for Work Package 230 (Spectral resolution). Band 1 wavelength range: 265-307nm. Surface albedo: 0.05. Scenarios arranged by latitude (left to right) and season (top to bottom).

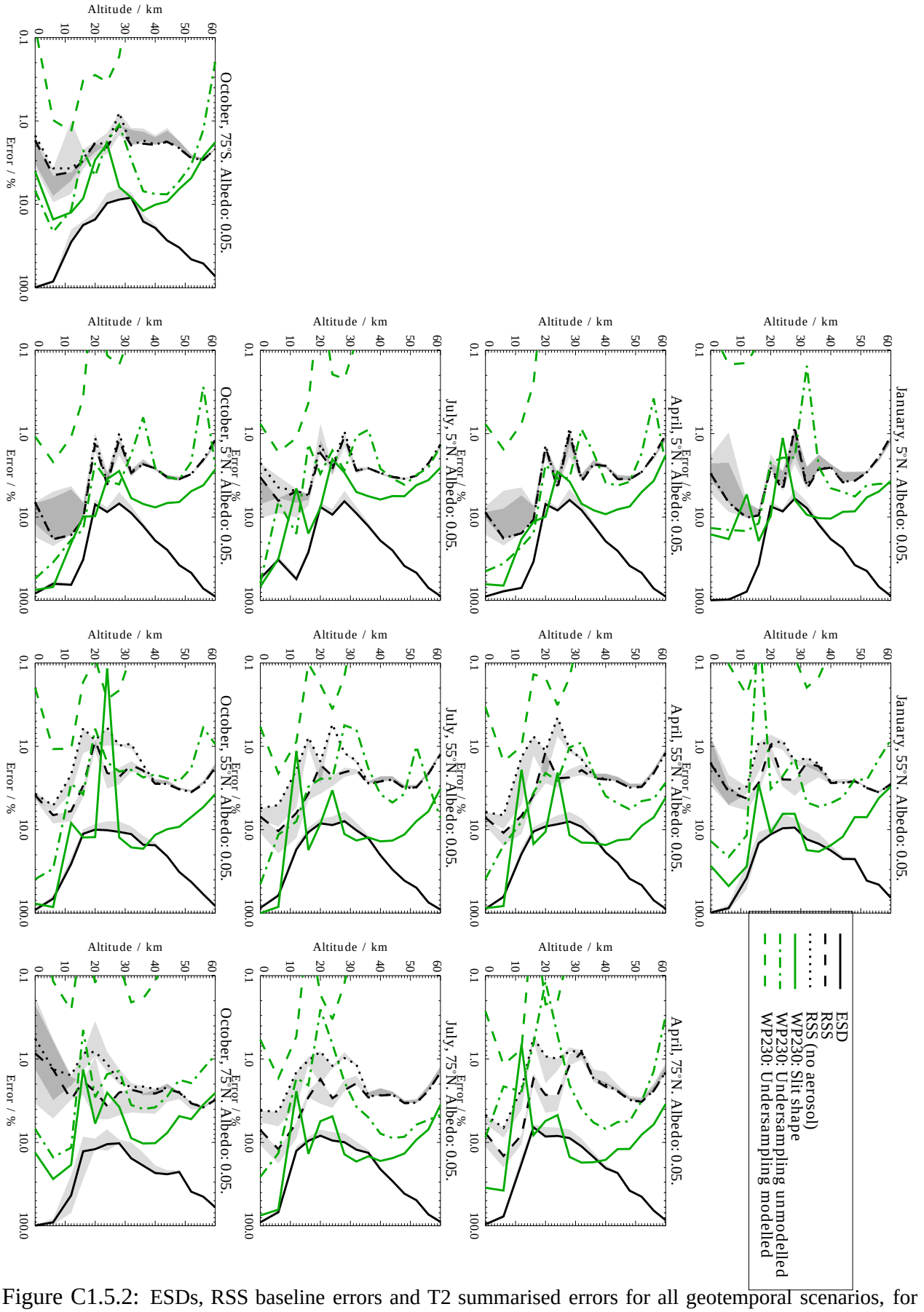

Figure C1.5.2: ESDs, RSS baseline errors and T2 summarised errors for all geotemporal scenarios, for Work Package 230 (Spectral resolution). Band 1 wavelength range: 265-314nm. Surface albedo: 0.05. Scenarios arranged by latitude (left to right) and season (top to bottom).

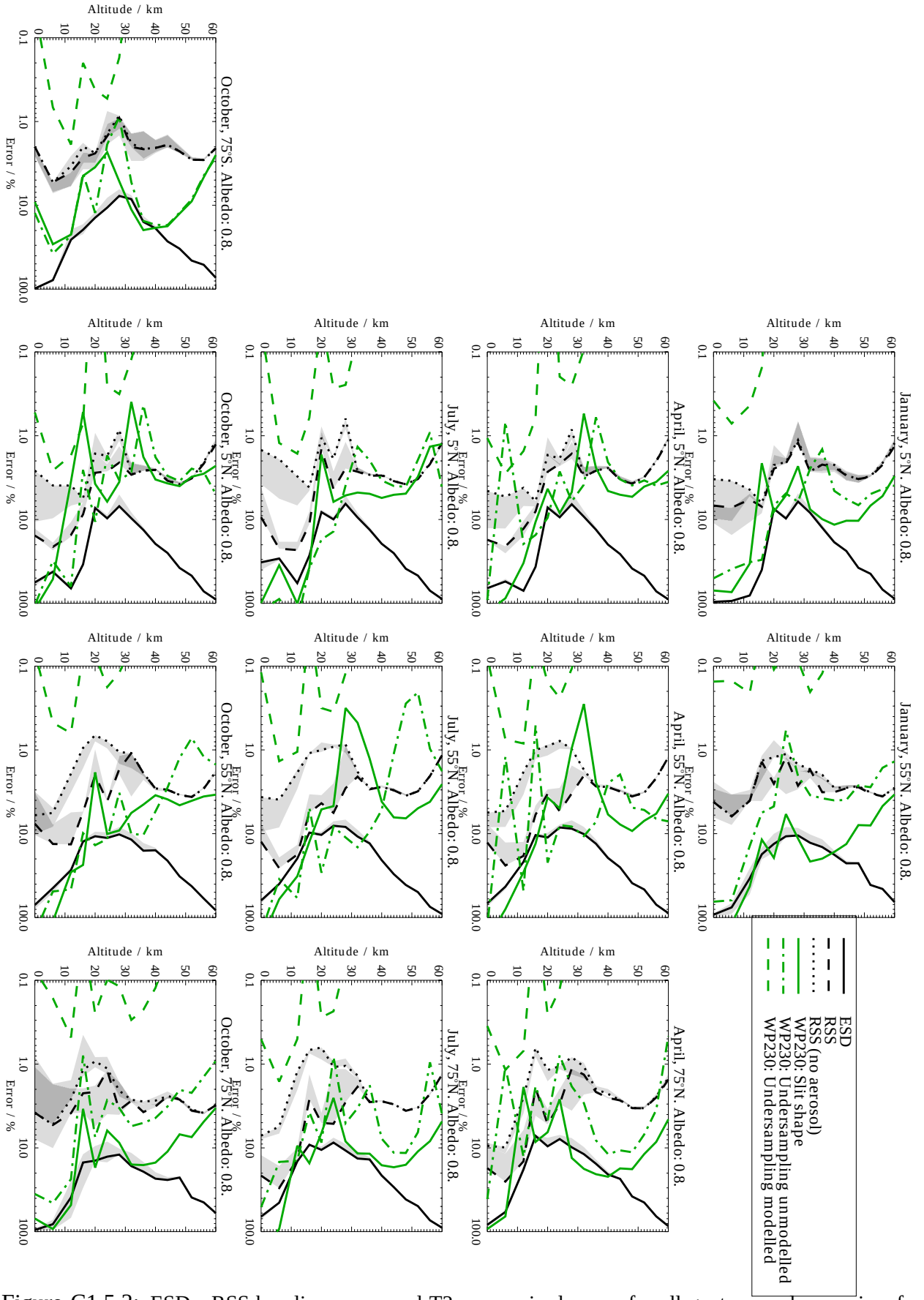

Figure C1.5.3: ESDs, RSS baseline errors and T2 summarised errors for all geotemporal scenarios, for Work Package 230 (Spectral resolution). Band 1 wavelength range: 265-307nm. Surface albedo: 0.8. Scenarios arranged by latitude (left to right) and season (top to bottom).

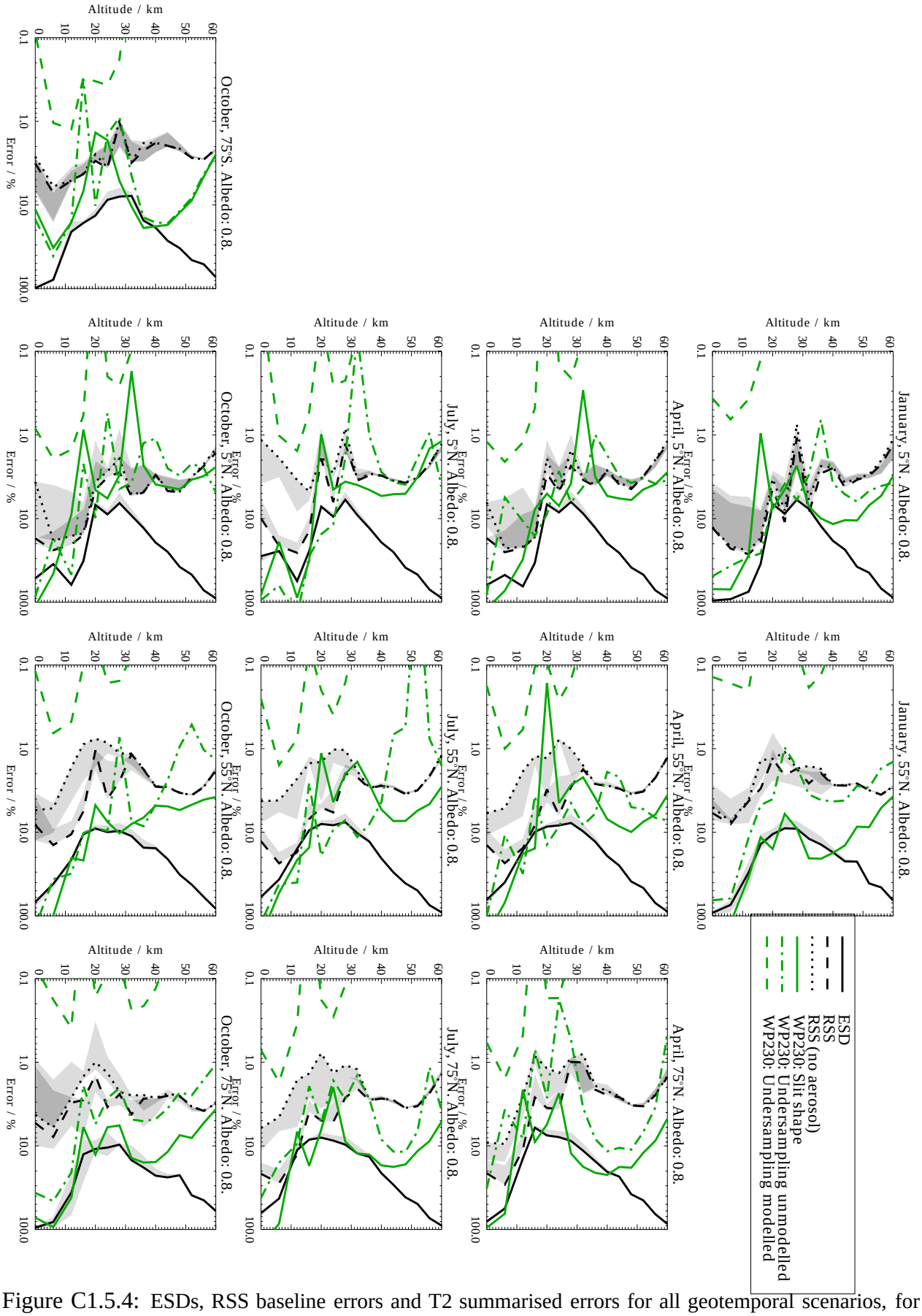

Figure C1.5.4: ESDs, RSS baseline errors and T2 summarised errors for all geotemporal scenarios, for Work Package 230 (Spectral resolution). Band 1 wavelength range: 265-314nm. Surface albedo: 0.8. Scenarios arranged by latitude (left to right) and season (top to bottom).

C1.6 Comparison of ESDs, base-line mapped errors and WP250 summarised errors over geo-temporal scenarios

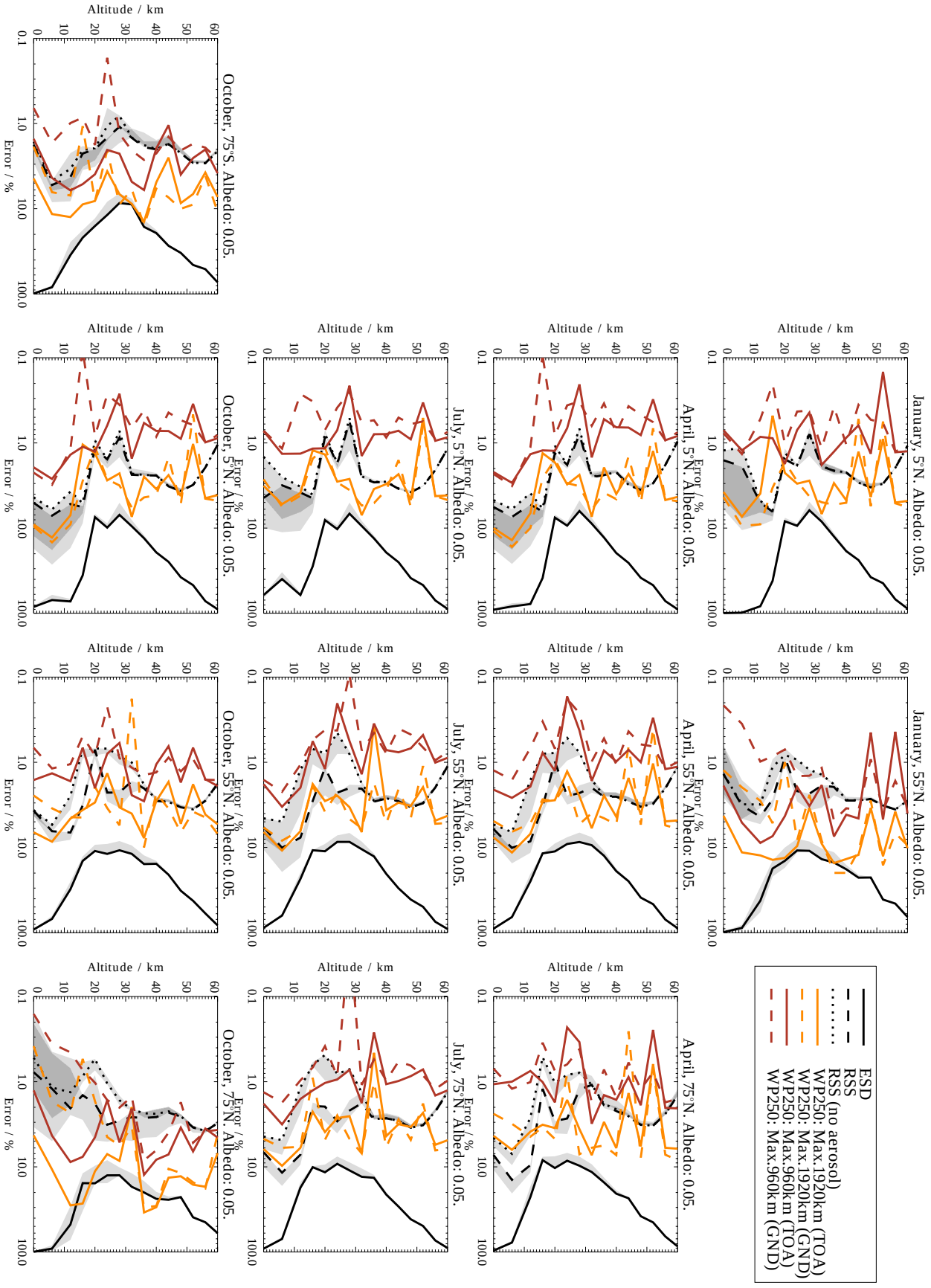

Figure C1.6.1: ESDs, RSS baseline errors and T2 summarised errors for all geotemporal scenarios, for Work Package 250 (Radiative transfer model assumptions). Band 1 wavelength range: 265-307nm. Surface albedo: 0.05. Scenarios arranged by latitude (left to right) and season (top to bottom).

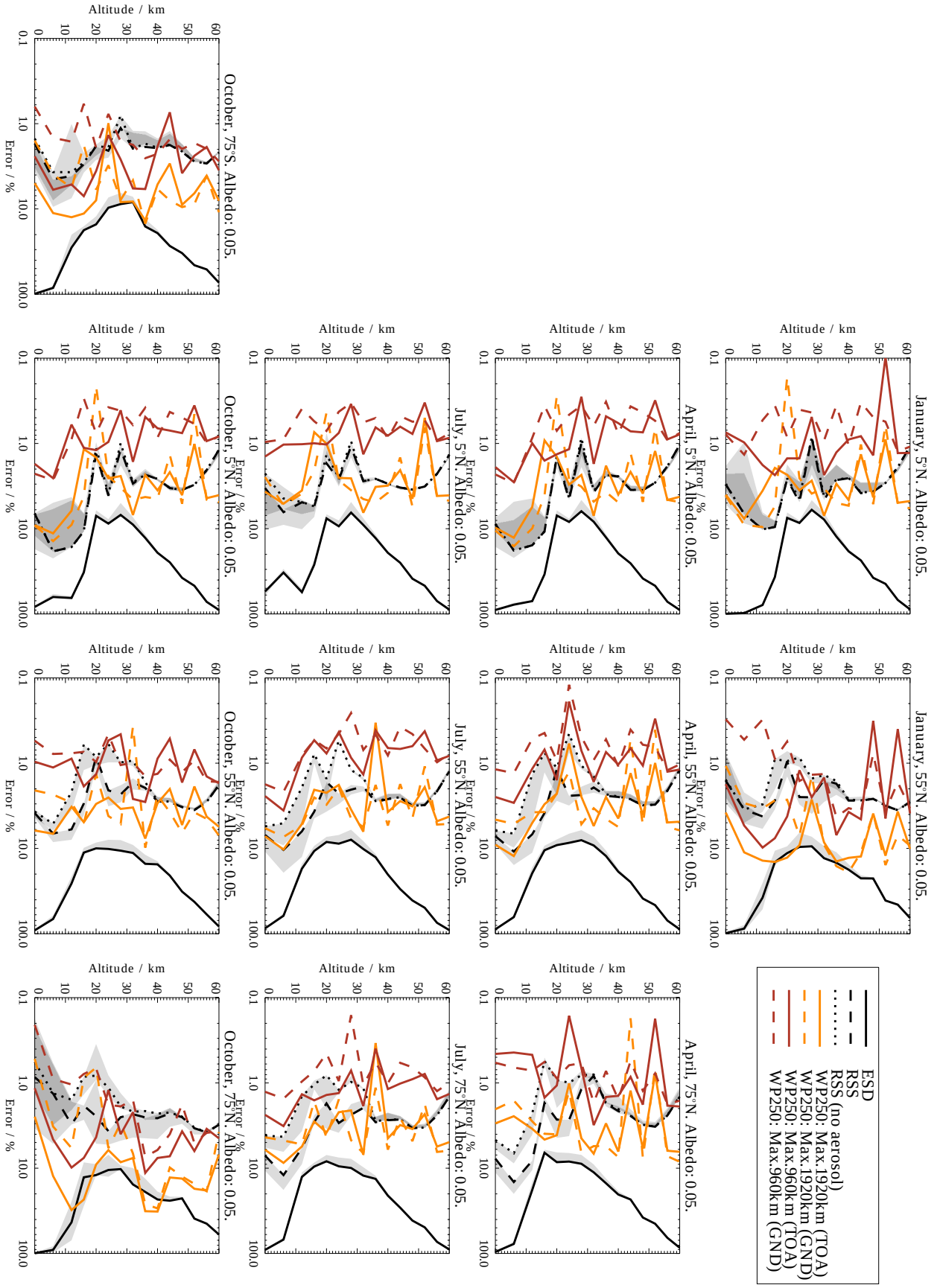

Figure C1.6.2: ESDs, RSS baseline errors and T2 summarised errors for all geotemporal scenarios, for Work Package 250 (Radiative transfer model assumptions). Band 1 wavelength range: 265-314nm. Surface albedo: 0.05. Scenarios arranged by latitude (left to right) and season (top to bottom).

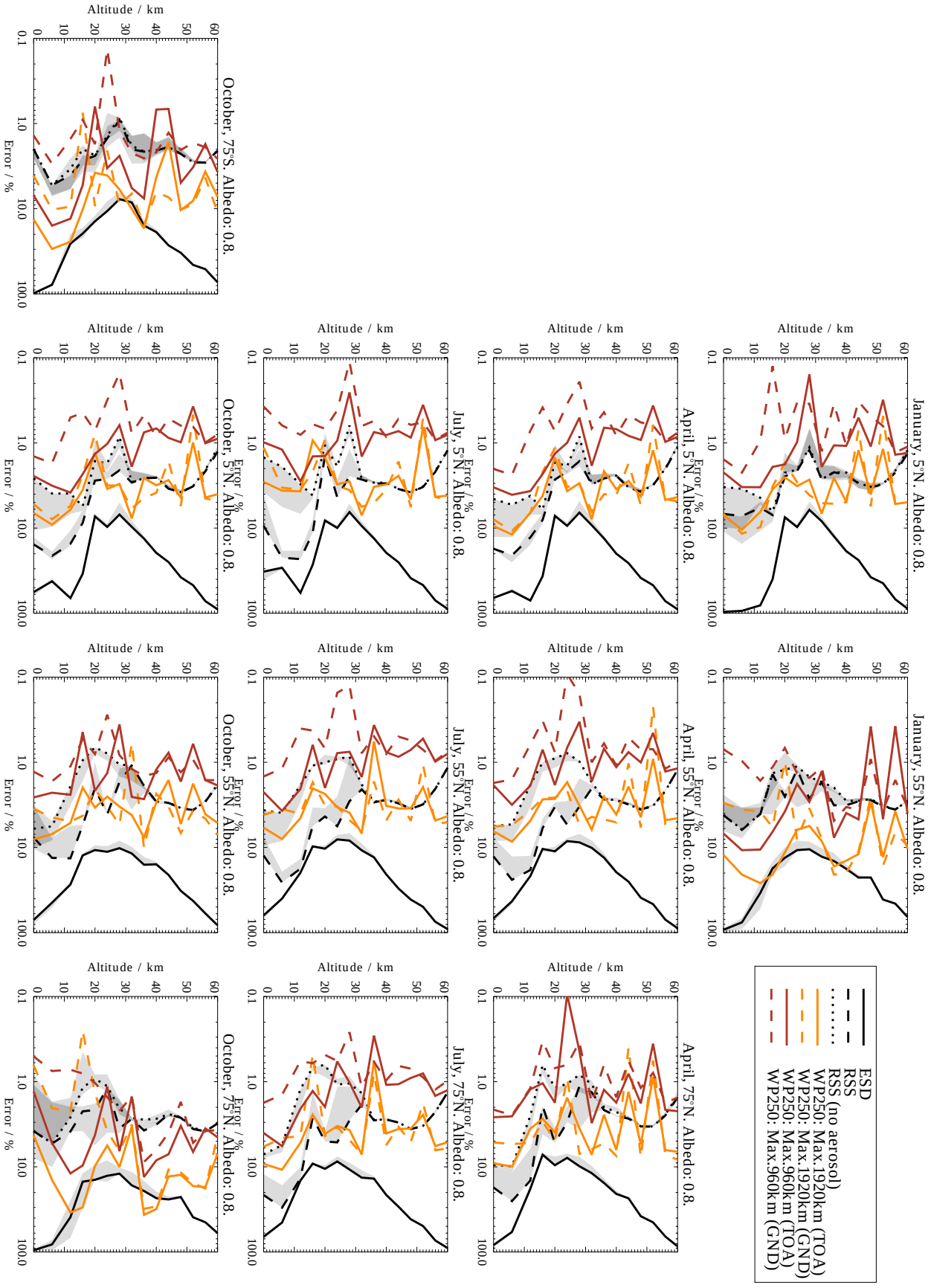

Figure C1.6.3: ESDs, RSS baseline errors and T2 summarised errors for all geotemporal scenarios, for Work Package 250 (Radiative transfer model assumptions). Band 1 wavelength range: 265-307nm. Surface albedo: 0.8. Scenarios arranged by latitude (left to right) and season (top to bottom).

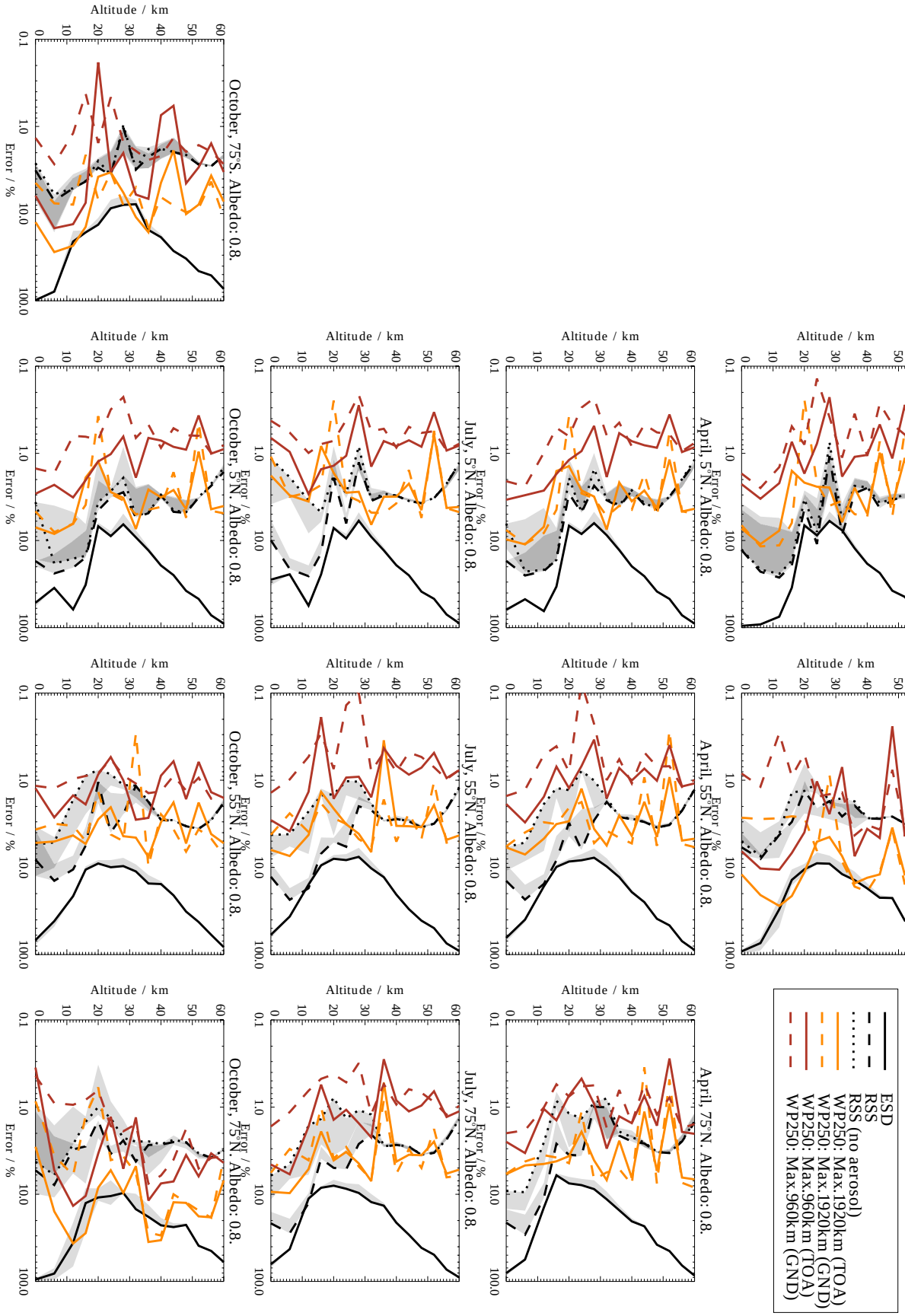

Figure C1.6.4: ESDs, RSS baseline errors and T2 summarised errors for all geotemporal scenarios, for Work Package 250 (Radiative transfer model assumptions). Band 1 wavelength range: 265-314nm. Surface albedo: 0.8. Scenarios arranged by latitude (left to right) and season (top to bottom).

C1.7 Comparison of ESDs, base-line mapped errors and WP260 summarised errors over geo-temporal scenarios

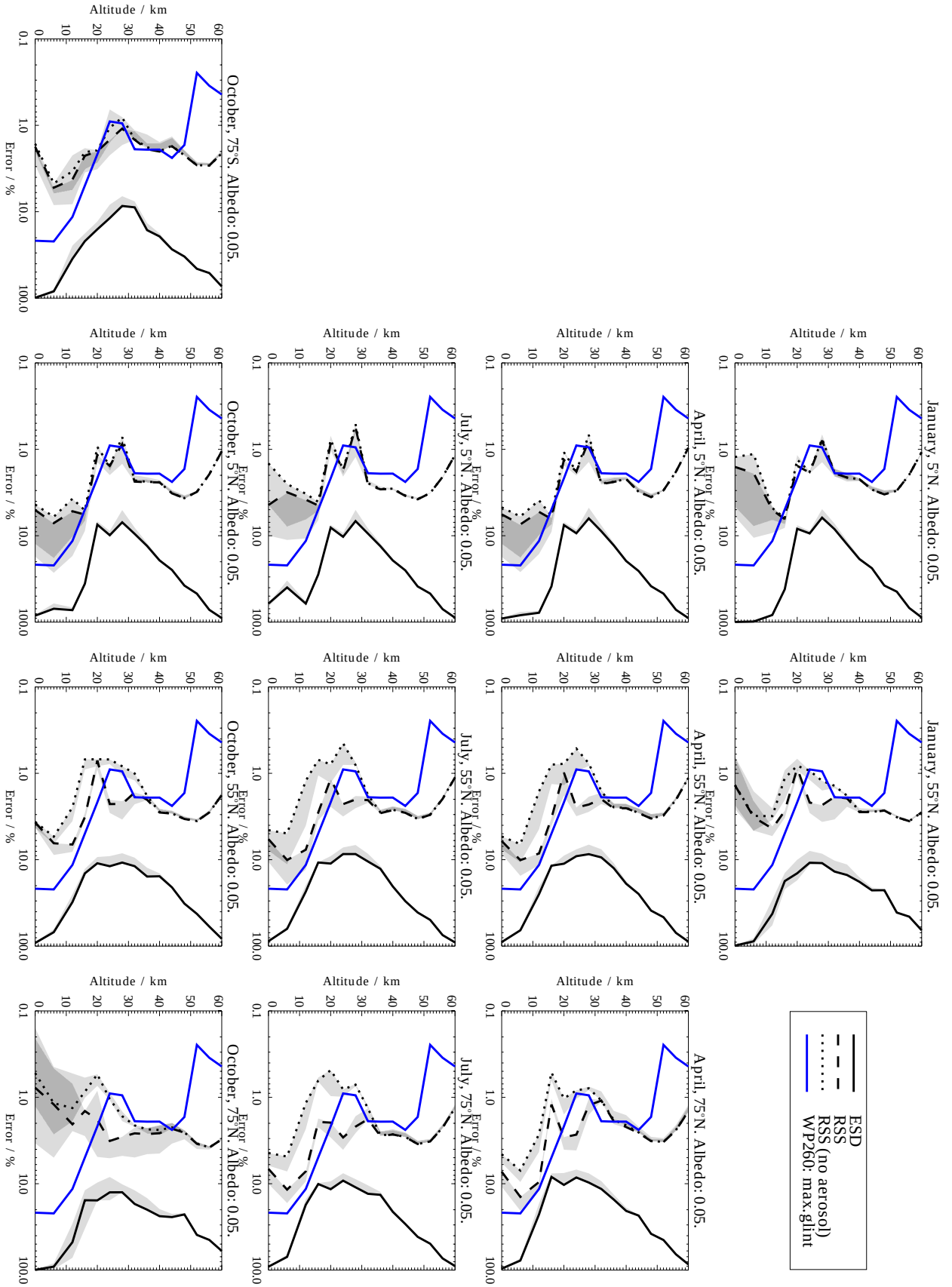

Figure C1.7.1: ESDs, RSS baseline errors and T2 summarised errors for all geotemporal scenarios, for Work Package 260 (Surface BRDF). Band 1 wavelength range: 265-307nm. Surface albedo: 0.05. Scenarios arranged by latitude (left to right) and season (top to bottom).

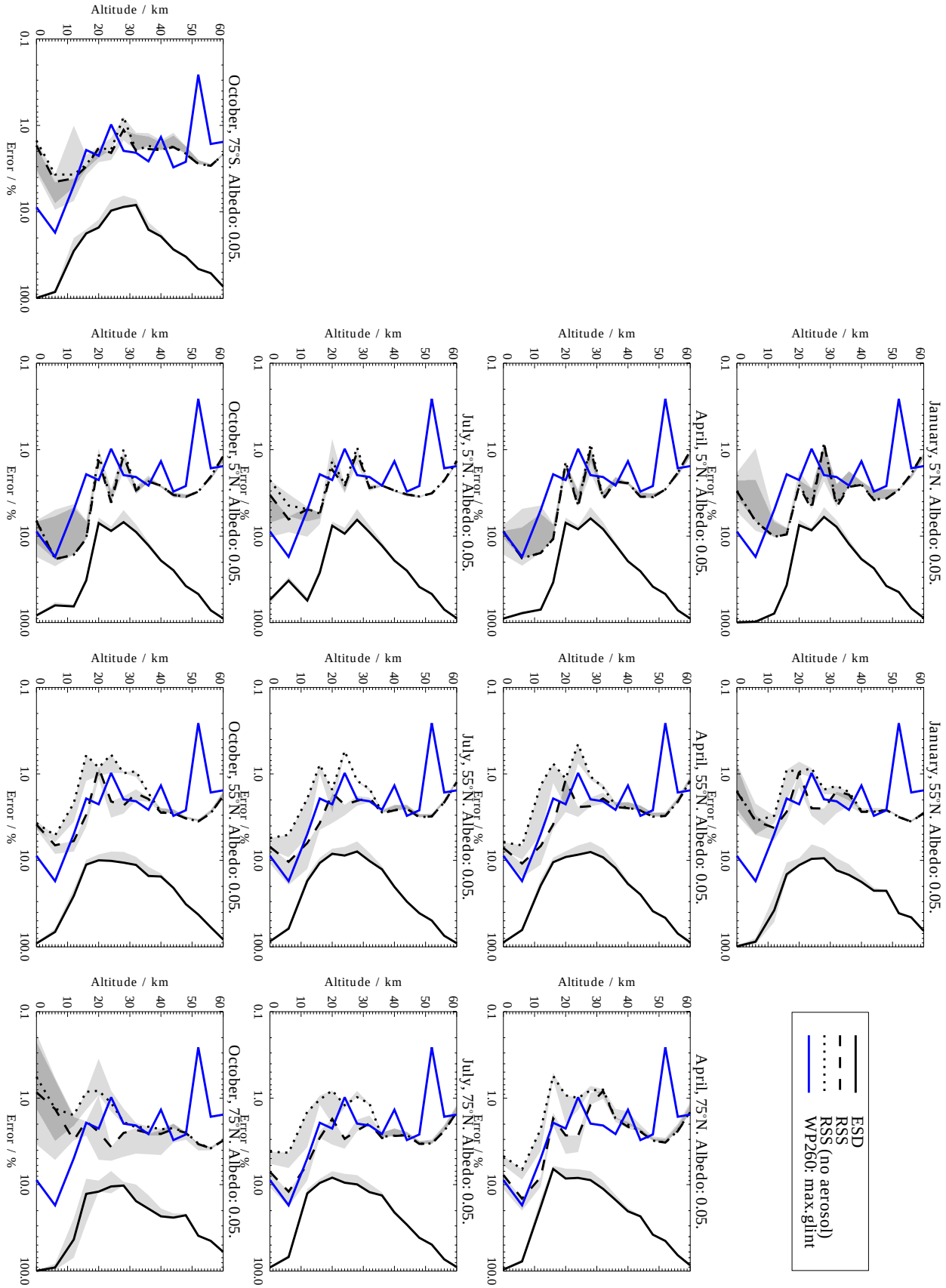

Figure C1.7.2: ESDs, RSS baseline errors and T2 summarised errors for all geotemporal scenarios, for Work Package 260 (Surface BRDF). Band 1 wavelength range: 265-314nm. Surface albedo: 0.05. Scenarios arranged by latitude (left to right) and season (top to bottom).

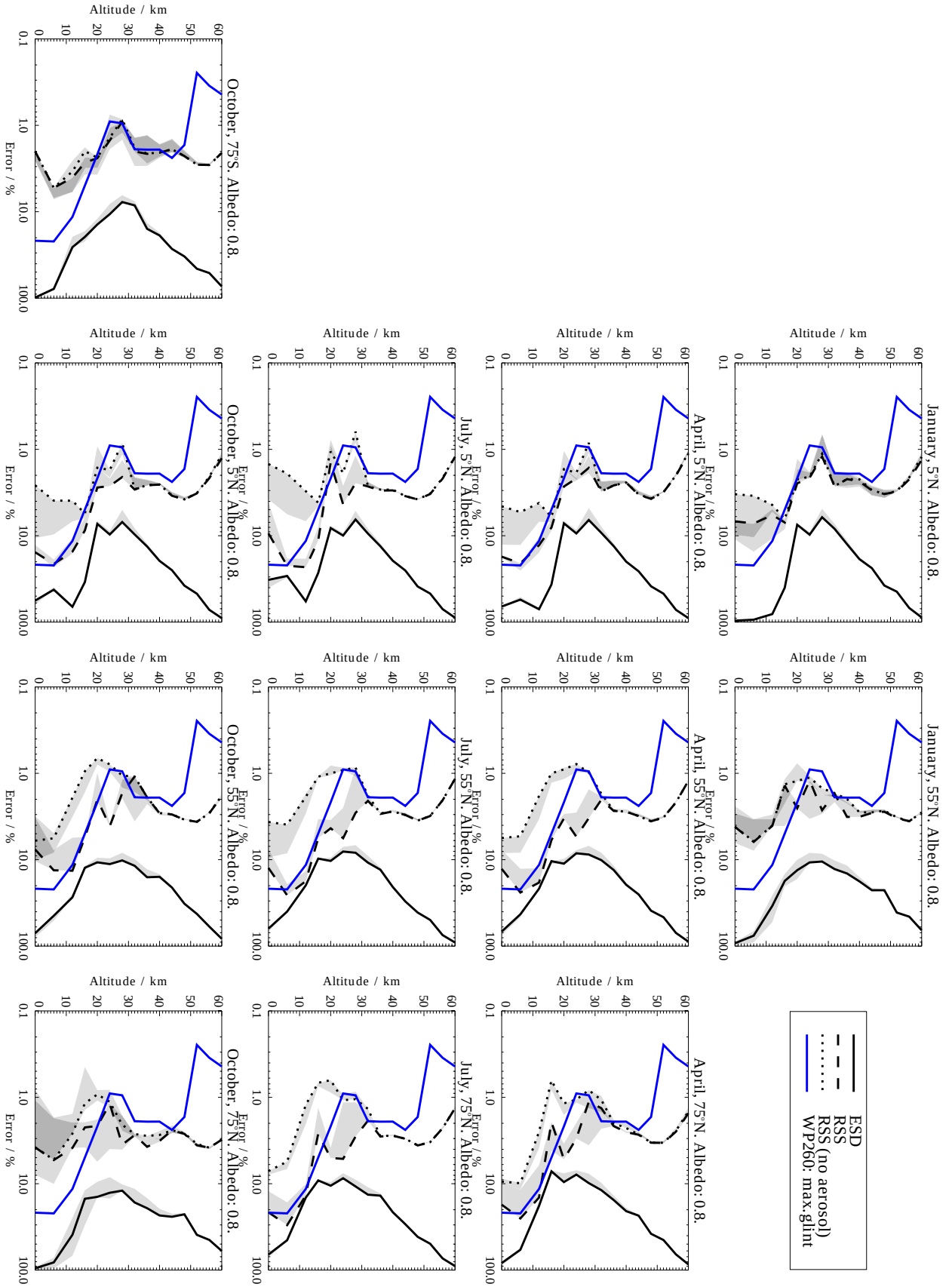

Figure C1.7.3: ESDs, RSS baseline errors and T2 summarised errors for all geotemporal scenarios, for Work Package 260 (Surface BRDF). Band 1 wavelength range: 265-307nm. Surface albedo: 0.8. Scenarios arranged by latitude (left to right) and season (top to bottom).

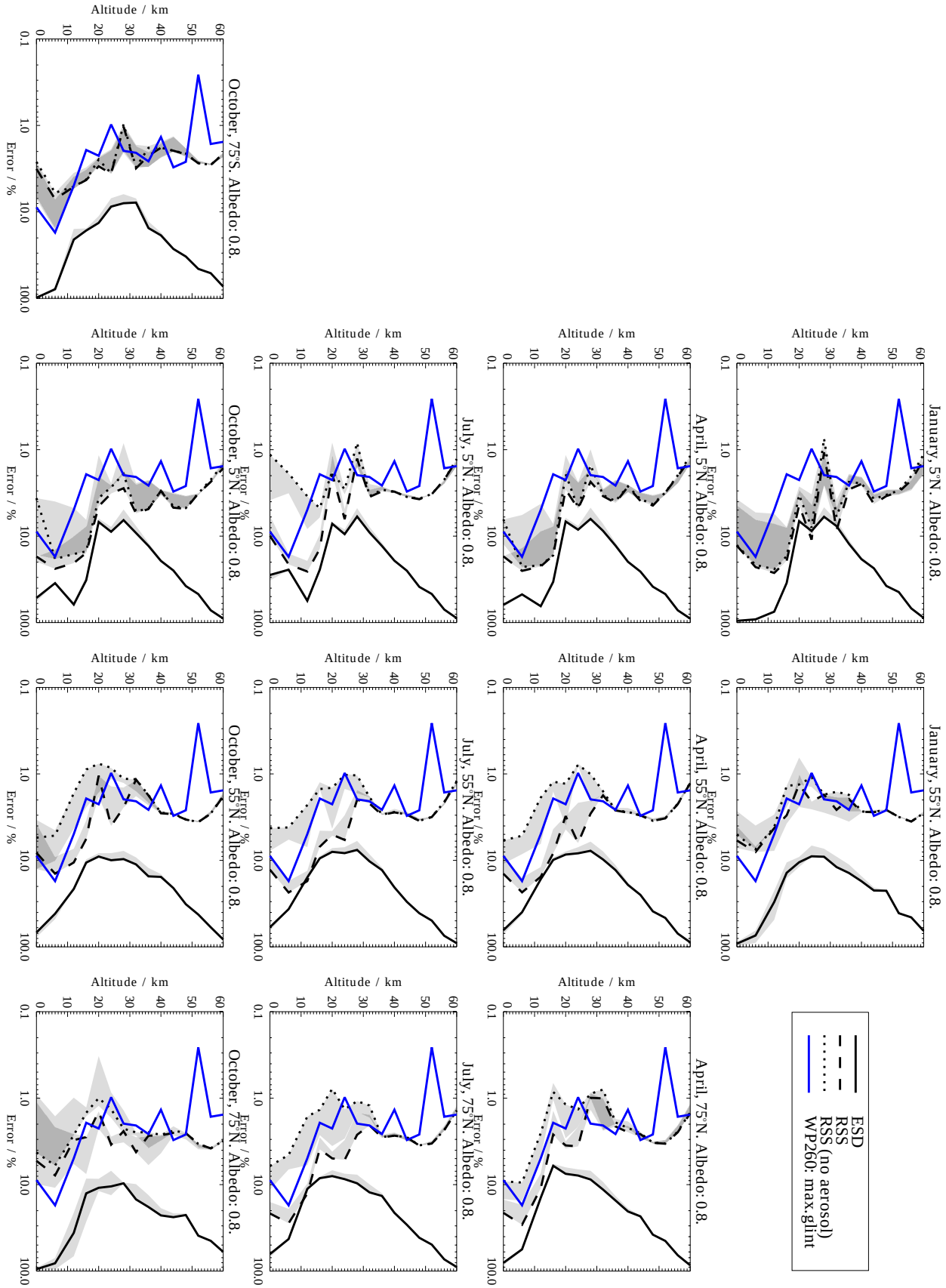

Figure C1.7.4: ESDs, RSS baseline errors and T2 summarised errors for all geotemporal scenarios, for Work Package 260 (Surface BRDF). Band 1 wavelength range: 265-314nm. Surface albedo: 0.8. Scenarios arranged by latitude (left to right) and season (top to bottom).

C1.8 Comparison of ESDs, base-line mapped errors and WP270 summarised errors over geo-temporal scenarios

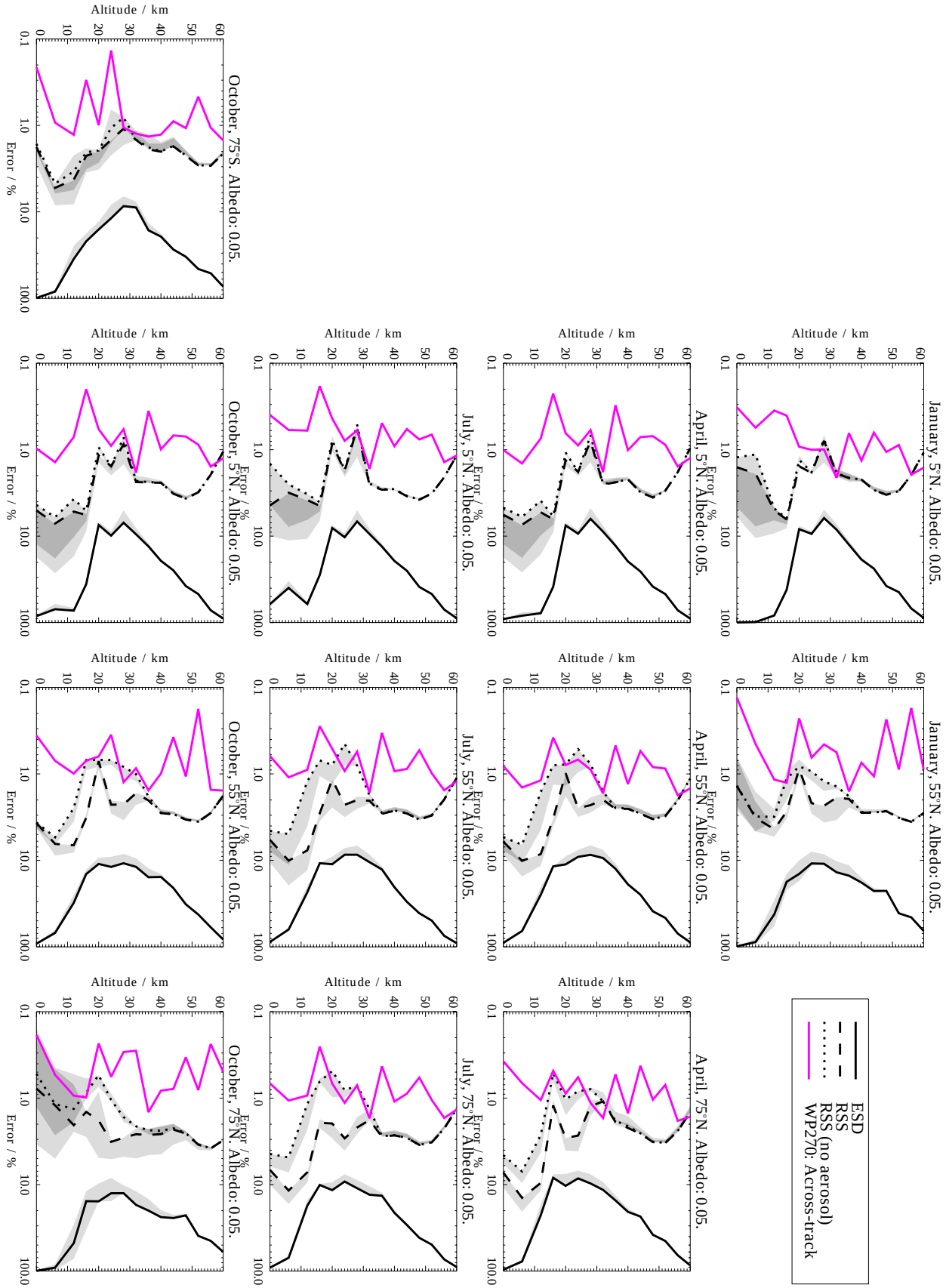

Figure C1.8.1: ESDs, RSS baseline errors and T2 summarised errors for all geotemporal scenarios, for Work Package 270 (Pointing). Band 1 wavelength range: 265-307nm. Surface albedo: 0.05. Scenarios arranged by latitude (left to right) and season (top to bottom).

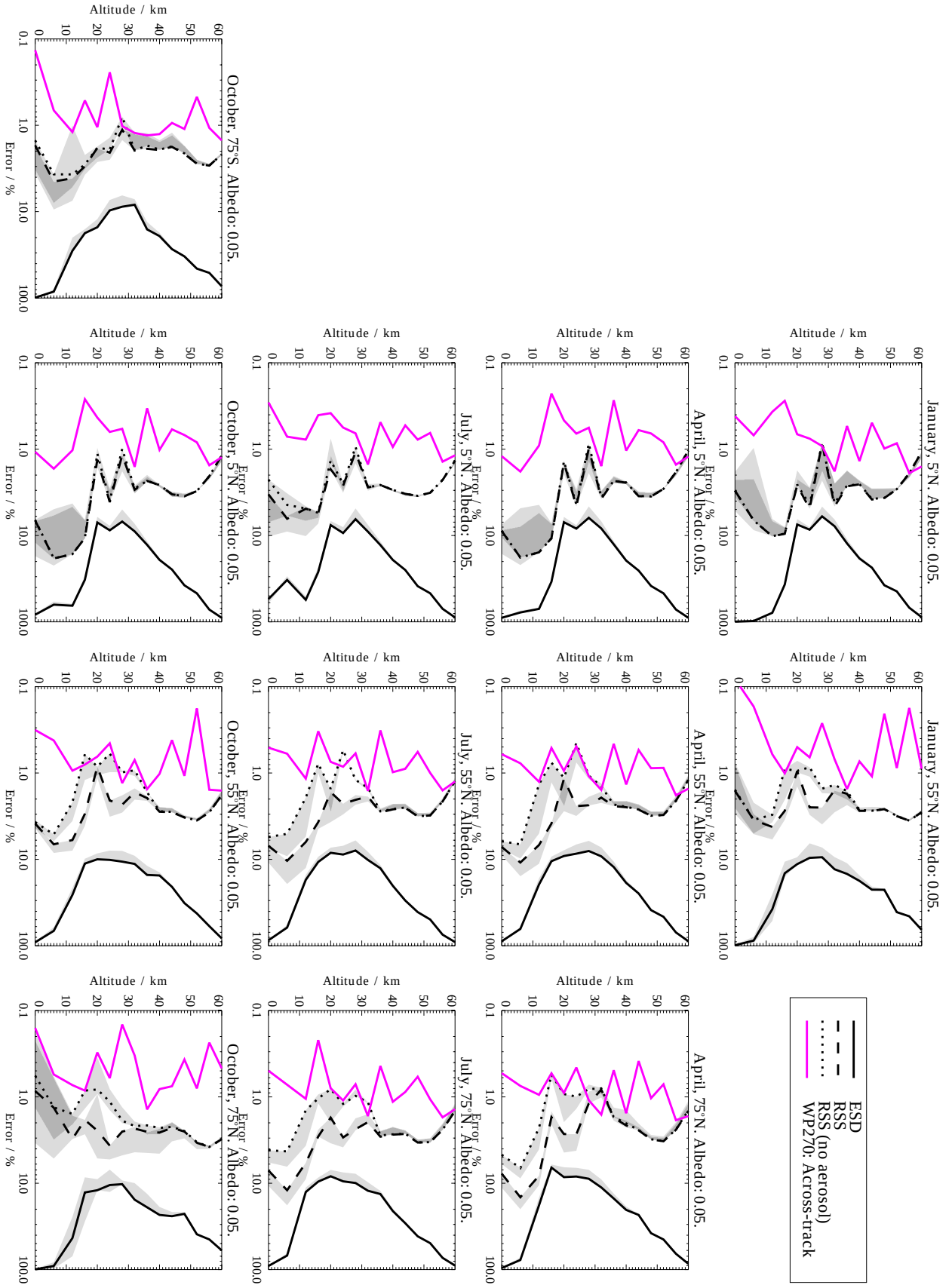

Figure C1.8.2: ESDs, RSS baseline errors and T2 summarised errors for all geotemporal scenarios, for Work Package 270 (Pointing). Band 1 wavelength range: 265-314nm. Surface albedo: 0.05. Scenarios arranged by latitude (left to right) and season (top to bottom).

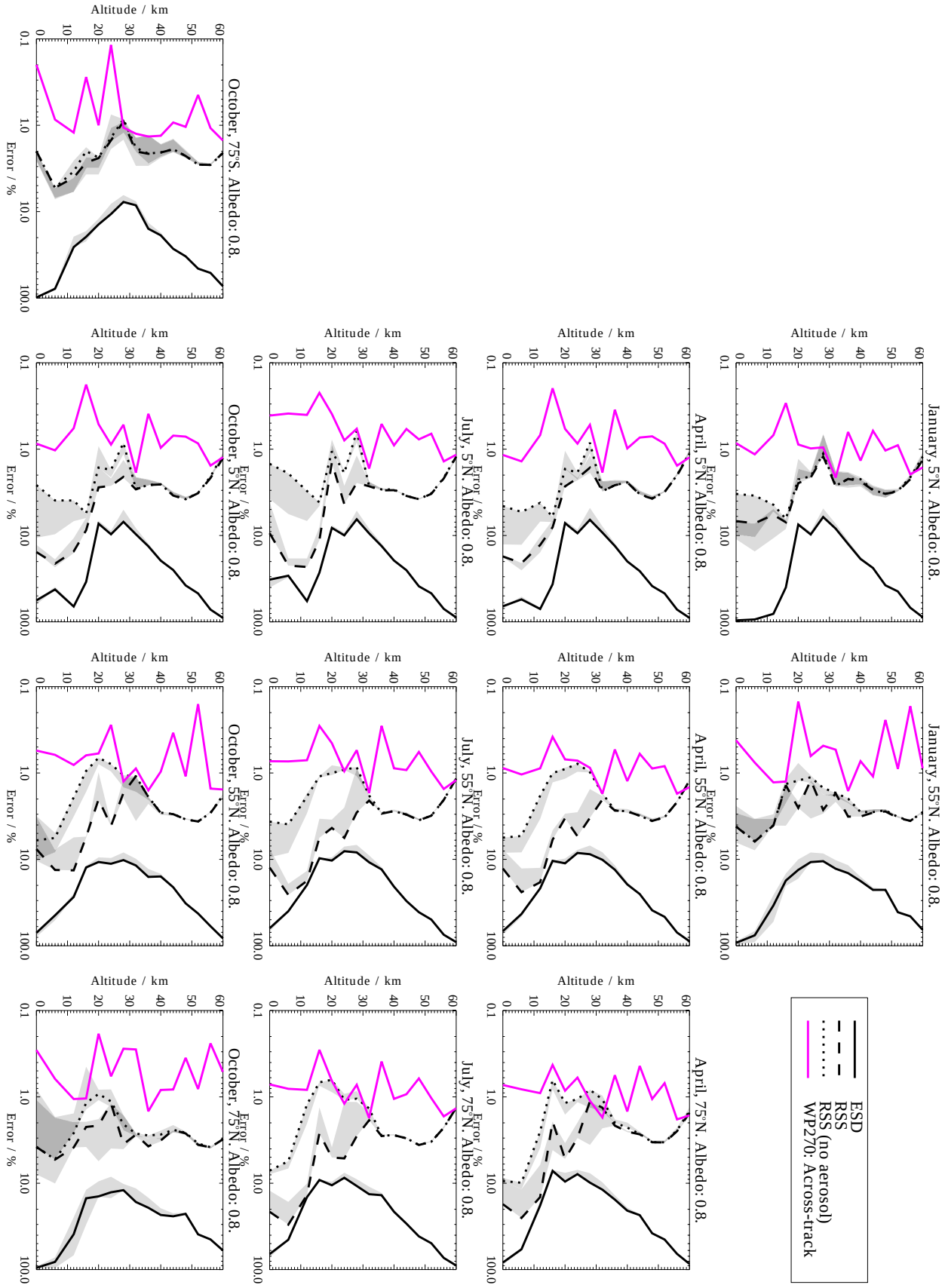

Figure C1.8.3: ESDs, RSS baseline errors and T2 summarised errors for all geotemporal scenarios, for Work Package 270 (Pointing). Band 1 wavelength range: 265-307nm. Surface albedo: 0.8. Scenarios arranged by latitude (left to right) and season (top to bottom).

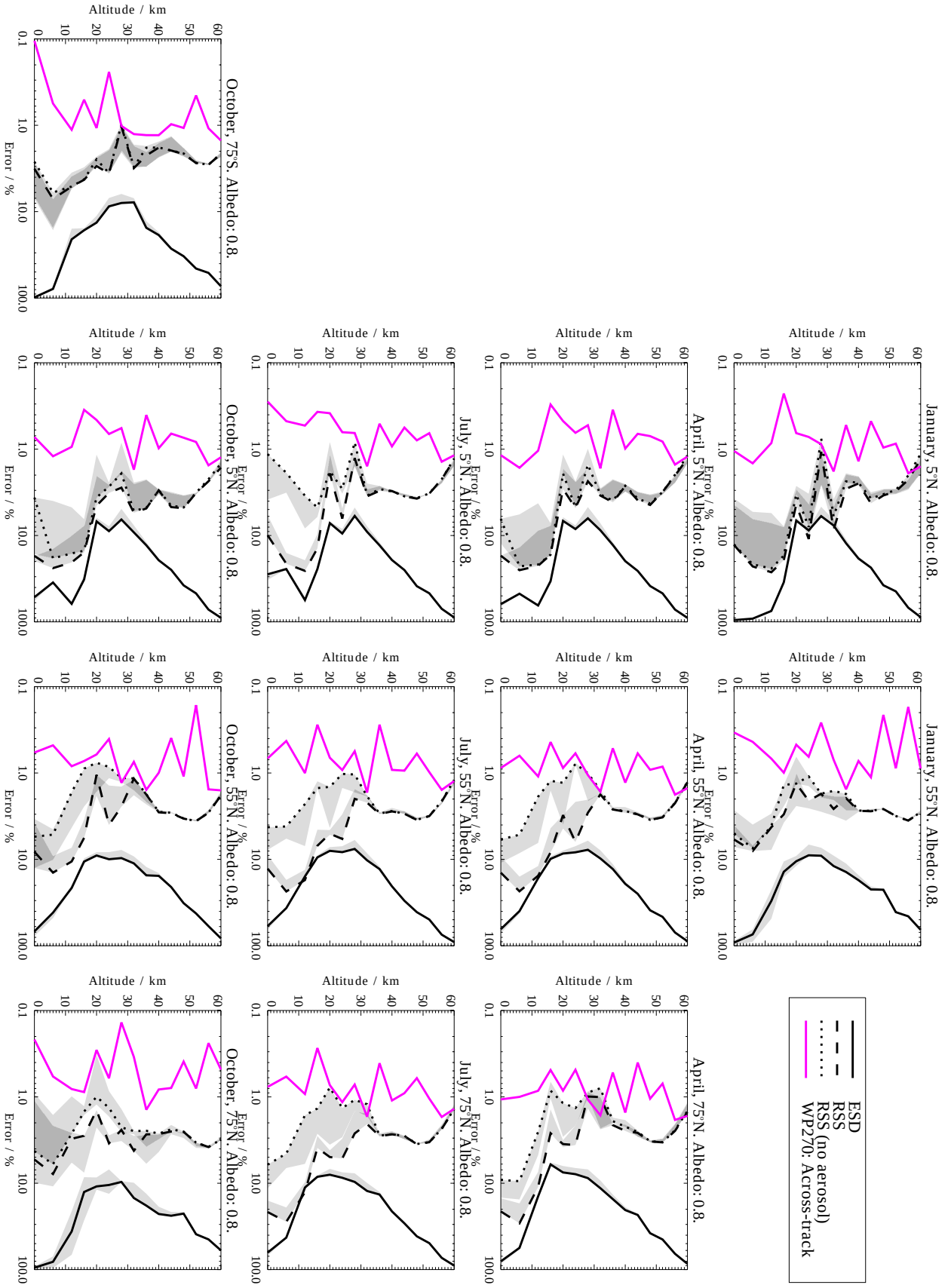

Figure C1.8.4: ESDs, RSS baseline errors and T2 summarised errors for all geotemporal scenarios, for Work Package 270 (Pointing). Band 1 wavelength range: 265-314nm. Surface albedo: 0.8. Scenarios arranged by latitude (left to right) and season (top to bottom).

C1.9 Comparison of ESDs and RSSs mapped errors for both B1 Coverage options

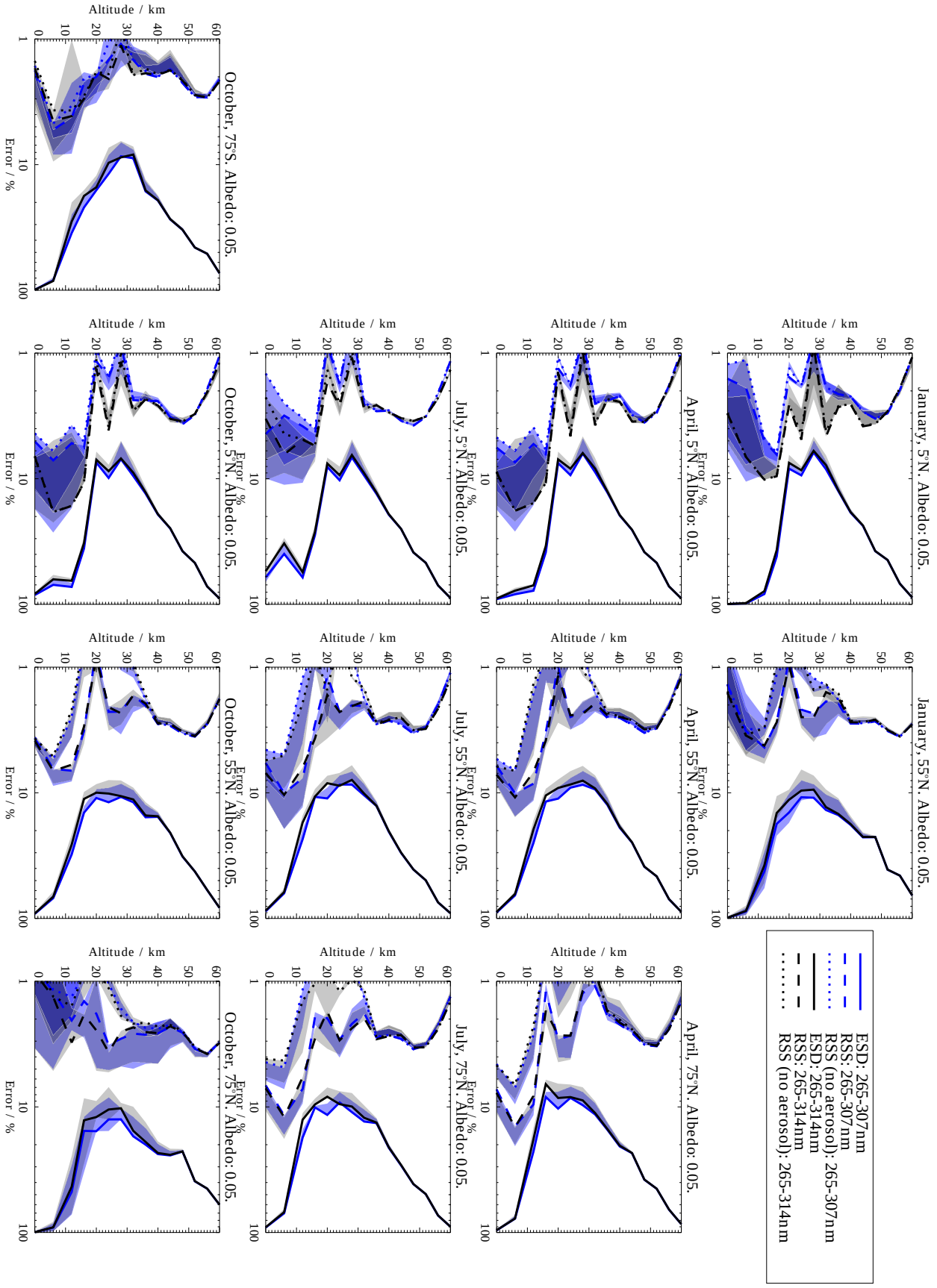

Figure C1.9.1: Comparison of ESDs, RSS baseline errors for both B1 coverage options and surface albedo 0.05.

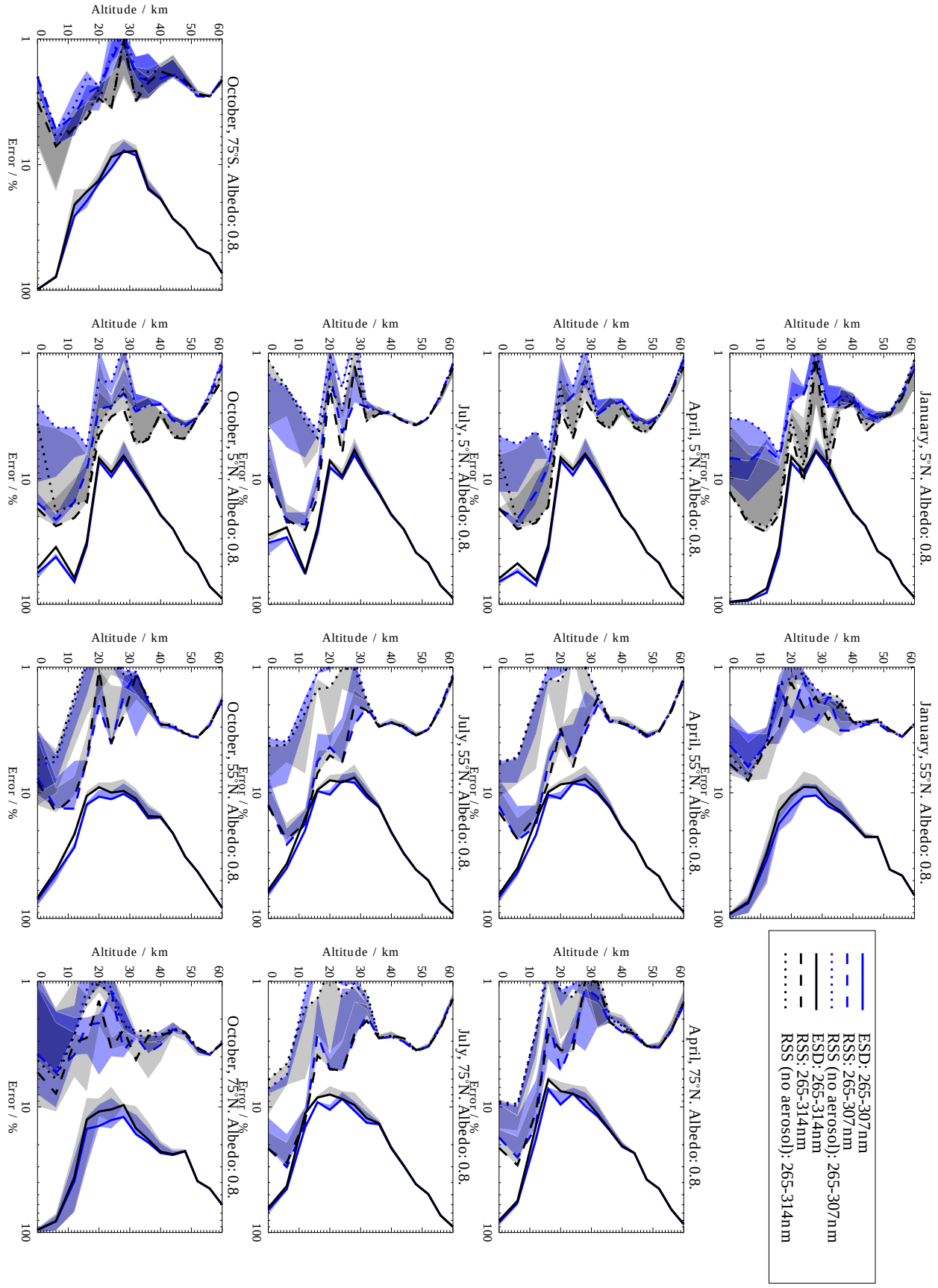

Figure C1.9.2: Comparison of ESDs, RSS baseline errors for both B1 coverage options and surface albedo 0.8.

GOME-2 Error Assessment

Appendix E

Experiences with SCIAMACHY

"Dichroic Features"

serco

Appendix E Experiences on SCIAMACHY "Dichroic Features" *(IUP)*

GOME-2 Error Assessment CD-ROM File: GOME-2_FR_Appendices.pdf

E Experiences on SCIAMACHY "Dichroic Features" *(IUP)*

E.1 Introduction

In the frame of the ESA Project SUPPRO (ESA/ESTEC Contract 13594/99/NL/PR) dedicated investigation to support the development and documentation of the SCIAMACHY Level 0-to-1b/c and the Level 1c-to-2 processing have been undertaken. Part of this have been focused on calibration issues, especially the polarisation correction processing.

In the frame of the SCIAMACHY Closed-Loop-Tests retrieval of fractional polarisation and the radiance polarisation correction application have been checked. Considered here is a distinct feature observed in on-ground measurements of SCIAMACHY channel3 around about 480 nm, which can be related to a dichroic mirror. Such measurements were used to characterize the polarisation sensitivity of SCIAMACHY.

E.2 SCIAMACHY Polarisation Correction Residuals

As for GOME-2, in SCIAMACHY a dichroic mirror splits off the light beam of wavelength range for channel 3, whereas light for channel 4 is transmitted. The end-to-end complete instrument is very sensitive to the polarisation state of the incident light. The dichroic mirror is the most polarisation sensitive optical element within the channel 3 optical path. It introduces spectral features into the polarisation characterisation measurements, which are part of the calibration key data (eta and zeta, see Figure E-1). In case of unperfected polarisation state retrieval, which is always present to a certain extend, these features are transferred to calibrated radiances via the polarisation correction scheme.

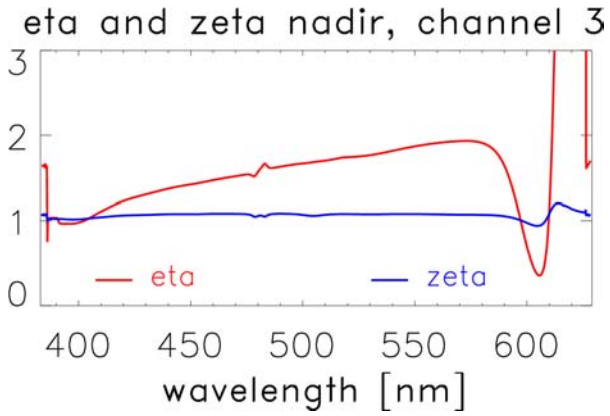

Figure E-1: Instrumental polarisation sensitivities to s-polarised (eta) and 45°-polarised input light (zeta)

The complete polarisation correction/characterisation is performed using information from the interchannel overlap regions, the 6-detector signal from the main Polarisation Measurement Device (PMD) unit, and from a seventh PMD detector. This seventh PMD detector is added to provide enough independent equations to characterise the complete system in the limb mode. A polarisation correction factor c_{pol} is applied onto radiances, which for the case of the tests made have known input polarisation. The ratio of such corrected radiance and an un-polarised reference is called Polarisation Correction Residual (PCR, see e.g. Figure E-2). For the ideal case, these should be equal to one.

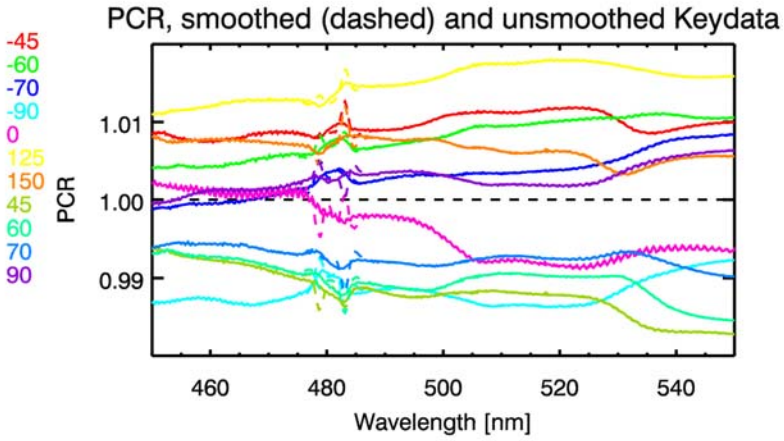

Figure E-2: Polarisation Correction Residuals for input light with various polarisation states

Polarisation Correction Residuals for input light having various polarisation states, parameterised via the Brewster-polariser angle (see legend in diagram). Dichroic features can be clearly identified

Potential sources of structured PCR are processing inaccuracies and the un-polarised reference, which has been generated by taking an adequate average of all available measurements. The sensitivity of DOAS retrieval for such structures has been investigated by directly fitting PCR spectra. The principle idea bases on the DOAS equation simplified for one absorber:

$$ln\frac{Rad}{Irr} = -\sigma * SC + Pol_1$$

where Rad is the radiance, Irr is the solar irradiance, σ is the absorption cross-section coefficient of the absorber, SC is the slant column density of the absorber, which is the fitting parameter, and Pol is a polynomial to account for broadband features. Including the PCR ratio $\frac{c_{pol}Rad_{pol}}{Rad}$ yields

$$ln\left(\frac{c_{pol}Rad_{pol}}{Rad} \times \frac{Rad}{Irr}\right) = -\sigma * SC^* + Pol_2 \,,$$
$$ln\frac{c_{pol}Rad_{pol}}{Rad} + ln\frac{Rad}{Irr} = -\sigma * SC^* + Pol_2 \,,$$

where Rad_{pol} is the measured radiance before polarisation correction. In the ideal case it is c_{pol} x Rad_{pol} = Rad, SC = SC^*, and ln(PCR) = 0. Including the first equation enables to identify a DOAS equation for the error term ΔSC = SC - SC^* as fitting parameter:

$$lnPCR - \sigma * SC + Pol_1 = -\sigma * SC^* + Pol_2 \,,$$
$$lnPCR = \sigma * SC + Pol_1 - \sigma * SC^* + Pol_2 \,,$$
$$lnPCR = \sigma * (SC - SC^*) + Pol_1 + Pol_2 \,,$$
$$lnPCR = \sigma * \Delta SC + Pol_3 \,.$$

Fitting ΔSC directly gives the error on SC w.r.t. PCR. For the case of ideal polarisation correction ΔSC equals zero.

DOAS fittings have been made using observed (Closed-Loop Tests) and simulated PCR, which have been calculated using eta and zeta functions (Figure 1-1) and true and erroneous Q and U components to calculate polarisation correction factors c_{pol} and c'_{pol}. The simulated erroneous radiance is: c'_{pol} x Rad_{pol} = c'_{pol} x 1/ c_{pol} = Rad', where the input radiance is the inverse of the true c_{pol}.

As an example, Figure E-3 shows the differential PCR from observations using 70°-polarised input light (dotted red) and the fitted O_3 cross-sections (dotted blue), which represents a column density of 1.4E18 p.cm^{-2}. Figure E-2 also shows similar results for PCR simulated as described using 5% errors in both, Q and U Stokes components (solid). A Column density of 2.5E18 p.cm^{-2} has been derived as ΔSC. The same fitting window as have been used in the GOME-2 study has been applied. For orientation, a typical magnitude of an O_3-slant column is about 2E19 for Nadir, April 55°N.

Observed PCR and simulations are not consistent in many respects. The polarisation correction uses spectra of the stokes components, a spectrally constant error as applied is unrealistic, the quality of the un-polarised reference is questionable, etc.. Also the evidence of such extreme polarisation is unrealistic for real situations in orbit and is therefore a worst-case scenario. This means, the presented results, which are preliminary, can only be used to draw general qualitative conclusions.

However, the study should emphasize the importance of an accurate polarisation correction scheme especially for spectral windows, which contain distinct instrumental features, even if the instrumental polarisation characteristic is accurate.

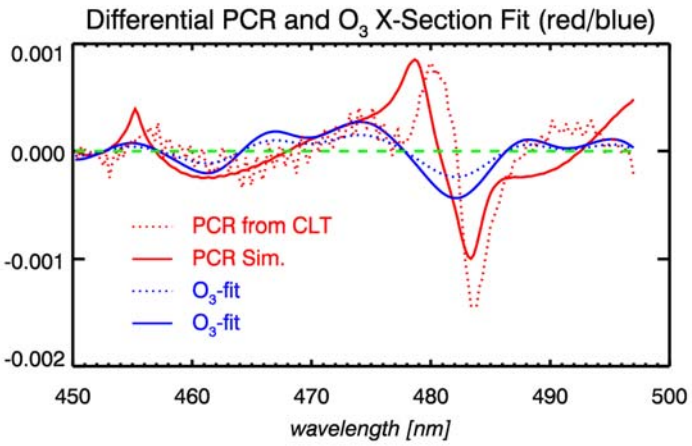

Figure E-3 **Fit of observed PCR for 70°-polarised input light using SCIAMACHY processor**

Fit of PCR observed for 70°-polarised input light using the SCIAMACHY Level 0-to-1b prototype processor. Red: differential PCR, blue: fitted O_3–cross-sections, representing a column density of 1.2E18 p.cm^{-2} (a spectral shift can be introduced e.g. due to differences in the polynomial fitting).

E.3 References

[E-1] SCIAMACHY Level 0-to-1 Processor Closed-Loop Tests, R. de Beek et al., Technical Report (ESA/ESTEC Contract 13594/99/NL/PR), IFE-SCIA-TR-280601, Issue 1, January 2002